INL/EXT-10-19973

High Temperature Reactor (HTR) Deep Burn Core and Fuel Analysis

Design Selection for the Prismatic Block Reactor

Francesco Venneri
Chang-Keun Jo
Jae-Man Noh
Yonghee Kim
Claudio Filippone
Jonghwa Chang
Chris Hamilton
Young-Min Kim
Ji-Su Jun
Moon-Sung Cho
Hong-Sik Lim
Michael A. Pople
Abderrafi M. Ougouag
Vincent Descotes

September 2010

The INL is a U.S. Department of Energy National Laboratory
operated by Battelle Energy Alliance

INL/EXT-10-19973
FCRD-Fuel- 2010-000197

High Temperature Reactor (HTR) Deep Burn Core and Fuel Analysis
Design Selection for the Prismatic Block Reactor

Francesco Venneri[1]
Chang-Keun Jo[2]
Jae-Man Noh[2]
Yonghee Kim[3]
Claudio Filippone[1]
Jonghwa Chang[2]
Chris Hamilton[1]
Young-Min Kim[2]
Ji-Su Jun[2]
Moon-Sung Cho[2]
Hong-Sik Lim[2]
Michael A. Pople
Abderrafi M. Ougouag
Vincent Descotes

[1]LOGOS NS
[2]KAERI
[3]UNIST

September 2010

Idaho National Laboratory
Fuel Cycle Research & Development
Idaho Falls, Idaho 83415

http://www.inl.gov

Prepared for the
U.S. Department of Energy
Office of Nuclear Energy
Under DOE Idaho Operations Office
Contract DE-AC07-05ID14517

Author:

Michael A. Pope 9/29/2010

Reviewed by:

Brian Boer 9/29/2010

Concurred by:

Abderrafi M. Ougouag 9/29/2010
(Work Package Manager)

CONTENTS

FIGURES

TABLES

Acronyms

ALWR	advanced light water reactors
BAF	Bacon Anisotropy Factor
BOC	Beginning of Cycle
BP	burnable poison
CB	Core barrel
CFD	computational fluid dynamics
CFP	coated fuel particle
CR	Control rod
DB	deep burn
DB	Deep Burn
DH	Double Heterogeneity
EFPD	effective full power day
ENDF-B/VII	Evaluated Nuclear Data Files
EOC	End of Cycle
FA	Fuel Assembly
FB	fuel block
FEM	finite element method
FIMA	fissions per initial metal atom
FP	fission product
FTC	fuel temperature coefficient
GA	General Atomics
GCR	Gas Cooled Reactor
HM	Heavy Metal
HTR	high-temperature reactor
INL	Idaho National Laboratory
IPyC	inner high-density pyrocarbon
JAEA	Japan Atomic Energy Agency
KAERI	Korean Atomic Energy Research Institute
LANL	Los Alamos National Laboratory
LPCC	low-pressure conduction cooling
LWR	Light Water Reactor
MCNP5	Monte Carlo N-Particle

MHR	modular helium reactor
MOC	Middle of Cycle
MTC	moderator temperature coefficient
PF	packing fraction
PF	packing fraction
RCCS	Reactor Cavity Cooling System
RCS	Reactor Cooling System
RPT	Reactivity-equivalent Physical Transformation
RPV	Reactor Pressure Vessel
RSC	Reserved Shutdown Channel
SC	self-cleaning
SHEM	Santamarina-Hafeidh Energy Mesh
TPEN	Triangle-based Polynomial Expansion Nodal
TRISO	tri-isotropic
TRU	transuranic
VCS	Vessel Cooling System
VHTR	Very High-Temperature Reactor

HIGH TEMPERATURE REACTOR (HTR) DEEP BURN CORE AND FUEL ANALYSIS

DESIGN SELECTION FOR THE PRISMATIC BLOCK REACTOR

1. SIGNIFICANT ACCOMPLISHMENTS

In Phase II of the Deep Burn Project, we conducted the nuclear analysis of transuranic (TRU) destruction/utilization in the high-temperature helium-cooled reactor (HTR) prismatic block design (Task 2.1), deep burn fuel/tri-isotropic (TRISO) microanalysis (Task 2.3), and synergy with fast reactors and other fuel cycles (Task 4.2). Task 2.1 covers the core physics design, thermo-hydraulic computational fluid dynamics (CFD) analysis, and the thermofluid and safety analysis (low pressure conduction cooldown [LPCC]) of the HTR prismatic block design. Task 2.3 details the analysis of the structural behavior of TRISO fuel containing TRU at very high burnup levels (i.e., exceeding 50% of fissions per initial metal atom [FIMA]). Task 4.2 includes the self-cleaning HTR based on recycle of HTR-generated TRU in the same HTR.

From the design and analysis results of the 600 MW_{th} DB-HTR core physics, the following accomplishments have been obtained:

- Based on a three-batch radial and axial hybrid fuel management scheme, over 60% TRU burnup can be achieved when the burnup reactivity swing is about 3000 pcm.
- With regard to burnable poison, both B_4C and Er_2O_3 are promising burnable poison (BP) material for the DM-HTR core, and B_4C provides a little higher fuel discharge burnup. The moderator temperature coefficient (MTC) of the core is positive with the B_4C, while it can be strictly negative with Er_2O_3. The power coefficient of the core with both BPs is negative at the full-power condition, while the power coefficient can be positive with B_4C at a low-power level. However, the cycle length of DB-HTR core with Er_2O_3 BP is shorter than that of the DB-HTR core with B_4C. If the B_4C and Er_2O_3 mixed burnable poison is used in the DB-HTR core, both the MTC and the power coefficient can be negative. Also, the cycle length of the DB-HTR core with B_4C and Er_2O_3 mixed BP can be considerably longer than that of the DB-HTR core with Er_2O_3 BP. Therefore, it recommends that the B_4C and Er_2O_3 mixed BP should be used in a TRU-loaded DB-HTR core.
- In terms of safety aspects such as a LPCC event, a 600 MW_{th} of a DB-HTR core cannot meet the nominal design limit 1600°C for an LPCC event. Therefore, it recommends that the thermal power should be reduced to 450 MW_{th} in a five-ring TRU-loaded DB-HTR core design.
- From the results of the decay heat of the 600 MW_{th} TRU-loaded DB core, the short-term decay heat of the TRU-loaded DB-HTR core is highly dependent on the fuel loading. The americium isotope in the DB-HTR core strongly affects the short-term decay heat of the DB-HTR core. For a given TRISO design, the fuel packing fraction (PF) should be minimized for a minimal decay heat of the TRU-loaded DB-HTR core.

From the results of the hot spot fuel temperature analysis of the fuel block in the DB-HTR, the following accomplishments have been obtained:

- The predicted hot spot fuel temperatures for the 600 MW_{th} DB-HTR cores (i.e., Case A and Case B) are 1243 and 1223°C, respectively. The predicted hot spot fuel temperatures for the 450 MW_{th} DB-HTR cores (i.e., Case C and Case D) are lower than those for the 600 MW_{th} designs by ~30°C.
- The predicted hot spot fuel temperature of the core design with a 0.2% UO_2 mixed TRU is found to be slightly higher than that with a 30% UO_2 mixed TRU.
- For all the considered cases, the predicted hot spot fuel temperatures are below the generic design limit of 1250°C in spite of the sufficiently conservative assumption about the local fuel pin power profile within fuel block.

From the analysis results of the thermal-fluid design performance at the steady state and LPCC analysis of the DB-HTRs, the following accomplishments have been obtained:

- Key design characteristics of the DB-HTR core are more fuel rings (five fuel-rings), less central reflectors (three rings) and the decay power curves due to the TRU fuel compositions that are different from the UO_2 fuel.
- At the steady state, average 88.7, 7.1, and 4.2% of total reactor cooling system (RCS) flow go to the coolant channel, the control rod/reserve shutdown channel (CR/RSC) hole, and the fuel block bypass gap, respectively. It shows that the maximum fuel and RPV temperatures are less than the normal operation limit of 1250°C for TRISO fuel and the SA508 steel limit of 371°C, respectively.
- For a 0.2% UO_2 mixed or a 30% UO_2 mixed TRU fuel loaded 600 MW_{th} DB-HTR, the reduced decay power obtained by removing the initial Am isotopes and by reducing the PF decreases the peak fuel temperature. However, the peak fuel temperatures are still higher than 1600°C due to the lack of heat absorber volume in the central reflector.
- The 450 MW_{th} DB-HTR core is suggested as the optimization core design, which has the allowable maximum power reactor of a 450 MW_{th} to the accident fuel design limit for 0.2% UO_2 mixed TRU (PF = 6.9%) or 30% UO_2 mixed TRU (PF = 8.0%) using the mixed burnable poison of B_4C and Er_2O_3.
- Based on the Japan Atomic Energy Agency (JAEA) method for the graphite annealing, the effect of graphite annealing on the peak fuel temperature is small. The General Atomics (GA) method indicates a much larger impact, but it may not be applicable to the fluence and temperature conditions of the HTR. In addition, it shows that the impact of the fuel block (FB) end-flux-peaking on the peak fuel temperature is not significant.

From the analysis results of the TRISO fuel microanalysis of the DB-HTRs, the following accomplishments have been obtained:

- All the fuels of the DB-HTRs had good mechanical and thermal integrity during normal operation. During the accident such as LPCC event, however, all coated fuel particles (CFPs) in the 600 MW_{th} DB-HTRs are broken. The failure fractions due to the pressure vessel failure are between 5.8 and00 MW_{th} 31.3%. These high failure fractions indicate that it is necessary to reduce the gas pressure in a CFP during the LPCC. The gas pressure can be reduced by increasing the buffer size of the CFP or by reducing the accident temperature. However, the failure fraction due to the thermal decomposition was 100% indicating that active core cooling systems must be used to prevent excessive temperatures in the event of a LPCC of the 600 MW_{th} DB-HTR core.

- In the 450 MW_{th} DB-HTRs, the failure fraction due the pressure vessel failure are between 1.79×10^{-3} and 2.09×10^{-2}, and the failure fraction due the thermal decomposition are between 1.51×10^{-3} and 3.00×10^{-2}. It is necessary to scrutinize if these failure fractions are acceptable. The 30% UO_2 mixed TRU-loaded DB-HTR is most favored in the aspect of fuel integrity.
- The fractional releases of all the fission products considered are below 0.001 during normal operation. They should be scrutinized through the environmental impact if they are acceptable. More than 40% of silver is released during an accident regardless of the reactor power and the fuel types. Some measures should be taken to prevent excessive occupational doses of silver. The fractional releases of cesium, strontium, and krypton are above 10% during an accident in the 600 MW_{th} DB-HTRs, which are very high. On the other hand, they are below 0.001 during an accident in the 450 MW_{th} DB-HTRs except the fractional release of strontium in the TRU-loaded 450 MW_{th} DB-HTR, 1.66×10^{-3}.
- It is desirable in the safety aspects of DB-HTR that the CFPs sufficiently survive some accident conditions of an HTR. Therefore, the 600 MW_{th} DB-HTR is not appropriate for burning TRU. It is judged that the failure fractions in the 450 MW_{th} DB-HTRs are not sufficiently low. Thus, it is necessary to decrease the thermal power more and increase the buffer size of a CFP.

From the design and analysis results of the self-cleaning HTR (SC-HTR) core physics, the following accomplishments have been obtained:

- The self-cleaning of self-generated TRUs is feasible and deep burning of the self-generated TRU can be achieved in SC-HTR. The TRU discharge burnups in SC-HTR is shown to be over 63%. It was found that transmutation of Pu-239 is near complete (~99%) in the SC-HTR core and that of Pu-241 is also extremely high.
- It is observed that the power distribution is rather flat within the uranium fuel zone, but the power sharing of TRU fuel zone is significantly lower due to the very high TRU fuel burnup.
- It is expected that the TRU deep-burn can be improved if the fuel management and core design are optimized.

2. PUBLICATIONS

1. Chang Keun Jo, Yonghee Kim, F. Venneri, Jae Man Noh, "Feasibility Study on TRU Deep-Burn with Inert Matrix Fuel in an MHR," *Trans. of the Korean Nuclear Society Spring Meeting*, Jeju, Korea, May 22, 2009.
2. Young Min Kim, Chang Keun Jo, Yonghee Kim, Jae Man Noh, Moon Sung Cho, F. Venneri, "A Fuel Performance Analysis of a 600 MWth DB-MHR Fuel," *Trans. of the Korean Nuclear Society Autumn Meeting*, Gyeongju, Korea, October 29–30, 2009.
3. Nam-il Tak, Chang Keun Jo, Ji Su Jun, Min-Hwan Kim, F. Venneri, "CFD Analysis for Hot Spot Fuel Temperature of Deep-Burn Modular Helium Reactor," *Trans. of the Korean Nuclear Society Autumn Meeting*, Gyeongju, Korea, Octorber 29–30, 2009.
4. Ji Su Jun, Hong Sik Lim, Chang Keun Jo, F. Venneri, "Thermal-Fluid and Safety Analysis of the TRU Deep-Burn MHR Core," *Trans. of the Korean Nuclear Society Autumn Meeting*, Gyeongju, Korea, Octorber 29–30, 2009.
5. Chang Keun Jo, Yonghee Kim, F. Venneri, Jae Man Noh, "Study on TRU Deep-Burn with a Silicon Carbide Inert Matrix Fuel in an MHR," *Trans. of the ANS 2009 Winter Meeting*, Vol. 101, Washington, DC, Nov. 15–19, 2009.
6. Chang Keun Jo, Yonghee Kim, F. Venneri, Jae Man Noh, "Minimization of the Decay Heat in an MHR for TRU Deep-Burn," *Trans. of the ANS 2010 Annual Meeting*, Vol. 102, San Diego, CA, June 13–17, 2010.
7. Chang Keun Jo, Yonghee Kim, F. Venneri, Jae Man Noh, "Deep-Burn MHR Neutronics Analysis with a SiC-Gettered TRU Kernel," *Trans. of the Korean Nuclear Society Spring Meeting*, Pyeongchang, Korea, May 27–28, 2010.
8. Ji Su Jun, Hong Sik Lim, Chang Keun Jo, F. Venneri, "Decay Heat Impact on the Maximum Transient Fuel Temperature of the various TRU Compositions in a Deep-Burn MHR Core," *Trans. of the Korean Nuclear Society Spring Meeting*, Pyeongchang, Korea, May 27–28, 2010.
9. Chang Keun Jo, Yonghee Kim, Jae Man Noh, F. Venneri, "Core Performance Analysis of a DB-HTR with SiC Kernel Getter TRU Fuel," *Proceedings of HTR-2010*, Prague, Czech Republic, October 18–20, 2010.
10. Chang Keun Jo, Yonghee Kim, F. Venneri, "TRU Self-Recycling in a High Temperature Modular Helium Reactor," *Proceedings of HTR-2010*, Prague, Czech Republic, October 18–20, 2010.
11. Young Min Kim, Chang Keun Jo, Moon Sung Cho, F. Venneri, "Fuel Microanalysis for a 600 MW_{th} Deep Burn-High Temperature Reactor," *Proceedings of HTR-2010*, Prague, Czech Republic, October 18–20, 2010.
12. Ji Su Jun, Hong Sik Lim, Chang Keun Jo, Jae Man Noh, F. Venneri, "Evaluation of the Transient TRU Fuel Temperature in a DB-HTR Core," *Proceedings of HTR-2010*, Prague, Czech Republic, October 18–20, 2010.
13. Michael A. Pope, Javier Ortensi, Abderrafi M. Ougouag, "Investigation of Supercells for Preparation of Homogenized Cross Sections for Prismatic Deep Burn VHTR Calculations," *Proceedings of HTR-2010*, Prague, Czech Republic, October 18–20, 2010.

3. INTRODUCTION

The Deep Burn (DB) Project is a U.S. Department of Energy sponsored feasibility study of Transuranic Management using high burnup fuel in the high-temperature helium-cooled reactor (HTR). The DB Project consists of seven tasks: project management, core and fuel analysis, spent fuel management, fuel cycle integration, transuranic (TRU) fuel modeling, TRU fuel qualification, and HTR fuel recycle.

In Phase II of the DB Project, nuclear analysis was conducted of TRU destruction/utilization in the HTR prismatic block design (Task 2.1), deep burn fuel/TRISO microanalysis (Task 2.3), and synergy with fast reactors (Task 4.2). Task 2.1 covers the core physics design, thermo-hydraulic computational fluid dynamics (CFD) analysis, and the thermofluid and safety analysis (low-pressure conduction cooling [LPCC]) of the HTR prismatic block design. Task 2.3 details the analysis of the structural behavior of tri-isotropic (TRISO) fuel containing TRU at very high burnup level (i.e. exceeding 50% of fissions per initial metal atom [FIMA]). Also, Task 4.2 includes the self-cleaning HTR based on recycle of HTR-generated TRU in the same HTR.

Section 4 contains the design and analysis results of the 600 MW_{th} Deep-Burn High-Temperature Reactor (DB-HTR) core physics with the cycle length, the average discharged burnup, heavy metal and plutonium consumptions, radial and axial power distributions, temperature reactivity coefficients. Also, it contains the analysis results of the 450 MW_{th} DB-HTR core physics and the analysis of the decay heat of a TRU-loaded DB-HTR core.

The evaluation of the hot spot fuel temperature of the fuel block in the DB-HTR core under full operating power conditions are described in Section 5. The investigated designs are the 600 MW_{th} and 460 MW_{th} DB-HTRs.

In Section 6, the thermo-fluid and safety of the 600 MW_{th} DB-HTRs has been analyzed to investigate a thermal-fluid design performance at the steady state and a passive safety performance during an LPCC event.

Section 7 describes the analysis results of the TRISO fuel microanalysis of the 600 MW_{th} and 450 MW_{th} DB-HTRs. The TRISO fuel microanalysis covers the gas pressure buildup in a coated fuel particle including helium production, the thermo-mechanical behavior of a CFP, the failure probabilities of CFPs, the temperature distribution in a CPF, and the fission product (FP) transport in a CFP and a graphite.

Section 8 describes the design and analysis results of the self-cleaning (or self-recycling) HTR core. The analysis is considered zero and 5-year cooling time of the spent LWR fuels.

4. CORE PHYSICS ANALYSIS AND OPTIMIZATION OF THE DEEP BURN PRISMATIC BLOCK REACTOR

4.1 Introduction

The DB concept has been proposed in which a graphite-moderated MHR is used to achieve an ultra-high TRU burnup without costly reprocessing and re-fabrication of TRU fuels.[1,2] Figure 1 shows a schematic fuel cycle of the DB-HTR concept, which illustrates that recovered TRUs are fabricated into ceramic-coated particulate fuels (TRISO) and irradiated in an HTR core, and the spent fuels of HTRs are either fed synergistically into fast reactors[3] or directly disposed of in a final repository.

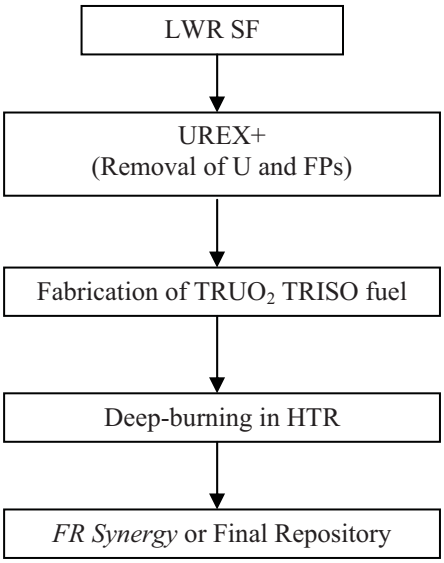

Figure 1. Fuel cycle concept of DB-HTR.

Figure 2 shows the schematic configurations of a DB-HTR core considered in this study. The DB-HTR core was modified from the original GT-MHR[4] of General Atomics (GA). In Figure 3, the fuel block configurations are depicted. In Table 1, major design parameters of the core are provided.

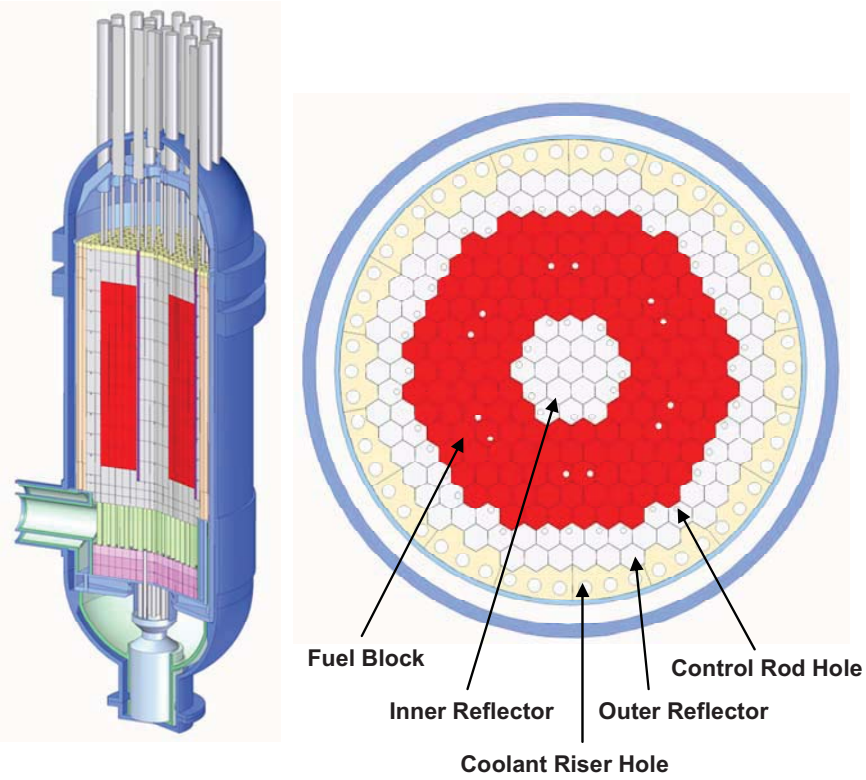

Figure 2. Core layout with 144 fuel columns.

As in the modern HTR core, the DB-HTR core is also annular type. However, the inner reflector volume is much smaller in the DB-HTR for improved neutron economy and higher fuel burnup. The active core consists of five fuel rings while only three fuel rings are used in the UO_2-loaded GT-MHR core. The DB-HTR core is comprised of nine axial layers, while the original design of GT-MHR has 10 axial layers. Consequently, the number of fuel blocks is 1296 in a core.

In Figure 3, the block configurations are shown. All the design parameters are the same as in the original GT-MHR design, except for the axial configuration of the block. Axial height of a block is 88.1 cm including 2.9-cm graphite zones at the top and bottom of a block. In the analysis, dowels are not modeled and the central hole is assumed to be filled with graphite. The original design has six BP holes, while a 12-hole BP loading is considered in this work. In a 12-hole BP loading, the additional BP holes are placed in the interior region of the block, as shown in Figure 3.

In this year, the SiC is added to the kernel as an oxygen getter to reduce the CO pressure in the buffer zone. The 350 μm diameter of the SiC-gettered kernel is also used to improve the fabricability of the TRISO fuel compared with the 200mm kernel diameter in the previous year. In the kernel design with SiC getter, the volume fraction of the SiC getter is about 24.3%. The coating thickness is as follows: 100 μm for the buffer, 35 μm for the inner PyC layer and SiC coating, and 40 μm for the outer PyC layer. In this work, various values of the TRISO packing fraction (PF) are considered to optimize the core performance. Table 2 shows the reference specifications of the TRISO fuel and fuel compact used in this work. Basically, two types of fuel composition are considered: $0.2\%UO_2 + 99.8\%(NpO_2+PuO_{1.8}) + SiC$ kernel getter [$0.2\%UO_2$ mixed TRU], and $30\%UO_2 + 70\%(NpO_2+PuO_{1.8}) + SiC$ kernel getter [$30\%UO_2$ mixed TRU]. The heavy metal nuclide composition as shown in Table 3 is used in this work. To reduce decay heat, the Am and Cm isotopes are not considered.

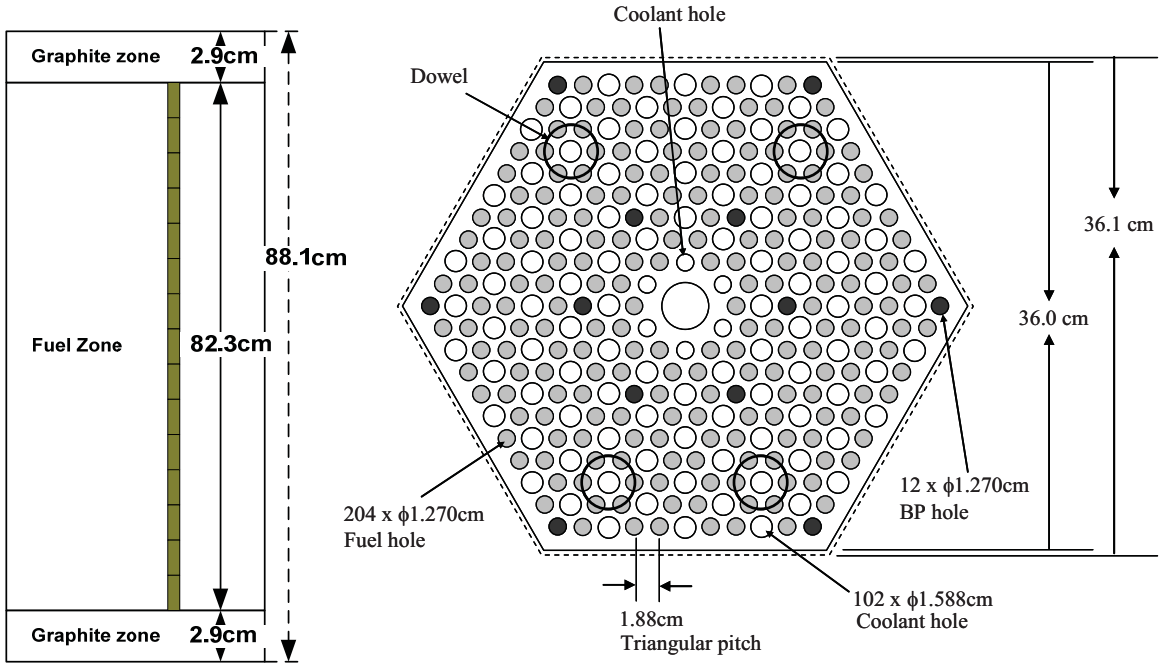

Figure 3. Fuel block configuration of DB-HTR.

Table 1. Major design parameters of DB-HTR.

Parameter	Value
Thermal power, MW	600
Coolant inlet/outlet temperature, °C	490/850
No. of fuel columns	108 or 144
Active core height, cm	792.9
Core radius, cm	340
Top/bottom reflector thickness, cm	120/120
No. of axial layers	9
Average power density, W/cm^3	4.66
Graphite block density, g/cm^3	1.74

Table 2. Specification of TRISO and fuel compact.

TRISO fuel	
Fuel type	$TRUO_2$
Kernel (diameter, μm/density, g/cm^3)	350/10.0
Buffer layer (thickness, μm/density, g/cm^3)	100/1.05
IPyC layer (thickness, μm/density, g/cm^3)	35/1.9
SiC layer (thickness, μm/density, g/cm^3)	35/3.18
OPyC layer (thickness, μm/density, g/cm^3)	40/1.9
Fuel Compact	
Radius, cm	0.6225
Matrix density, g/cm^3	1.70
Packing fraction, %	Various

Table 3. Heavy metal nuclide compositions.

Nuclides	Fraction, wt%	
	0.2%UO_2 + 99.8%(NpO_2+$PuO_{1.8}$) + SiC kernel getter	30%UO_2 + 70%(NpO_2+$PuO_{1.8}$) + SiC kernel getter
U-235	0.0014	0.21
U-238	0.20	29.67
Np-237	4.94	3.47
Pu-238	3.00	2.11
Pu-239	58.11	40.83
Pu-240	21.97	15.44
Pu-241	5.18	3.64
Pu-242	6.60	4.64

In this report, a physics study on the DB-HTR has been performed to characterize the DB-HTR core. Based on the previous studies, the reference fuel and core design models were derived and the core performance and characteristics were evaluated for the equilibrium core in terms of the TRU fuel burnup, power distributions, core temperature distributions, burnup reactivity swing, reactivity feedback coefficients. The core design and analysis were performed with the HELIOS[5]/MASTER-GCR[6] code system. The decay heat loaded with TRU-fueled DB-HTR core were calculated by using the McCARD code.

To improve the core characteristics, burnable poison (BP) is considered in this work. As the BP material, both B_4C and Er_2O_3 are considered. The primary purpose of the BP loading is to minimize the burnup

reactivity swing and the power peaking. In addition, the BP is also used to achieve favorable temperature coefficients of the core.

The core analysis methods and computer code systems are described in Section 4.2. Section 4.3 contains the core design and analysis results for various fuel and BP loading strategies. Summary and conclusions are provided in Section 4.4.

4.2 Core system for Analysis of Prismatic Block Reactor Core

For the DB-HTR core analysis, a thermal-hydraulic-coupled neutron analysis is used in this work. First, the double-heterogeneous fuel compact is transformed into a conventional single-heterogeneous problem by using the Reactivity-equivalent Physical Transformation (RPT)[7] method, and then the conventional two-step core analysis is done. Thus, a Monte Carlo and deterministic hybrid method is used for the DB-HTR core analysis.

4.2.1 RPT (Reactivity-equivalent Physical Transformation) Method

For an accurate analysis of a TRISO-fueled HTR core, the double-heterogeneity of the TRISO fuel should be correctly modeled. In particular, the double-heterogeneity effect is very large in a reactor-grade TRU-loaded HTR. Generally, a direct modeling of the TRISO fuel requires a huge memory requirement and an extremely long computing time for 3-D core depletion calculations. Therefore, the RPT method is adopted to convert a double-heterogeneous fuel compact into a conventional single-heterogeneous material. Figure 4 shows the concept of the RPT method. It has been shown that the RPT model is almost identical to the original problem. With the aid of the RPT method, the HTR core can be analyzed very efficiently with the conventional deterministic code systems.

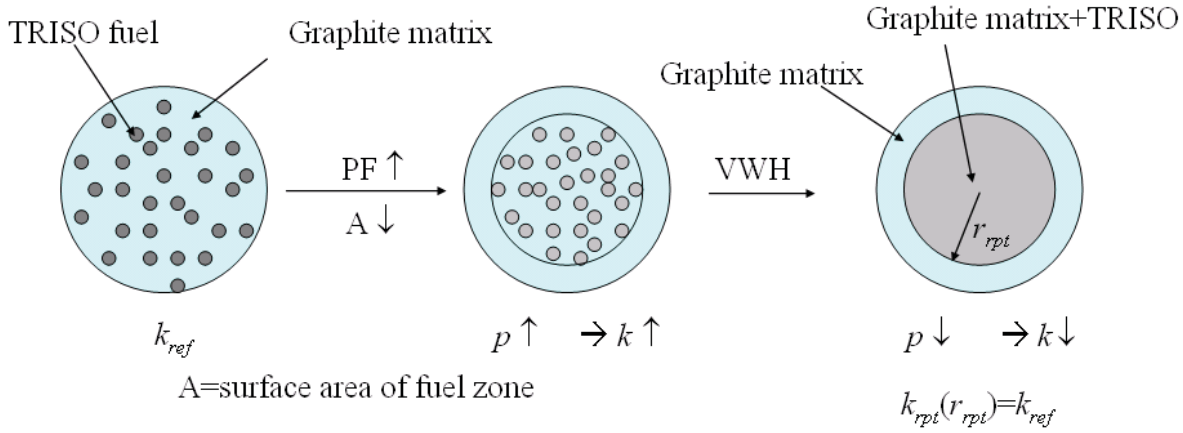

Figure 4. Concept of the RPT method.

For the RPT method, the reference reactivity should be calculated in advance by using a high-fidelity method. In this work, the reference reactivity of a unit fuel cell is determined by the continuous energy Monte Carlo code McCARD.[8] McCARD can directly handle the double-heterogeneous fuel used in HTRs. In particular, randomness of the TRISO fuel particles can also be taken into consideration—locations of TRISO fuels are randomly determined. In addition, McCARD has a built-in depletion routine, thus it can be used in a stand-alone mode for the reactor depletion analysis. In a Monte Carlo depletion calculation, it is important to consider fission products as much as possible. In the current MCCARD depletion calculation, all actinides and over 160 fission products nuclides are considered and

the fission product poisoning can be almost completely accounted. The cross-section libraries are generated from the ENDF-B/VII data.

4.2.2 HELIOS/MASTER-GCR Code system

KAERI has developed unique methodologies for the analysis of Very High-Temperature Reactor (VHTR) reactor cores, both prismatic and pebble-bed. Figure 5 shows the calculational procedures in KAERI's computer code system for a prismatic HTR. Basically, the procedure is a conventional 2-step procedure adopted in the core design of PWRs, except for a unique step to deal with the challenging double-heterogeneity of TRISO fuels.

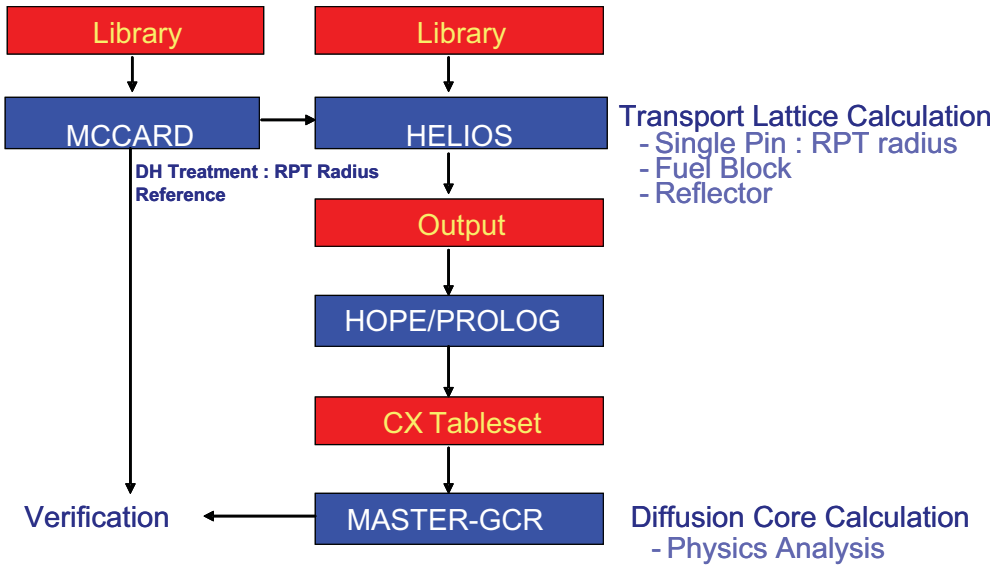

Figure 5. KAERI's analysis procedures and computer codes for the VHTR core design.

In the two-step calculation, the fuel block is homogenized by using the HELIOS code and the results are processed to generate a few-group cross-section library for a subsequent multi-dimensional core analysis. The MASTER-GCR code is used for the multi-dimensional core analysis, which is based on the diffusion theory. MASTER-GCR was originally developed for the PWR core analysis and it was refined for the VHTR core design.

4.2.2.1 HELIOS Code

HELIOS is a multigroup 2-dimensional lattice code for neutron and gamma transport calculations, developed by Studsvik-Scandpower. HELIOS makes use of a 190-group neutron library, from 0 to 20 MeV and 18 gamma energy groups. This library is derived from the ENDF/B-VI data files and is also available in a 47-group structure (for Version 1.8). The HELIOS code is a neutron transport code making use of the current-coupling collision probability method.

For the VHTR core analysis, HELIOS code performs the lattice depletion calculation for a single fuel block with the reflective boundary condition using a 190 group library based on ENDF/B-VI to generate multigroup cross sections.

4.2.2.2 MASTER-GCR Code

In the MASTER-CGR[9] code, various neutronic solvers are available, depending on the problems of interest, to solve the few-group neutron diffusion equations. For the VHTR core design, the solution is obtained by using a nodal method for hexagonal geometry. Through a transverse leakage approximation, the 3-D problem is decomposed into 2-D plane and 1-D axial problems. In the 2-D plane geometry, a polynomial expansion method, called Triangle-based Polynomial Expansion Nodal (TPEN) method, in which the solution is expanded by third-order polynomials for six triangles in each hexagon node. In the axial direction, a conventional nodal expansion method employing fourth-order polynomials is utilized.

A thermal feedback calculation module for prismatic VHTR cores has been implemented in the MASTER-GCR code. This module requires the core power level, pressure, core averaged inlet and outlet coolant temperatures, pitches and radii for fuel compact and coolant hole, coolant mass flux, and fast fluence information for the thermal feedback calculation. In the thermal-hydraulic calculations, material properties such as graphite conductivity are calculated from a pre-generated data set. For a given temperature distribution, cross sections are determined and the power distribution is obtained by the neutron diffusion equation. Those coupled calculations are repeated until convergence.

In the MASTER-CGR code, one can easily define a fuel reloading strategy. Both radial and axial block shuffling and their combinations can be simulated in the MASTER code. An equilibrium core can be found by repeated depletion calculations for a given fuel shuffling scheme.

A thermal feedback calculation module for prismatic VHTR cores has been implemented in the MASTER code. This module requires the core power level, pressure, core averaged inlet and outlet coolant temperatures, pitches and radii for fuel compact and coolant hole, coolant mass flux, and fast fluence information for the thermal feedback calculation. The calculation procedure is as follows:

- Calculate the core average enthalpy rise from pressure and inlet and outlet coolant temperatures.
- Calculate the mass flow rate from enthalpy rise and core power.
- Calculate the enthalpy rise from the node power and the mass flow rate for each node.
- Calculate the coolant temperature from the node enthalpy rise for each node.
- Calculate the graphite surface temperature with the following equation:

$$T_c = T_b - \frac{q''}{h}, \tag{1}$$

where T_b is a coolant temperature, q'' a heat flux, and h a heat transfer coefficient.

Calculate the fuel surface temperature with the following equation:

$$T_s = T_c - \frac{2A_g}{P_c + P_s}\frac{q_s''}{k_c}, \tag{2}$$

where A_g is a graphite area, q_s'' a heat flux at the fuel compact surface, P_c a coolant channel arc-length, P_s a fuel compact arc-length, and k_c a graphite conductivity.

Calculate the fuel centerline temperature with the following equation:

$$T_m = T_s - \frac{r_f}{2}\frac{q_s''}{k_f}, \tag{3}$$

where r_f is a fuel radius, and k_f a conductivity of a fuel compact.

Calculate the average fuel and graphite temperatures with the following equations:

$$\begin{aligned} \bar{T}_f &= (1-w_f)T_s + w_f T_m, \quad w_f = 0.66 \\ \bar{T}_g &= (1-w_g)T_c + w_g T_s, \quad w_g = 0.61 \end{aligned}. \tag{4}$$

In the thermal-hydraulic calculations, material properties such as graphite conductivity are calculated from a pre-generated data set. For a given temperature distribution, cross sections are determined and the power distribution is obtained by the neutron diffusion equation. Those coupled calculations are repeated until convergence.

In the MASTER-GCR code, one can easily define a fuel reloading strategy. Both radial and axial block shuffling and their combinations can be simulated in the MASTER-GCR code. An equilibrium core can be found by repeated depletion calculations for a given fuel shuffling scheme.

4.3 Results of the core physics analysis

4.3.1 Introduction

In this section, the core design analysis is performed by taking into account the BP loading in the DB-HTR core with a SiC kernel getter. Two fuel kernels are considered as described in Section 4.1. The major core design objectives and constraints are as follows:

- Maximize the fuel discharged burnup and the cycle length
- Minimize the decay heat at the abnormal event
- Ensure maximum fuel temperature is less than 1250°C during normal operation
- Satisfy the inherent safety.

4.3.2 BP Design Concepts

In general, BP can be used for multi-purposes in DB-HTR: (1) the burnup reactivity swing or change should be minimized during an equilibrium cycle and the control rod movement should be minimized, (2) the core power distribution should be appropriately controlled to minimize the maximum fuel temperature in the core, and (3) the core temperature coefficient can strongly affected by BP. Obviously, the residual reactivity by BP should be minimized for a minimal burnup penalty induced by the BP.

In this work, B_4C, Er_2O_3, and mixed B_4C and Er_2O_3 were investigated as the BP material. The natural composition of each BP material is used in the calculation. The sintered mixture of BP and graphite was considered for a relatively cheap BP compact fabrication.[10,11] The BP compact is depicted in Figure 6. As shown in Figure 7, 12-hole BP application was considered for comparison. In this work, it is assumed that the Er_2O_3 BP is compatible with the graphite matrix. If there were any compatibility problem between

Er_2O_3 and graphite, Er_2O_3 can be replaced by Er_2C_3, which should be compatible with graphite and is virtually equivalent Er_2O_3 in terms of the neutronic effect.[10]

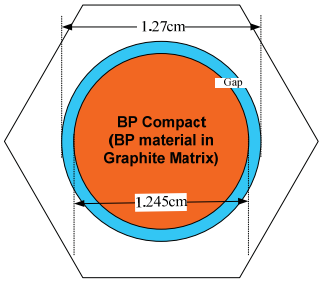

Figure 6. Configuration of BP compact.

4.3.3 Various Core Design Approaches

In the DB-HTR core, the core design flexibility is greatly affected by the fuel shuffling scheme, which should be done at every reloading cycle. A shown in the previous year results, the axial-only shuffling scheme provides a satisfactory performance during the normal operation of the DB-HTR core. However, it turns out that the peak fuel temperature can be much higher than the general upper limit of 1,600°C during the LPCC accident due to the relatively high axial power peaking. To reduce the peak fuel temperature during LPCC accident, a radial and axial hybrid fuel shuffling scheme is introduced. Figure 7 shows the three-batch hybrid shuffling scheme. For the radial shuffling scheme, the fresh fuels are loaded into the fourth fuel ring and the once-burned fuels are moved to the outer-most fuel ring, and the twice-burned fuels are loaded into the two inner rings. In the other core region (third fuel ring), independent three-batch axial shuffling is applied. In the axial shuffling scheme, the most-burned fuel blocks are placed at both bottom and top of each fuel column to minimize the axial neutron leakage. In the current core design, the control rod holes are only reserved in the third fuel ring, and the radial shuffling can be implemented without any problem.

With the combination of the TRISO PF, types of burnable poison, and uranium mixed fraction, a total of 20 design options were evaluated in terms of the core performance and characteristics. Table 4 shows the 20 core design cases. The Table 5 shows the equivalent TRISO packing fraction as an aspect of the heavy metal mass in a fuel compact. For example, the 6.9% TRISO packing fraction with 350 mm kernel diameter is equivalent to the 19.23% TRISO packing fraction with 200 mm kernel diameter as shown in the table.

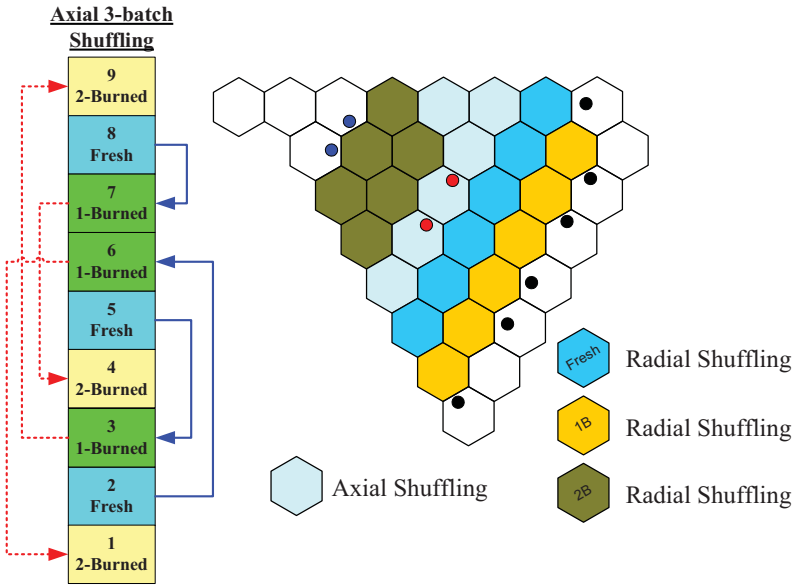

Figure 7. Radial and axial hybrid fuel shuffling scheme.

Table 4. Various core design approaches.

No.	TRISO PF (%)	Fuel type	BP Fraction (%)
C-01	4.9	Case I	No BP
C-02		Case I	B_4C 0.9
C-03		Case I	Er_2O_3 3.5
C-04		Case I	B_4C 0.15 and Er_2O_3 2.7
C-05	5.9	Case I	No BP
C-06		Case I	B_4C 0.9
C-07		Case I	Er_2O_3 3.5
C-08		Case I	B_4C 0.20 and Er_2O_3 2.3
C-09	6.9	Case I	No BP
C-10		Case I	B_4C 0.9
C-11		Case I	Er_2O_3 3.5
C-12		Case I	B_4C 0.3 and Er_2O_3 2.0
C-13	7.0	Case II	No BP
C-14		Case II	B_4C 0.65
C-15		Case II	Er_2O_3 2.5
C-16		Case II	B_4C 0.10 and Er_2O_3 2.0
C-17	8.0	Case II	No BP
C-18		Case II	B_4C 0.6
C-19		Case II	Er_2O_3 2.2
C-20		Case II	B_4C 0.15 and Er_2O_3 1.5
Case I : 0.2%UO_2 + 99.8%(NpO_2+$PuO_{1.8}$)+SiC kernel getter Case II : 30%UO_2 + 70%(NpO_2+$PuO_{1.8}$)+SiC kernel getter			

Table 5. Calculation of the equivalent packing fraction with kernel diameter.

	Fuel Type	Kernel diameter (350 nm)	Kernel diameter (200 nm)	Heavy Metal Mass per Compact (g)[a]
Packing Fraction	Case I	4.9%	13.73%	0.021737
		5.9%	16.37%	0.025910
		6.9%	19.23%	0.030431
	Case II	7.0%	19.56%	0.030461
		8.0%	22.52%	0.035081
a. The height of fuel compact is 0.5cm.				

4.3.4 Core Performance and Characteristics

For the various core design options, equilibrium cycle analyses were performed with the HELIOS/MASTER-GCR code system and the results are summarized in Table 6 and Table 7 for major core performance indexes. For each case, an equilibrium cycle is directly searched by repetitive cycle-wise calculations as shown in Figure 8 for the Reference C-02. In the equilibrium cycle analysis, the EOC k-effective value was set to ~1.005 and the amount of BP loading was adjusted in each case such that the burnup reactivity swing should be about 3,000 pcm for a fair comparison.

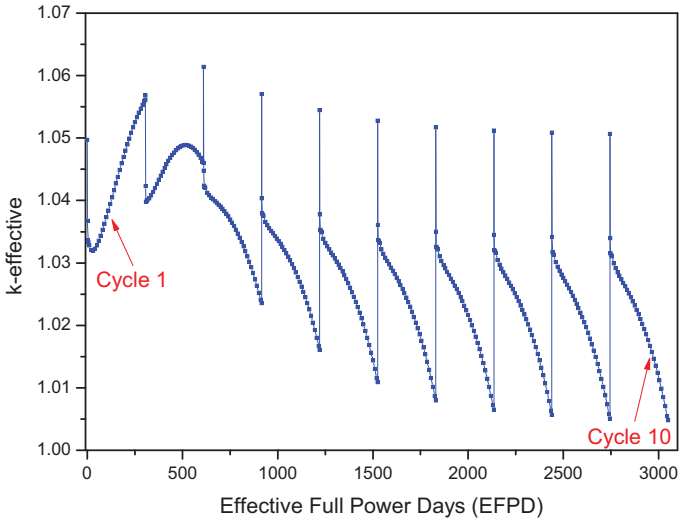

Figure 8. Determination of equilibrium cycle in C-02.

Table 6. Summary I of the core analysis results.

Case	Feed Fuel Mass (Kg)	Cycle Length (day)	Reactivity Swing (pcm)	Reactivity (k-eff)		Average Discharged Burnup (GWd/tHM)
				Beginning of Cycle	End of Cycle	
Case 1	312.6	335	16,006	1.163	1.0033	640.67
Case 2		305	2,916	1.034	1.0048	584.69
Case 3		270	2,916	1.033	1.0034	518.33
Case 4		284	3,035	1.035	1.0051	544.92
Case 5	372.6	402	14,190	1.148	1.0056	645.24
Case 6		372	3,160	1.037	1.0052	598.23
Case 7		330	2,841	1.034	1.0052	531.42
Case 8		353	3,079	1.035	1.0045	568.09
Case 9	437.4	474	12,703	1.132	1.0045	648.10
Case 10		438	3,096	1.037	1.0058	599.96
Case 11		402	3,036	1.035	1.0047	551.09
Case 12		426	3,040	1.035	1.0049	583.68
Case 13	438.0	340	12,248	1.127	1.0050	464.74
Case 14		311	2,990	1.034	1.0042	425.77
Case 15		283	2,741	1.033	1.0052	387.68
Case 16		294	2,869	1.034	1.0052	402.66
Case 17	504.6	393	10,776	1.112	1.0044	466.67
Case 18		359	3,058	1.037	1.0060	426.85
Case 19		340	3,019	1.035	1.0051	404.36
Case 20		355	3,203	1.037	1.0046	422.08

Table 7. Summary II of the core analysis results.

Case	Maximum Fuel Temp. at Steady State (°C)[a]		Fuel Consumption (%)			Peak Fuel Temp. at LPCC Event (°C)	
	BOC (No Xe)	EOC	Total HM	Pu-total	Pu-239	GA Method	JAEA Method
Case 1	1,075	1,133	63.9	69.1	98.2	1528	n/a
Case 2	942	1,032	58.5	63.3	96.1	1580	1755
Case 3	948	965	51.9	56.2	91.8	1671	1875
Case 4	942	991	54.5	59.1	94.0	1645	1842
Case 5	1,056	1,114	64.5	70.3	98.1	n/a	n/a
Case 6	928	1,025	59.9	65.4	96.2	1644	1844
Case 7	952	957	53.3	58.1	92.2	1715	1928
Case 8	933	994	56.9	62.1	94.8	1681	1888
Case 9	1,040	1,094	64.9	71.2	97.8	n/a	n/a
Case 10	934	1,006	60.2	66.1	95.9	1685	1897
Case 11	940	960	55.3	60.8	93.0	1733	1953
Case 12	945	992	58.6	64.3	95.1	1705	1920
Case 13	1,037	1,085	46.4	66.9	96.7	1,545	n/a
Case 14	932	1,002	42.6	61.3	94.0	1617	1803
Case 15	944	958	38.8	56.0	90.5	1674	1879
Case 16	936	976	40.3	58.1	92.1	1654	1853
Case 17	1,020	1,062	46.7	67.1	96.2	n/a	n/a
Case 18	928	985	42.9	61.6	93.4	1647	1847
Case 19	935	961	40.5	58.3	91.4	1687	1897
Case 20	939	982	42.3	60.8	93.0	1664	1869

a. Fuel block average value at steady state.

From the results in Table 6 and Table 7, the followings are observed. As shown in Table 6, the fresh fuel loading at each cycle is dependent on the TRISO PF. Then, the cycle length of the core is dependent on the TRISO PF. For example, in the 0.2% UO_2 mixed TRU cases (C-01, C-05, C-09) without burnable poison, the cycle lengths are 335, 402, 474 effective full power day (EFPD) for C-01 (PF = 4.9%), C-05 (PF = 5.9%), C-09 (PF = 6.9%), respectively. Also, it is clear that BP loading results in a noticeably reduced fuel burnup (10–20%), depending on the BP type. Comparing C-02 and C-03 indicates that B_4C provides a slightly higher fuel burnup than Er_2O_3 when the burnup swing is comparable for the two BP types. This is because B_4C deplete a little faster than Er_2O_3. In the B_4C and Er_2O_3 mixed BP cases, the cycle lengths are slightly higher than those of the Er_2O_3 BP cases. The average discharged burnup is highly dependent on the TRISO PF and burnable poison. The fuel burnup of No BP case is the highest comparing with B_4C, Er_2O_3, and B_4C and Er_2O_3 mixed BP cases. Also, the fuel burnup in the TRISO PF 6.9% is higher than that of the other cases. Clearly, the case C-09 (No BP, 6.9% PF, 0.2% UO_2 mixed fuel) provides the highest fuel burnup, ~648 GWD/tHM. However, the burnup reactivity swing is relatively big because of absence of burnable poison.

From the view points of maximum fuel temperature at a steady state condition, the temperature of the Er_2O_3 BP cases and/or the B_4C and Er_2O_3 mixed BP cases are lower than those of the No BP cases and/or the B_4C BP cases because the block power distribution of the Er_2O_3 BP cases are more flattened than those the B_4C BP cases.

Also, the fuel consumption rates of all the cases are shown in Table 7. As shown this table, the consumption rate of total heavy metal is also highly dependent on the burnable poison. The consumption rate of total heavy metal is above 50% for all cases in the 0.2% UO_2 mixed TRU fuels, while the consumption rate is below 50% for all cases in the 30% UO_2 mixed TRU fuels. From the results, it indicates that the consumption rate of the total heavy metal highly affected by the amount of additional uranium. From the results of consumption rate of plutonium isotope, the consumption rate of plutonium isotopes of the No BP cases with PF = 4.9%, 5.9%, and 6.9% are about 69.1%, 70.3%, and 71.2%, respectively, in the 0.2% UO_2 mixed TRU fuel. Those of the B_4C BP cases with PF = 4.9%, 5.9%, and 6.9% are about 63.3%, 65.4%, and 66.1%, respectively. Those of the Er_2O_3 BP cases with PF = 4.9%, 5.9%, and 6.9% are 56.2%, 58.1%, and 60.8%, respectively. Finally, the fuel consumption rate of the B_4C and Er_2O_3 mixed BP cases with PF = 4.9%, 5.9%, and 6.9% are 59.1%, 62.1%, 64.3%, respectively. In the 30% UO_2 mixed TRU fuel, the consumption rate of plutonium isotope of the No BP cases with PF = 7.0% and PF = 8.0% are 66.9% and 67.1%, respectively. Those of the B_4C BP cases with PF = 7.0% and PF = 8.0% are 61.3% and 61.6%, respectively. Those of the Er_2O_3 BP cases with PF = 7.0% and PF = 8.0% are 56.0% and 58.3%, respectively. Finally, those of the B_4C and Er_2O_3 mixed BP cases with PF = 7.0% and 8.0% are 58.1% and 60.8%, respectively. Also, the results show that the consumption rates of Pu-239 are above 90% for the all cases.

As shown in Table 7, the peak fuel temperatures of LPCC event were evaluated by using two different methods. The method is different in an annealing effect of the irradiated thermal conductivity of graphite, which describes detailed in Jun et al.'s 2010 document.[12] By using the GA method for graphite annealing effect, the peak fuel temperature of LPCC event in the case C-02 is 1,580°C, which is below nominal design limit 1600°C, while that of other cases is above 1600°C. However, the peak fuel temperature of LPCC event is above 1750°C in the JAEA method. From the results, it indicates that the peak fuel temperature of LPCC event is highly affected by annealing effect of the irradiated thermal conductivity of graphite. If the JAEA method is used for the graphite annealing effect, the nominal design limit of 1600°C cannot be satisfied in any case.

In Figure 9, Figure 10, and Figure 11, the reactivity change during an equilibrium cycle is compared for the 20 cases. The results indicate that the burnup reactivity swings are well managed by burnable poison. The block-wise core radial power distributions of all cases (C-01 to C-20) are provided in Figure 12 through Figure 31. The core radial power profiles of the all No BP cases are quite similar, respectively. Comparing the B_4C BP cases and Er_2O_3 BP cases, the radial power of the B_4C BP cases is slightly smaller than those of the Er_2O_3 BP case in the central ring. It causes the higher peak fuel temperature in LPCC event in Er_2O_3 BP cases. The core axial power profiles distributions of the all cases are shown in the Figure 32 through Figure 36.

For comparison of safety characteristics of the design options, several reactivity temperature coefficients were also evaluated for the various cases. Figure 37, Figure 38, and Figure 39 show the fuel temperature coefficient (FTC) for the B_4C, Er_2O_3, and B_4C and Er_2O_3 mixed BP cases, respectively. The FTCs are negative at the operating condition in the case of three BP types. The moderator temperature coefficient (MTC) for the three BP types is shown in Figure 40 through Figure 42. From the figures, one can note that the MTCs in the B_4C BP cases are positive at the operating condition, while the MTCs in the Er_2O_3 and B_4C and Er_2O_3 mixed BP cases are negative at the all operating condition. Figure 43, Figure 44, and Figure 45 show the power coefficient at the full power condition. The power coefficients in all BP cases

are negative at the full power condition. Figure 46 to Figure 51 show the power coefficient with power levels for all BP cases at BOC and EOC operating conditions. From Figure 46 and Figure 49, it is observed that the power coefficient of the B_4C BP cases is positive at the low power level at both BOC and EOC conditions. In the C-02 case (small heavy metal fuel loading) with B_4C BP, the power coefficient is positive up to 80% power level. But, in both Er_2O_3 BP and B_4C and Er_2O_3 mixed BP cases (Figure 47, Figure 48, Figure 49, Figure 50, and Figure 51), the power coefficients are negative at both BOC and EOC conditions except the C-04 (B_4C and Er_2O_3 mixed BP, PF = 4.9%) case at nearly zero power level.

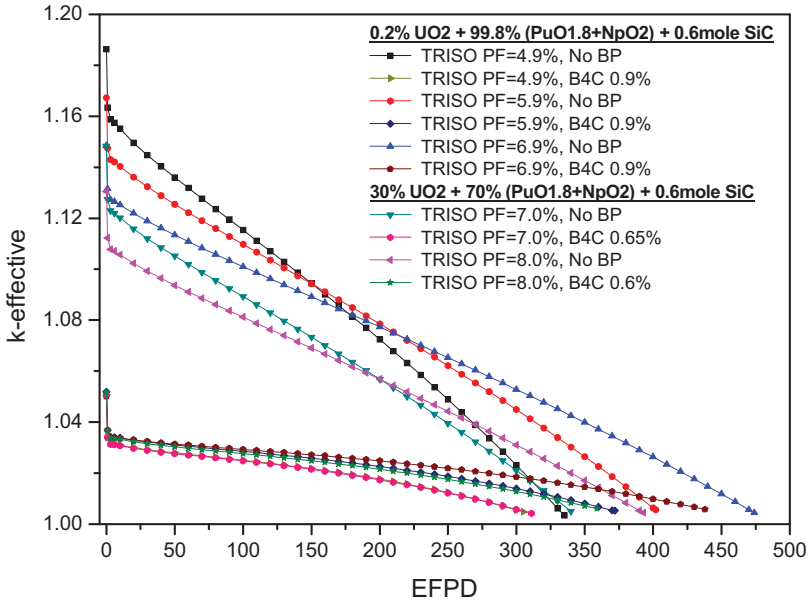

Figure 9. Evolution of the k-effective values during equilibrium cycle (B_4C).

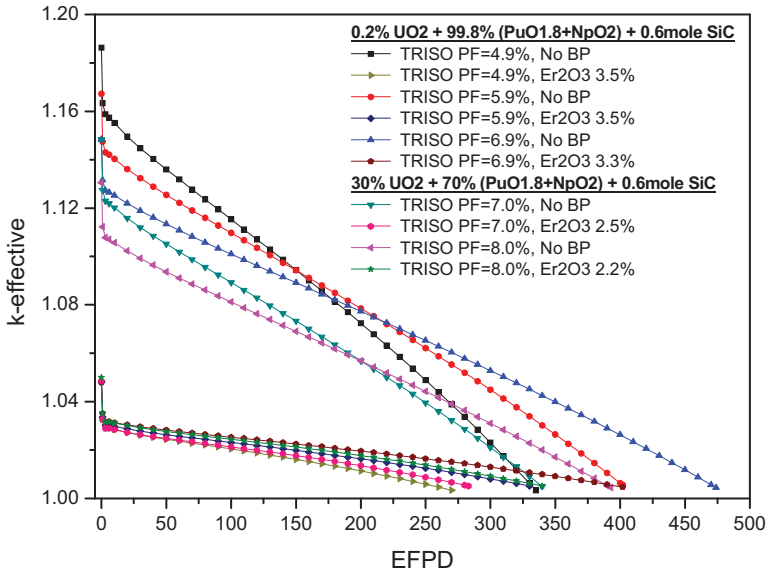

Figure 10. Evolution of the k-effective values during equilibrium cycle (Er_2O_3)

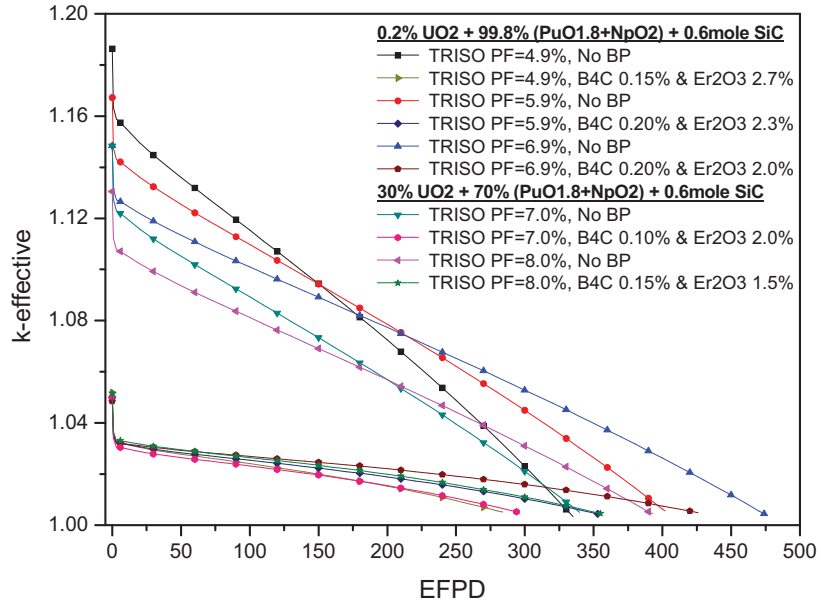

Figure 11. Evolution of the k-effective values during equilibrium cycle (B_4C and Er_2O_3 mixed).

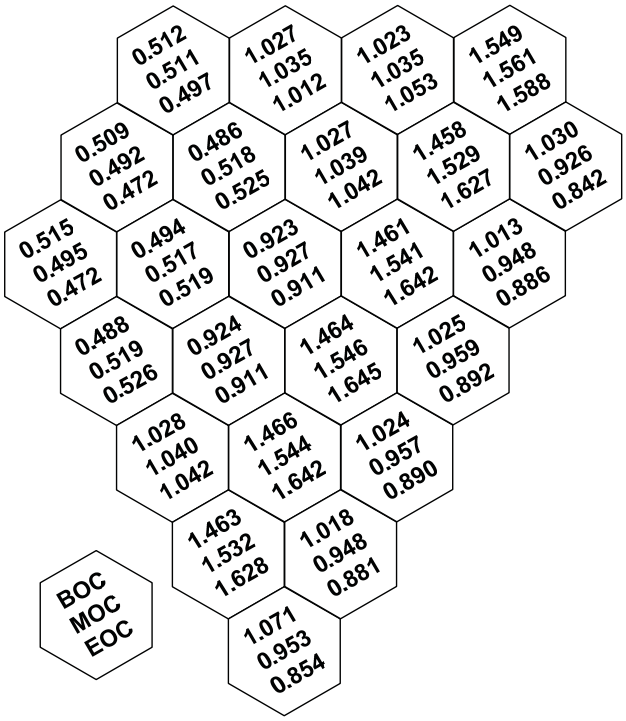

Figure 12. Radial power distribution (C-01).

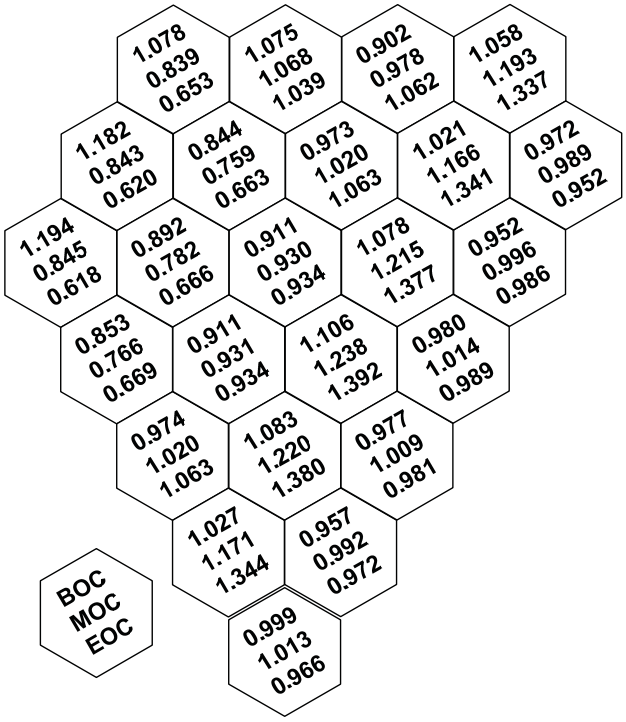

Figure 13. Radial power distribution (C-02).

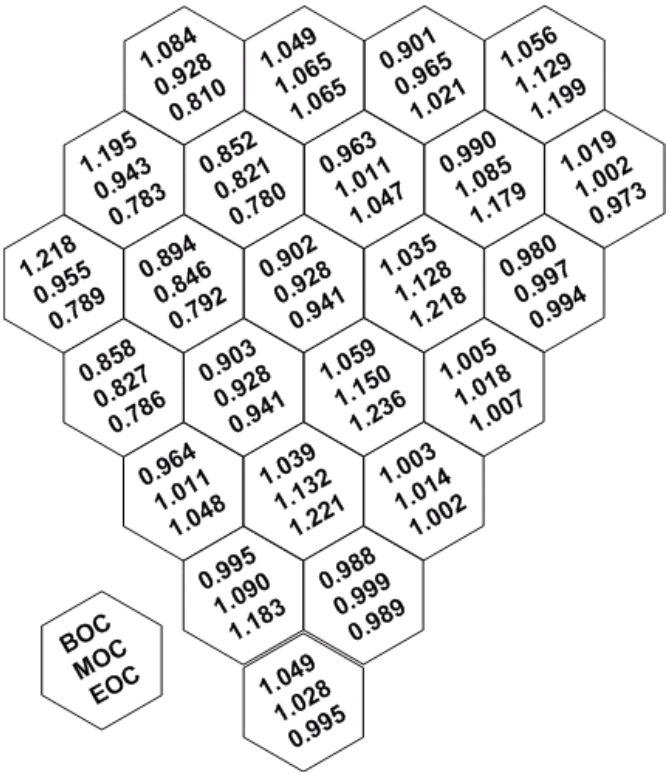

Figure 14. Radial power distribution (C-03).

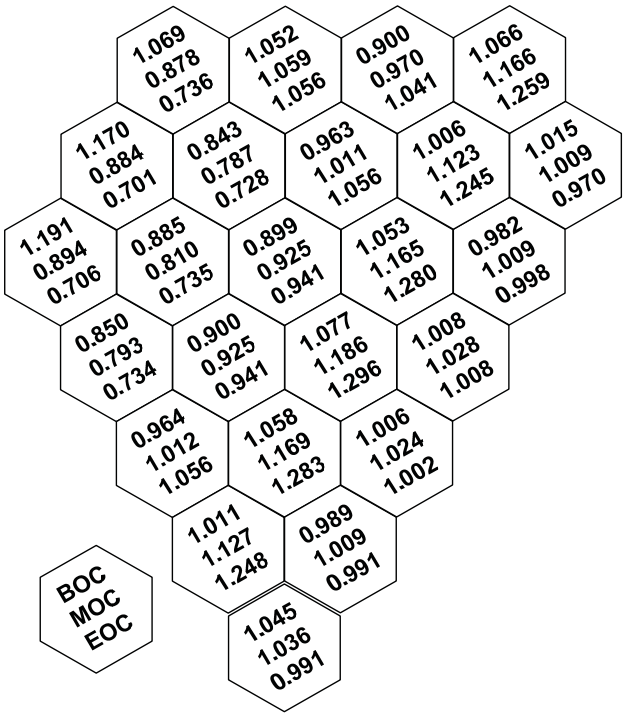

Figure 15. Radial power distribution (C-04).

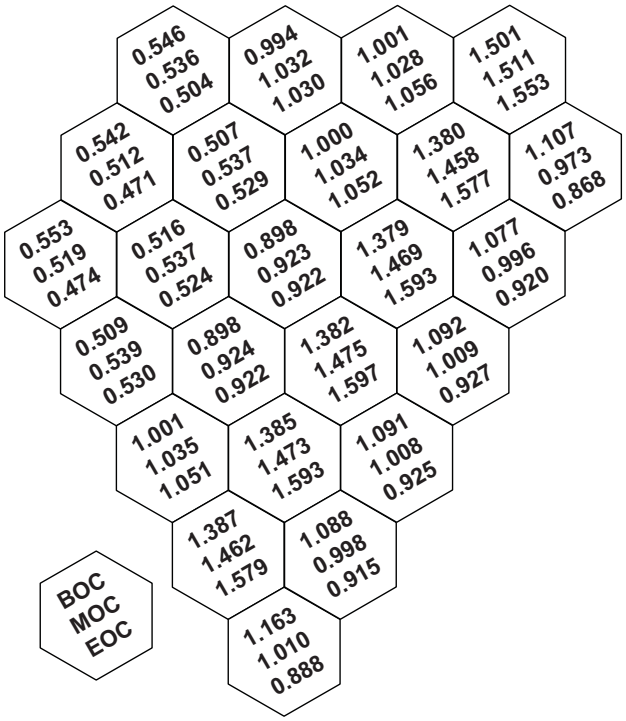

Figure 16. Radial power distribution (C-05).

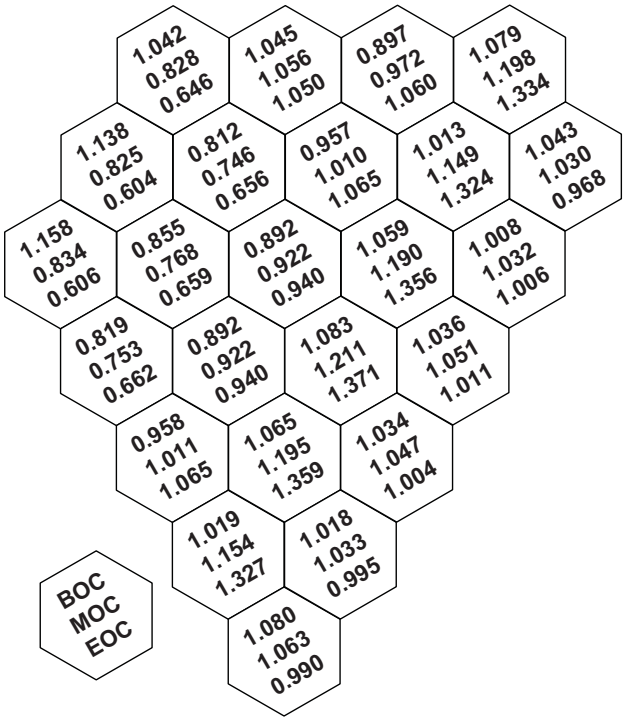

Figure 17. Radial power distribution (C-06).

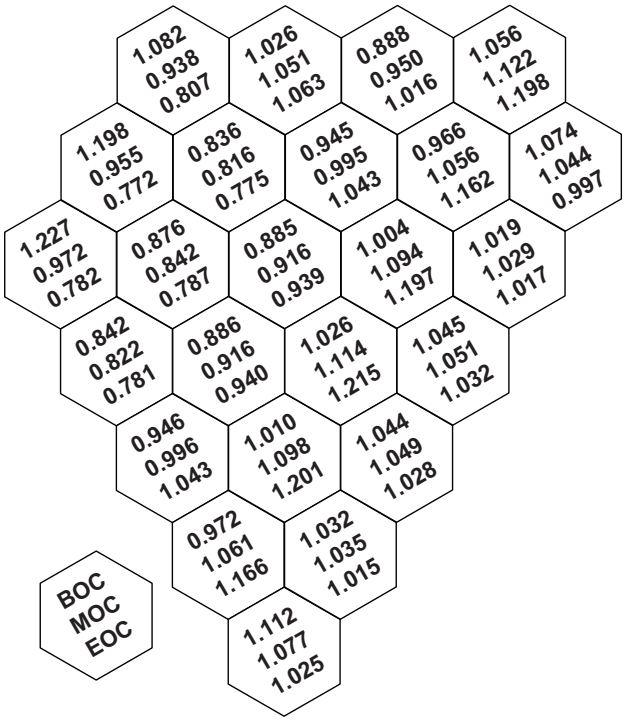

Figure 18. Radial power distribution (C-07).

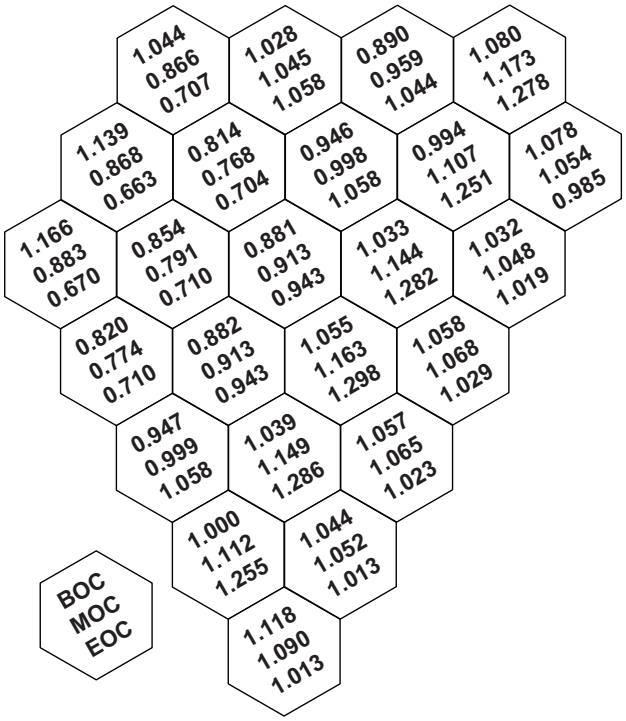

Figure 19. Radial power distribution (C-08).

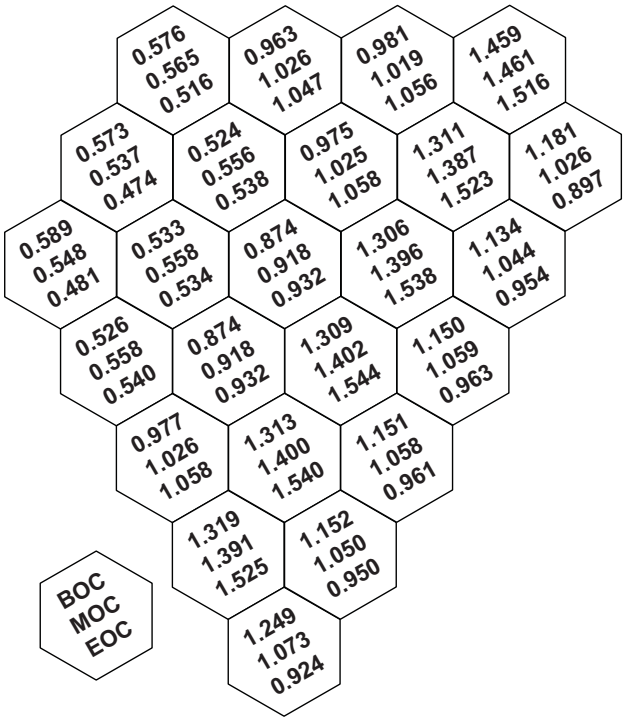

Figure 20. Radial power distribution (C-09).

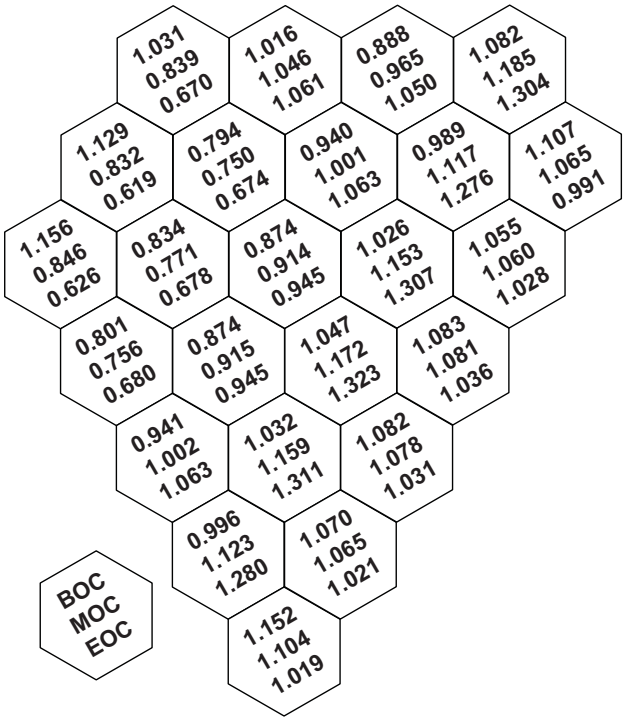

Figure 21. Radial power distribution (C-10).

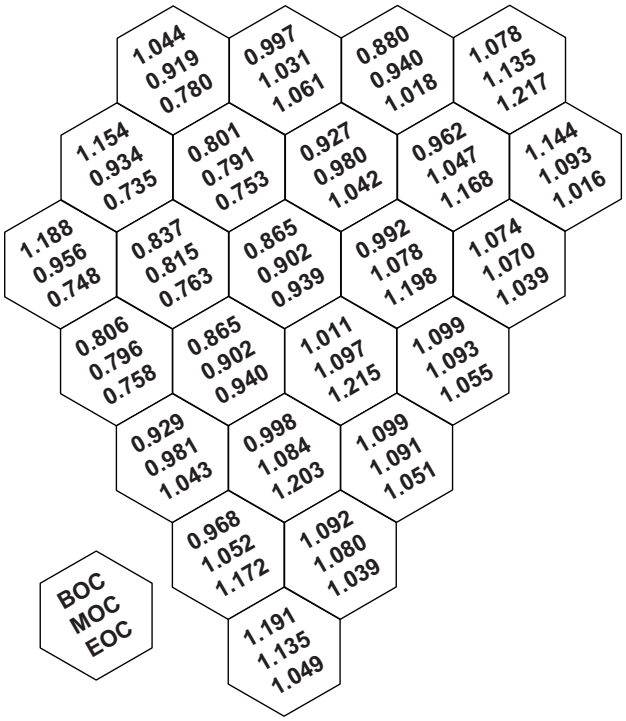

Figure 22. Radial power distribution (C-11).

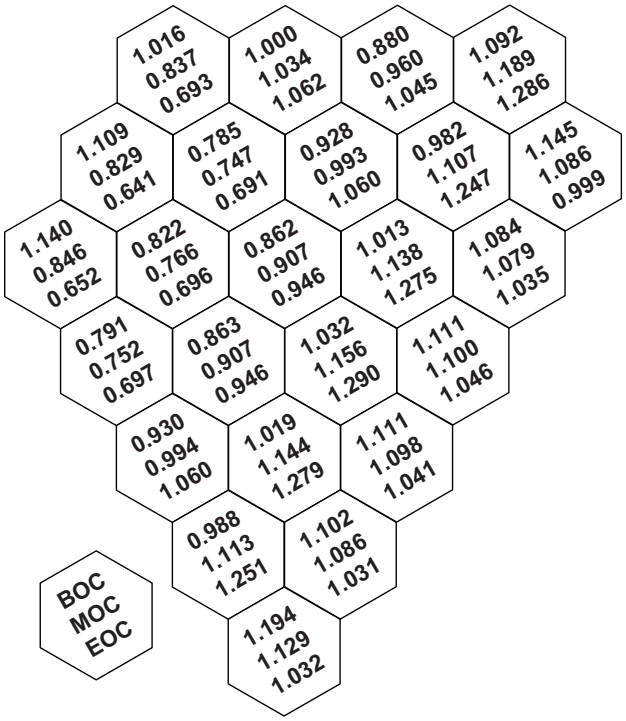

Figure 23. Radial power distribution (C-12).

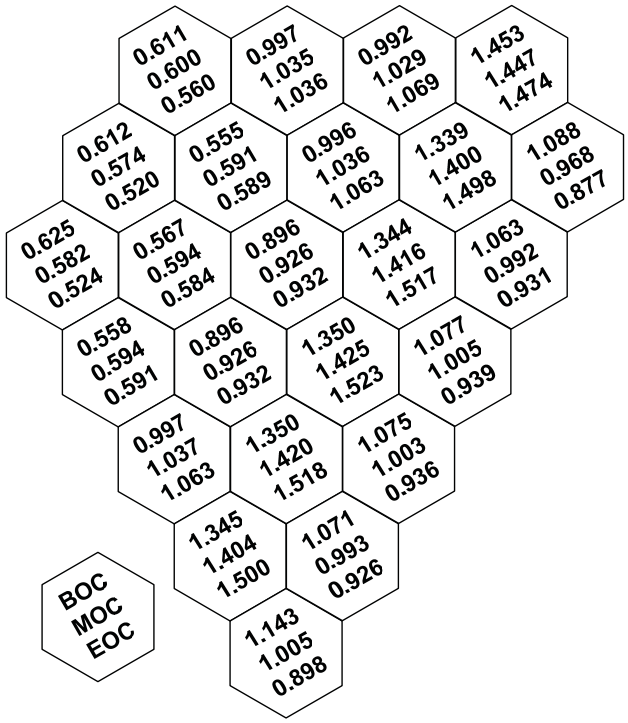

Figure 24. Radial power distribution (C-13).

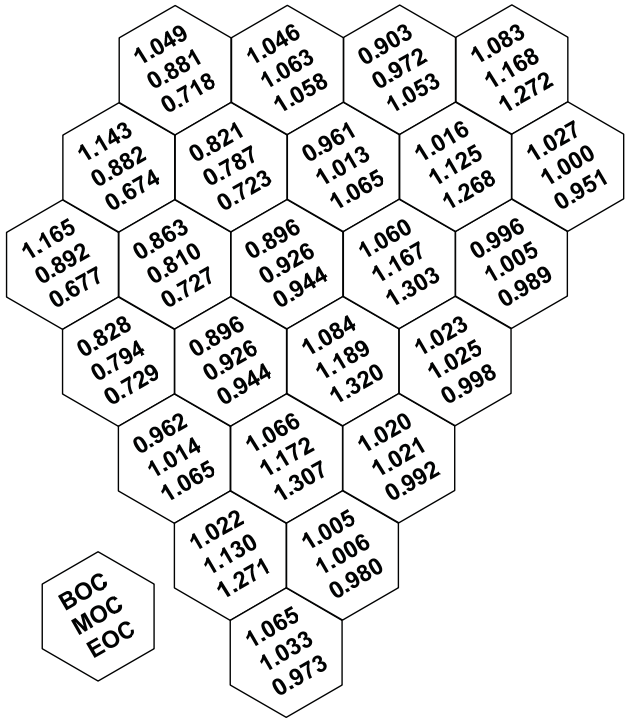

Figure 25. Radial power distribution (C-14).

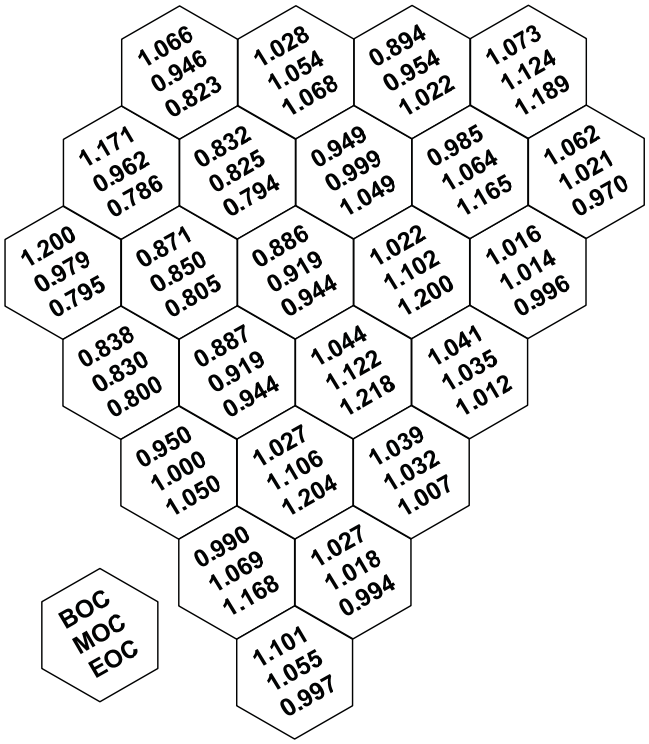

Figure 26. Radial power distribution (C-15).

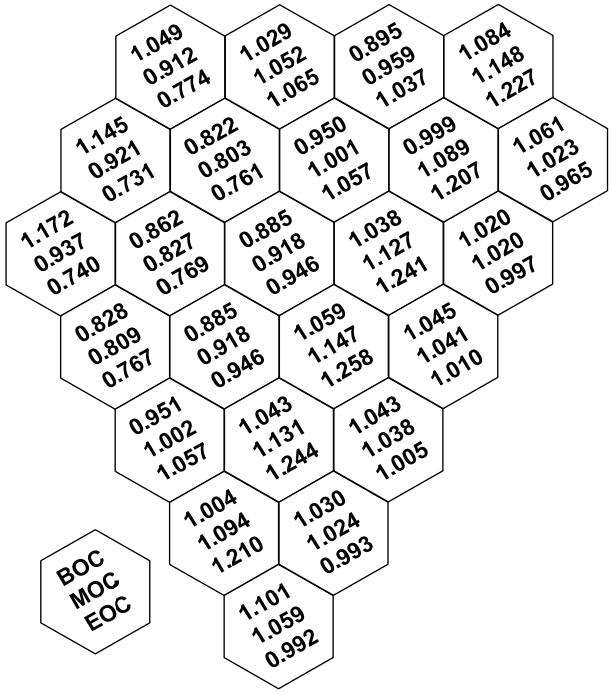

Figure 27. Radial power distribution (C-16).

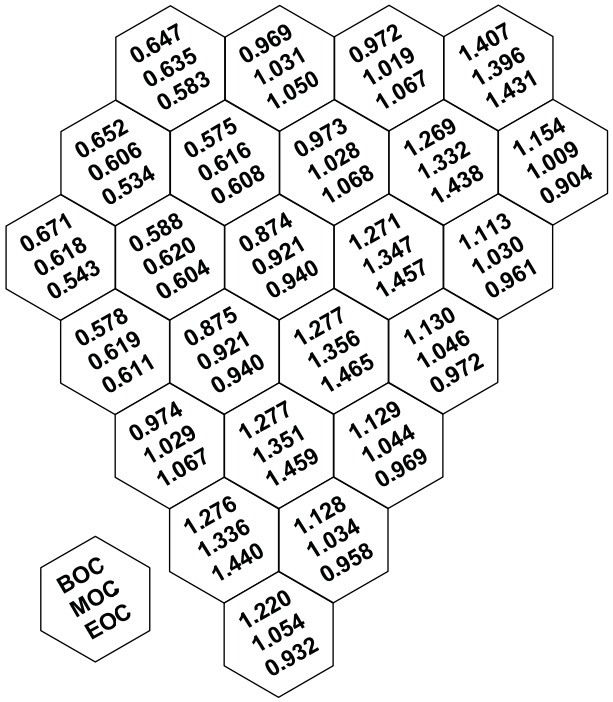

Figure 28. Radial power distribution (C-17).

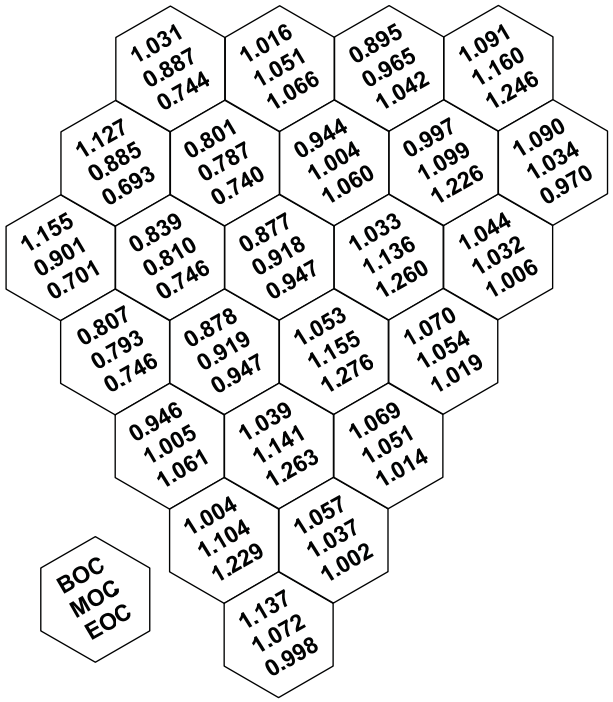

Figure 29. Radial power distribution (C-18).

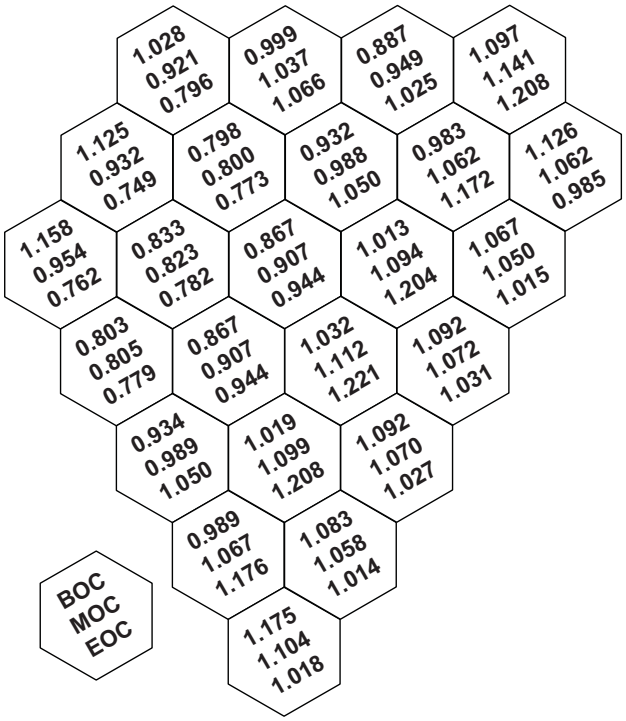

Figure 30. Radial power distribution (C-19).

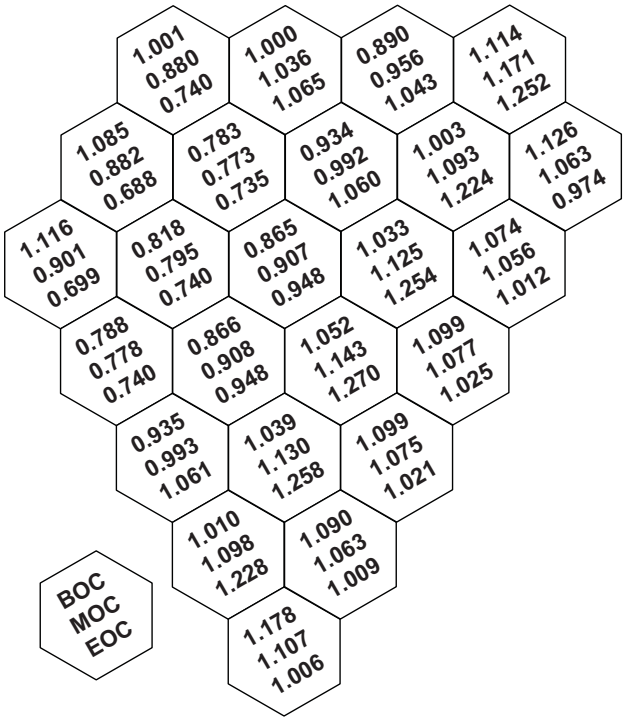

Figure 31. Radial power distribution (C-20).

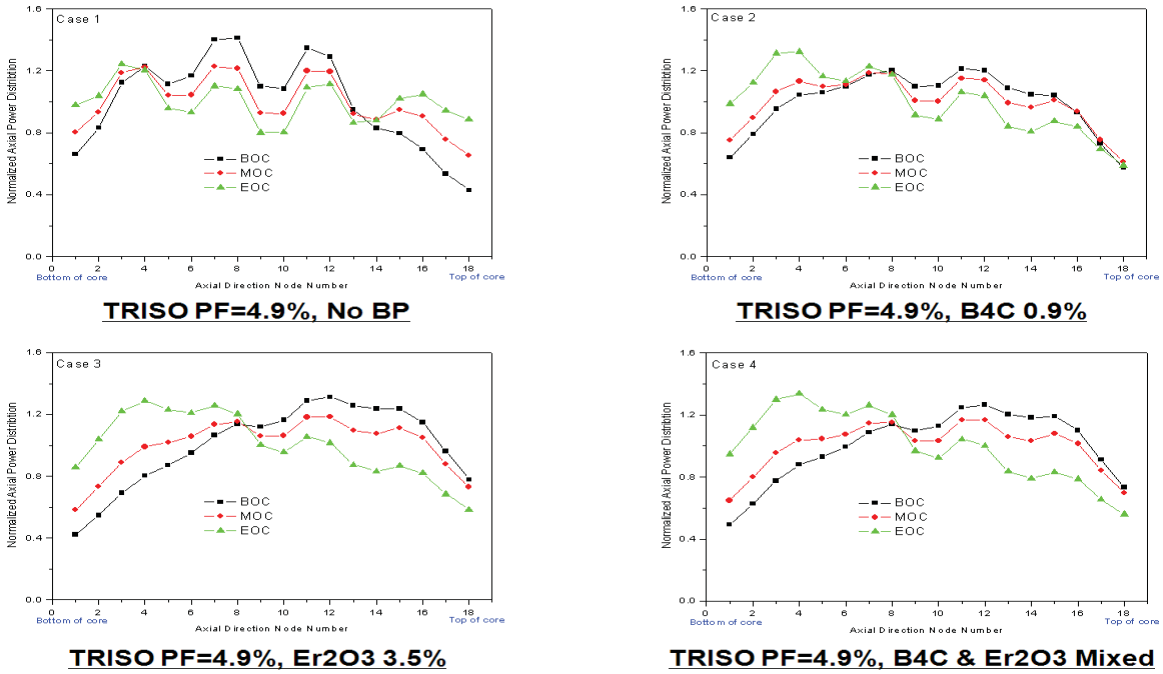

Figure 32. Axial power distribution (C-01, C-02, C-03, C-04).

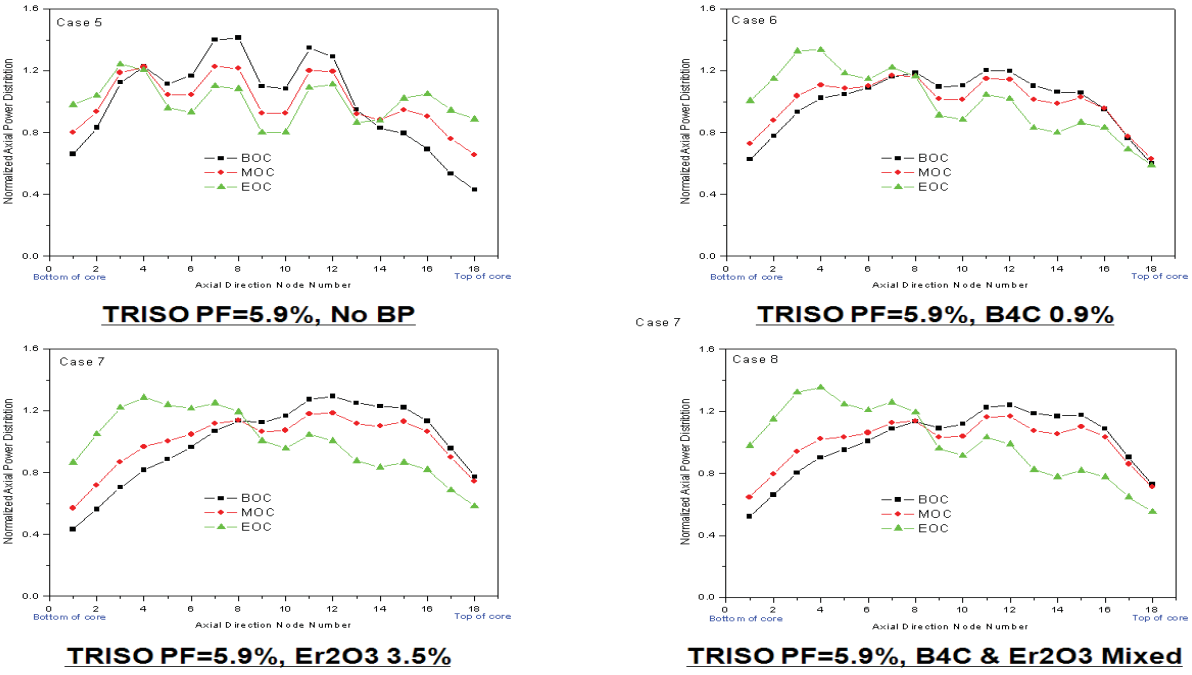

Figure 33. Axial power distribution (C-05, C-06, C-07, C-08).

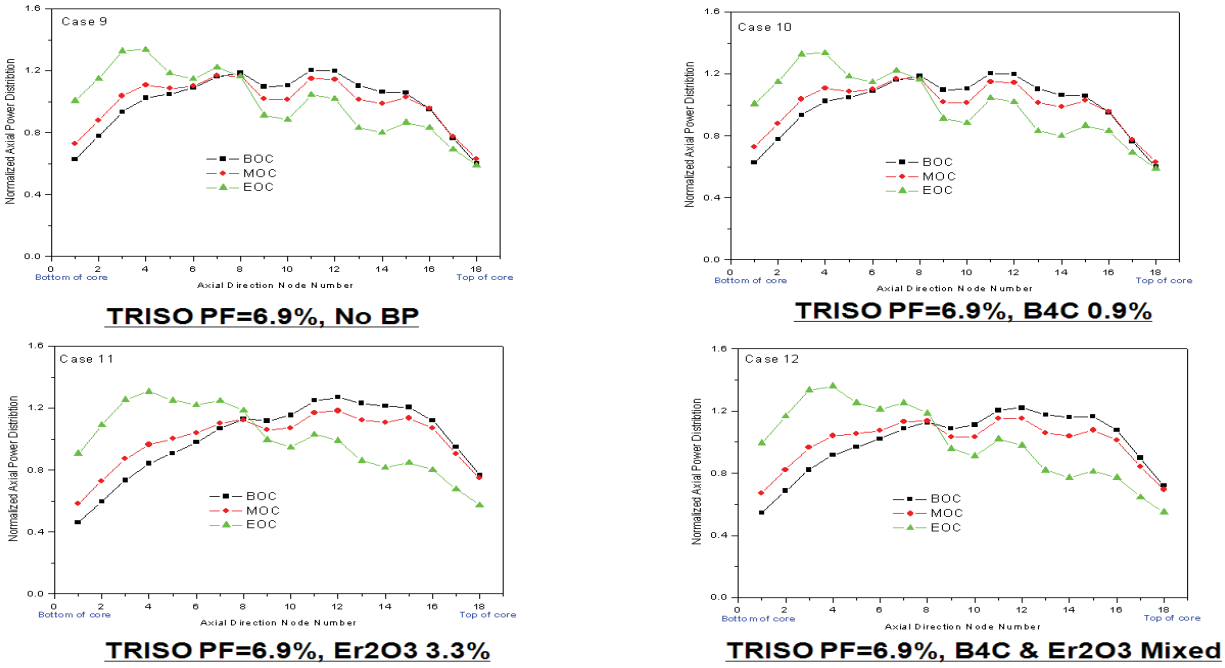

Figure 34. Axial power distribution (C-09, C-10, C-11, C-12).

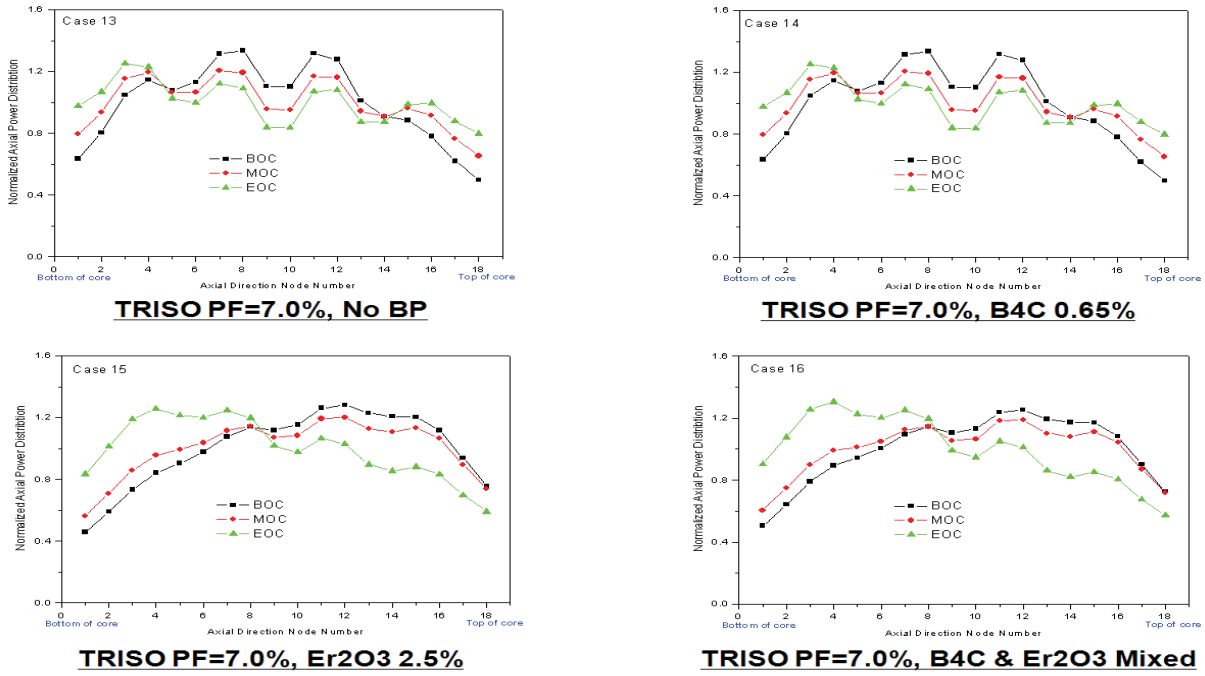

Figure 35. Axial power distribution (C-13, C-14, C-15, C-16).

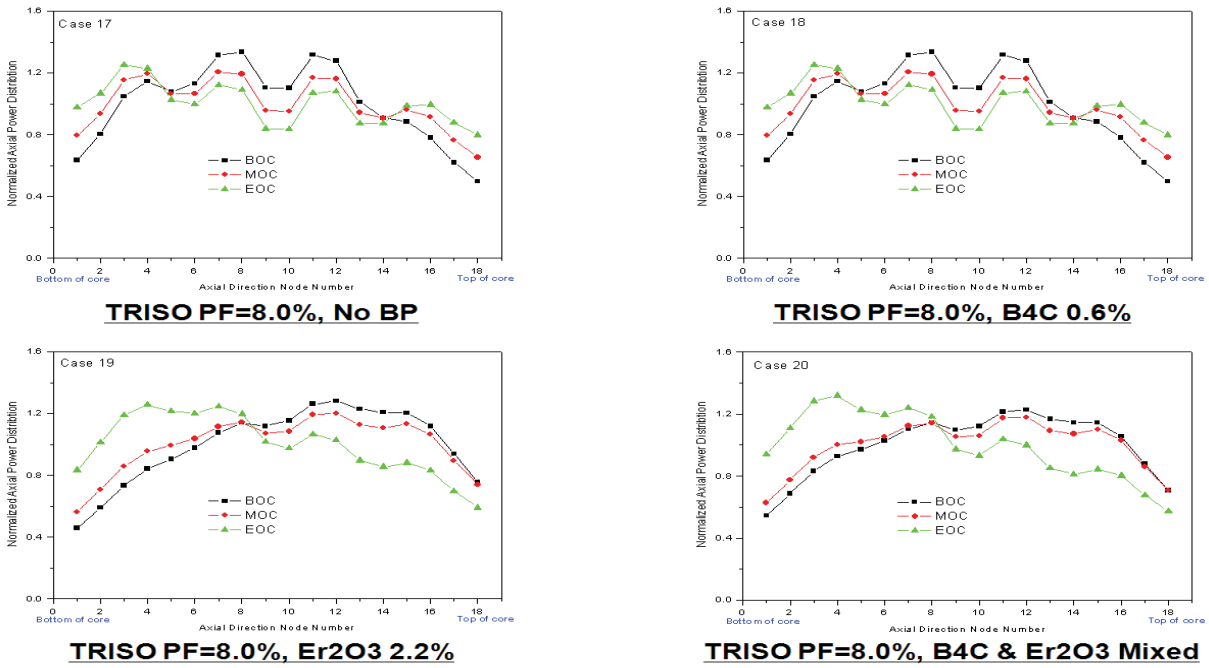

Figure 36. Axial power distribution (C-17, C-18, C-19, C-20).

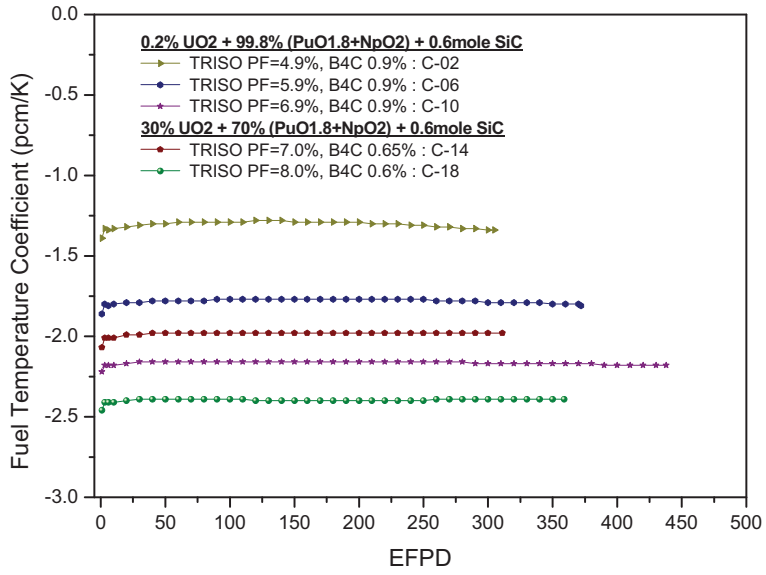

Figure 37. Fuel temperature coefficient (C-02, C-06, C-10, C-14, C-18, BP: B_4C).

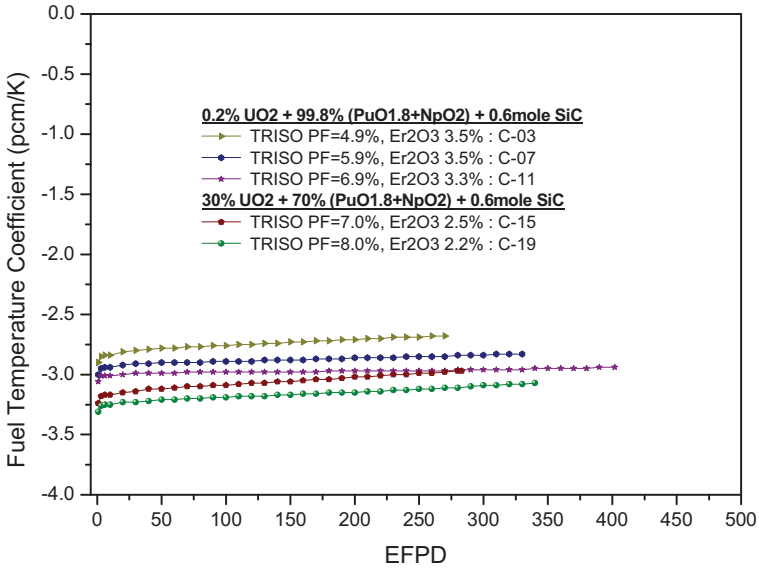

Figure 38. Fuel temperature coefficient (C-03, C-07, C-11, C-15, C-19, BP: Er_2O_3).

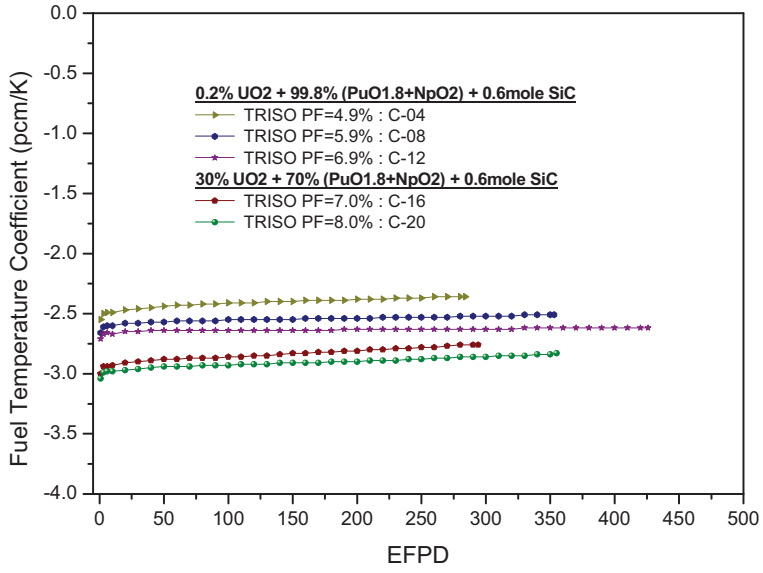

Figure 39. Fuel temperature coefficient (C-04, C-08, C-12, C-15, C-20, BP: B_4C and Er_2O_3 mixed).

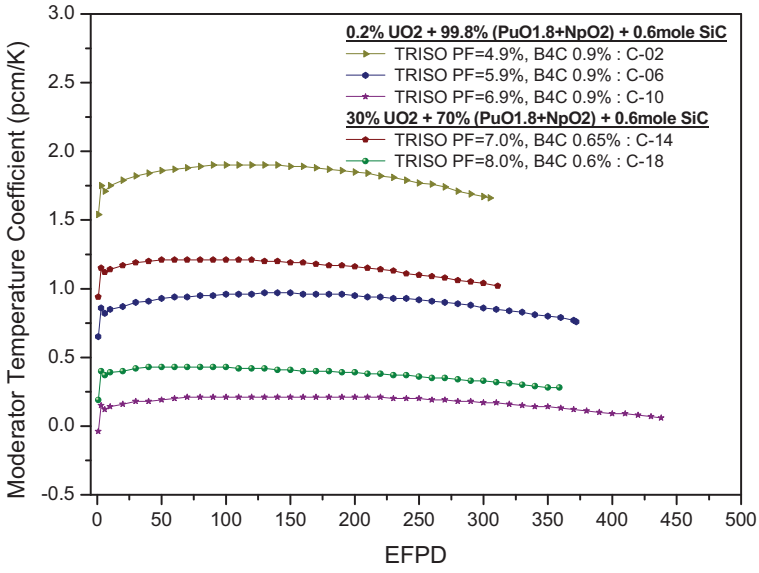

Figure 40. Moderator temperature coefficient (C-02, C-06, C-10, C-14, C-18, BP: B_4C).

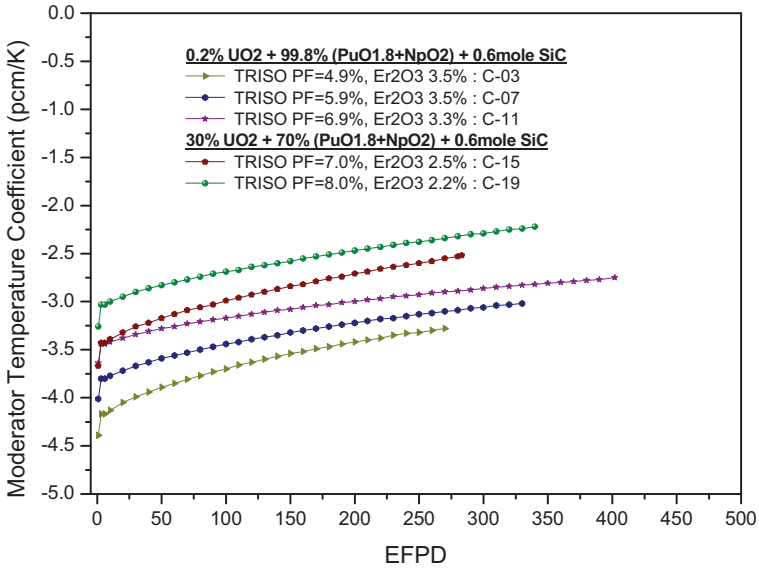

Figure 41. Moderator temperature coefficient (C-03, C-07, C-11, C-15, C-19, BP: Er_2O_3).

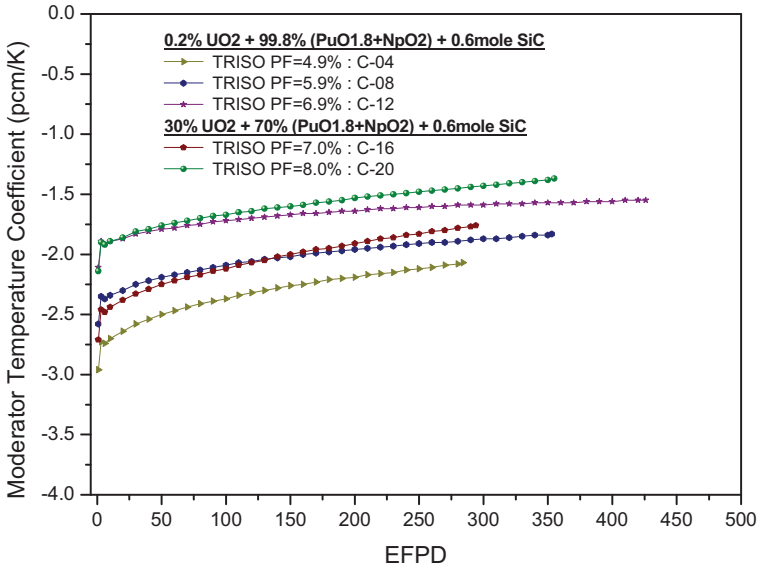

Figure 42. Moderator temperature coefficient (C-04, C-08, C-12, C-15, C-20, BP: B_4C and Er_2O_3 mixed).

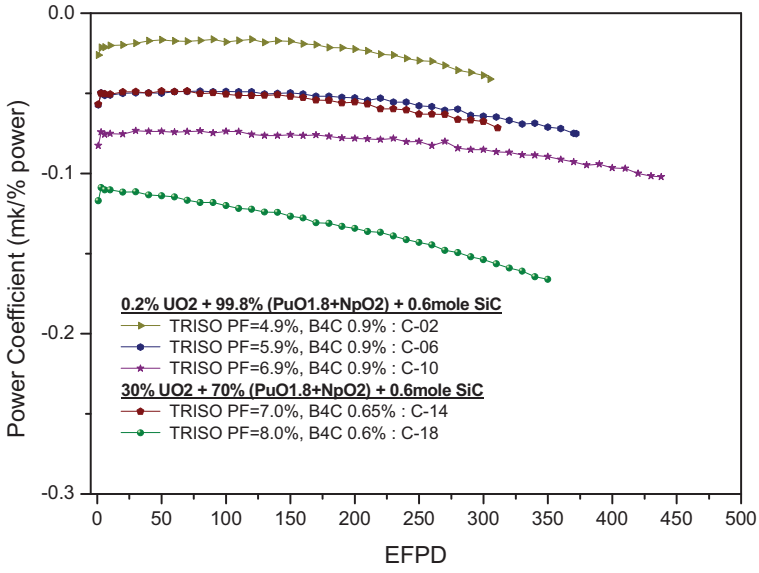

Figure 43. Power coefficient (C-02, C-06, C-10, C-14, C-18, BP: B_4C).

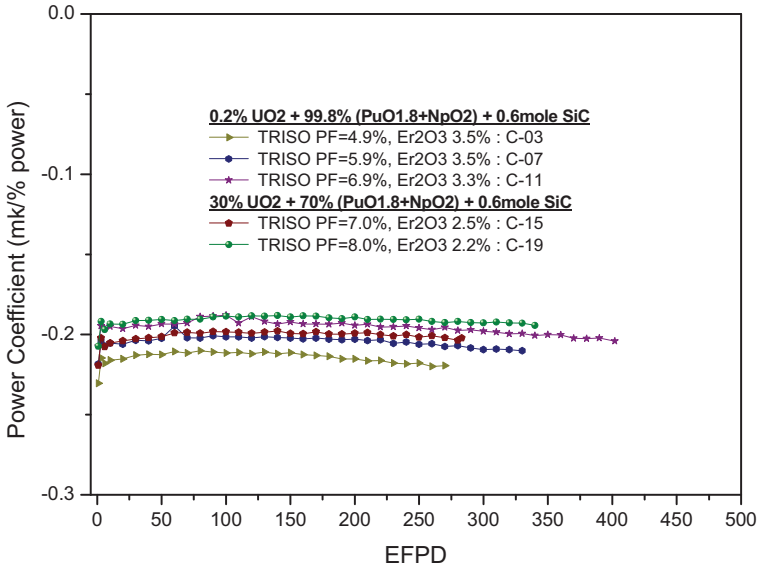

Figure 44. Power coefficient (C-03, C-07, C-11, C-15, C-19, BP: Er_2O_3).

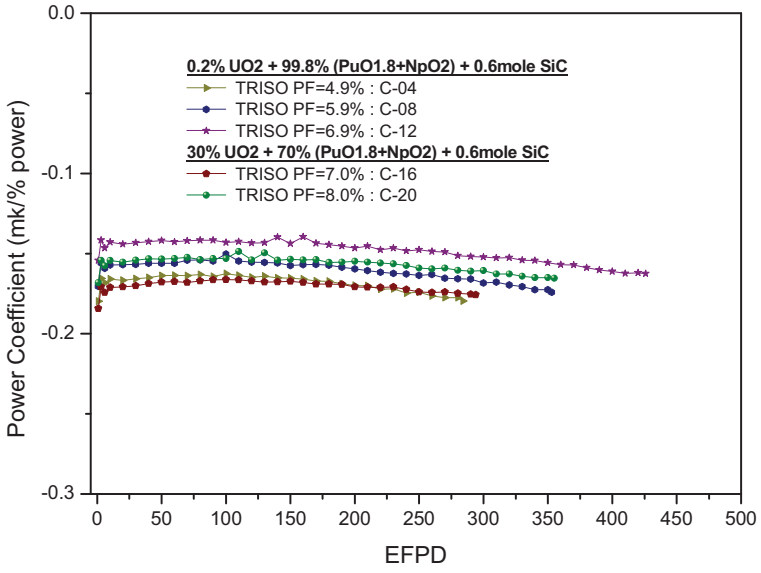

Figure 45. Power coefficient (C-04, C-08, C-12, C-15, C-20, BP: B_4C and Er_2O_3 mixed).

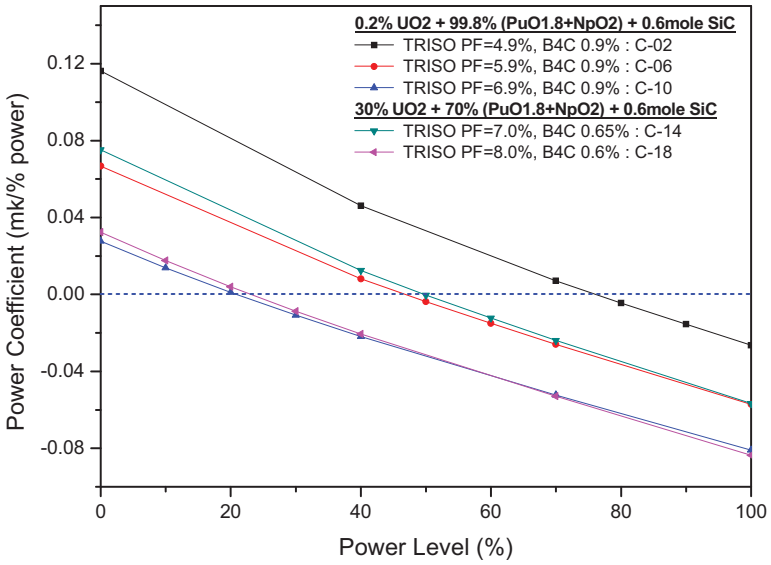

Figure 46. Power coefficient with power level at BOC (C-02, C-06, C-10, C-14, C-18, BP: B_4C).

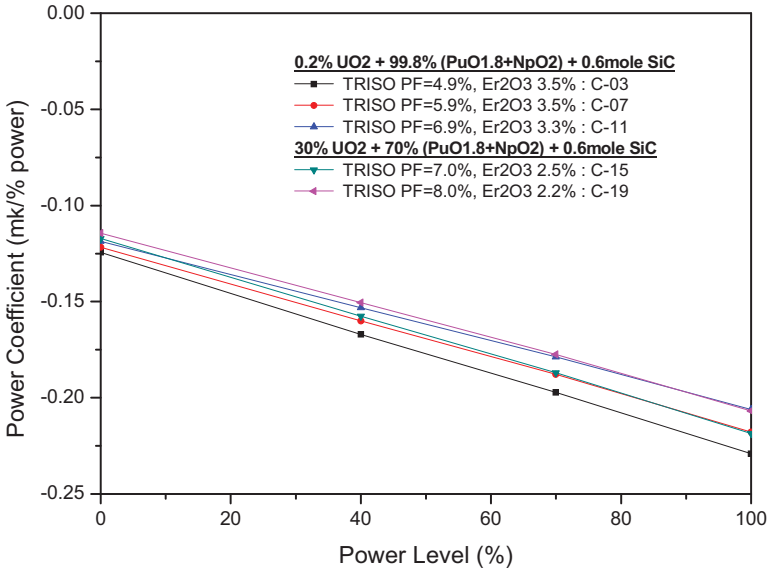

Figure 47. Power coefficient with power level at BOC (C-03, C-07, C-11, C-15, C-19, BP: Er_2O_3).

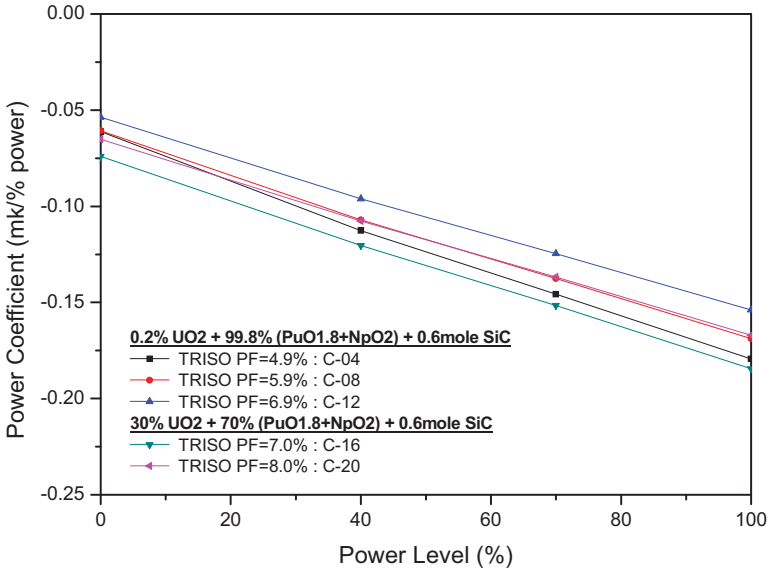

Figure 48. Power coefficient with power level at BOC (C-04, C-08, C-12, C-15, C-20, BP: B_4C and Er_2O_3 mixed).

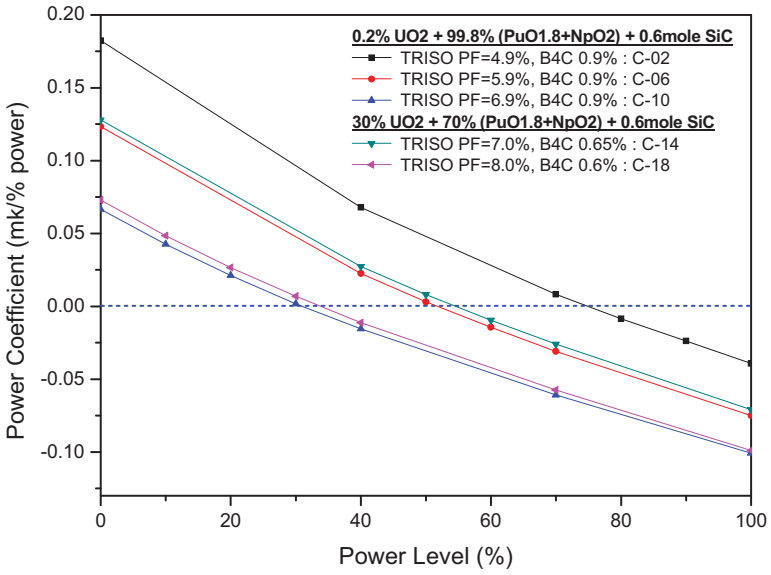

Figure 49. Power coefficient with power level at EOC (C-02, C-06, C-10, C-14, C-18, BP: B_4C).

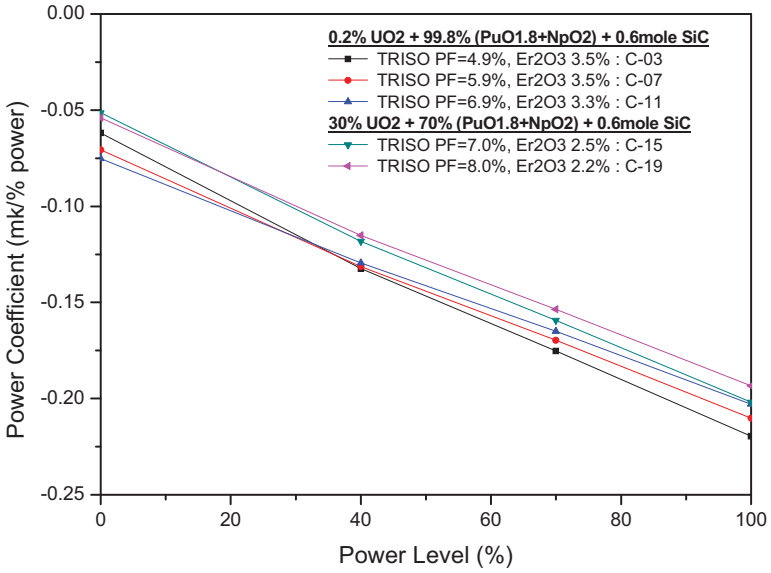

Figure 50. Power coefficient with power level at EOC (C-03, C-07, C-11, C-15, C-19, BP: Er_2O_3).

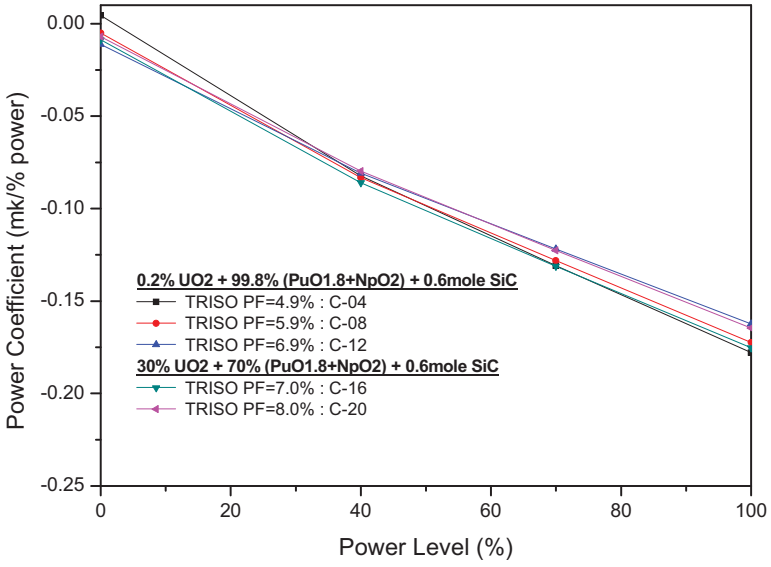

Figure 51. Power coefficient with power level at EOC (C-04, C-08, C-12, C-15, C-20, BP: B_4C and Er_2O_3 mixed).

4.3.5 Reduction of Thermal Power

As shown in the previous section, the core design of the 600 MW_{th} DB-HTR core provides a satisfactory performance during the normal operation in most cases, except that the moderator temperature coefficient and power coefficient can be slightly positive with the B_4C. However, the peak fuel temperature can be much higher than the general upper limit of 1,600°C during the LPCC accident when adopting the recently-developed JAEA's method for the graphite annealing effect.[12]

To reduce the peak fuel temperature during LPCC accident, the core thermal power is reduced to 450 MW_{th} and the major core performances are evaluated in this section.

Table 8 shows 2 additional core design models considered in the 450 MW_{th} DB-HTR core. In the case of C-21, the PF is 6.9% and fuel type is Case I. It can be compared with the C-12 case of the 600 MWth DB-HTR core. In the cases of the C-21 and C-22, the B_4C and Er_2O_3 mixed BP was used for the core design analysis as shown in Table 8. The fraction of BP was adjusted in each case such that the burnup reactivity swing should be about 3,000 pcm for a fair comparison.

Table 8. Design approaches of the 450 MW_{th} DB-HTR core.

No.	TRISO PF (%)	Fuel type	BP Fraction (%)
C-21	6.9	Case I	B_4C 0.3 and Er_2O_3 2.0
C-22	8.0	Case II	B_4C 0.15 and Er_2O_3 1.5
Case I : 0.2%UO_2 + 99.8%(NpO_2+$PuO_{1.8}$)+SiC kernel getter Case II : 30%UO_2 + 70%(NpO_2+$PuO_{1.8}$)+SiC kernel getter			

Table 9 and Table 10 show the summary of the core design analysis of the 450 MW_{th} DB-HTR core. Also, it shows the results of the C-12 and C-20 case of the 600 MW_{th} DB-HTR core for a comparison. As shown in Table 9, the cycle length of C-21 is 554 EFPD and that of C-22 is 465 EFPD while cycle length of C-12 and C-20 is 426 and 355 EFPDs, respectively. Also, the burnup reactivity swings are similar to about 3,000 pcm. However, the averaged discharged burnups of the C-21 and C-22 are slightly lower than those of the C-12 and C-20, respectively. In terms of fuel consumption, the consumption rates of total heavy metal and plutonium of the C-21 are slightly lower than those of the C-12, as shown in Table 10. Also, the consumption rates of total heavy metal and plutonium of the C-22 are slightly lower than those of the C-20. The maximum fuel temperatures of the fuel block at the steady state for the C-21 and C-22 are slightly lower than those of the C-12 and C-20 cases, respectively, as shown in Table 10.

Table 9. Summary I of the core analysis results of the 450MW_{th} DB-HTR core.

Case	Feed Fuel Mass (Kg)	Thermal Power (MWth)	Cycle Length (day)	Reactivity Swing (pcm)	Reactivity (k-eff)		Average Discharged Burnup (GWd/tHM)
					BOC	EOC	
C-12	437.4	600	426	3,040	1.035	1.0049	583.684
C-21		450	554	3,074	1.036	1.0054	569.404
C-20	504.6	600	355	3,203	1.037	1.0046	422.082
C-22		450	465	3,316	1.038	1.0046	414.672

Table 10. Summary II of the core analysis results of the 450MW_{th} DB-HTR core.

Case	Thermal Power (MWth)	Maximum Fuel Temp. at Steady State (°C)[a]		Fuel Consumption (%)			Peak Fuel Temp. at LPCC Event (°C) (by using JAEA Method)
		BOC (No. Xe)	EOC	Total HM	Pu-total	Pu-239	
C-12	600	945	992	-58.55	-64.3	-95.14	1,920
C-21	450	932	977	-57.29	-63.07	-94.48	1,596
C-20	600	939	982	-42.30	-60.81	-93.00	1,869
C-22	450	935	972	-41.67	-60.08	-92.54	1,549
a. Fuel block average value at steady state.							

The peak fuel temperatures during the LPCC event of the C-21 and C-22 were evaluated by using JAEA's method for graphite annealing effect as shown in Table 10. The peak fuel temperature of the C-21 (450 MW_{th} DB-HTR core) is 1,596°C, which is below nominal design limit 1600°C, while it was 1,920°C for the C-12 case of the 600 MW_{th} DB-HTR core. Also, the peak fuel temperature of the C-22 (450 MW_{th} DB-HTR core) is 1,549°C, which is much lower than that of the C-20 (600 MW_{th} DB-HTR core).

The reactivity changes during an equilibrium cycle of the C-21 and C-22 are shown in Figure 52. Also, the reactivity changes of the C-12 and C-20 are depicted in the same figure for the comparison. As shown in Figure 52 and Table 9, the cycle length of the C-21 is longer than that of the C-12, and the cycle length of the C-22 is also longer than that of the C-20.

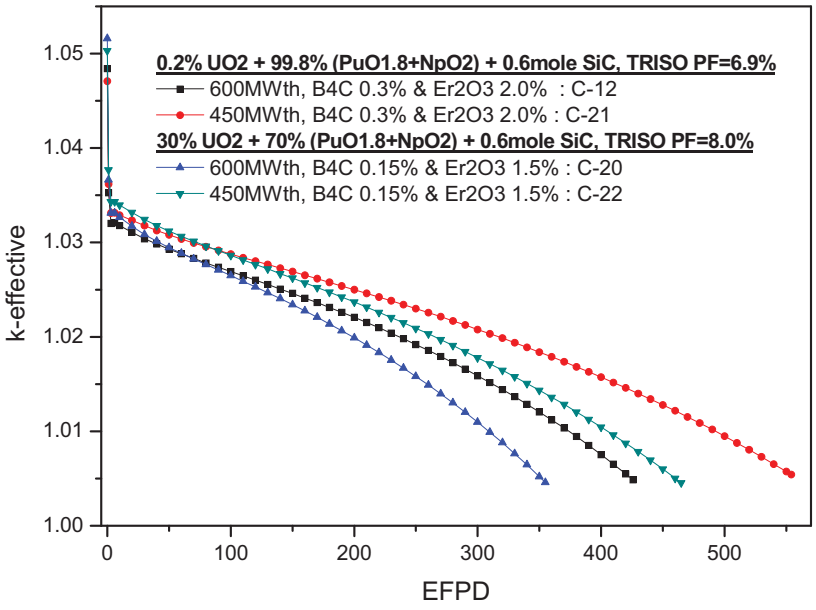

Figure 52. Evolution of the k-effective values during equilibrium cycle.

The block-wise core radial power distributions of the C-21 and C-22 are shown in Figure 53 and Figure 54, respectively. The radial power distribution of the C-21 is very similar to the radial power distribution of the C-12, and the radial power distribution of the C-22 is also similar to that of the C-20.

The core axial power distribution of the C-21 and C-22 is shown in Figure 55. In general, the axial power distributions of the 450 MW_{th} DB-HTR core (C-21 and C-22) are similar to those of the 600 MW_{th} DB-HTR core (C-12 and C-20).

For comparison of safety characteristics of the 450 MW_{th} and 600 MW_{th} DB-HTR cores, several reactivity temperature coefficients were evaluated for the C-21 and C-22 cases. The FTCs of the C-21 and C-22 are shown in Figure 56 with the FTCs of the C-12 and C-20. From the figure, note that the FTC of the C-21 is slightly lower than that of the C-12, and the FTC of the C-22 is also slightly lower than that of the C-20. The FTCs of the both cases are negative for the full-power operating conditions. The MTCs of the C-21 and C-22 are provided in Figure 57. The MTCs of the C-21 and C-22 are slightly lower than those of the C-12 and C-20, respectively, in the higher burnup. Figure 58 shows the power coefficient of the C-21 and C-22 at the full power operating conditions. The power coefficients of the both cases are negative for the full power operating conditions. From the figure, note that the power coefficient of the C-21 is similar to that of the C-12, but the power coefficient of the C-22 is lower than that of the C-20. Figure 59and Figure 60 show the power-dependent power coefficients of the C-21 and C-22 at the BOC and EOC state, respectively. The power coefficients of the 450 MW_{th} DB-HTR core (C-21 and C-22) at the BOC and EOC state are slightly lower than those of the 600 MW_{th} DB-HTR core (C-12 and C-20).

From the results of the 450 MW_{th} DB-HTR core design analysis, it is noted that the core performance of the heavy metal and plutonium is similar to that of the 600 MW_{th} DB-HTR core design, and the temperature coefficients are all clearly negative. Also, it is noted that the peak fuel temperature of the 450MW_{th} DB-HTR core at LPCC event can be maintained below nominal design limit of 1600°C.

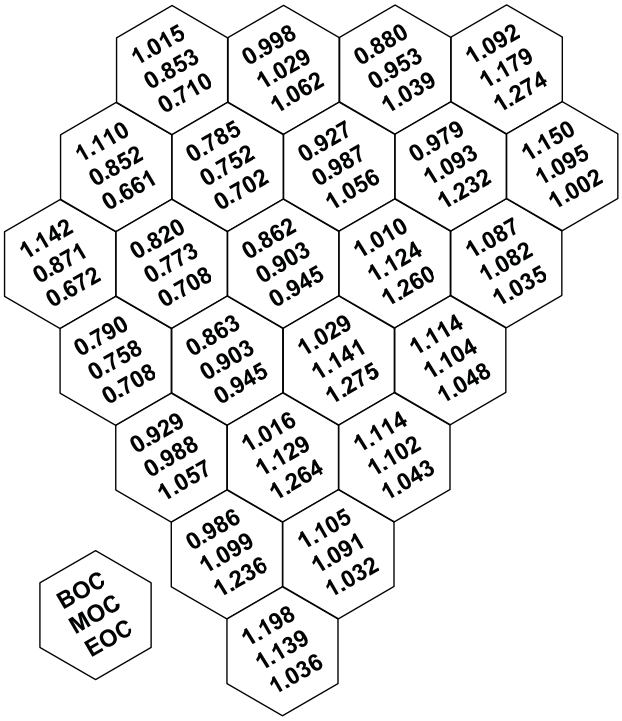

Figure 53. Radial power distribution (C-21).

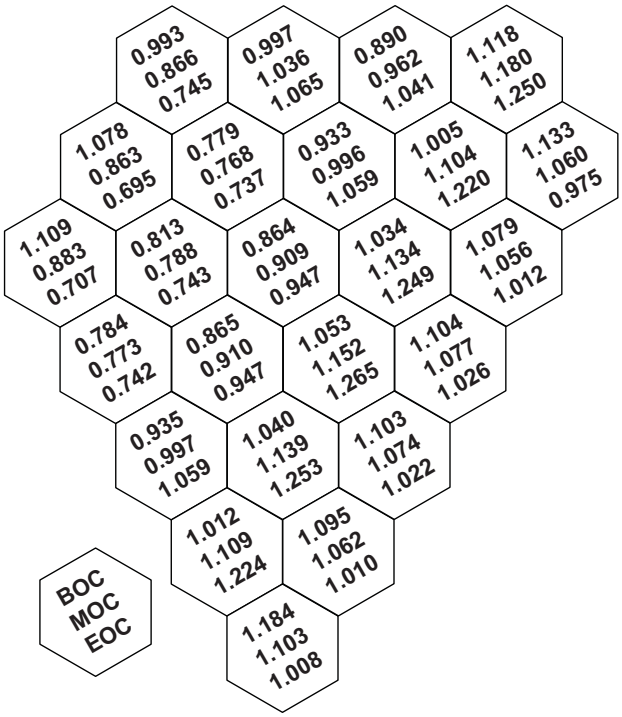

Figure 54. Radial power distribution (C-22).

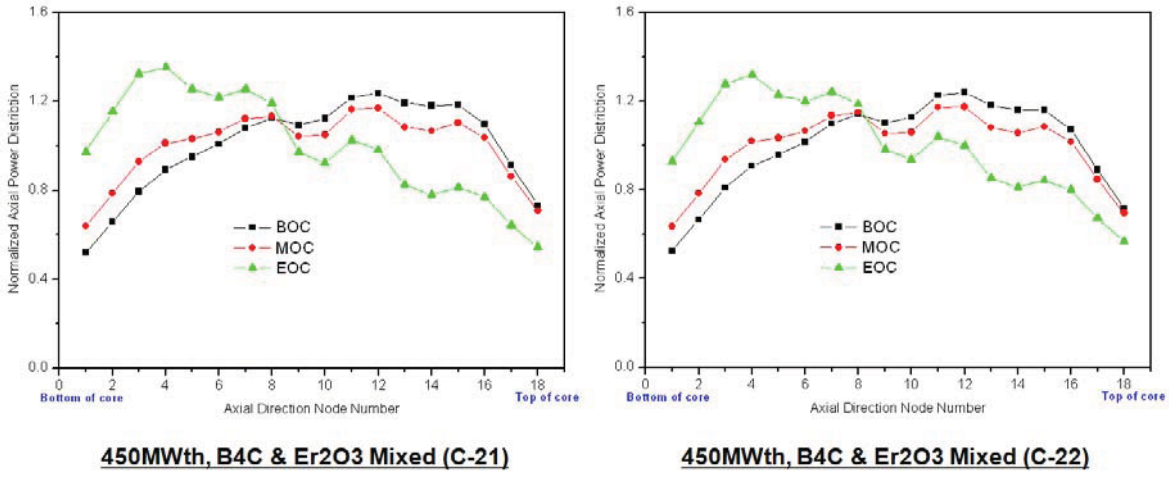

Figure 55. Axial power distribution (C-21, C-22).

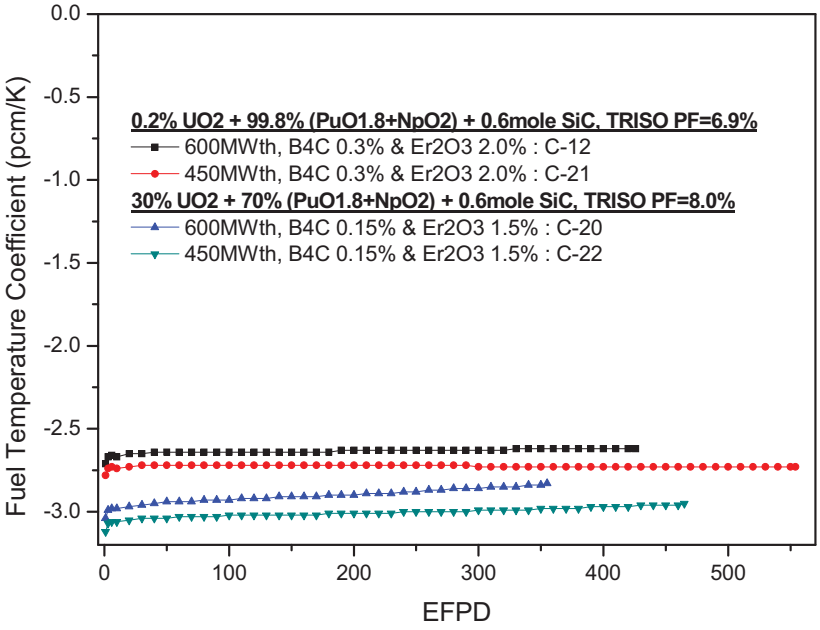

Figure 56. Fuel temperature coefficient (C-12, C-20, C-21, C-22).

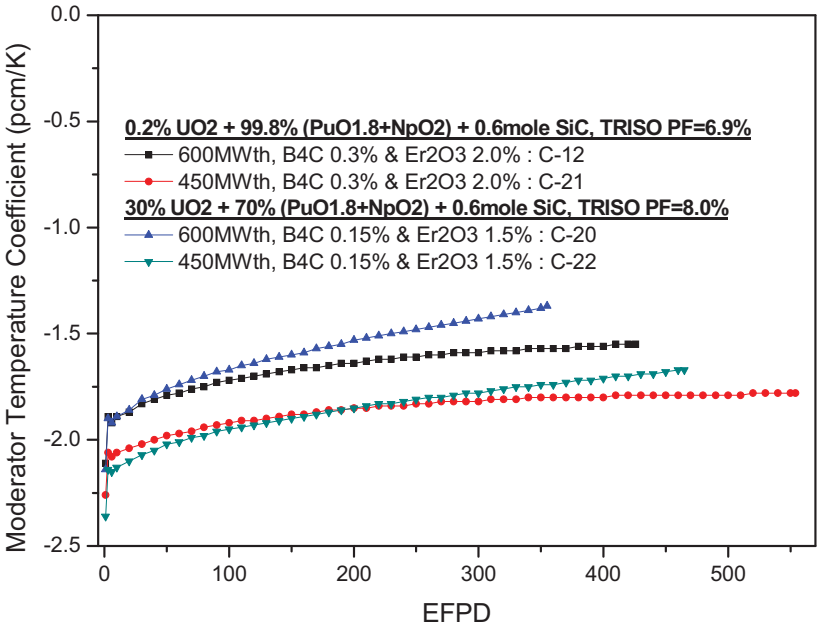

Figure 57. Moderator temperature coefficient (C-12, C-20, C-21, C-22).

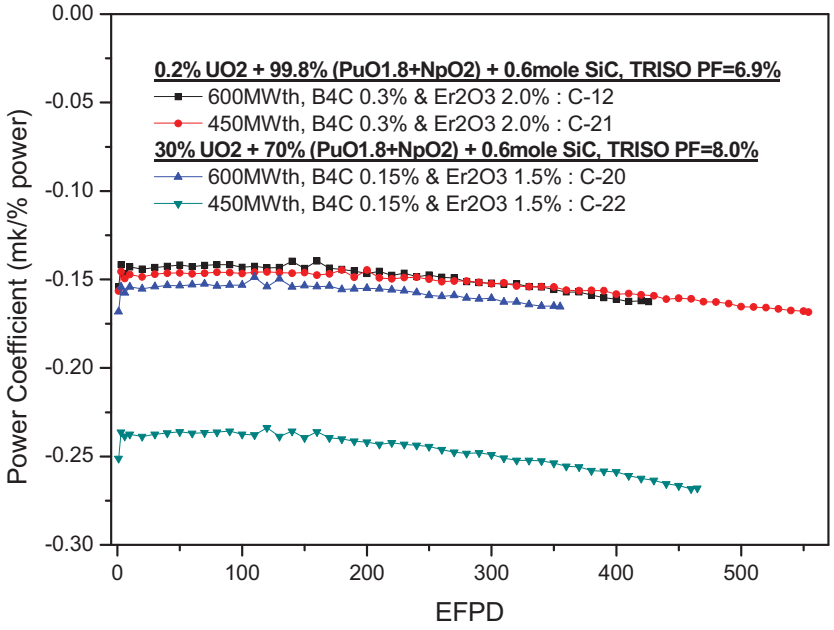

Figure 58. Power coefficient (C-12, C-20, C-21, C-22).

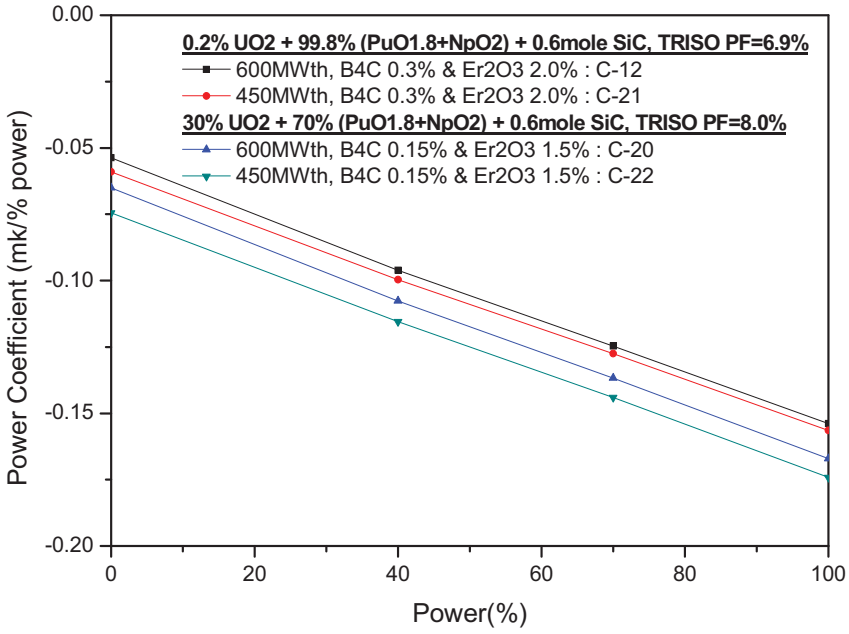

Figure 59. Power coefficient with power level at BOC (C-12, C-20, C-21, C-22).

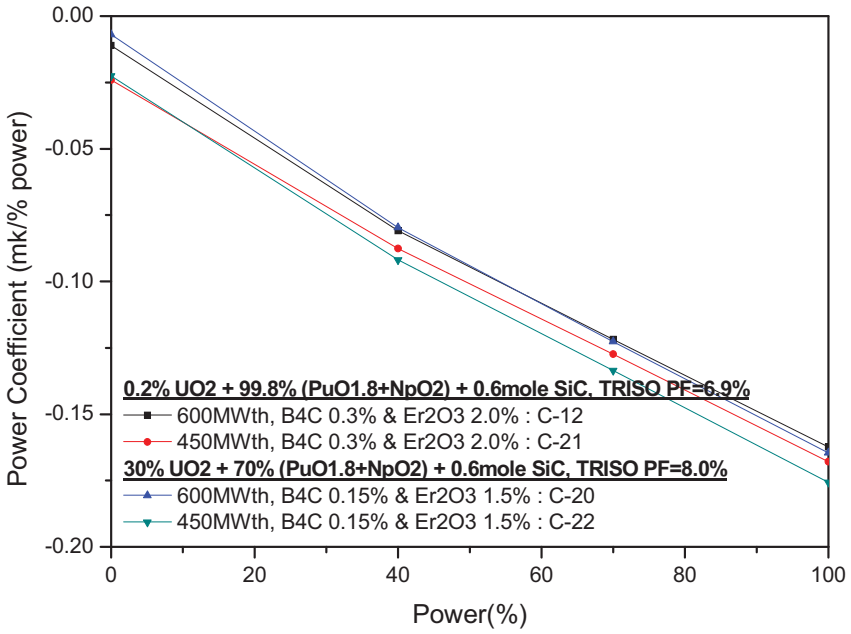

Figure 60. Power coefficient with power level at EOC (C-12, C-20, C-21, C-22).

4.3.6 Decay Heat Analysis

Decay heat of the TRU-loaded DB-HTR cores with a SiC kernel getter was calculated with a Korean Atomic Energy Research Institute's (KAERI's) procedure.[13] Figure 61 shows the calculational procedure for decay heat evaluation of an equilibrium cycle. In this procedure, the fuel compositions are determined by the McCARD code with 3-D whole core depletion and the ORIGEN code[14] is only used to calculate the decay heat. For the whole core, McCARD depletion calculations were performed to find equilibrium cycle for each fuel types. In the core depletion calculation, the temperature of the whole core is assumed to be constant at 900 K. The ENDF/B-VI nuclear data library is used for the decay heat calculation.

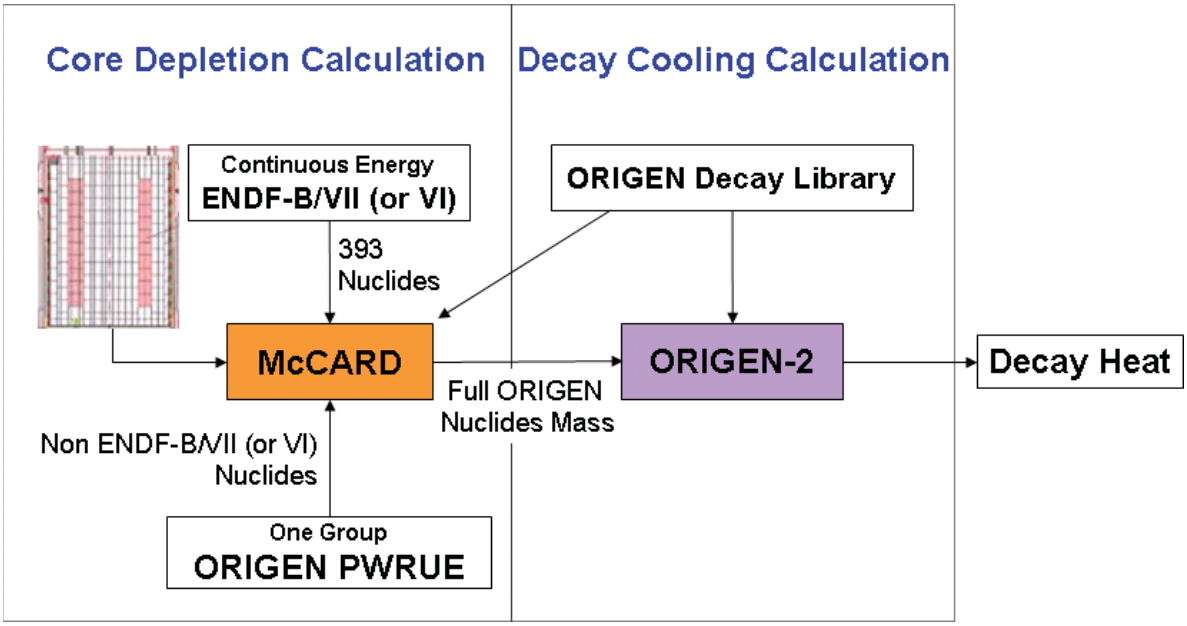

Figure 61. Procedure for the decay heat evaluation.

To calculate the decay heat of the DB-HTR core, a three-batch axial-only fuel block shuffling scheme is used and also a radial and axial hybrid shuffling scheme is considered for comparison as shown in Figure 62. In this decay heat calculation, six BP holes are considered and the BP holes are assumed to be filled with graphite. Table 11 shows the seven cases of the decay heat calculation.

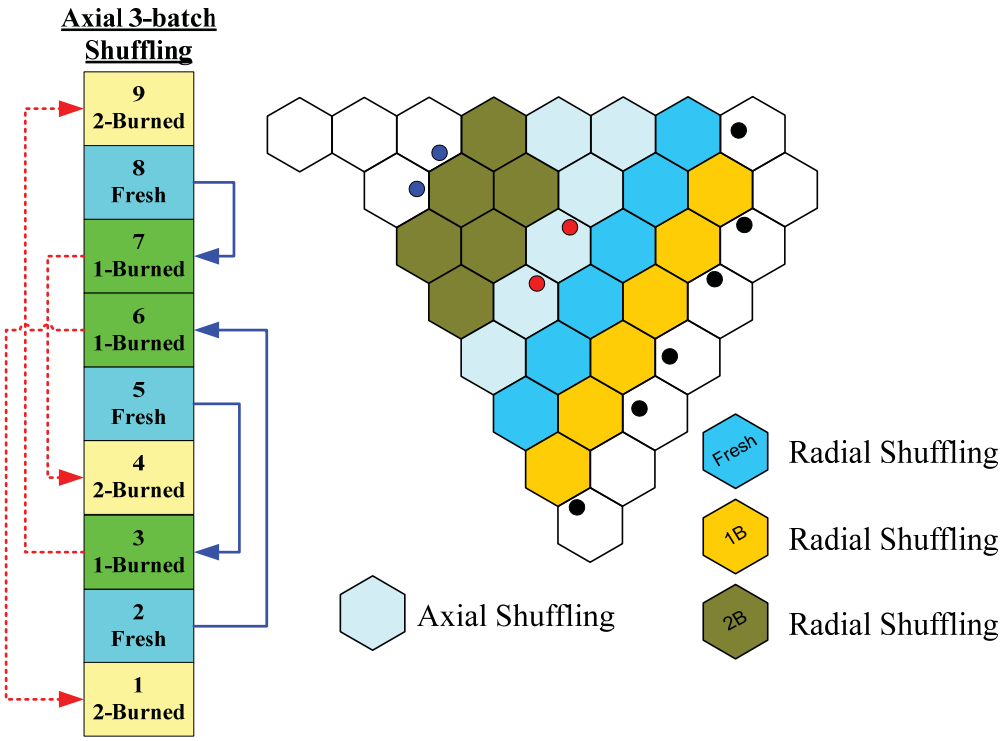

Figure 62. Fuel shuffling scheme for decay heat calculation.

Table 11. Cases of the decay heat calculations.

Case	TRISO PF(%)	Fuel Type	Fresh HM feed mass (kg)	Fuel Shuffling Scheme
DH-1	4.9	Case I	312.6	Axial-only
DH-2	5.9	Case I	372.6	Axial-only
DH-3	6.9	Case I	437.4	Axial-only
DH-4	7.0	Case II	438.0	Axial-only
DH-5	8.0	Case II	504.6	Axial-only
DH-6	6.9	Case I	437.4	Hybrid
DH-7	8.0	Case II	504.6	Hybrid
Case I : 0.2%UO_2 + 99.8%(NpO_2+$PuO_{1.8}$)+SiC kernel getter Case II : 30%UO_2 + 70%(NpO_2+$PuO_{1.8}$)+SiC kernel getter				

In this decay heat calculation, we focused on the short-term decay heat. The short-term decay heat directly affects the peak fuel temperature during the LPCC event.

The decay heat of the DH-1, DH-2, DH-3, DH-4 and DH-5 are shown in Figure 63 through Figure 67. From the figures, it can be observed that the decay heat of the DB-HTR core increases with EFPD for all cases. The decay heats of five cases at EOC state are summarized in Figure 68 with the typical decay heat of a UO_2 loaded core for a comparison. Also, the decay heat of a 100% TRU-loaded DB-HTR core (200 mm of kernel diameter and 27% TRISO packing fraction) with/without americium isotopes is depicted in Figure 68. It is noted that decay heats of the DB-HTR core for the DH-1, DH-2, DH-4, and DH-5 are distinctly lower than that of the UO_2 core when the cooling time is shorter than 100 hours. The comparison of the decay heat for fuel block shuffling schemes is shown in Figure 69. The fuel block shuffling scheme does not affect the decay heat of the DH-HTR core.

From results of the decay heat analysis, it should be noted that the short-term decay heat of the TRU-loaded DB-HTR core strongly depends on the fuel loading. Also, it is found that the americium isotope in the DB-HTR core strongly affects the short-term decay heat of the DB-HTR core. Those decay heat is used to calculate the peak fuel temperature of the LPCC event.

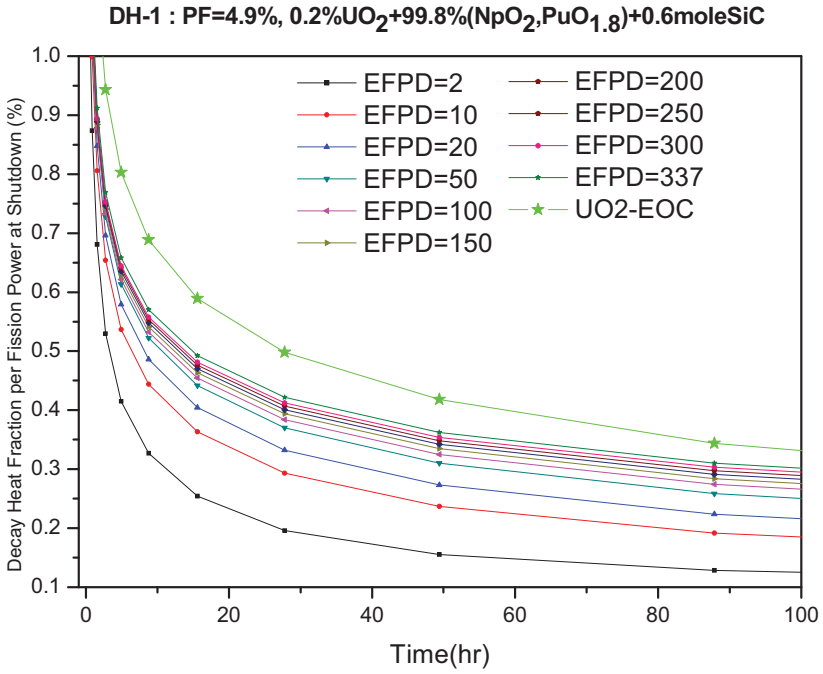

Figure 63. Core-average decay heat with EFPD of the DH-1 case.

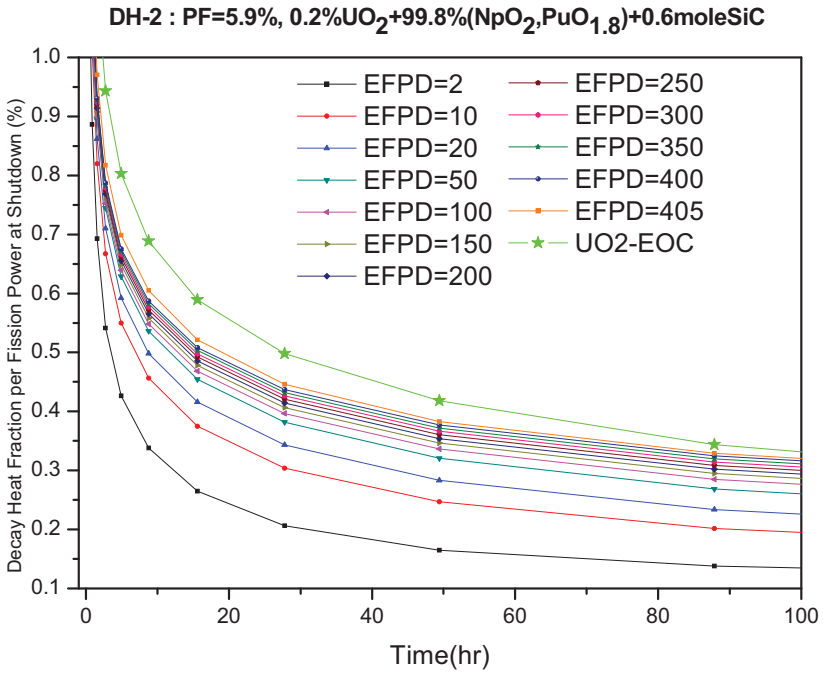

Figure 64. Core-average decay heat with EFPD of the DH-2 case.

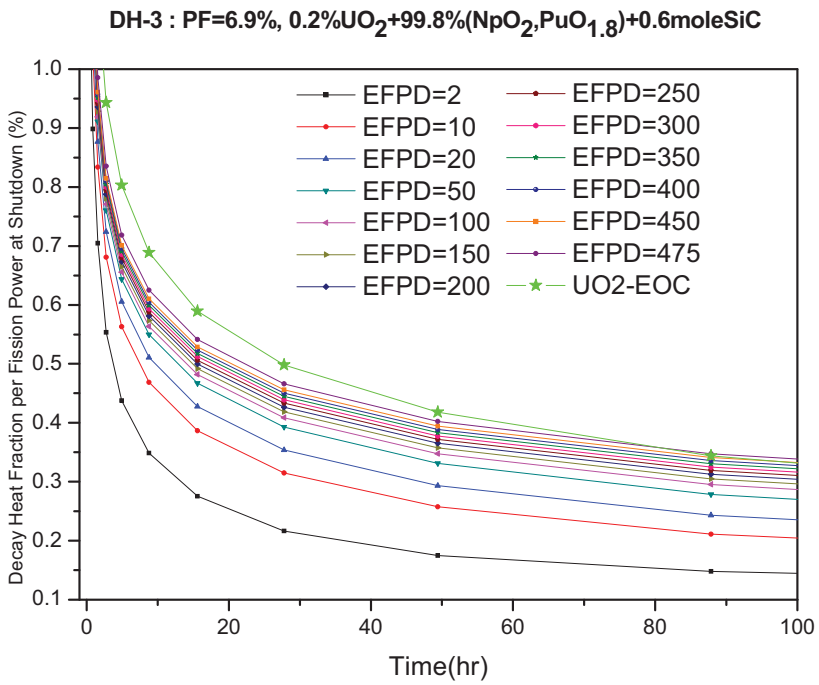

Figure 65. Core-average decay heat with EFPD of the DH-3 case.

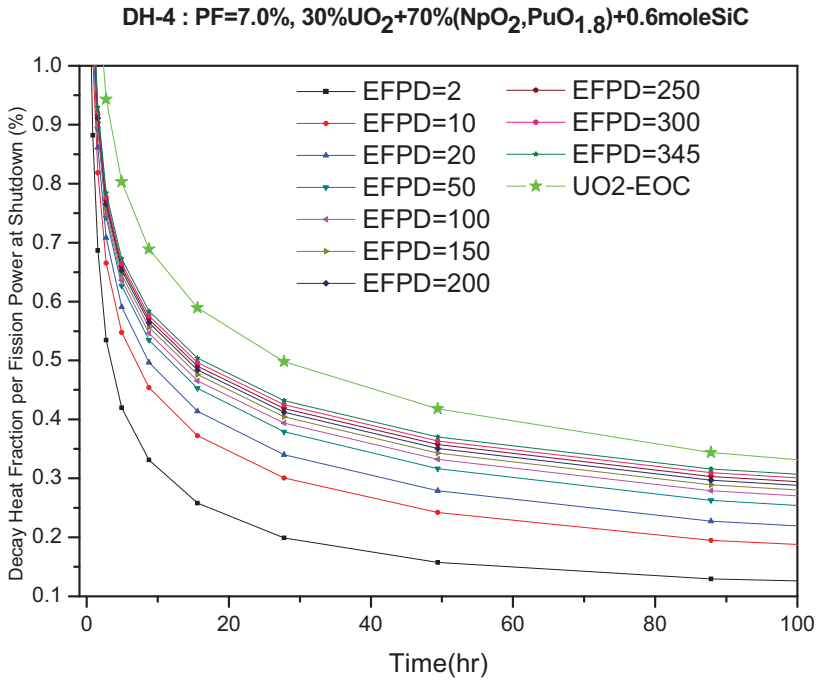

Figure 66. Core-average decay heat with EFPD of the DH-4 case.

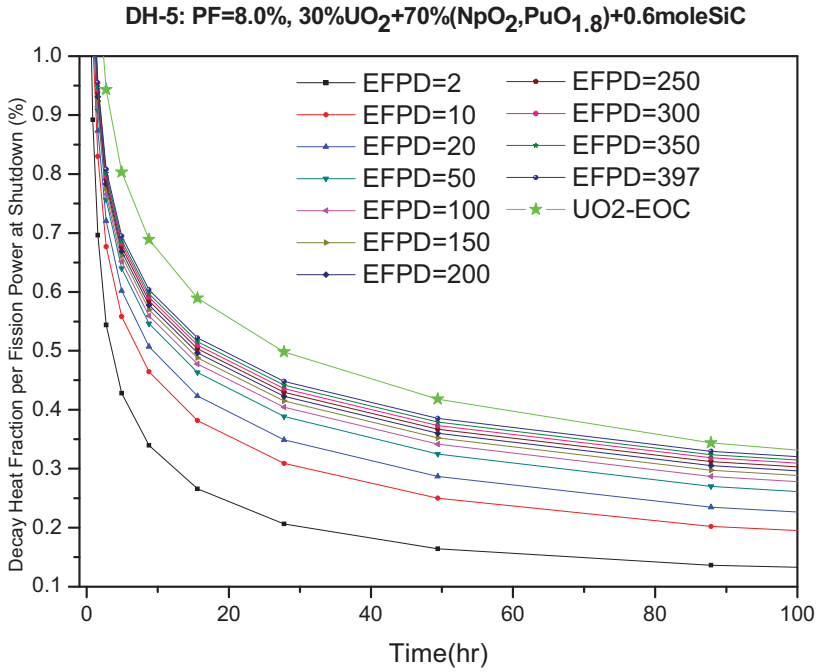

Figure 67. Core-average decay heat with EFPD of the DH-5 case.

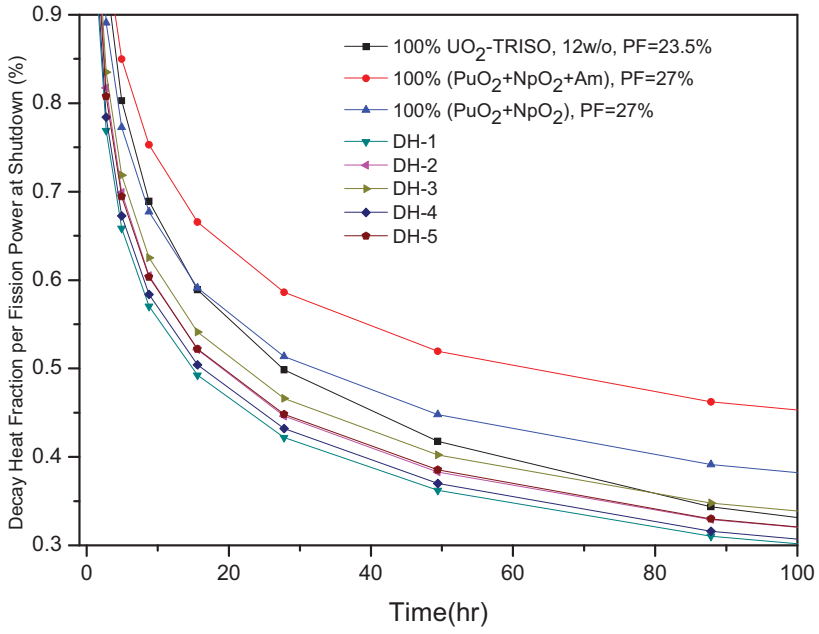

Figure 68. Core-average decay heat at EOC.

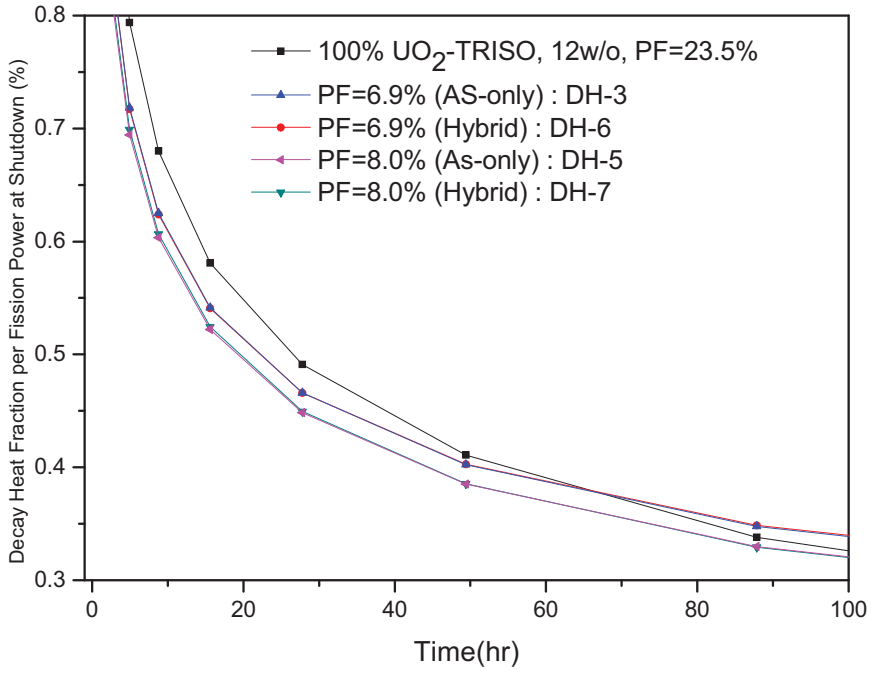

Figure 69. Comparison of a decay heat with fuel block shuffling scheme.

4.4 Summary and Conclusions

For a five-ring 600 MW_{th} TRU-loaded DB-HTR core with a [0.2%UO_2+ 99.8%($PuO_{1.8}$+ NpO_2)]+0.6mole SiC kernel getter or a [30%UO_2+ 70%($PuO_{1.8}$+NpO_2)]+0.6mole SiC kernel getter, a core physics study has been performed in terms of the neutronic performance and core safety characteristics. To satisfy the nominal fuel temperature limit of 1600°C during an Low Pressure Conduction Cooldown (LPCC) event, a core physics analysis of five-ring 450 MW_{th} DB-HTR core has also been performed. Also, a short-term decay heat of a 600 MW_{th} TRU-loaded DB-HTR core has been calculated. The following conclusions are drawn from the current work.

- Based on a three-batch radial and axial hybrid fuel management scheme, an over 60% plutonium burnup can be achieved when the burnup reactivity swing is about 3000 pcm.
- With regard to burnable poison, both B_4C and Er_2O_3 are promising BP material for the DM-HTR core, and B_4C provides a little higher fuel discharge burnup. The MTC of the core is positive with the B_4C, while it can be strictly negative with Er_2O_3. The power coefficient of the core with both BPs is negative at the full power condition, while the power coefficient can be positive with B_4C at a low power level. But, the cycle length of DB-HTR core with Er_2O_3 BP is very shorter than that of the DB-HTR core with B_4C. If the B_4C and Er_2O_3 mixed BP is used in the DB-HTR core, all of the MTC, power coefficient and power coefficient can be negative. Also, the cycle length of the DB-HTR core with B_4C and Er_2O_3 mixed BP can be considerably longer than that of the DB-HTR core with Er_2O_3 BP. Therefore, it recommends that the B_4C and Er_2O_3 mixed BP should be used in a TRU-loaded DB-HTR core.

- In terms of safety aspects such as a LPCC event, a 600 MW_{th} of a DB-HTR core cannot meet the nominal design limit 1600°C for an LPCC event. Therefore, it recommends that the thermal power should be reduced to 450MW_{th} in a five-ring TRU-loaded DB-HTR core design.
- From the results of the decay heat of the 600 MW_{th} TRU-loaded DB core, the short-term decay heat of the TRU-loaded DB-HTR core is highly dependent on the fuel loading. The americium isotope in the DB-HTR core strongly affects the short-term decay heat of the DB-HTR core. For a given TRISO design, the fuel PF should be minimized for a minimal decay heat of the TRU-loaded DB-HTR core.

4.5 References

1. A. Baxter, C. Rodriguez, and F. Venneri, "The Application of Gas-Cooled Reactor Technologies to the Transmutation of Nuclear Waste," *Progress in Nuclear Energy*, **38**, p. 81, 2001.
2. C. Rodriguez, et al., "Deep-Burn: Making Nuclear Waste Transmutation Practical," *Nuclear Engineering and Design*, **222**, 299, 2003.
3. S. G. Hong, Y. Kim, and F. Venneri, "Neutronic Characterization of Sodium-cooled Fast Reactor in an MHR-SFR Synergy for TRU Transmutation," ICAAP 2007, Nice, France, 2007.
4. Potter and A. Shenoy, "Gas Turbine-Modular Helium Reactor (GTMHR) Conceptual Design Description Report," GA Report 910720, Revision 1, General Atomics, July 1996.
5. R. J. Stamm'ler, et al., "HELIOS Method," Studsvik Scanpower, 1998.
6. B. O. Cho, et al., "MASTER-3.0: Multi-purpose Analyzer for Static and Transient Effects of Reactors," KAERI/TR-2061/2002, Korea Atomic Energy Research Institute, 2002.
7. Y. Kim and M. Baek, "Elimination of Double-Heterogeneity through a Reactivity-Equivalent Physical Transformation," GLOBAL 2005, Tsukuba, Japan, October 9–13, 2005.
8. H. J. Shim et al., "Numerical Experiment on Variance Biases and Monte Carlo Neutronic Analysis with Thermal Hydraulic Feedback," Int. Conf. On Supercomputing in Nuclear Applications, SNA 2003, September 22–24, 2003, Paris, France.
9. K.S. Kim, et. al., "Development of a Physics Analysis Procedure for the Prismatic Very High Temperature Gas-cooled Reactors," *Annals of Nuclear Energy*, **34**, p. 849, 2007.
10. C. K. Jo, et al., "Burnable Poison for Reactivity Management in a Very High Temperature Reactor," *Annals of Nuclear Energy*, **36**, 298, 2009.
11. H. Matsuo, et al., "Irradiation Behavior of Boronated Graphite for HTTR," Proc. IAEA Specialists Meeting on the Present Status of graphite Development for GCRs, Tokai, 1991.
12. J. S. Jun, et al., "Evaluation of the Transient TRU Fuel Temperature in a DB-HTR core," HTR-2010, October 18–20, 2010, Prague, Czech Republic, To be published.
13. H. C. Lee, et al., "Decay Heat Analysis of a VHTR Core by Monte Carlo Core Depletion Calculation," GLOBAL 2009, September 10, 2009, Paris, France.
14. A. G. CROFF, "ORIGEN-2: A Versatile Computer Code for Calculating the Nuclide Compositions and Characteristics of Nuclear Materials," *Nuclear Technology*, **62**, p. 335, 1983.

5. THERMO-FLUID CFD ANALYSIS OF THE DEEP BURN PRISMATIC BLOCK REACTOR

5.1 Introduction

The present work describes the evaluation of the hot spot fuel temperature of the fuel block in the DB-HTR core[1,2] under full operating power conditions. The investigated designs are the DB-HTR cores with two thermal powers: 600 MW_{th} and 450 MW_{th}. For each thermal power, two versions of fuel compositions (0.2% UO_2 mixed TRU and 30% UO_2 mixed TRU) are investigated. The combination results in four cases for the thermo-fluid analysis. For accurate analysis, the computational fluid dynamics (CFD) analysis has been performed on the 1/12 fuel block using a commercial CFD code, CFX 12.[3] As boundary conditions, the present analysis uses the results of the other codes (i.e., MASTER-GCR,[4,5,6,7,8] McCARD,[9,10] and GAMMA+[11,12]). Three dimensional power profiles for assemblies are provided by MASTER-GCR. The McCARD code can provide a local fuel pin power profile within the block. To obtain a conservative estimate, the worst case of the McCARD result has been adopted for a local fuel pin power profile within block. GAMMA+ provides the inlet temperature and the flow rate of the coolant flowing through the fuel block.

5.2 DB-HTR Core Design

Figure 70 shows the schematic configuration of the reference DB-HTR core. The DB-HTR core consists of 144 fuel columns in five annular rings with nine fuel blocks per fuel column in the active core. The height of the active core is 7.93 m. Table 12 shows the major design parameters of the reference DB-HTR core. The candidate thermal powers are 600 and 450 MW_{th}, and the coolant inlet/outlet temperatures are 490 and 850°C, respectively. This work considers two alternative fuel compositions for the TRU kernel: 0.2% UO_2 mixed TRU kernel and 30% UO_2 mixed TRU kernel. The diameter of the TRU kernel is 350 μm. For both types of the fuel compositions, the TRU kernel contains 0.6 mole SiC getter to prevent the possible kernel migration due to the production of noble fission gases and CO with high burnup.[13] The kernel is surrounded by four successive layers: buffer, inner PyC, SiC, and outer PyC. The considered volumetric packing fractions for 0.2% UO_2 mixed and 30% UO_2 mixed TRU particles are 6.9% and 8.0%, respectively.

Figure 71 shows the geometry of the standard fuel blocks of DB-HTR. The standard fuel block has a hexagonal shape, 881 mm high and 360 mm across the flats. It has 204 fuel holes, 108 coolant holes, and 12 BP holes. The fuel compacts are stacked in the fuel holes and plugged by the graphite cover. The heat generated in the fuel compacts is conducted through the graphite block and it is finally removed by the coolant. There is no direct contact between the fuel compacts and the coolant. A very tiny gap with a thickness of 0.125 mm exists between the fuel compact and the graphite block.

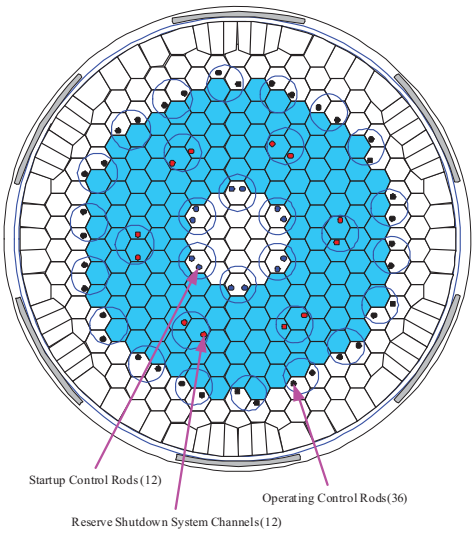

Figure 70. Reference DB-HTR core design configuration.

Table 12. Major design parameters of DB-HTR.

Parameter	Value
Thermal power, MW_{th}	600 or 450
Coolant inlet/outlet temperature, °C	490/850
No. of fuel columns	144
Active core height, m	7.93
Core radius, m	3.4
Top/bottom reflector height, m	1.586/1.586
No. of axial layers	9

Table 13. TRISO fuel particle and fuel compact.

TRISO fuel particle	
Fuel compositions	0.2%UO_2+99.8%($PuO_{1.8}$+NpO_2)+0.6mole SiC getter or 30%UO_2+70%($PuO_{1.8}$+NpO_2)+0.6mole SiC getter
Diameter of kernel , μm	350
Thickness of buffer layer, μm	100
Thickness of Inner PyC layer, μm	35
Thickness of SiC layer, μm	35
Thickness of Outer PyC layer, μm	40
Fuel Compact	
Radius, cm	0.6225
Volumetric packing fraction of TRISO particles	6.9 % for 0.2% UO_2 mixed TRU 8.0 % for 30% UO_2 mixed TRU

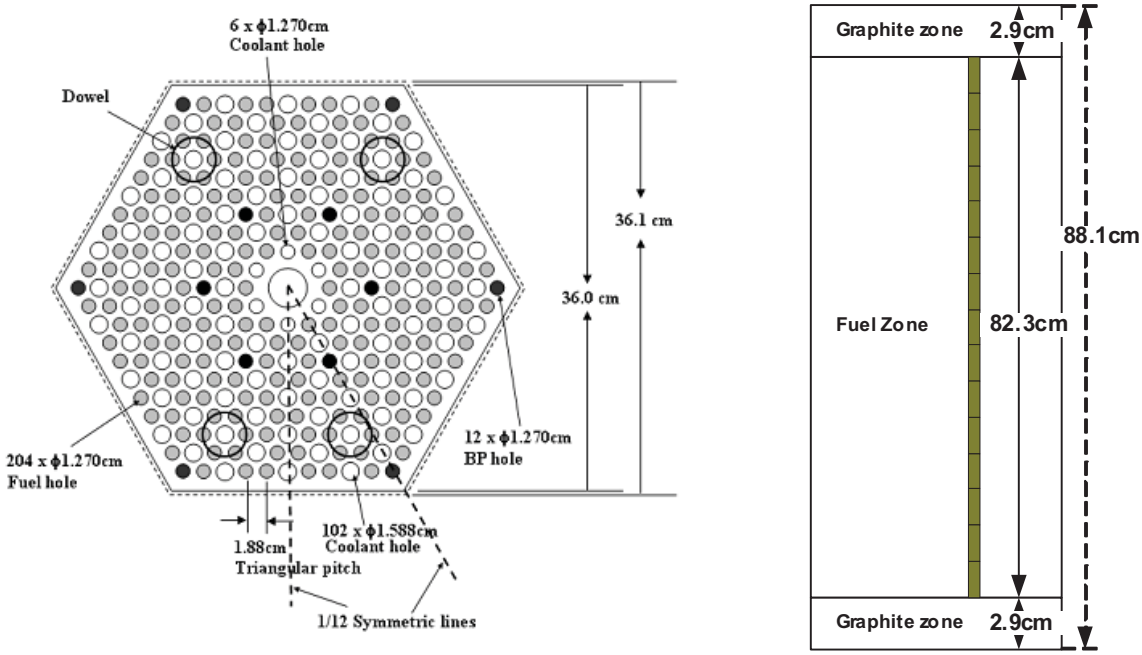

Figure 71. The geometry of standard fuel block.

5.3 Power Distribution of DB-HTR Core

The investigated designs are the four DB-HTR cores with two thermal powers (600 and 450 MW_{th}) and two versions of fuel compositions (0.2% UO_2 mixed TRU and 30% UO_2 mixed TRU). Each core design has different power distribution. Therefore, the considered cases in this work are:

1. Case A: 600 MW_{th} core with 0.2% UO_2 mixed TRU kernel
2. Case B: 600 MW_{th} core with 30% UO_2 mixed TRU kernel
3. Case C: 450 MW_{th} core with 0.2% UO_2 mixed TRU kernel
4. Case D: 450 MW_{th} core with 30% UO_2 mixed TRU kernel.

The three-dimensional power profiles were obtained by the MASTER-GCR code for the considered cases.[5–8] Figure 72–Figure 75 present the two-dimensional power profiles for the considered core designs. The numbers shown in these figures indicate the relative power produced within each fuel column. Table 14 summarizes the relative power of the hot block and its location for each core design. It shows that the locations of the hot block are changed from the burnup, but they are the same among the core designs. The relative powers of the hot block reach the maximum at EOC for all the considered cases.

Table 14. Relative power of hot block and its location.

	Case A	Case B	Case C	Case D
BOC (Beginning of Cycle)	1.194 Block (8,7)	1.178 Block (8,7)	1.198 Block (8,7)	1.184 Block (8,7)
MOC (Middle of Cycle)	1.189 Block (7,1)	1.171 Block (7,1)	1.179 Block (7,1)	1.180 Block (7,1)
EOC (End of Cycle)	1.290 Block (7,4)	1.270 Block (7,4)	1.275 Block (7,4)	1.265 Block (7,4)

Figure 76 through Figure 87 show the axial power profiles of all the fuel blocks for the considered four designs at BOC, MOC, and EOC. Non-fuel zones between the fuel blocks (the graphite plugs) are not shown to simply the figures. An examination of the power profile generally indicates the position of the hot spot fuel block. The hot spot fuel temperature should be located either locally hotter fuel, where the heat flux from the fuel is higher, or hotter block, where the coolant temperature is higher. Figure 76 through Figure 87 clearly indicate the location of the blocks, which contain the hot spot fuel temperature. At BOC, higher local power exists near the top fuel blocks, which have colder coolant temperatures. The position of the power peak moves to the bottom with the burnup. Finally EOC has higher local power near the bottom layers of the fuel blocks which have higher coolant temperatures. In addition, EOC has the highest block power as shown in Table 14. Therefore, it is obvious that the hot spot fuel temperatures exist at EOC. The same conclusions are valid for all the considered cases. It is not clear from the power profiles; however, that the hot spot fuel temperature exist at either Block (7,4) or Block (5,1). Block (7,4) has the highest coolant temperature, whereas Block (5,1) has the highest heat flux from the fuel. The CFD results confirmed later that the hot spot fuel temperature occurs at Block (7,4). Therefore, the CFD results of the present work are described only for Block (7,4).

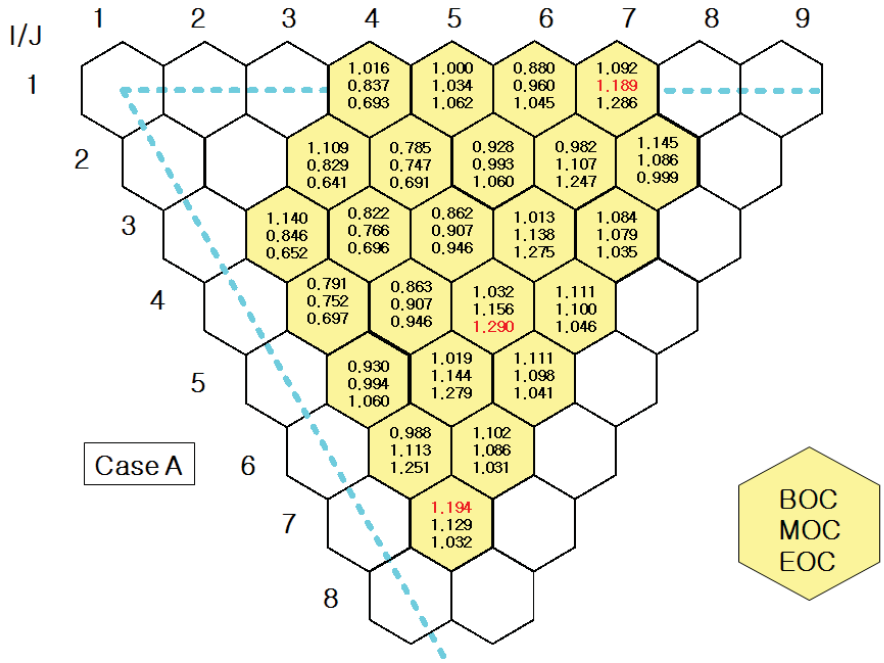

Figure 72. 2-D power distribution for Case A core (600 MW_{th} core with 0.2% UO_2 mixed TRU kernel).

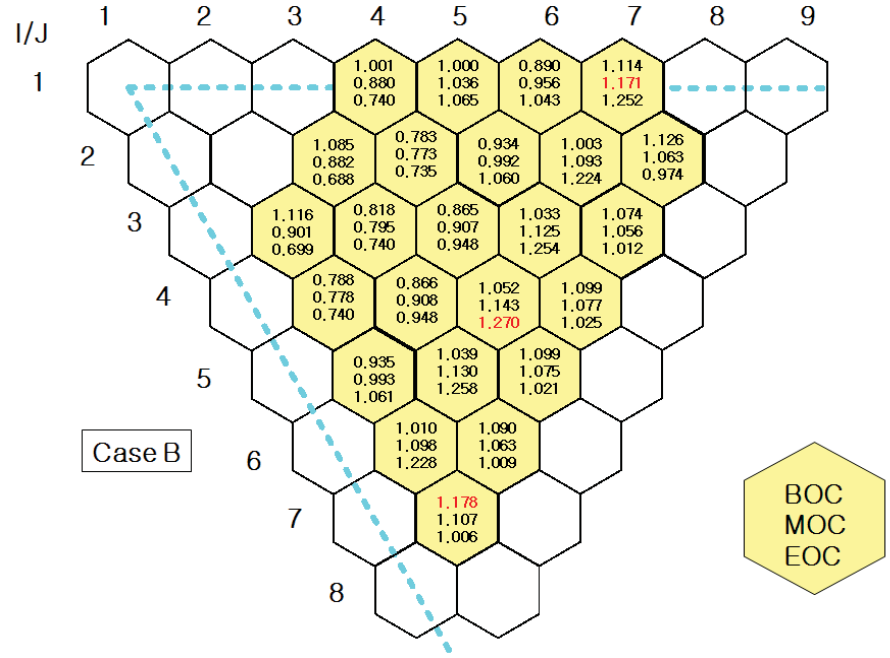

Figure 73. 2-D power distribution for Case B core (600 MW_{th} core with 30% UO_2 mixed TRU kernel).

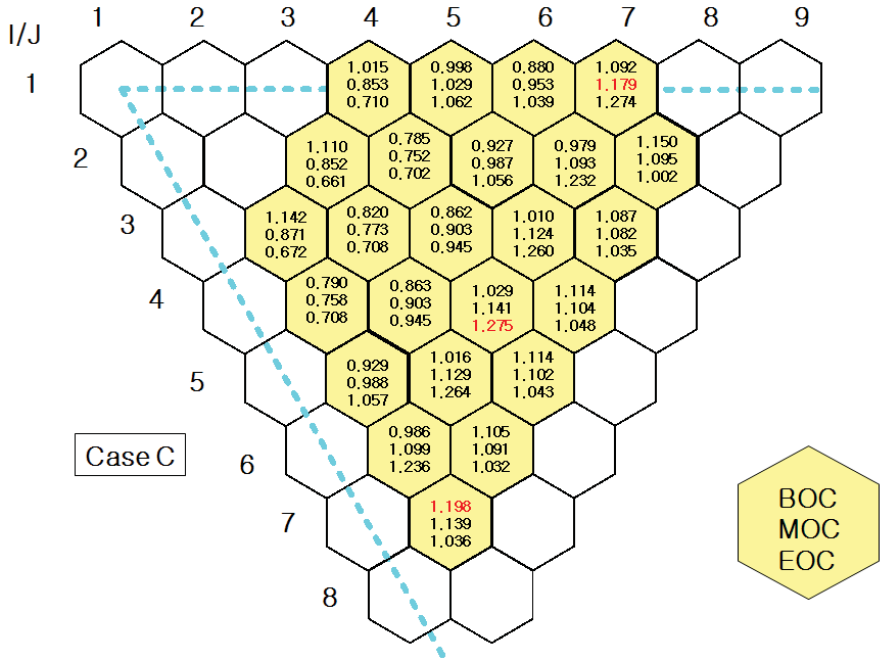

Figure 74. 2-D power distribution for Case C core (450 MW_{th} core with 0.2% UO_2 mixed TRU kernel).

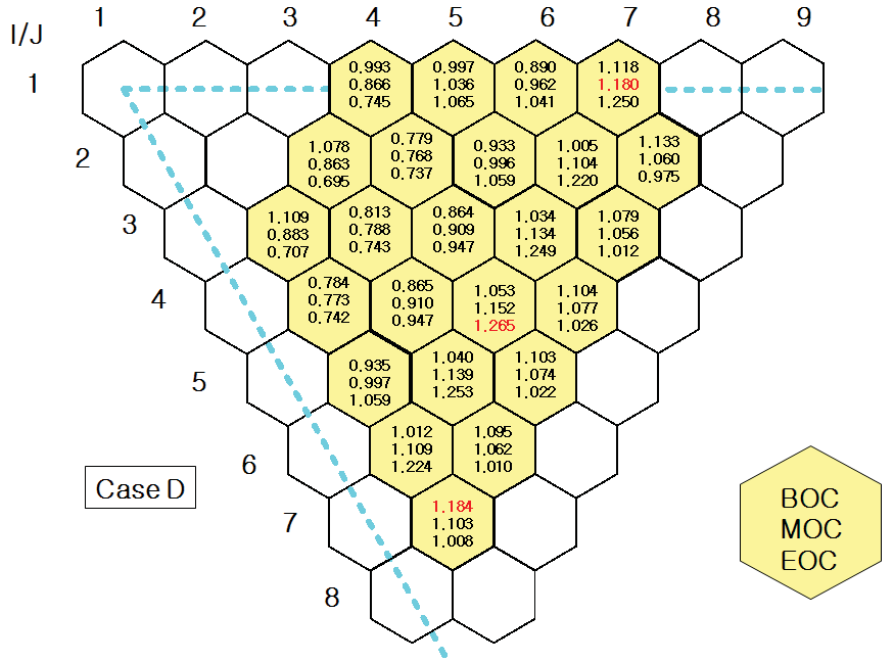

Figure 75. 2-D power distribution for Case D core (450 MW_{th} core with 30% UO_2 mixed TRU kernel).

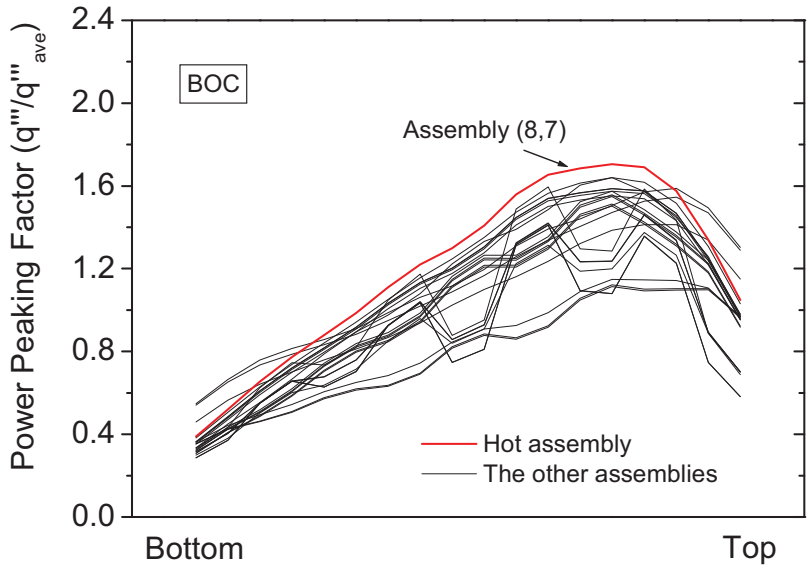

Figure 76. Axial power distribution for Case A core (600 MW_{th} core with 0.2% UO_2 mixed TRU kernel) at BOC.

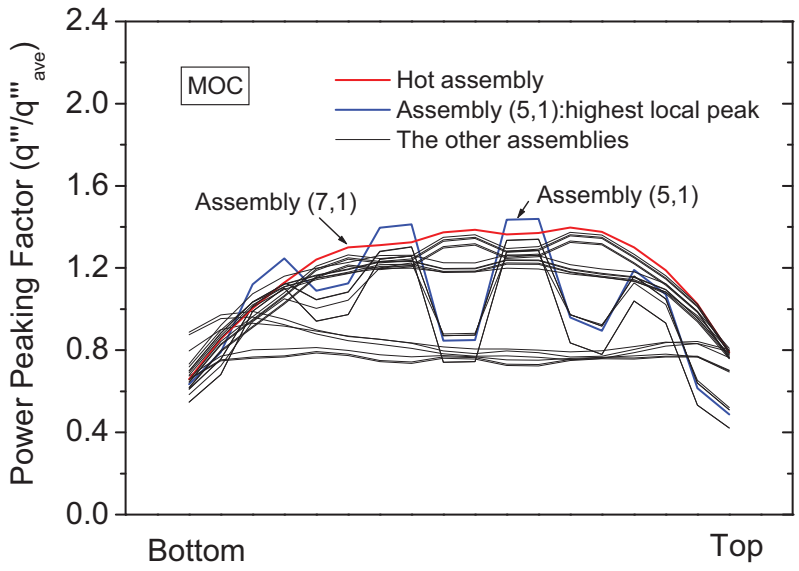

Figure 77. Axial power distribution for Case A core (600 MW_{th} core with 0.2% UO_2 mixed TRU kernel) at MOC.

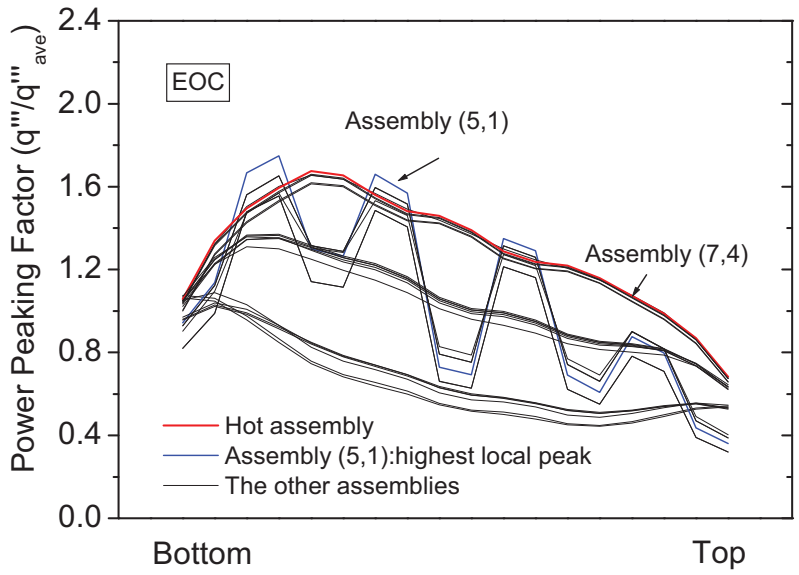

Figure 78. Axial power distribution for Case A core (600 MW_{th} core with 0.2% UO_2 mixed TRU kernel) at EOC.

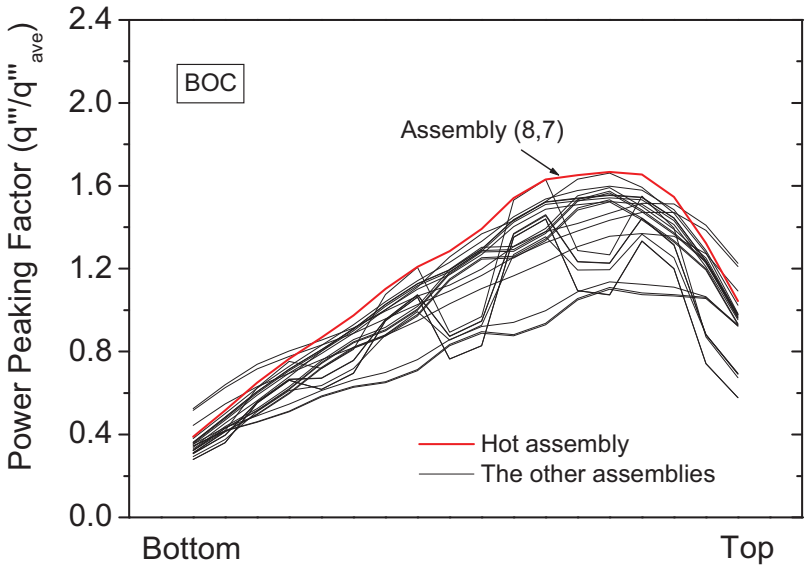

Figure 79. Axial power distribution for Case B core (600 MW_{th} core with 30% UO_2 mixed TRU kernel) at BOC.

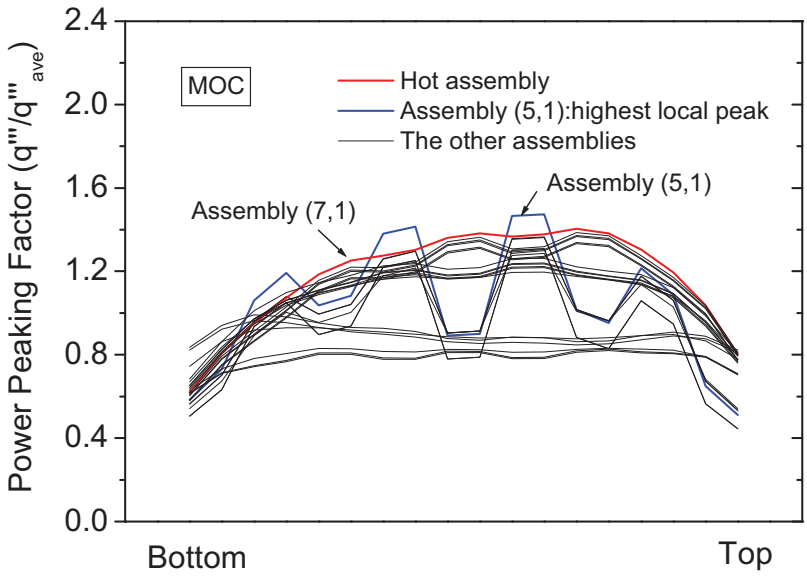

Figure 80. Axial power distribution for Case B core (600 MW_{th} core with 30% UO_2 mixed TRU kernel) at MOC.

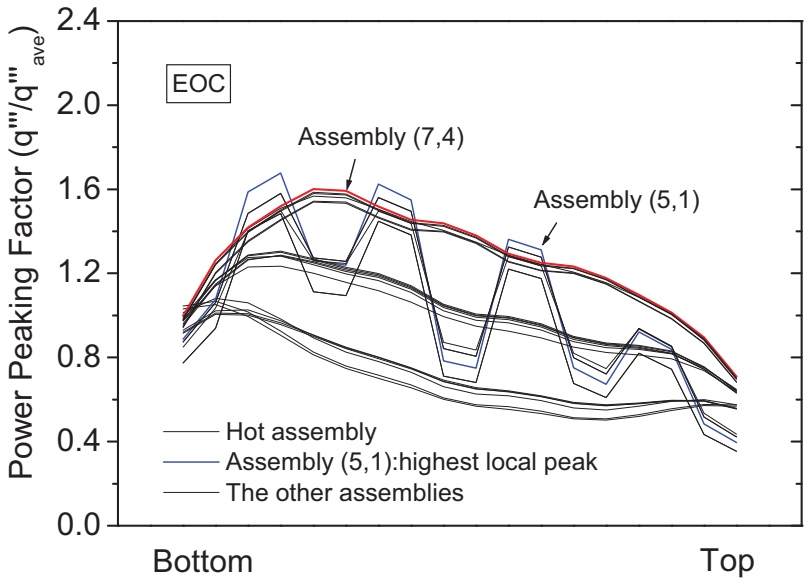

Figure 81. Axial power distribution for Case B core (600 MW_{th} core with 30% UO_2 mixed TRU kernel) at EOC.

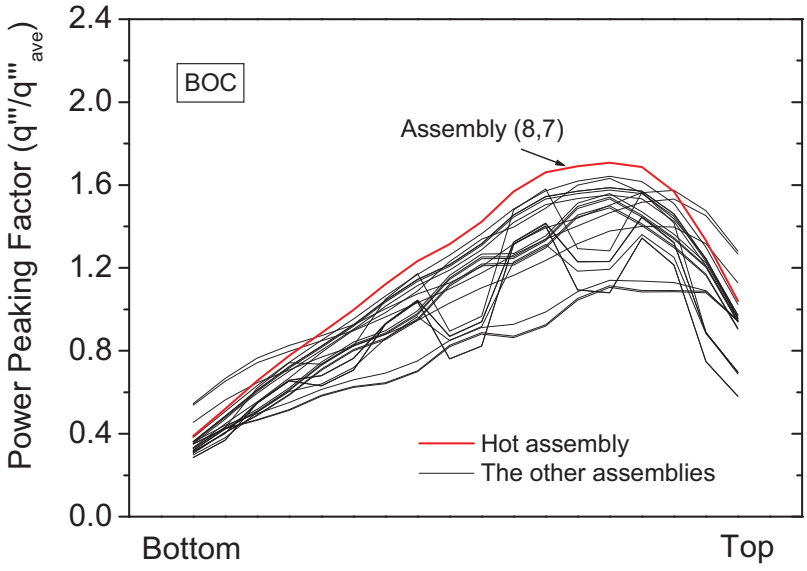

Figure 82. Axial power distribution for Case C core (450 MW_{th} core with 0.2% UO_2 mixed TRU kernel) at BOC.

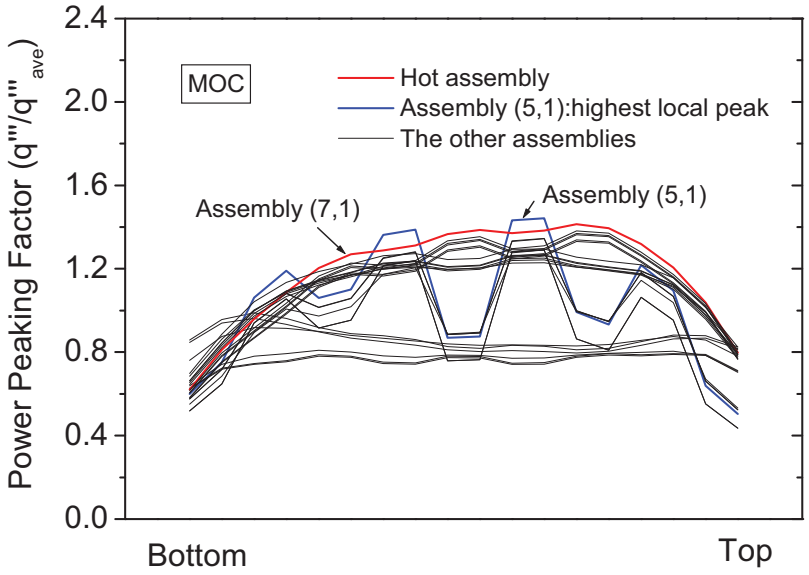

Figure 83. Axial power distribution for Case C core (450 MW_{th} core with 0.2% UO_2 mixed TRU kernel) at MOC.

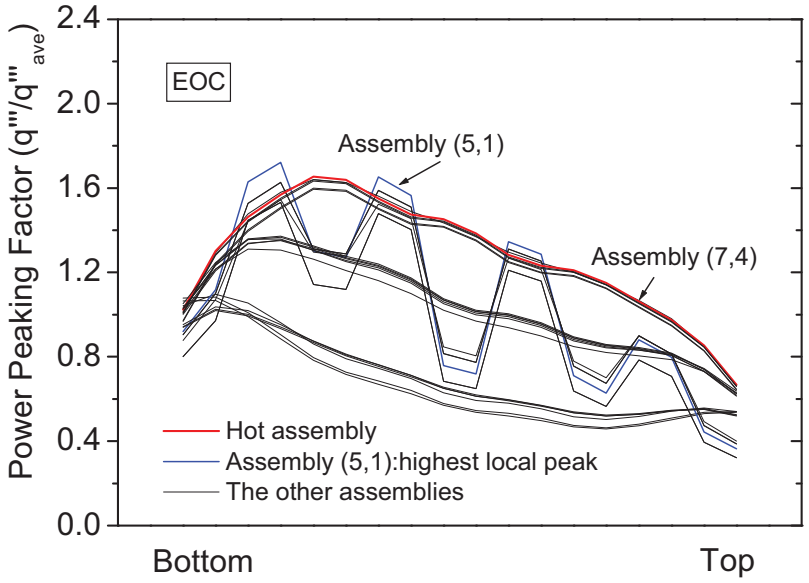

Figure 84. Axial power distribution for Case C core (450 MW_{th} core with 0.2% UO_2 mixed TRU kernel) at EOC.

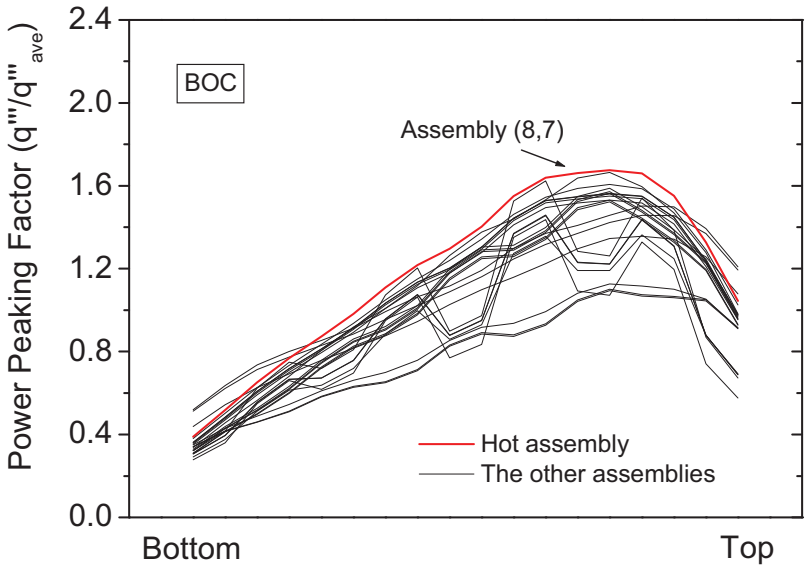

Figure 85. Axial power distribution for Case D core (450 MW_{th} core with 30% UO_2 mixed TRU kernel) at BOC.

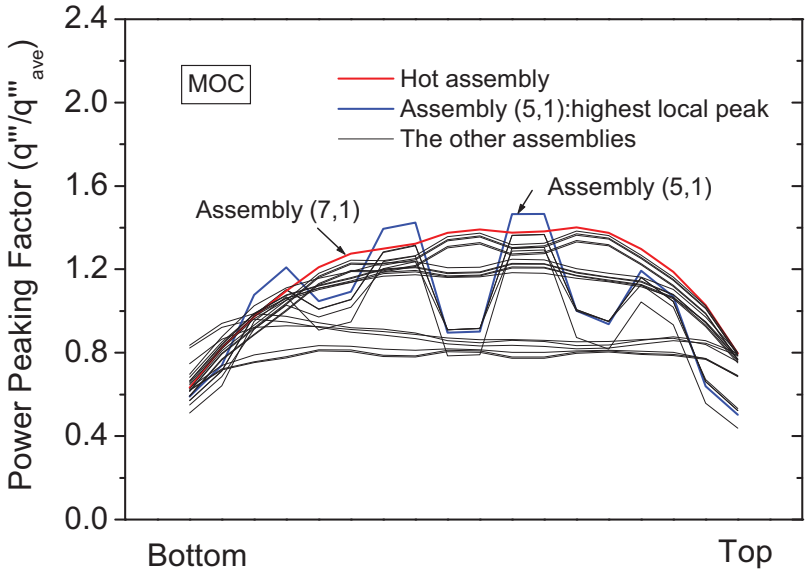

Figure 86. Axial power distribution for Case D core (450 MW_{th} core with 30% UO_2 mixed TRU kernel) at MOC.

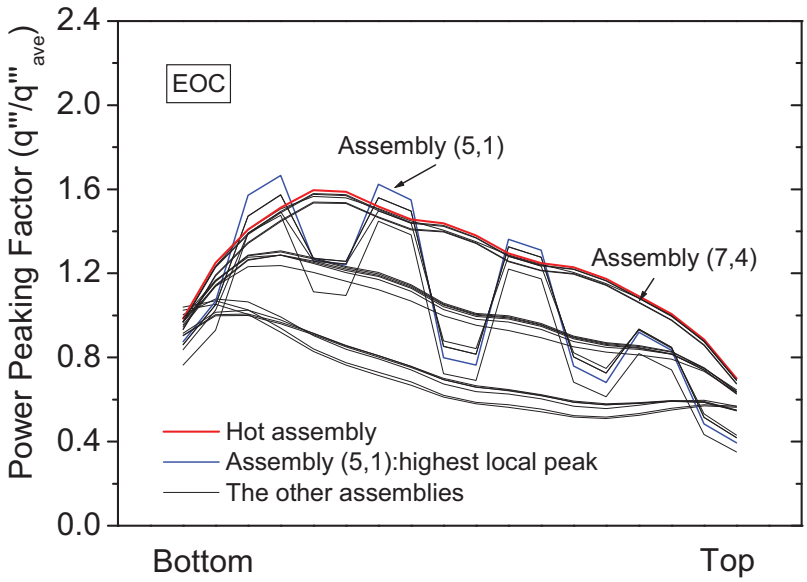

Figure 87. Axial power distribution for Case D core (450 MW_{th} core with 30% UO_2 mixed TRU kernel) at EOC.

The current version of the MASTER-GCR code does not provide an accurate pin-by-pin power profile within the block. However, each fuel compact at the same axial position could have significant power variation within the block. In particular, fuel blocks neighbored with the reflector blocks are known to have steep fuel pin power distributions within the block. Figure 88 shows one example of the McCARD result.[10] The numbers in Figure 88 indicate the normalized pin power within block. The fuel pin power profile shown in Figure 88 was the worst case among the full core calculation result by McCARD. The fuel pin power profile shown in Figure 88 was obtained for the block neighbored with the side reflectors. In this work, the fuel pin power profile shown in Figure 88 was applied for all the cases regardless of the location of the fuel block. Therefore, it can be regarded that the present results of the CFD analyses are very conservative estimates since the analyzed fuel block (i.e., Block (7,4) is not neighbored with any reflectors (see Figure 72 through Figure 75).

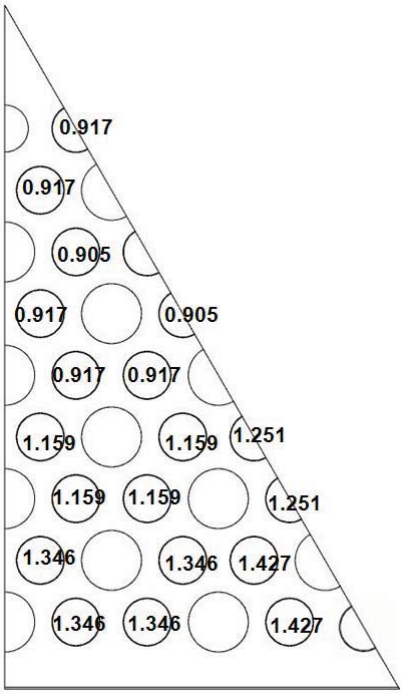

Figure 88. The adopted local fuel pin power profile within block.
(Number indicates relative pin power within block.)

5.4 CFD Model and Boundary Conditions

By assuming that the effects of the four dowels are negligible, the entire fuel block shown in Figure 71 can be simulated by its 1/12 section due to its symmetry.[14] Figure 89 shows the computational domain of the 1/12 fuel block model for the CFD analysis. The computational domain covers 17 fuel holes, 8.5 large coolant holes, a 0.5 small coolant hole, and 1/12 sections of the graphite block and the bypass gap. Parts of the upper reflector and the lower reflector blocks are included to consider the axial heat transfer and the flow development in the coolant channel. No heat generation is modeled in the locations where graphite plugs are placed. The bypass gap size is set to be 2 mm in this work. The same size was used for the GAMMA+ calculations. Figure 90 shows a top view of the reference meshes for the present CFD analysis. The hexahedron and prism meshes are effectively combined to reflect the complex geometry of the fuel block. Finer meshes are applied in the boundary layers of the coolant channels and the solid regions where large temperature gradients are expected. The total number of nodes for the reference meshes is ~2 million. A series of calculations with different mesh sizes confirmed that the meshes shown in Figure 90 are sufficiently fine. The standard k-e turbulence model with the scalable wall function is applied to the coolant channels while the bypass flow through the gap is assumed to be laminar. For the 600 MW_{th} cores, typical Reynolds numbers for the coolant channels and the bypass gap are ~35000 and ~2000, respectively.

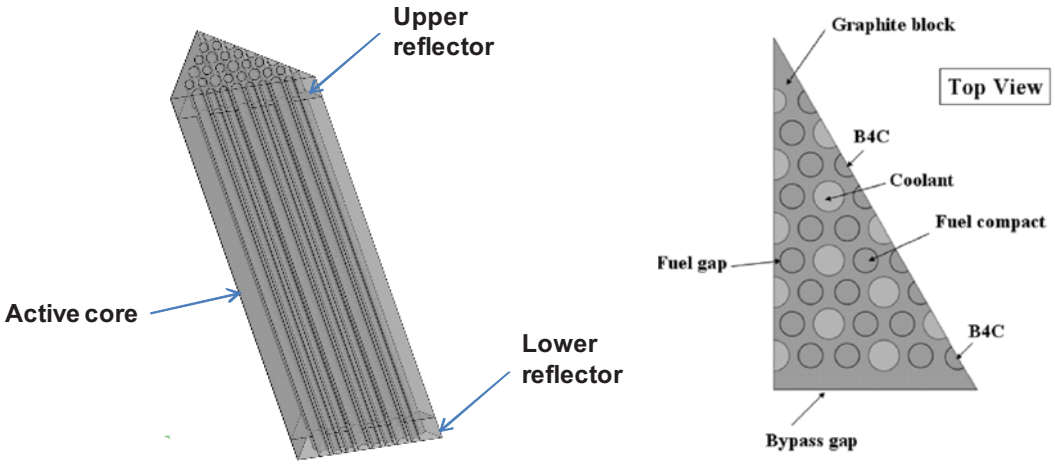

Figure 89. The computational domain of the 1/12 fuel block model for the CFD analysis.

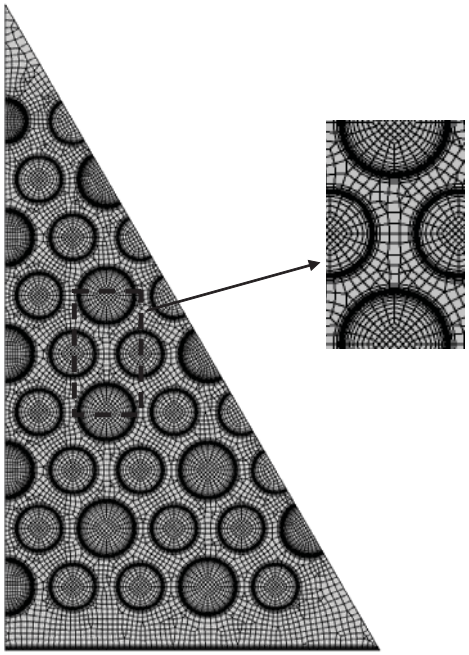

Figure 90. Reference meshes for the present CFD analysis (top view).

The thermal conductivity of the TRU fuel compact is not well known. The thermal conductivity of the TRU kernel would be similar as that of PuO_2 since the TRU kernel is mainly composed of the Pu isotopes. Figure 91 compares the conductivities of UO_2 and PuO_2. It shows that the difference in the thermal conductivity is not significant. Therefore, it is expected that the thermal conductivity of the UO_2 mixed TRU kernel would be similar as that of the pure TRU kernel. However, note that the thermal conductivity of SiC getter is much higher than that of PuO_2 as shown in Figure 92. In this work volume averaged values are used for the thermal conductivity of the SiC and TRU fuel mixtures, also shown in Figure 92. The thermal conductivity of the fuel compact is also derived based on the packing fraction of the mixture of graphite and TRISO kernel as shown Figure 93. The thermal conductivities of coating layers are neglected in Figure 93 since the packing fractions of the TRU fuel particle are small.

For the thermal conductivity of the graphite block, the irradiated thermal conductivity of H451 graphite is used. The applied thermal conductivity for the graphite block is shown in Figure 93. The same values were used for the steady-state GAMMA+ calculations.

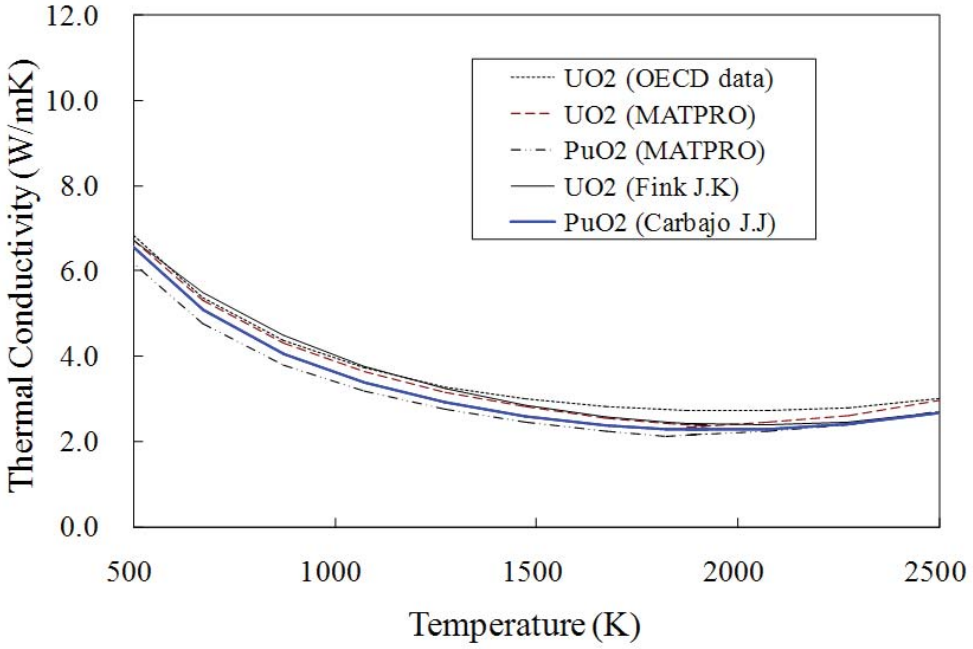

Figure 91. Comparison of thermal conductivities of UO_2 and PuO_2.[15,16]

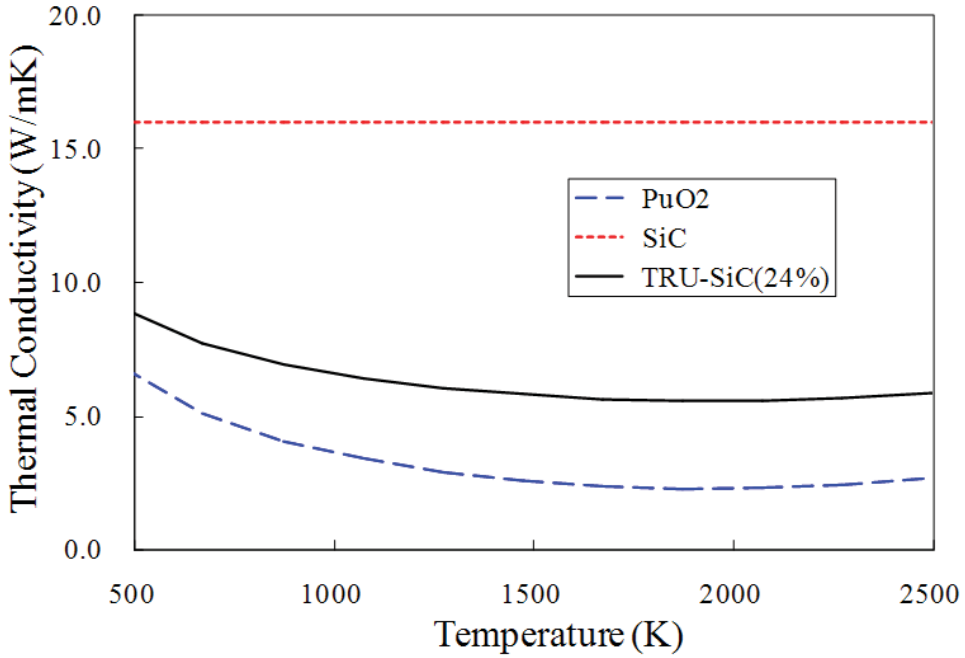

Figure 92. Thermal conductivity of TRU kernel with SiC getter.

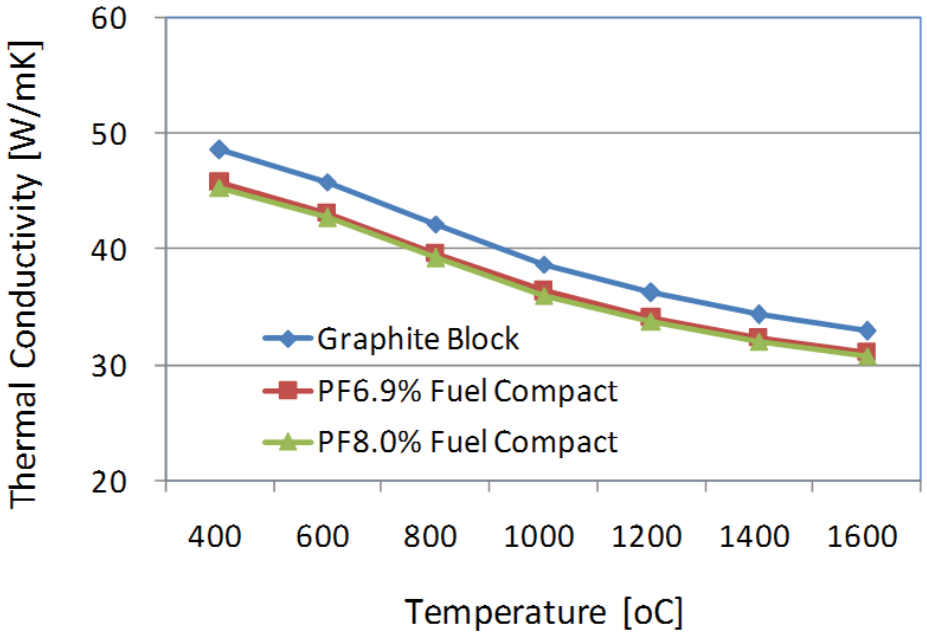

Figure 93. Thermal conductivities used in the present work.

Table 15 shows the reference boundary conditions applied. The three-dimensional power profiles[5–8] calculated by the MASTER-GCR code are applied in the fuel compact. The McCARD result,[10] shown in Figure 88, is used for the local fuel pin power profile within block. The fluid boundary conditions at the inlet (upper plenum of the core) are obtained from the GAMMA+ results.[12] As described in Section 5.3, the hot spot fuel temperature at EOC is expected to be higher than that of BOC or MOC. Therefore, the EOC conditions are applied for all the cases of the CFD analysis. Although the power profile is changed with the fuel burnup as shown in Section 5.3, the fluid boundary conditions are hardly affected by the fuel burnup. GAMMA+ predicted that the helium temperature flowing into the core is slightly lower than the nominal inlet temperature of the reactor (= 490°C). This is mainly due to heat losses at the inlet riser channels and the upper plenum of the core. It should be noted that the coolant mass flow rate is changed with the thermal power of the core. The predicted fractions of the bypass gap flow were 2.74–2.76% for all the cases. It is assumed that there is no crossflow between the coolant channels and the bypass gap.

Table 15. Analysis cases and boundary conditions for CFD analysis.

Analysis Cases				
	Case A	Case B	Case C	Case D
Core power, MW_{th}	600		450	
TRU fuel composition	0.2% UO_2 mixed	30% UO_2 mixed	0.2% UO_2 mixed	30% UO_2 mixed
Fuel burnup condition	EOC			
Boundary Conditions				
Block power profile	Figure 78	Figure 81	Figure 84	Figure 87
Fuel pin power profile within block	Figure 88	Figure 88	Figure 88	Figure 88
Coolant inlet temperature, °C	488	488	487	487
1/12 assembly flow rate (kg/s)	0.1699	0.1707	0.1278	0.1276
Bypass gap flow fraction within block (%)	2.75	2.74	2.75	2.76

5.5 CFD Results

Figure 94 and Figure 95 show the velocity contours calculated by CFX 12 for Case A at EOC. The calculated velocity contours for Case B are very similar with those in Figure 94 and Figure 95 since velocity is not significantly affected by small temperature difference. Figure 94 shows that the coolant velocity is increased in the coolant flow direction due to the change of its density. The maximum velocity for Case A is predicted to be 47.2 m/s. The velocity at the bypass gap is much smaller than that at the coolant channels. Figure 96 shows the velocity contour calculated for Case C. The calculated velocity contour for Case D is very similar with that in Figure 96. The predicted maximum velocity for Case C is decreased to 35.0 m/s with the decrease in the coolant mass flow rate.

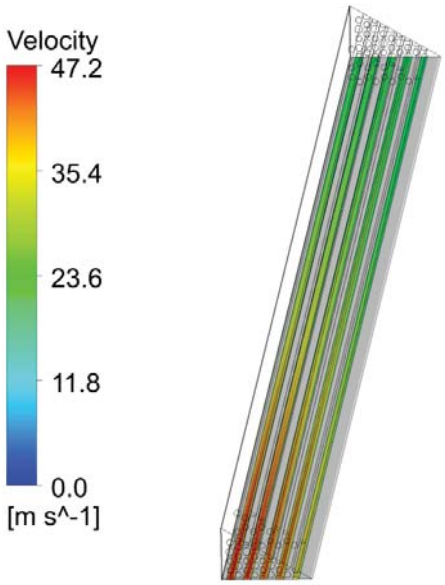

Figure 94. Velocity contour for Case A (600 MW_{th} core with 0.2% UO_2 mixed TRU kernel).

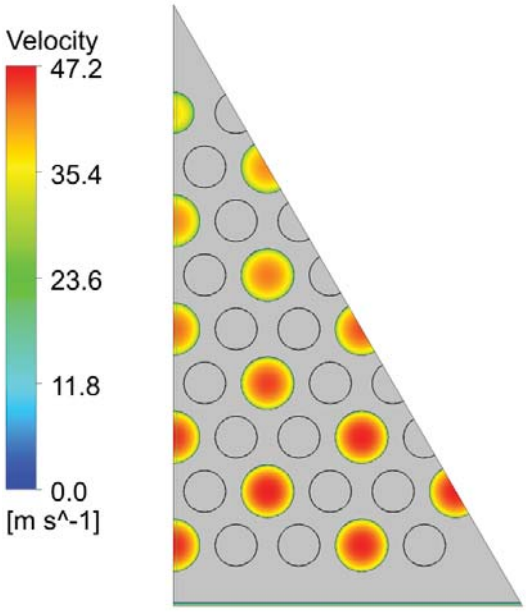

Figure 95. Velocity contour for Case A (600 MW_{th} core with 0.2% UO_2 mixed TRU kernel) at the maximum temperature plane.

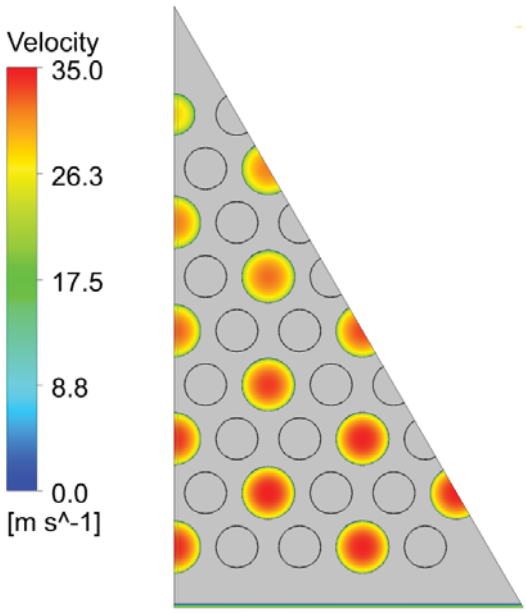

Figure 96. Velocity contour for Case C (450 MW_{th} core with 0.2% UO_2 mixed TRU kernel) at the maximum temperature plane.

Figure 97 through Figure 100 show the temperature contours calculated by CFX 12 for the considered four cases. The contours are plotted at the maximum fuel temperature plane. Table 16 summarizes the hot spot fuel temperature and its location. The predicted hot spot fuel temperatures for the 600 MW_{th} cores (i.e., Case A and Case B) are 1243 and 1223°C, respectively. The predicted hot spot fuel temperatures for the 450 MW_{th} cores (i.e., Case C and Case D) are lower than those for the 600 MW_{th} designs by ~30°C. For all the considered cases, the predicted hot spot fuel temperatures are below the generic design limit of 1250°C under full power operating conditions. Note that the worst pin power profile within block shown in Figure 88 was applied for the all cases. Since Block (7,4) is not neighbored with the reflector blocks (see Figure 72 through Figure 75), the pin power profile shown in Figure 88 is considered to be sufficiently conservative. Therefore, it can be concluded that the predicted hot spot fuel temperatures in this work are sufficiently conservative estimates. Table 16 also shows that the predicted hot spot fuel temperature of the core design with a 0.2% UO_2 mixed TRU is slightly higher than that with a 30% UO_2 mixed TRU. The hot spot fuel temperatures are located at the first fuel block from the bottom of the active core for all the considered cases.

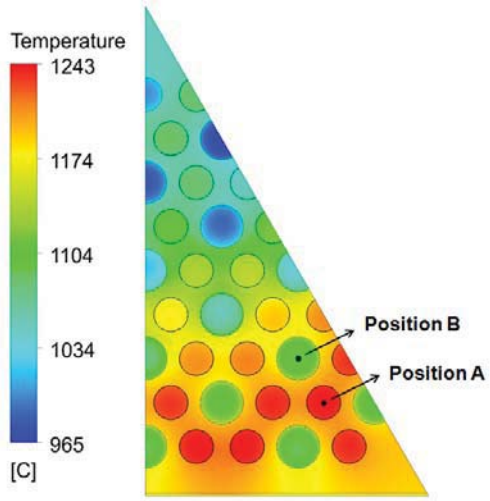

Figure 97. Temperature contour for Case A (600 MW_{th} core with 0.2% UO_2 mixed TRU kernel) at the maximum temperature plane.

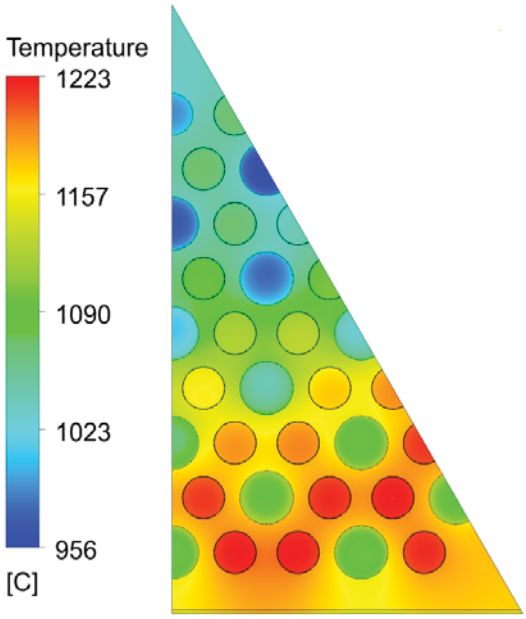

Figure 98. Temperature contour for Case B (600 MW_{th} core with 30% UO_2 mixed TRU kernel) at the maximum temperature plane.

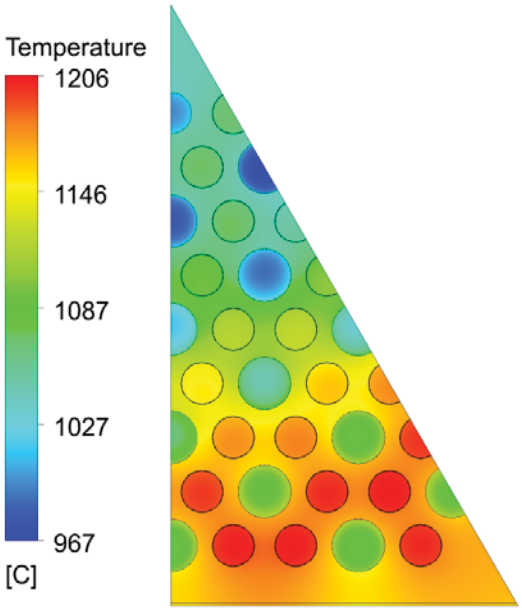

Figure 99. Temperature contour for Case C (450 MW_{th} core with 0.2% UO_2 mixed TRU kernel) at the maximum temperature plane.

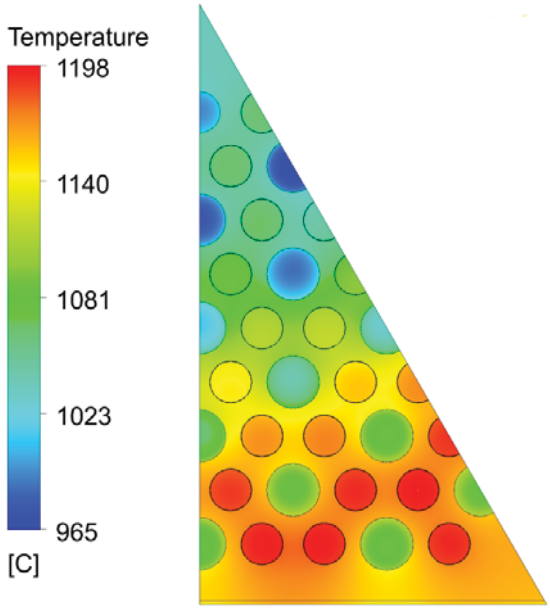

Figure 100. Temperature contour for Case D (450 MW_{th} core with 30% UO_2 mixed TRU kernel) at the maximum temperature plane.

Table 16. The predicted hot spot fuel temperature and its location.

Case	Hot spot fuel temperature	Location of hot spot fuel temperature
Case A: 600 MW_{th} core with 0.2% UO_2 mixed TRU	1243°C	Block (7,4), First block from bottom
Case B: 600 MW_{th} core with 30% UO_2 mixed TRU	1223°C	Block (7,4), First block from bottom
Case C: 450 MW_{th} core with 0.2% UO_2 mixed TRU	1206°C	Block (7,4), First block from bottom
Case D: 450 MW_{th} core with 30% UO_2 mixed TRU	1198°C	Block (7,4), First block from bottom

To examine the axial temperature profile, two points (Position A and Position B) are defined at the fuel and the coolant center, shown in Figure 97. Then, the axial temperature profiles are plotted along the Position A (fuel center) and the Position B (coolant center), shown in Figure 101 through Figure 104. The sharp temperature drops between the fuel blocks are shown in the figures. These are due to the non-fuel zones between the fuel blocks. The figures clearly show that the hot spot temperatures are located at the first block from the bottom of the active core.

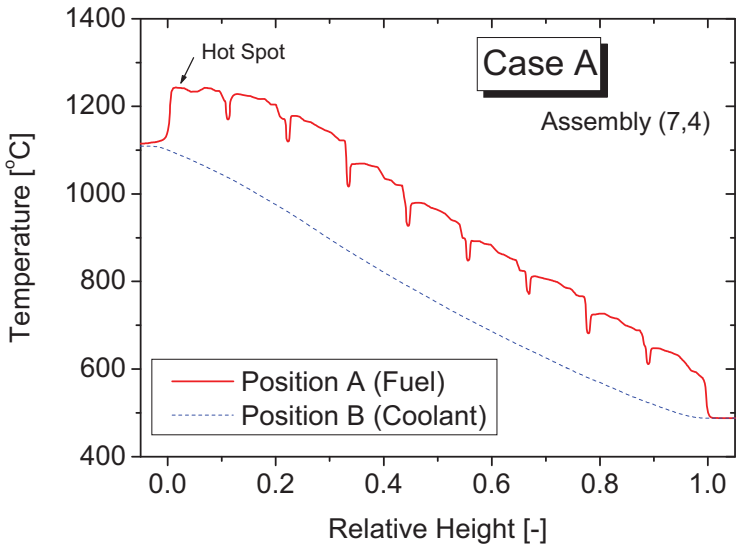

Figure 101. Axial temperature profile for Case A (600 MW_{th} core with 0.2% UO_2 mixed TRU kernel) at Positions A and B.

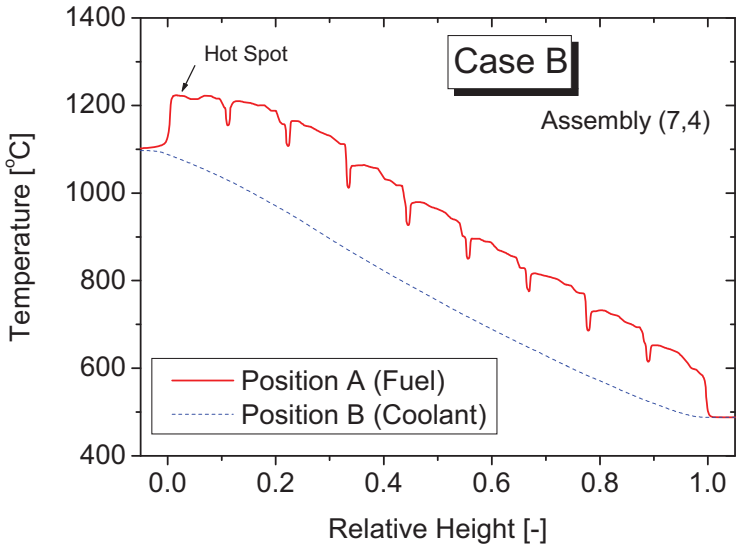

Figure 102. Axial temperature profile for Case B (600 MW_{th} core with 30% UO_2 mixed TRU kernel) at Positions A and B.

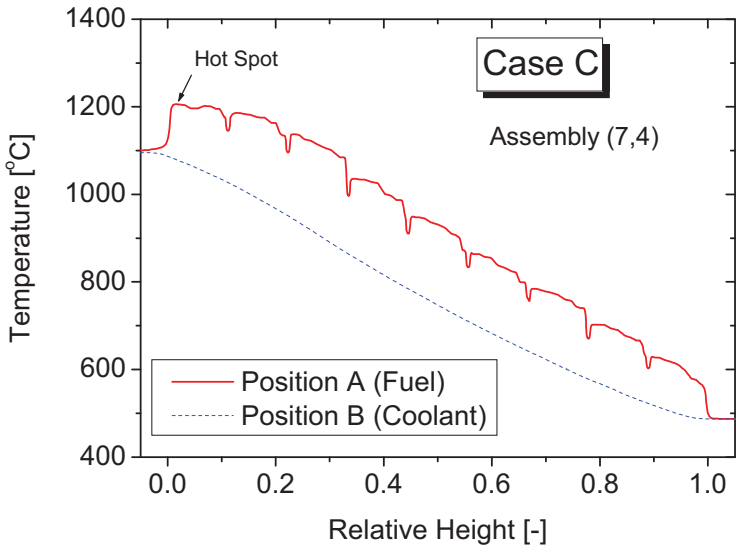

Figure 103. Axial temperature profile for Case C (450 MW_{th} core with 0.2% UO_2 mixed TRU kernel) at the Positions A and B.

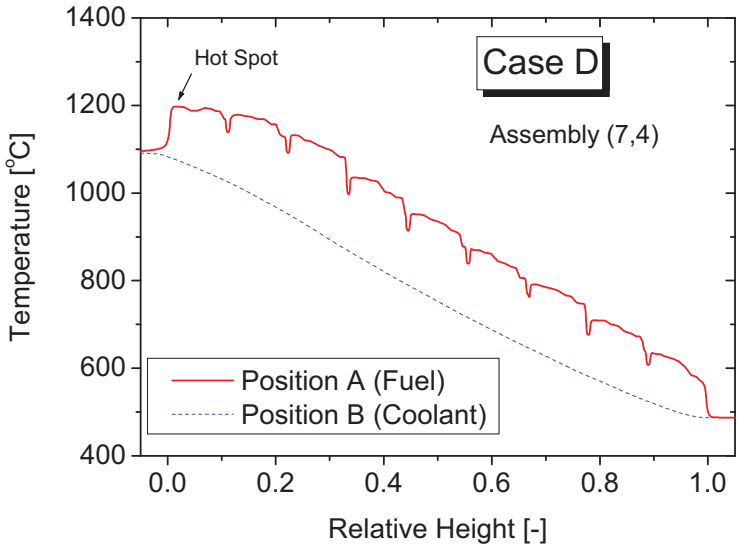

Figure 104. Axial temperature profile for Case D (450 MW_{th} core with 30% UO_2 mixed TRU kernel) at Positions A and B.

5.6 Summary

The CFD analysis was performed on the 1/12 fuel block to evaluate the hot spot fuel temperature of the DB-HTR core under normal operating conditions. Four core designs were investigated. They are the DB-HTR cores with two thermal powers (600 MW_{th} and 450 MW_{th}) and two versions of fuel compositions (0.2% UO_2 mixed TRU and 30% UO_2 mixed TRU). The results of MASTER-GCR, McCARD, and GAMMA+ were used as the boundary conditions of the present analysis. The worst fuel pin power profile within block was applied to obtain a conservative estimate.

It is found by the examination of the power profiles obtained by MASTER-GCR that the hot spot fuel temperatures exist within Block (7,4) at EOC for all the considered cases. Since Block (7,4) is not neighbored with the reflectors, it is regarded that the predicted hot spot fuel temperatures in this work are sufficiently conservative estimates.

The results of CFX show that the predicted hot spot fuel temperatures for the 600 MW_{th} cores (Case A and Case B) are 1243 and 1223°C, respectively. The predicted hot spot fuel temperatures for the 450 MW_{th} cores (i.e., Case C and Case D) are lower than those for the 600 MW_{th} designs by ~30°C. The predicted hot spot fuel temperature of the core design with a 0.2% UO_2 mixed TRU is found to be slightly higher than that with a 30% UO_2 mixed TRU. For all the considered cases, the predicted hot spot fuel temperatures are below the generic design limit of 1250°C in spite of the sufficiently conservative assumption about the local fuel pin power profile within block.

5.7 References

1. Yonghee Kim, "Physics Study on TRU Deep-Burn in MHRs," KAERI-GA-1-2006, February 3, 2007.
2. Yonghee Kim, Francesco Venneri, "Optimization of TRU Burnup in Modular Helium Reactor," Proceedings of ICAPP 2007 Nice, France, May 13–18, 2007.
3. ANSYS Incorporated, ANSYS CFX – Solver Theory Guide, Release 12.1, November, 2009.
4. Jae Man Noh et. al., "Development of a Computer Code System for the Analysis of Prism and Pebble Type VHTR Cores," *Annals of Nuclear Energy*, 35, pp.1919–1928, 2008.
5. Chang Keun Jo, "MASTER Code Results of the DB-MHR 600 MW_{th} Reactor, 0.2% UO_2 mixed TRU Kernel: DBR600_MAS_TRUO1.8_PF6.9_B4C_V0.3_Er2O3_ V2.0_12BH_RS_AS_Case23.dat," Internal data file, 2010.5.
6. Chang Keun Jo, "MASTER Code Results of the DB-MHR 600 MW_{th} Reactor, 30% UO_2 mixed TRU Kernel: DBR600_MAS_UTRUO1.8_PF8.0_B4C_V0.15_ Er2O3_1.5_12BH_RS_AS_Case23.dat," Internal data file, 2010.5.
7. Chang Keun Jo, "MASTER Code Results of the DB-MHR 450 MW_{th} Reactor, 0.2% UO_2 mixed TRU Kernel: DBR450_MAS_TRUO1.8_PF6.9_B4C_V0.3_Er2O3_ V2.0_12BH_RS_AS_Case23.dat," Internal data file, 2010.5.
8. Chang Keun Jo, "MASTER Code Results of the DB-MHR 450 MW_{th} Reactor, 30% UO_2 mixed TRU Kernel: DBR450_MAS_TRUO1.8_PF6.9_B4C_V0.3_Er2O3_ V2.0_12BH_RS_AS_Case23.dat," Internal data file, 2010.5.
9. H. J. Shim et al., "Numerical Experiment on Variance Biases and Monte Carlo Neutronic Analysis with Thermal Hydraulic Feedback," Int. Conf. On Supercomputing in Nuclear Applications, SNA 2003, September 22–24, 2003, Paris, France.
10. Chang Keun Jo, "McCARD Result of Pin-by-Pin Power Profile for a Deep Burn Core : TRU100_2BAS_480efpd_Er2O3BPv0.60_v0.10_sum_d010.dat," Internal data file, 2009.9.
11. Hong Sik Lim, Hee Cheon No, "GAMMA Multidimensional Multicomponent Mixture Analysis to Predict Air Ingress Phenomena in an HTGR," *Nuclear Science and Engineering*, 152, 2006, 1-11, 2006.
12. Ji Su Jun, "A Thermal-Fluid and Safety Analysis for the 600MW_{th} Deep-Burn HTR Core (Phase II)," NHDD-RD-CA-10-008, Rev. 0, July 2009.
13. Theodore M. Besmann, "Thermochemical Assessment of Oxygen Gettering by SiC or ZrC in PuO_2-x TRISO Fuel," *Journal of Nuclear Materials*, 2010.
14. Nam-il Tak, Min-Hwan Kim, Won Jae Lee, "Numerical Investigation of a Heat Transfer within the Prismatic Fuel Assembly of a Very High Temperature Reactor," Annals of Nuclear Energy, Vol. 35, pp. 1892–1899, 2008.
15. Juan J. Carbajo, Gradyon L. Yoder, Sergey G. Popov and Victor K. Ivanov, "A Review of the Thermophysical Properties of MOX and UO_2 fuels," *Journal of Nuclear Materials*, 299, 181–198, 2001.
16. J.K. Fink, "Thermophysical Properties of Uranium Dioxide," *Journal of Nuclear Materials*, 279, 1-18, 2000.

6. LPCC ANALYSIS OF THE DEEP BURN PRISMATIC BLOCK REACTOR

6.1 Introduction

The Deep Burn concept[1] was originally proposed by GA and Los Alamos National Laboratory (LANL) to achieve a very high burnup of TRU fuel, made from reprocessing of Light Water Reactor (LWR) spent fuel. From the view point of maximizing the TRU discharge burnup, the original GT-MHR design (GA/OKBM) was modified for the DB-HTR core,[2,3] which has five fuel rings with 144 fuel columns, nine axial layers (1296 fuel blocks) and a three-ring central reflector.

At the previous study for the TRISO of 100% (PuO_2+NpO_2+Am) with the kernel diameter of 200 μm, the buffer layer thickness of 120 μm and the volumetric packing fraction of 27%, the peak fuel temperature during the LPCC event was evaluated as 2011°C,[4,5] which was much higher than the nominal transient fuel design limit of 1600°C. That was obviously caused by the lack of the heat absorber due to the reduction of 70% volume in the central reflector as well as by the increased decay power due to TRU fuel compositions, respectively.

Thus, the various TRU fuel compositions are considered to reduce the decay power by removing the initial Am isotopes and reducing the volumetric packing fraction of TRISO particles. This study intends to characterize the decay heat impact[6] on the maximum transient fuel temperature of the various TRU compositions. The volumetric PF of 4.9%, 5.9%, and 6.9% are applied for the TRISO of (0.2%UO_2+99.8%($PuO_{1.8}$+NpO_2)+0.6mole SiC getter) and the PFs of 7.0% and 8.0% are used for the TRISO of (30%UO_2+70%($PuO_{1.8}$+NpO_2)+0.6mole SiC getter), respectively, with the kernel diameter of 350 μm and the buffer layer thickness of 100 μm. In addition to the impact of decay power, this study evaluates the annealing effect of the irradiated thermal conductivity of H451 graphite[7] on the peak fuel temperature during LPCC. The reduced thermal conductivity is expected to be recovered by annealing of irradiation-induced defects when the graphite components are heated above the irradiation temperatures. Annealing effect is investigated by using the GA method[8] and JAEA method.[9]

To be satisfied with passive safety performance, core power level is reduced to the allowable maximum power reactor of a 450 MW_{th} to the accident fuel design limit for 0.2%UO_2 mixed TRU (PF = 6.9%) or 30%UO_2 mixed TRU (PF = 8.0%) using the mixed burnable poison of B_4C and Er_2O_3. For the 450MW_{th} DB-HTR core, the peak fuel temperature is evaluated by using JAEA method. It also evaluates the impact of the FB end-flux-peaking on the peak fuel temperature using the detailed axial power distribution for fine mesh.

6.2 DB-HTR Core Design

The DB Project is evaluating the feasibility of the DB-HTR to achieve a very high utilization of TRU derived from the recycle of LWR spent fuel. The design of the prismatic block DB-HTR is different from the original GT-MHR, in that the core is entirely fueled with TRU, and uses a five-fuel-ring configuration instead of three rings, for better neutron economy.

Figure 105 shows the schematic configuration of the reference DB-HTR core with nine axial layers considered in this study. As shown in Figure 105 (a), 12 startup Control Rod (CR), 12 Reserved Shutdown Channel (RSC), and 36 operating CR holes are located at the third ring of the central reflector, the ring-3 Fuel Assembly (FA) and the side reflector, respectively. As shown in Figure 105 (b), the

cooling system of the DB-HTR is composed of the Reactor Cooling System (RCS), the Vessel Cooling System (VCS), and the air-cooled Reactor Cavity Cooling System (RCCS).

Table 17 shows the major design parameters of the reference DB-HTR core, which has the thermal power of 600 MW_{th}, the coolant inlet/outlet temperature of 490/850°C and the active core height of 7.93 m. The design specifications of TRISO fuel particle and fuel compact are listed in Table 18. The fuel composition of TRU kernel is changed from 100%(PuO_2+NpO_2+Am) with a 27% volumetric packing fraction of TRISO particles to (0.2%UO_2+99.8%($PuO_{1.8}$+NpO_2)+0.6mole SiC getter) or (30%UO_2+70%($PuO_{1.8}$+NpO_2)+ 0.6mole SiC getter) using a smaller packing fraction (4.9%–8.0%) to reduce the decay power, with SiC introduced as an oxygen getter. The kernel diameter is increased from 200 μm to 350 μm using the current fuel fabrication technologies. The thickness of the buffer layer is decreased from 120 μm to 100 μm.

Figure 106 shows the geometry specifications of a fuel block, a fuel compact and a TRISO particle. The hexagonal fuel block is assumed to have the same the flat-to-flat width, the number of coolant channels and the number of fuel compacts with those of the conventional fuel block. However, the height of a fuel block is increased from 79.3 cm to 88.1 cm due to nine axial layers instead of 10 axial layers. The number of BP (B_4C or Er_2O_3) holes is increased from 6 to 12. Thus, the number of fuel holes is decreased from 210 to 204. The TRU kernel contains 0.6 mole SiC getter[10] to prevent the possible kernel migration due to the production of noble fission gases and CO with high burnup. The kernel is surrounded by four successive layers: buffer, inner PyC, SiC, and outer PyC.

Table 17. Major design parameters of DB-HTR.

Parameter	Value
Thermal power, MW_{th}	600
Coolant inlet/outlet temperature, °C	490/850
No. of fuel columns	144
Active core height, m	7.93
Core radius, cm	340
Top/bottom reflector height, m	1.586/1.586
No. of axial layers	9
Average power density, W/cm^3	4.66
Graphite block density, g/cm^3	1.74

Table 18. TRISO fuel particle and fuel compact.

TRISO fuel	
Fuel type	$TRUO_2$
Kernel : diameter, μm density, g/cm^3	200 (old) 350 (new) 10.0
Buffer layer : thickness, μm density, g/cm^3	120 (old) 100 (new) 1.05
IPyC layer : thickness, μm density, g/cm^3	35 1.9
SiC layer : thickness, μm density, g/cm^3	35 3.18
OPyC layer : thickness, μm density, g/cm^3	40 1.9
Fuel Compact	
Radius, cm	0.6225
Matrix density, g/cm^3	1.70
Volumetric packing fraction of TRISO particles, % 100%(PuO_2+NpO_2+Am) : 0.2%UO_2+99.8%($PuO_{1.8}$+NpO_2)+0.6 mole SiC getter : 30%UO_2+70%($PuO_{1.8}$+NpO_2)+0.6 mole SiC getter :	 27 (old) 4.9, 5.9, 6.9 (new) 7.0, 8.0 (new)

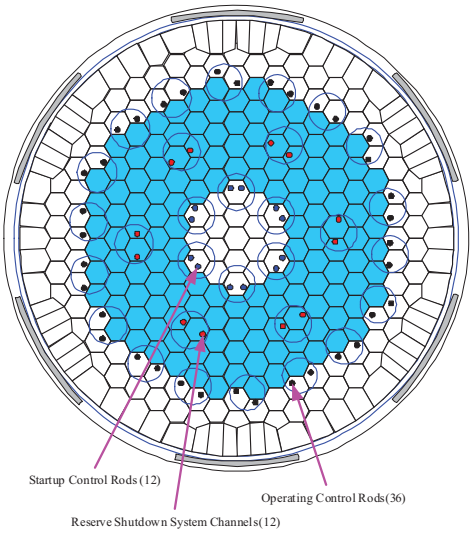

(a) Cross section view of five-ring-fuel core.

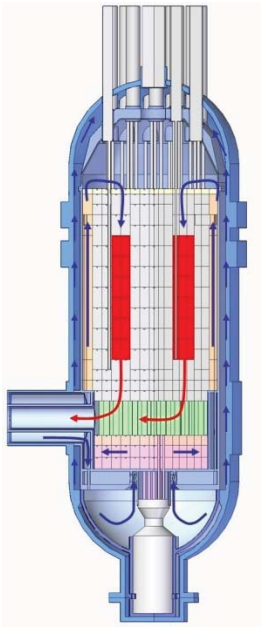

(b) Reactor cooling system.

Figure 105. Reference DB-HTR core design configuration.

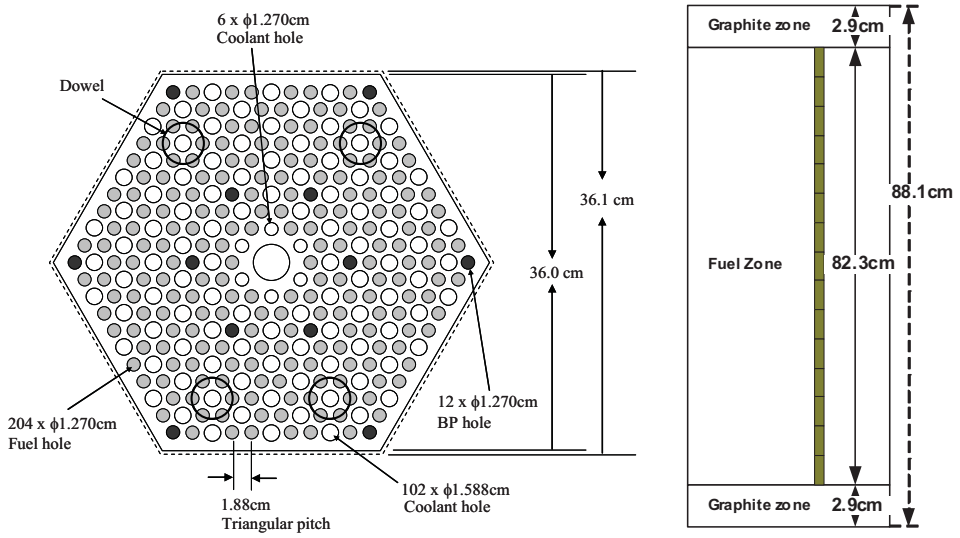

(a) Fuel block geometry.

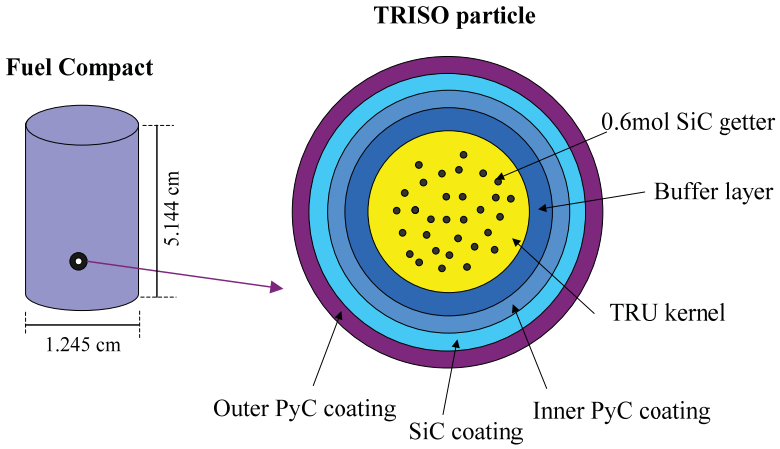

(b) Fuel compact and TRISO particle.

Figure 106. Fuel block, fuel compact, and TRISO particle.

6.3 Analysis Method

6.3.1 Description of GAMMA+ Code

The GAMMA+ code[11] was developed to predict thermo-fluid transients, including LPPC and air ingress phenomena, in the VHTR. The code has enhanced the capability for the functions of fluid transport and material properties, multi-dimensional heat conduction, multi-dimensional fluid flow, chemical reactions, multi-component molecular diffusion, fluid heat transfer and pressure drop, heat generation and dissipation, and radiation heat transfer.

The fluid flow and heat transport is solved unsteadily by two sets of equations for both the gas and the solid. Equations 5–8 and 9–11 are the governing equations of the gas and the solid, respectively. The equations are formulated with a porous media model[12] to consider heat transport in solid-fluid mixed

components. In addition to the multi-dimensional analysis feature, the GAMMA+ code has one-dimensional analysis capability for modeling a general network of pipe flow to simulate the complicate core flow distributions including the coolant channel flow, the axial bypass flow and the cross flow.

$$\frac{\partial \varphi\rho}{\partial t}+\frac{\partial \rho u_i}{\partial x_i}=\varphi\sum_s R_s \quad \text{(mass)} \tag{5}$$

$$\frac{1}{\varphi}\frac{\partial \rho u_j}{\partial t}+\frac{u_i}{\varphi^2}\frac{\partial \rho u_j}{\partial x_i}=B_j-\frac{\partial P}{\partial x_j}+\frac{1}{\varphi}\frac{\partial}{\partial x_i}\left[\mu\left(\frac{\partial u_i}{\partial x_j}+\frac{\partial u_j}{\partial x_i}\right)\right]+\rho g_j \quad \text{(momentum)} \tag{6}$$

$$\frac{\partial \varphi\rho H}{\partial t}+\frac{\partial \varphi\rho u_i H}{\partial x_i}=\frac{\partial}{\partial x_i}\left(\varphi\lambda\frac{\partial T}{\partial x_i}\right)-\frac{\partial}{\partial x_i}\left(\varphi\sum_{s=1}^{m}H_s J_{si}\right)+\dot{q}'''_{ch}+\dot{q}'''_{sf} \quad \text{(energy)} \tag{7}$$

$$\frac{\partial \varphi\rho Y_s}{\partial t}+\frac{\partial \varphi\rho u_i Y_s}{\partial x_i}=-\frac{\partial \varphi J_{si}}{\partial x_i}+\varphi R_s \quad \text{(mass of species)} \tag{8}$$

In the equations above, φ is the porosity and R_s is the species generation rate due to the chemical reaction. B_j is the additional body force in the porous medium approach. J_{si} is the molecular diffusion flux. $\dot{q}'''_{ch}$ is the heat generation rate due to chemical reaction, and $\dot{q}'''_{sf}$ is the heat exchange between the fluid and the solid part. Y_s is the mole fraction of each species.

The heat transport in the solid parts is modeled by the continuous porous medium approach. As shown in Figure 107, the solid region in a reactor core is divided into two zones: the fuel region and the non-fuel region (the graphite matrix). One-dimensional heat conduction is used in the fuel region, Equation 5 for TRISO particle and Equation 6 for fuel compact rod. In the non-fuel region, a multi-dimensional heat conduction of Equation 7 is modeled by a continuous porous medium approach.

$$\left(\rho C_p\right)_p\frac{\partial T_p}{\partial t}=\frac{1}{r^2}\frac{\partial}{\partial r}\left(r^2\lambda_p\frac{\partial T_p}{\partial r}\right)+\dot{q}'''_N-\dot{q}'''_{pf} \quad \text{(1-D TRISO particle)} \tag{9}$$

$$\left(\rho C_p\right)_f\frac{\partial T_f}{\partial t}=\frac{1}{\xi}\frac{\partial}{\partial r}\left(\xi\lambda_f\frac{\partial T_f}{\partial r}\right)+\dot{q}'''_{pf}-\dot{q}'''_{gf} \quad \text{(1-D fuel compact)} \tag{10}$$

$$\left[(1-\varphi)\varphi_g\left(\rho C_p\right)_g\right]\frac{\partial T_g}{\partial t}=\frac{\partial}{\partial x_i}\left(\lambda_{eff}\frac{\partial T_g}{\partial x_i}\right)+\dot{q}'''_{het}-\dot{q}'''_{sf}+\dot{q}'''_{gf} \quad \text{(2/3-D graphite FB)} \tag{11}$$

The graphite temperature (T_g), the fuel mesh temperatures (T_f), and the TRISO particle mesh temperatures (T_p) are implicitly coupled by heat exchange terms between particle and fuel ($\dot{q}'''_{pf}$), and between fuel and graphite block ($\dot{q}'''_{gf}$). Equation 7 is coupled explicitly with the fluid governing equations by the term of $\dot{q}'''_{sf}$. In the equations above, $\dot{q}'''_N$ and $\dot{q}'''_{het}$ is a volumetric nuclear heat production and the heat generation due to the graphite oxidation, respectively. ξ is r for a compact rod or r^2 for a pebble

sphere. λ_{eff} is the effective thermal conductivity including the contact conductance, gas conductance and void radiation. φ_g is the volume fraction of the graphite zone of a fuel block.

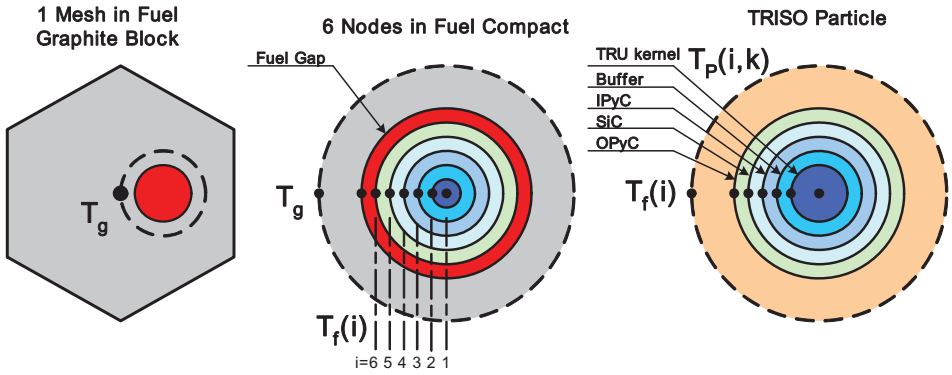

Figure 107. Two zone heat conduction models for a fuel block.

6.3.2 Modeling of DB-HTR System

Figure 108 shows the reference coordinates in the radial and the axial directions for the main components. Figure 109 shows the GAMMA+ nodal scheme for the whole DB-HTR system. The model of fluid parts is composed of the RCS, the air-cooled RCCS, and the VCS. The main RCS flow goes through the inlet plenum, the bottom plenum, the riser holes in the permanent reflector, the top plenum, the core coolant channels, and then the outlet plenum. The VCS flow goes through the gap between the core barrel and the reactor pressure vessel (RPV). The VCS is designed[13] to use the conventional SA533/SA508 steel[14] for the RPV.

Most fluid parts use a one-dimensional network model of pipe flow to simulate the complicate core flow distributions. Figure 110 shows a core flow network model of the GAMMA+ code for the inlet riser, the core coolant channels, the FA gap bypasses, and the RSC/CR channels. The active core flow is modeled as five flow channels with 23 axial nodes including 18 nodes for fuel blocks (two nodes per fuel block), one node for upper restraint block, two nodes for top reflector blocks, and two nodes for bottom reflector blocks.

The other bypass flow from the top plenum and the outlet plenum is modeled as 10 flow channels, which consist of three gap flow channels between central reflector blocks, five gap flow channels between FA blocks, and two gap flow channels between outer reflector blocks. These gap flow channels are interconnected to each other and also interconnected to the FA coolant flow channels and RSC/CR flow channels through cross-flow junctions. The uniform gap sizes of 2 mm for the horizontal gaps and 1.5 mm for the vertical gaps between the fuel blocks are used in the present analysis.

The air-cooled RCCS is composed of 292 rectangular riser tubes (2 x 10 inches) in the reactor cavity. The RCCS riser tube uses three-dimensional meshes to consider the radiation heat transfer for both inside surfaces and outside surfaces of tube. All the other solid regions are two-dimensionally modeled for the reactor components including FA, central reflector, top/bottom reflectors, side reflector, core barrel (CB), and RPV. As shown in Figure 111, the core cross section has a 1/6 symmetry with 24 fuel block assemblies in five radial rings. The GAMMA+ code is able to simulate specific 24 fuel block assemblies. For simplifying input models in this calculation, fuel blocks are grouped as one ring-fuel at each ring.

That is, 18, 24, 30, 36, and 36 fuel blocks are contained in ring-1, ring-2, ring-3, ring-4, and ring-5 fuel, respectively. The heat transfer between the adjacent ring fuels is considered by the face-to-face area ratio.

The thermal radiation heat transfers are considered in the top plenum, the bottom plenum, the annulus between the core barrel and the RPV, the reactor cavity containing the RCCS panels, and the annulus between the downcomer wall and the reactor cavity wall. The radiation heat transfer in the core zone is considered by the effective thermal conductivity including the contact conductance, gas conductance, and void radiation.

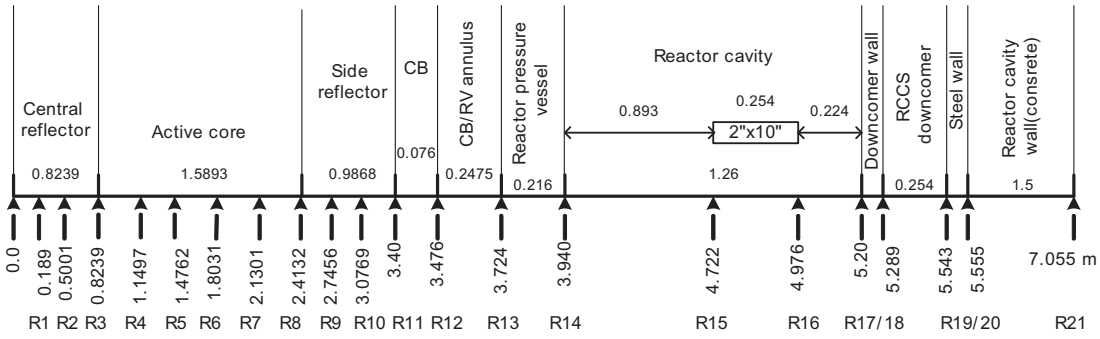

(a) R-axis,

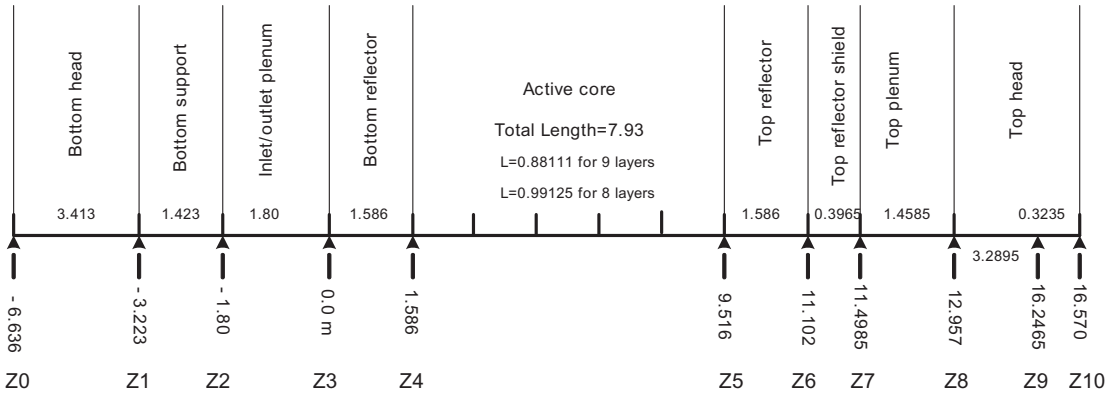

(b) Z-axis,

Figure 108. R-Z coordinates of the 600 MW_{th} DB-HTR.

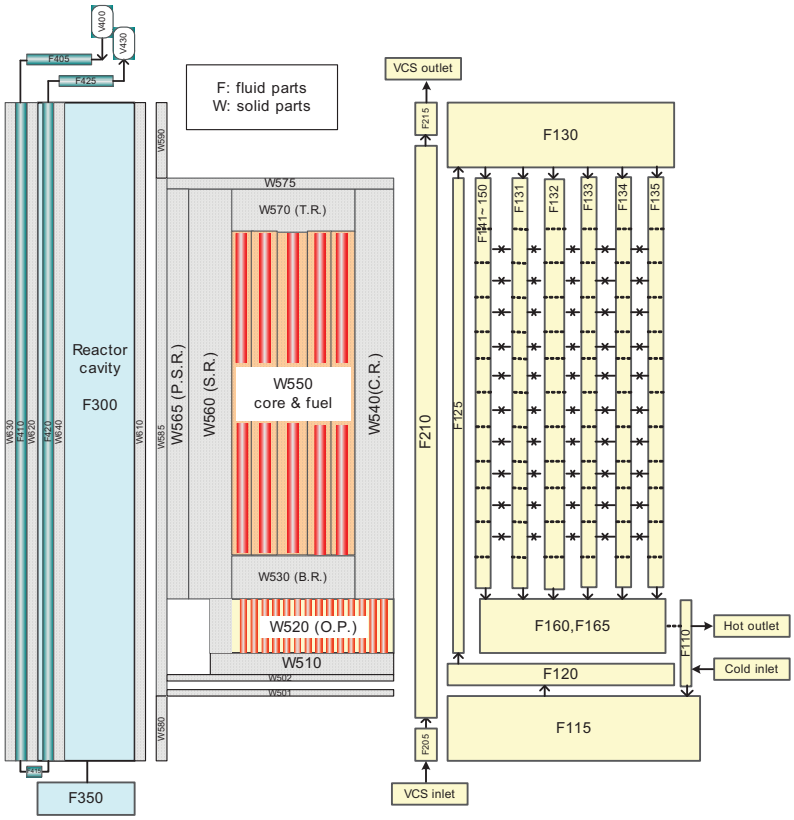

Component	Description of WB	Meshes
W501,502	Lower metal support plate	8x1,11x1
W510	Bottom support	9x2
W511, 521	Insulation Cover	3x2, 3x3
W520	Outlet plenum	9x3
W530	Bottom reflector	5x2
W540	Central reflector	3x22
W550	Fuel & core reflector	5x18
W560	Side reflector	2x22
W565	Permanent side reflector	1x22
W570	Top reflector	5x2
W575	Top support shroud	11x1
W580	Lower plenum cover	4x2
W585	Core barrel	3x31
W590	Upper shroud	4x3
W610	Reactor pressure vessel	5x37
W620	RCCS downcomer wall	3x37
W630	Reactor cavity wall	4x37
W640	RCCS panel	2x37x4

Component	Description of FB	Meshes
F110	Inlet plenum	6
F115	Lower plenum	2
F120	Metal support zone	1
F125	Inlet riser holes	28
F130	Upper plenum	3
F131~135	Core coolant channels	23 (all)
F141~150	FA bypass channels	23 (all)
F151~153	CR/RSC channels	23 (all)
F160,F165	Outlet plenum	1,1
F205,F210, F215	CB/RPV annulus (VCS flow path)	1,3x34,1
F300	Reactor cavity (RCCS)	3x37
F350	Reactor cavity (remain)	1
F405	RCCS inlet header	1
F410	RCCS downcomer	37
F415	RCCS lower plenum	1
F420	RCCS tube riser	37
F425	RCCS outlet header	1

Figure 109. GAMMA+ code analysis model of the 600 MW_{th} DB-HTR.

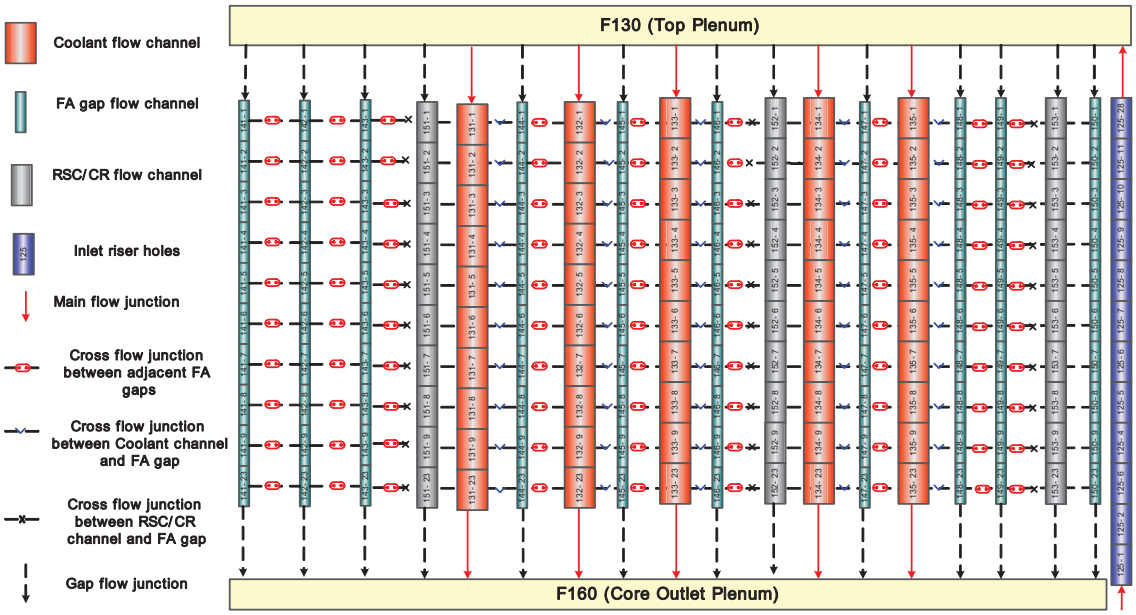

Figure 110. Core flow network model for GAMMA+ code analysis.

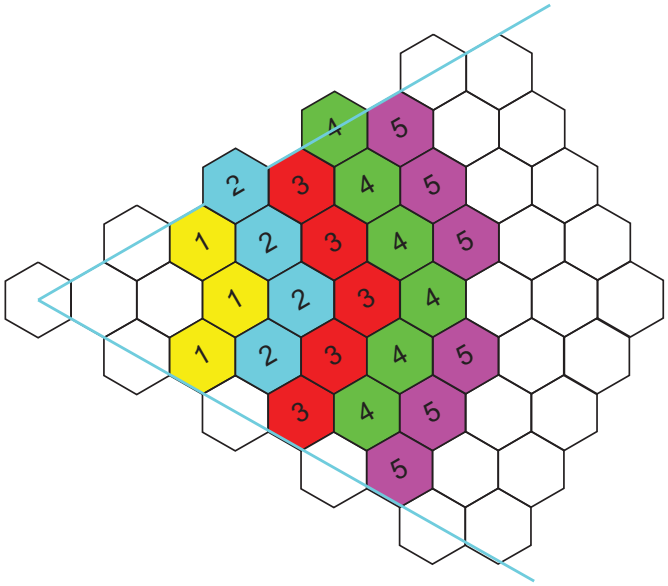

Figure 111. Numbering the fuel block for GAMMA+ code analysis.

6.3.3 Irradiated Thermal Conductivity of H451 Graphite

Main core components of DB-HTR core, such as fuel blocks and reflectors, are made of the graphite material. Most part of fuel compact in a fuel block is also composed of the graphite except the TRISO particles. The thermal conductivity and the volumetric heat capacity of TRU kernel and the graphite are necessary for Equations 9–11, as described in Section 6.3.1. The thermophysical properties of TRU kernel are different from UO_2 kernel. For a TRU of 100%(PuO_2+NpO_2+Am), the properties of TRU kernel are assumed[4,5] as those of PuO_2 material because the kernel is mainly composed of the Pu isotopes.

In this study, for a TRU of 99.8%($PuO_{1.8}$, NpO_2)+0.2%UO_2+0.6 mole SiC getter or a TRU of 70%($PuO_{1.8}$, NpO_2)+30%UO_2+0.6 mole SiC getter, the properties of TRU kernel are assumed to be volume-averaged values of those of PuO_2 and SiC. It assumes that 0.6 mole SiC getter is about 24% volumetrically scattered in the kernel. As shown in Figure 112, the properties of TRU kernel become higher than those of PuO_2 due to the high thermal performance of SiC material. However, the thermophysical properties of TRU kernel hardly affect the temperature distributions of core, fuel, and TRISO particle because the heat conduction in the core is dominantly determined by the graphite material.

The H451 graphite is used as the reference graphite of fuel blocks and reflectors in this analysis. Neutron irradiation remarkably reduces the thermal conductivity of graphite components in a DB-HTR core. The irradiated thermal conductivity, $K(T)$ of H451 graphite[8] is expressed as a superposition of three temperature-dependent resistance mechanisms of the following Equation 12.

$$\frac{1}{K(T)} = \alpha\left[\frac{1}{K_u(T)} + \frac{b}{K_b(T)} + \frac{d}{K_d(T)}\right] \tag{12}$$

where, α is a porosity-tortuosity factor, $K_u(T)$ is the crystallite conductivity with Umklapp processing dominating, b is the inverse of the crystallite boundary spacing, $K_b(T)$ is the effect of the grain boundary scattering, d is the irradiation damage parameter, and $K_d(T)$ is the effect of the irradiation damage.

The reduced thermal conductivity is expected to be recovered by annealing of irradiation-induced defects, when the graphite components are heated above the irradiation temperatures. This phenomenon can occur at the accident conditions such as LPCC event. Thus, this study evaluates the annealing effect of the irradiated thermal conductivity of the graphite on the peak fuel temperature during LPCC, using two kinds of correction factor for the graphite thermal annealing effect, GA method,[8] and JAEA method .[9]

GA method uses the simple annealing temperature-dependent correction factor for d of the irradiation damage parameter as shown in the following Equation 13.

$$d = d\left(1 - \frac{T - 1273}{300}\right), \quad if \quad T > 1273K \tag{13}$$

Thermal annealing on thermal conductivity appears to begin at 1273 K and is completed by 1573 K. The irradiation damage parameter, d in Equation 13 is assumed to decrease linearly to zero over the above temperature range. However, this approach can be applied only to low fast-neutron fluence and low-irradiation temperature condition.

Alternatively, based on the various experimental data, the JAEA method provides the thermal conductivity recovery factor due to the annealing effect, which is dependent on fast-neutron fluence (Φ), annealing temperature, and irradiation temperature (T_i) as shown in Equation 14.

$$\frac{K_{ma}}{K_m} = \left(1 - 2.2\times10^{-7}T^2\right)\left[A(T) + B(T)\frac{\Phi}{T_i}\right], \quad if \quad T \le 1200\ ^oC$$

$$\frac{K_{ma}}{K_m} = 0.72\left[A(T) + B(T)\frac{\Phi}{T_i}\right], \quad if \quad T > 1200\ ^oC$$

$$\text{Therfore } K(T) = \frac{K_{ma}}{K_m}K(T)^{Eq(8)} \tag{14}$$

Figure 113 shows the thermal conductivity recovery factor due to the annealing effect. GA method is close only to low fast-neutron fluence and the low-irradiation temperature condition of the JAEA method. This study assumes that the fast-neutron fluences for core and reflector graphites are $3.0\text{x}10^{21}$ n/cm^2 and $1.0\text{x}10^{21}$ n/cm^2, respectively.

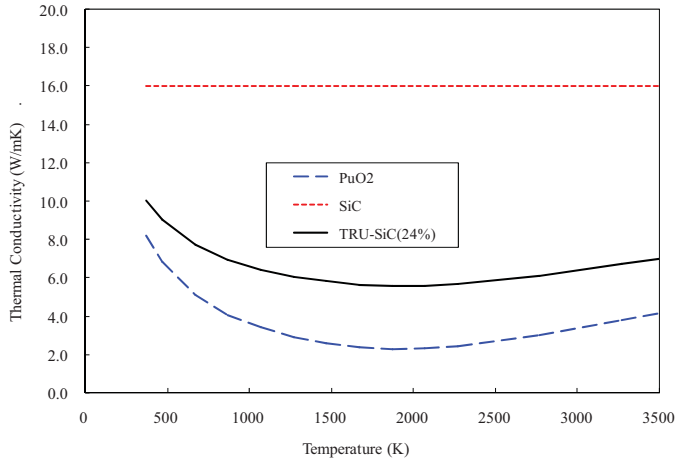

(a) Thermal conductivity.

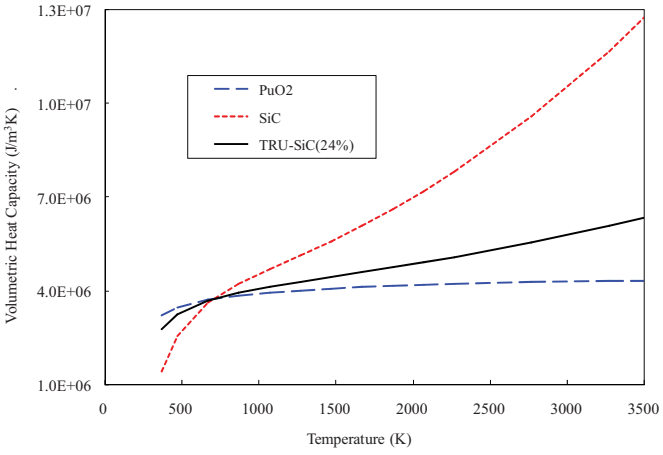

(b) Volumetric heat capacity.

Figure 112. Thermophysical properties of TRU kernel with SiC getter.

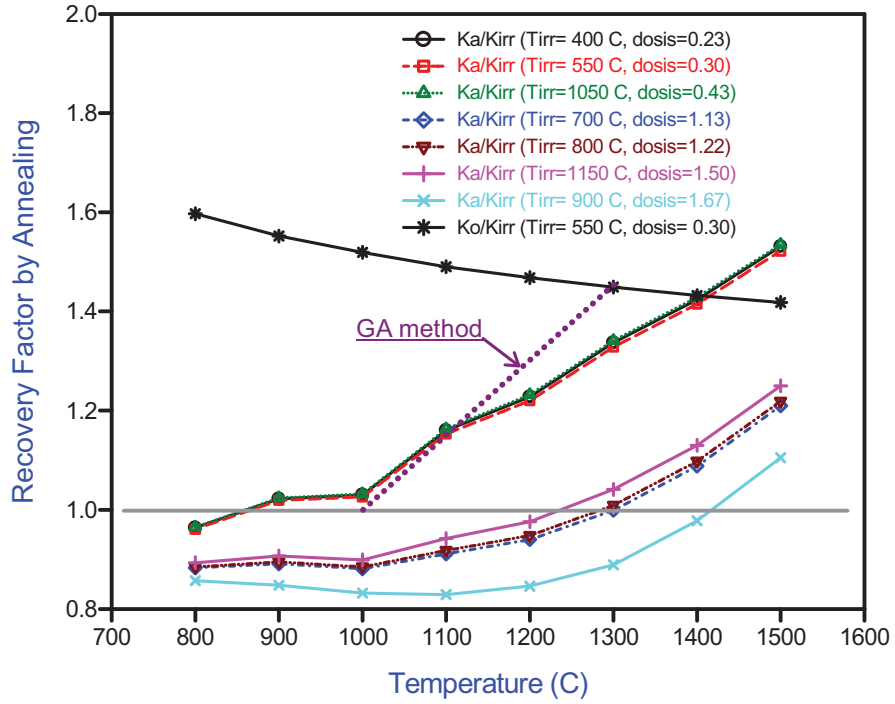

Figure 113. Thermal conductivity recovery factor due to the annealing effect.

6.3.4 Core Power Distribution and Decay Power

The TRU fuel of the DB-HTR has different power distribution of the fuel block and the decay power curve from the UO_2 fuel. In addition to the fuel composition, the power distribution is highly dependent on the fuel shuffling scheme. Based on the hybrid refueling scheme (using both axial and radial shuffling) and the use of B_4C or Er_2O_3 as a BP, MASTER code[15] calculation provides the specific fuel block power data, and the ring-averaged power data of Figure 114 through Figure 118 are used in this analysis. The axial power distribution of Er_2O_3 is more top-core skewed than that of B_4C, and the power peaking factor of B_4C is a little less than that of Er_2O_3 in the ring-1 FA, where the peak fuel temperature occurs during LPCC event.

The decay power curve is calculated using the McCARD[16] and ORIGEN[17] codes. As shown in Figure 119, the decay power curves[18,19] of the various TRU fuel compositions are compared with that of UO_2 fuel. The TRUs contained in 100% (PuO_2+NpO_2+Am) with 27% PF produce higher decay power than those in UO_2 kernels. Removing the initial Am from the TRUs and using the same 27% PF, the decay power is remarkably decreased, but it is still higher after 10 hours than for the UO_2 kernels.

The reduced volumetric packing fraction of TRU in addition to the removal of the initial Am isotopes can provide even lower decay power.[20] Figure 119 shows the decay power curves of 0.2%UO_2 mixed TRU (PF = 4.9%, 5.9%, 6.9%) and the decay power curves of 30% UO_2 mixed TRU (PF = 7.0%, 8.0%), where the decay power is lower than that of UO_2 fuel. In the case of a 0.2% UO_2 mixed TRU (PF = 6.9%), the decay power after 70 hours becomes higher than that of UO_2 fuel. The decay power of a 30% UO_2 mixed TRU (PF = 7.0%) is less than that of a 0.2% UO_2 mixed TRU (PF = 6.9%) due to the reduced amount of ($PuO_{1.8}$+NpO_2). It is concluded that the decay power of TRU fuel is highly sensitive to the amounts of Pu and Am isotopes.

In this analysis, the axial power distribution and the decay power are obtained at BOC and EOC, respectively, to evaluate the maximum fuel temperature conservatively.

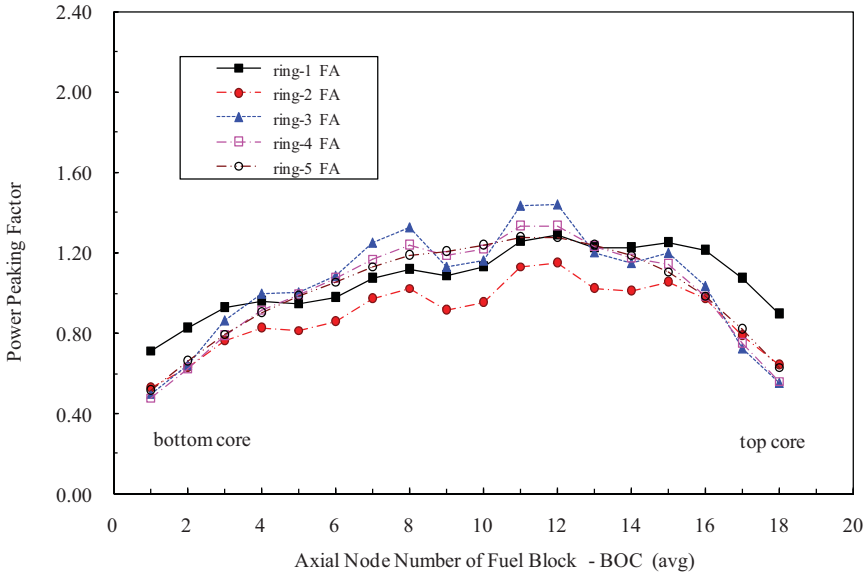

(a) For 0.2%UO_2+99.8%($PuO_{1.8}$+NpO_2)+0.6 mole SiC getter (B_4C).

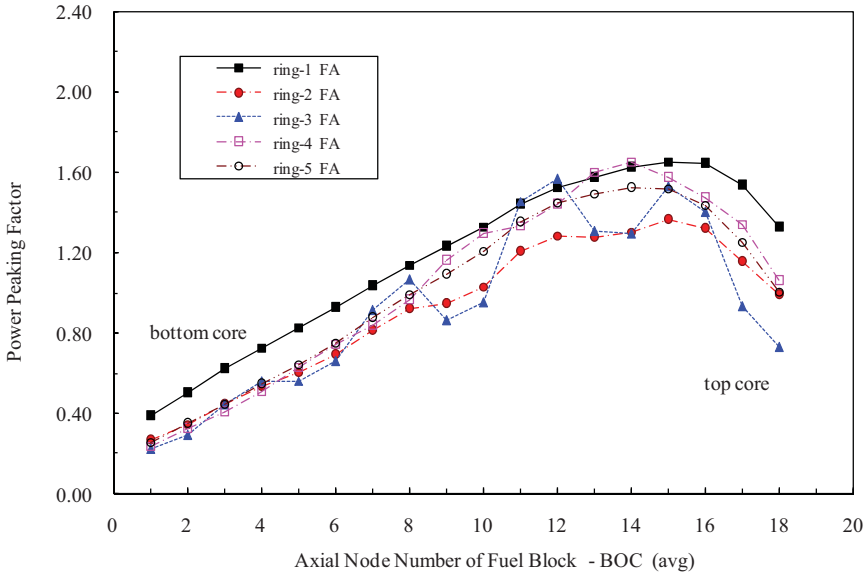

(b) For 0.2%UO_2+99.8%($PuO_{1.8}$+NpO_2)+0.6 mole SiC getter (Er_2O_3).

Figure 114. Average ring power distribution of 0.2% UO_2 mixed TRU (PF = 4.9%).

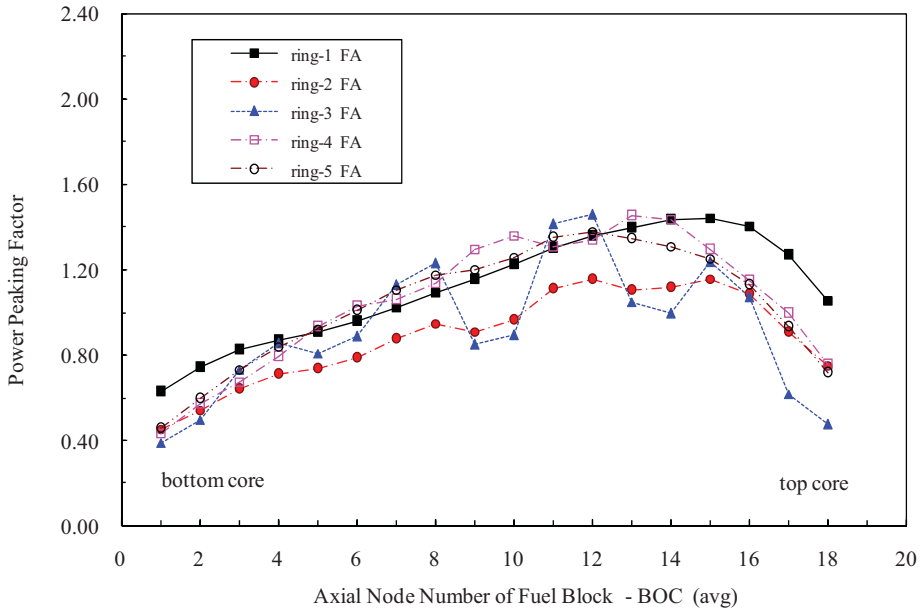

(a) For 0.2%UO_2+99.8%($PuO_{1.8}$+NpO_2)+0.6 mole SiC getter (B_4C).

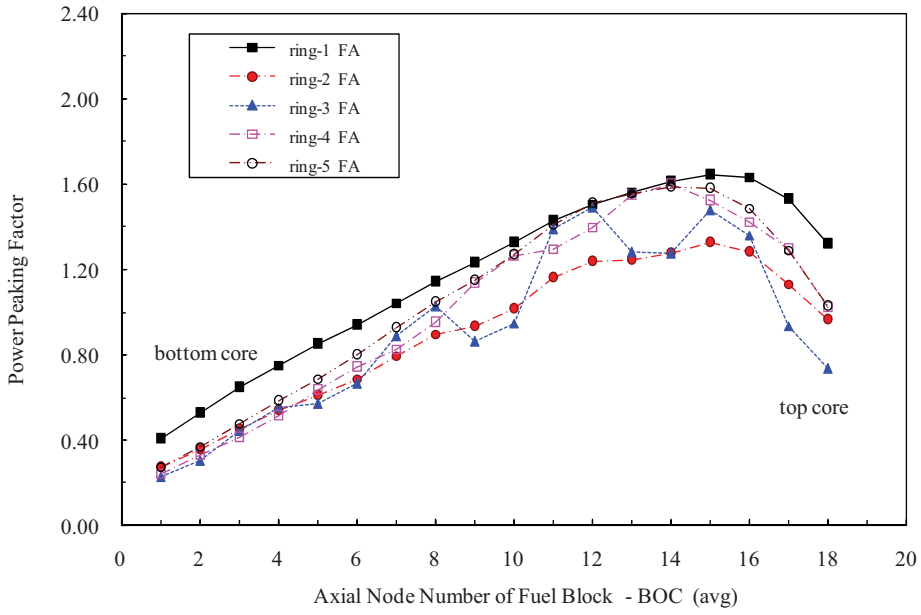

(b) For 0.2%UO_2+99.8%($PuO_{1.8}$+NpO_2)+0.6 mole SiC getter (Er_2O_3).

Figure 115. Average ring power distribution of 0.2% UO_2 mixed TRU (PF = 5.9%).

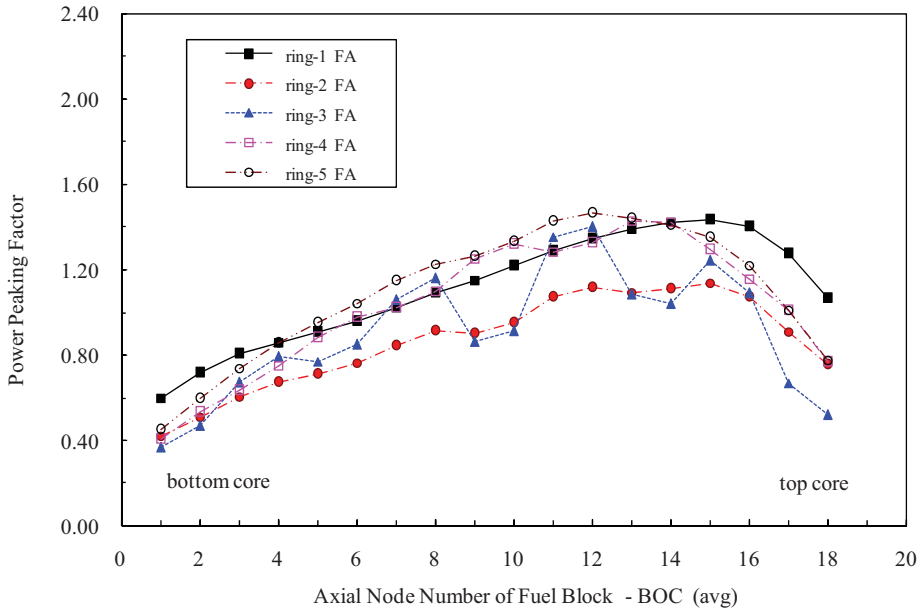

(a) For 0.2%UO_2+99.8%($PuO_{1.8}$+NpO_2)+0.6 mole SiC getter (B_4C).

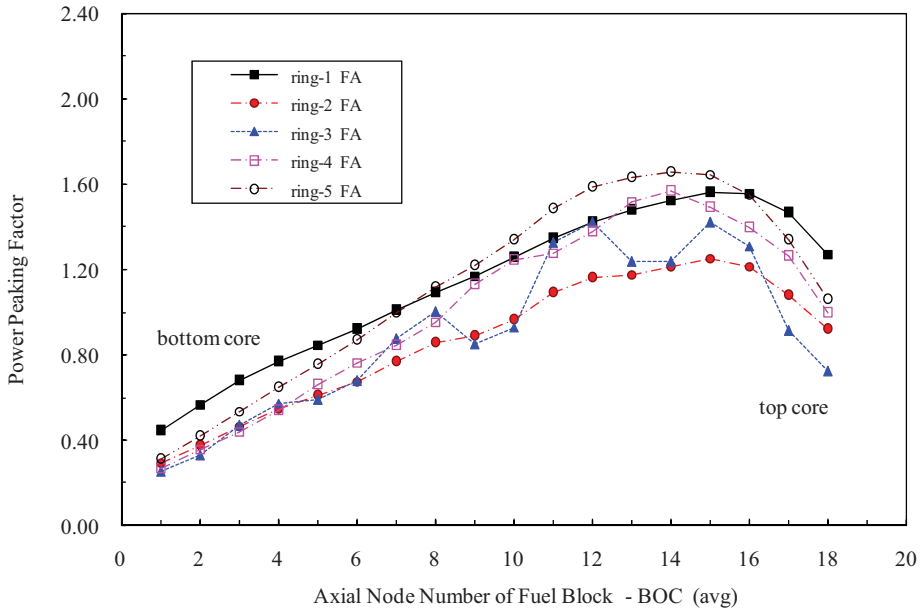

(b) For 0.2%UO_2+99.8%($PuO_{1.8}$+NpO_2)+0.6 mole SiC getter (Er_2O_3).

Figure 116. Average ring power distribution of 0.2% UO_2 mixed TRU (PF = 6.9%).

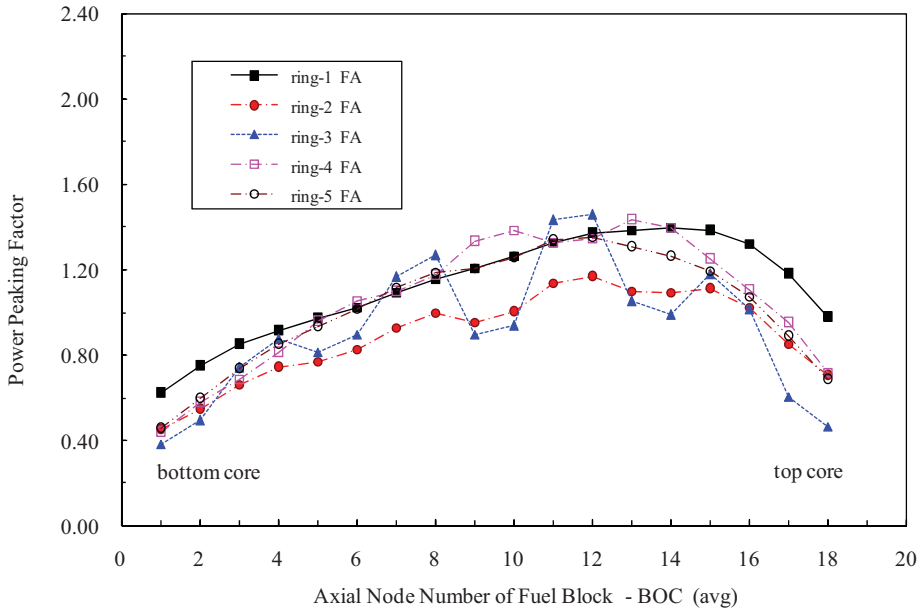

(a) For 30%UO_2+70%($PuO_{1.8}$+NpO_2)+0.6 mole SiC getter (B_4C).

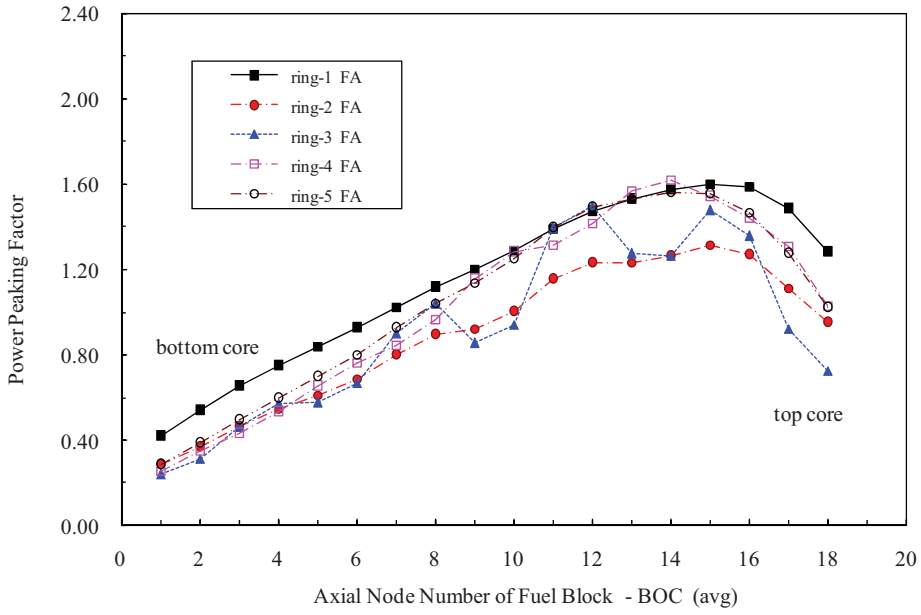

(b) For 30UO_2+70%($PuO_{1.8}$+NpO_2)+0.6 mole SiC getter (Er_2O_3).

Figure 117. Average ring power distribution of 30% UO_2 mixed TRU (PF = 7.0%).

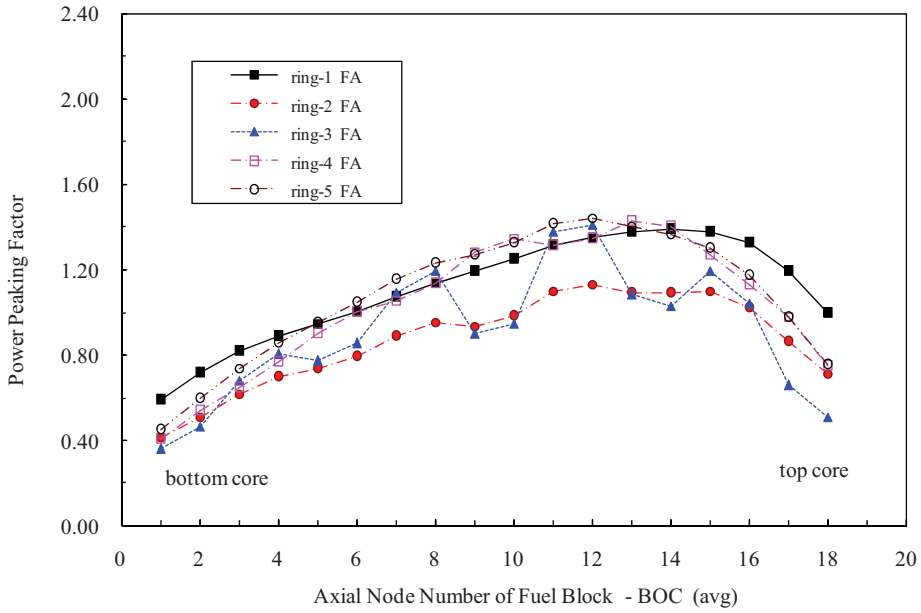

(a) For 30%UO_2+70%($PuO_{1.8}$+NpO_2)+0.6 mole SiC getter (B_4C).

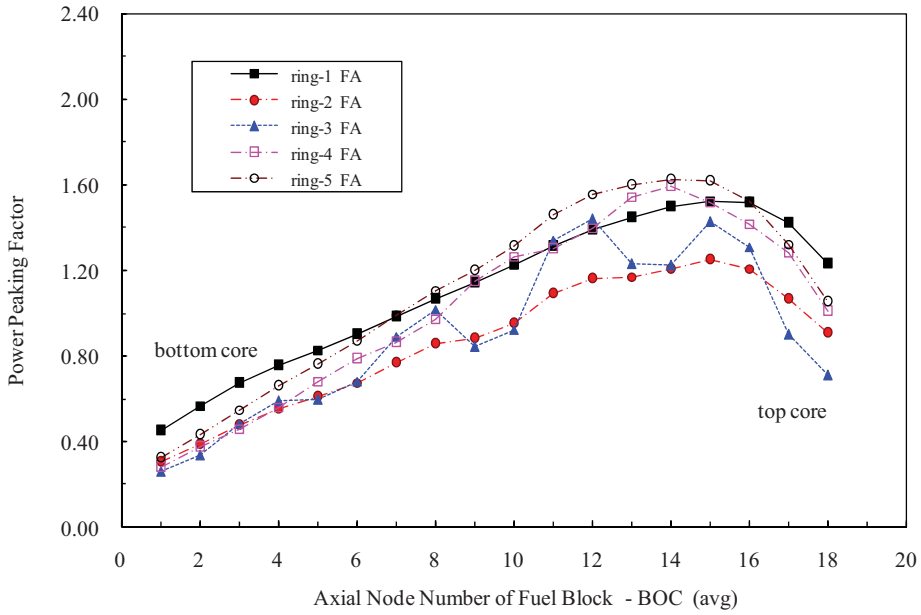

(b) For 30UO_2+70%($PuO_{1.8}$+NpO_2)+0.6 mole SiC getter (Er_2O_3).

Figure 118. Average ring power distribution of 30% UO_2 mixed TRU (PF = 8.0%).

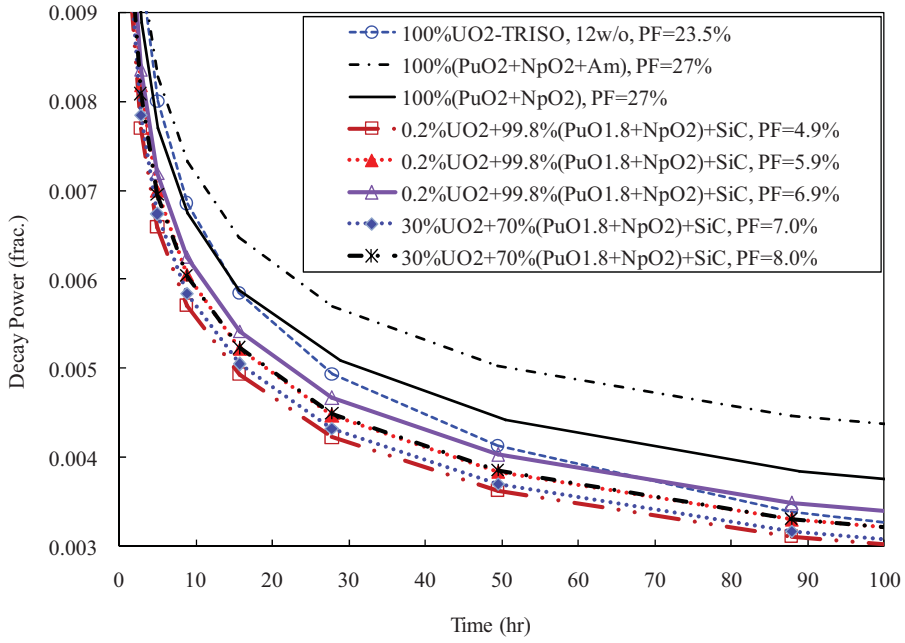

Figure 119. Decay power curves of the various TRU kernel fuel compositions.

6.4 Analysis Results

6.4.1 Steady State Results

6.4.1.1 Flow Distribution

The steady state analyses of DB-HTR with the various TRU fuels such as a TRU of 100%(PuO_2+NpO_2+Am), a TRU of 0.2%UO_2+99.8%($PuO_{1.8}$+NpO_2)+0.6 mole SiC getter or a TRU of 30%UO_2+70%($PuO_{1.8}$+NpO_2)+0.6 mole SiC getter are performed to obtain the initial conditions for the transient analysis. Although the axial power distribution is different for each other fuel composition, the distributions of axial channel flow, bypass flow, and cross flow are very similar. Thus, this report describes the results of flow distribution[4] only for a TRU of 100%(PuO_2+NpO_2+Am) with 27% PF as the followings.

The total RCS flow rate is 318.8 kg/s at the steady state conditions with the inlet temperature of 490°C, the outlet temperature of 850°C, and the outlet pressure of 7.0 MPa. The inlet temperature and the flow rate of the VCS are 140°C and 3.0 kg/s, respectively. The inlet air temperature of the RCCS is 43°C. The heat loss to the reactor air cavity is estimated to be 1.23 MW_{th}, which is less than 1.0 % normal power.

Figure 120 shows the axial channel flow distribution at five fuel rings of the DB-HTR core. The flow rate changes at the axial locations due to the effects of the cross flow and the bypass flow. The detailed core flow results show that the maximum bypass flow occurs at the middle core (Z = 6.2 m), where the flow rates of ring-1, ring-2, ring-3, ring-4 and ring-5 are 11.3%, 15.4%, 17.9%, 22.4%, and 21.7% of the RCS flow rate, respectively. The steady state flow results are summarized in Table 19.

Figure 121 shows the axial bypass flow distribution at 10 FA gaps. The axial flow of sixth FA gap is much fluctuated because the high cross flow occurs at ring-3 fuel block due to the RSC hole. As shown in

Figure 122, the bypass flow through RSC hole is much greater than CR hole. This is caused by the assumption that the CR holes are filled with the CR drive structures, but the RSC holes are empty. Thus, it is modeled that the flow area of the CR hole is much less than that of RSC hole although the diameter of the CR guide tube (0.1016 m) is greater than that of the RSC hole (0.09525 m). As shown in Figure 123, total RCS flow distributes to the fuel channel, the CR/RSC hole and the FA bypass gap, which fractions at the middle height of the core are 88.7%, 7.1%, and 4.2%, respectively.

Figure 124 through Figure 126 show the distribution of the cross flow between the adjacent FA gaps, the cross flow between FA gap and CR/RSC hole, and the cross flow between FA gap and the coolant channel, respectively. All cross flows at ring-3 fuel block are very high. The cross flow direction of the fuel channel to the FA gap shows different from that of the CR/RSC hole to the FA gap, which causes the fluctuation of the cross flow between the adjacent FA gaps.

It is noted that this flow distribution is based on the assumption of the uniform gap size—2 mm for the horizontal gaps and 1.5 mm for the vertical gaps between the fuel blocks.

Table 19. Steady state flow results at the middle core height.

Parameter	Value
RCS Total Flow Rate, kg/s	318.8
Channel Flow Rate, kg/s at:	
Ring-1	36.0 (11.3)[a]
Ring-2	49.3 (15.4)
Ring-3	57.0 (17.9)
Ring-4	71.3 (22.4)
Ring-5	69.1 (21.7)
Total Core Flow Rate, kg/s	282.8 (88.7)
Bypass Flow Rate, kg/s at:	
FA gap	13.4 (4.2)
CR hole	4.4 (1.4)
RSC hole	18.2 (5.7)
Heat loss to RCCS, MW_{th}	1.23

a. The value in () is the percentage of flow fraction to the RCS total flow rate

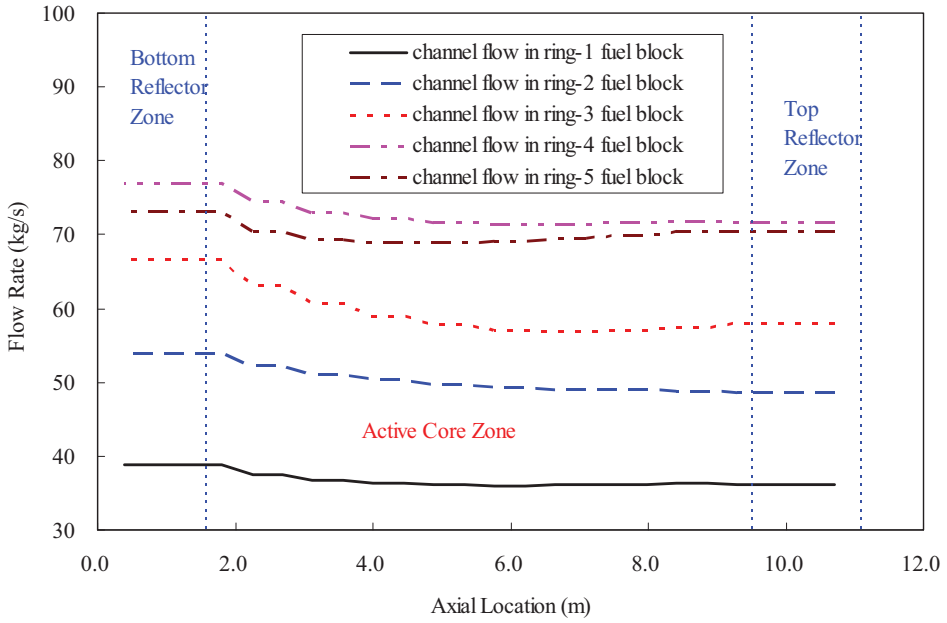

Figure 120. Fuel channel flow distribution.

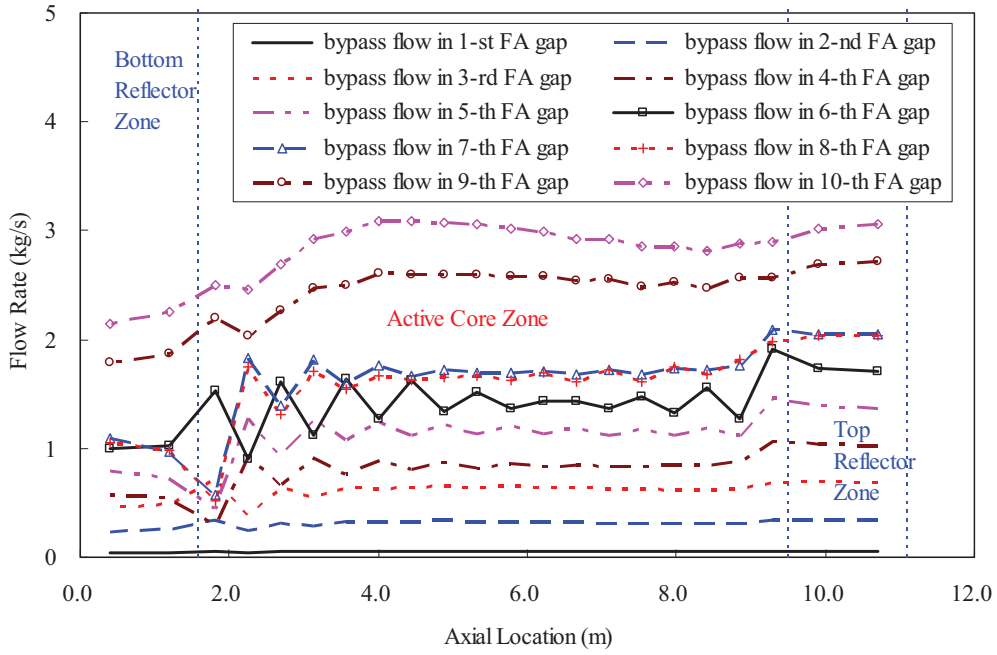

Figure 121. FA gap bypass flow distribution.

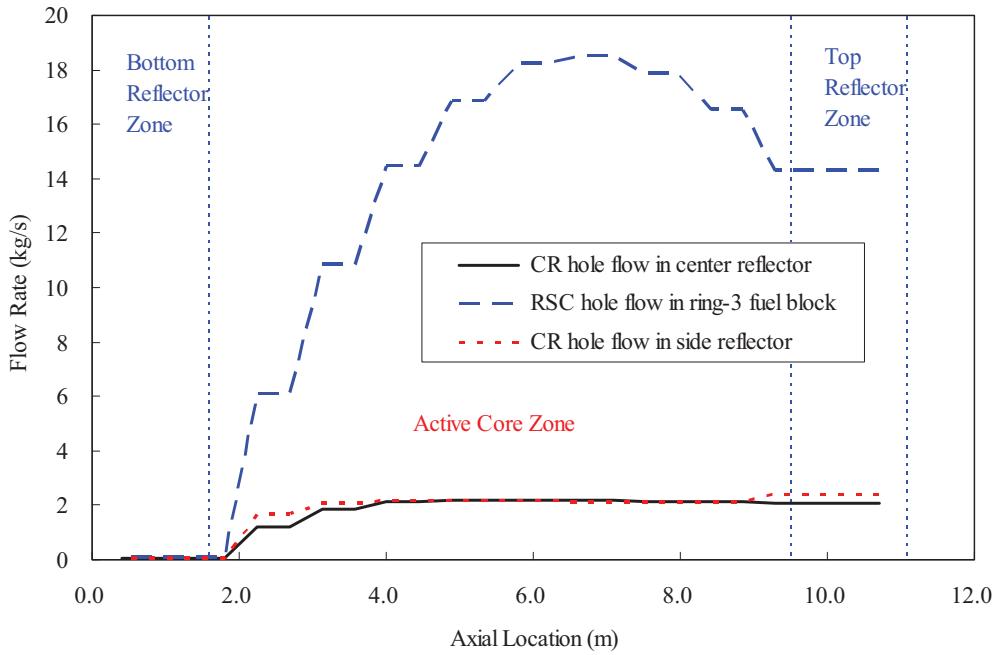

Figure 122. CR/RSC hole bypass flow distribution.

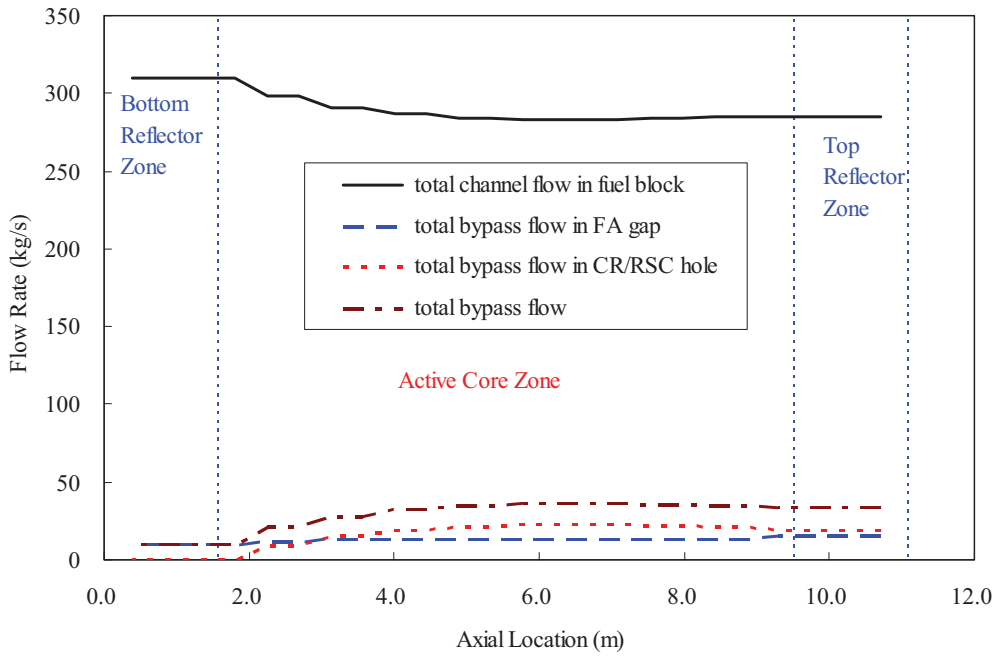

Figure 123. Total channel flow and bypass flow distribution.

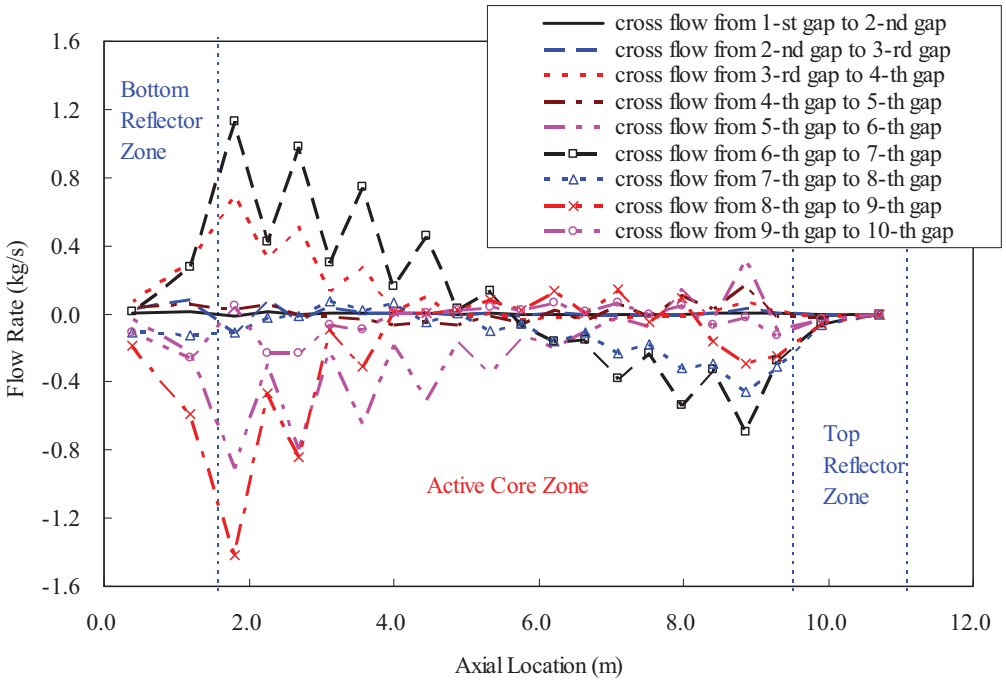

Figure 124. Cross flow between the adjacent FA gaps.

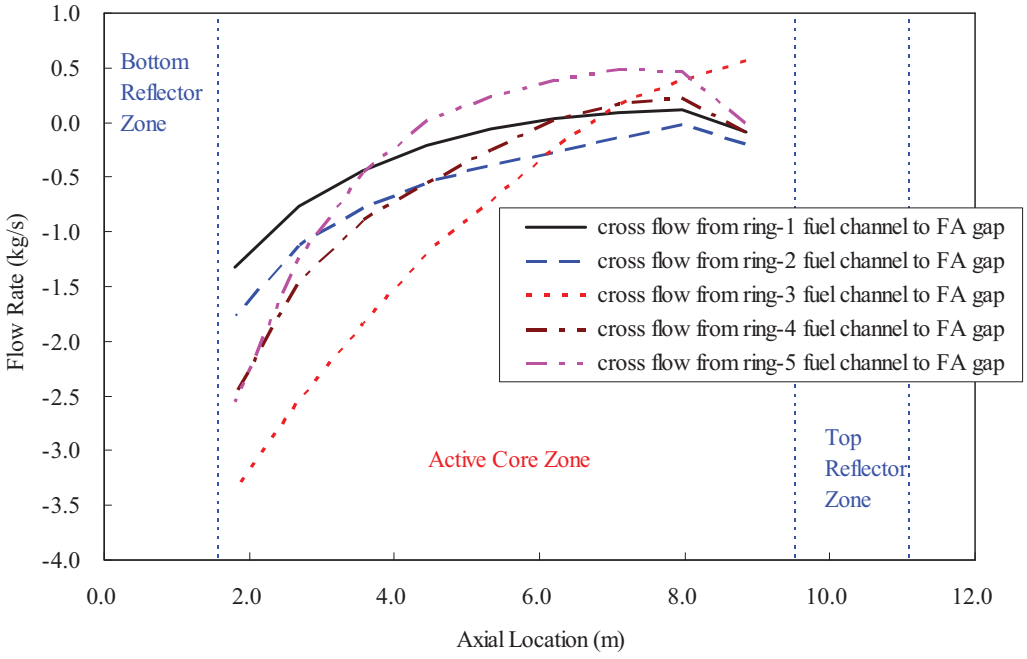

Figure 125. Cross flow between fuel channel and FA gap.

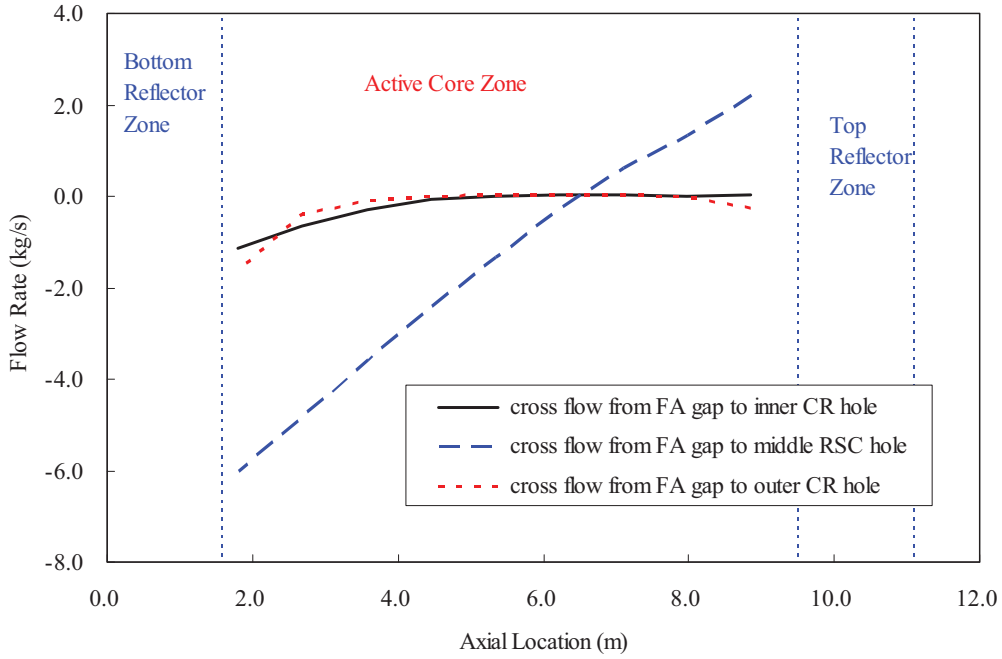

Figure 126. Cross flow between FA gap and CR/RSC hole.

6.4.1.2 Core Temperature Distribution

Although the flow distribution is very similar, core temperature distributions such as the axial temperature, the radial temperature and the maximum fuel temperature are a little different due to the axial power distribution for each fuel composition. All figure data of core temperature distribution at the steady state are listed in Subsection 6.6.

This section describes the results of core temperature distribution only for a TRU of $0.2\%UO_2+99.8\%(PuO_{1.8}+NpO_2)$+0.6 mole SiC getter with 6.9% PF and for the use of B_4C as the burnable poison.

Figure 127 shows the axial core graphite temperature distributions at the main core components including the central reflector, five fuel rings, side reflector, CB, and RPV. The axial temperature profile of five fuel rings shows a bottom-skewed distribution due to the increase of the coolant temperature through the flow direction although the power is skewed to the top core. The maximum RPV temperature of 311°C, below the SA508 steel limit 371°C,[14] is obtained by the VCS flow of 3.0 kg/s.

Figure 128 shows the radial core graphite temperature distributions at the core height levels including the bottom reflector, the active core and the top reflector zones. In the active core zone, the radial temperature profile is a concaved or flat shape due to the power distribution of the DB-HTR. Figure 129 and Figure 130 show the coolant temperature and the maximum fuel temperature profiles at each fuel ring, respectively. The maximum fuel temperature is located at the center of fuel compact rod. The peak fuel temperature of 982°C is less than the normal operation limit of 1250°C for TRISO fuel.[21] The temperature difference between fuel kernel and coolant is 118°C at the hottest location.

As described in Section 6.3.1 of the GAMMA+ code features, two zone heat conduction models for a fuel block are used for predicting a TRISO particle temperature profile. TRISO particles are assumed to be

uniformly distributed in a fuel compact. TRISO particles are grouped to a particle at each fuel node in a fuel compact. The heat conduction length from fuel node to a particle is determined by the volumetric packing fraction of TRISO particles in a fuel compact. At the hottest location of the second layer ring-1 fuel block (Z = 2.687 m), the internal temperature profile of a TRISO particle is shown in Figure 131, where the most of temperature gradient occurs at the buffer layer. The temperature difference between the TRU kernel center and the outer PyC is 22°C, which is much higher than that of 27% PF TRU (10°C) because the TRISO power (58.88 mW) for low PF of 6.9% is much higher than the TRISO power (11.47 mW) for high PF of 27%.[4]

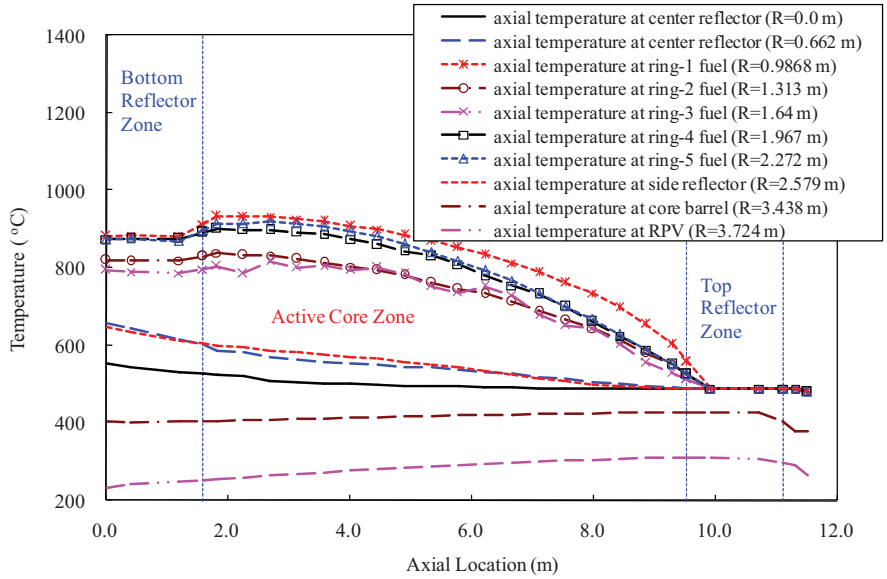

Figure 127. Axial core graphite temperature distribution.

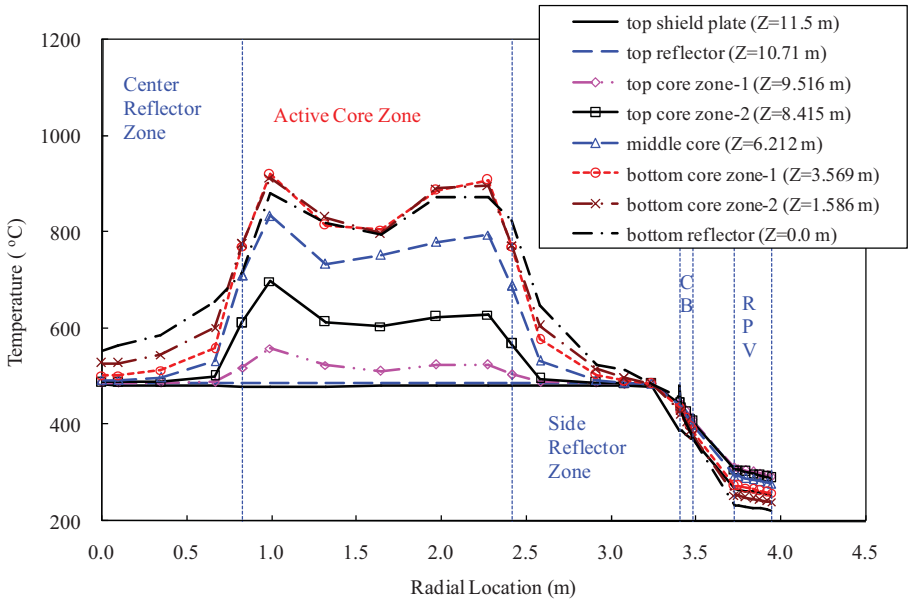

Figure 128. Radial core graphite temperature distribution.

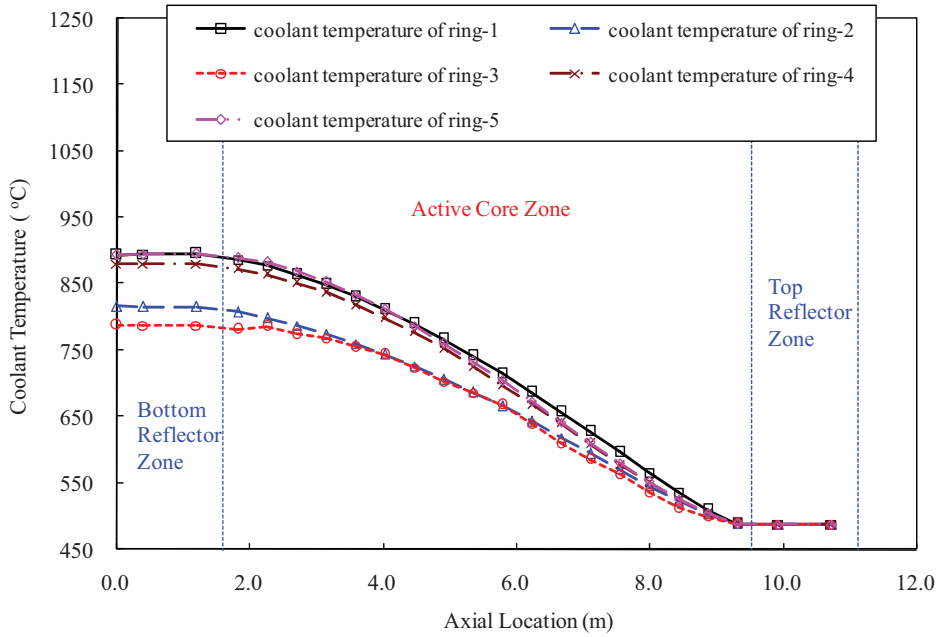

Figure 129. Coolant temperature.

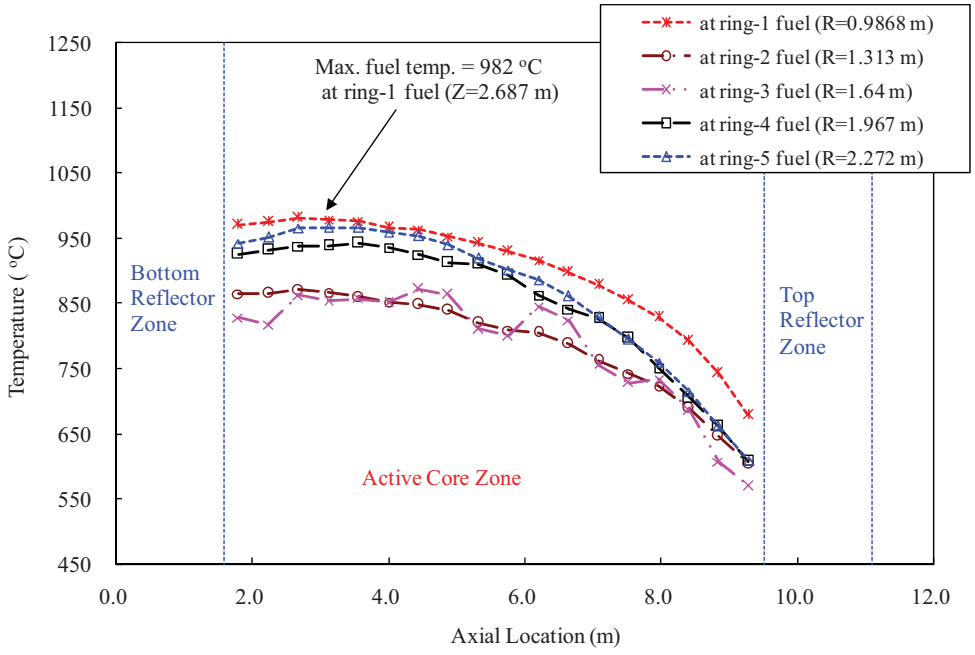

Figure 130. Maximum fuel temperature.

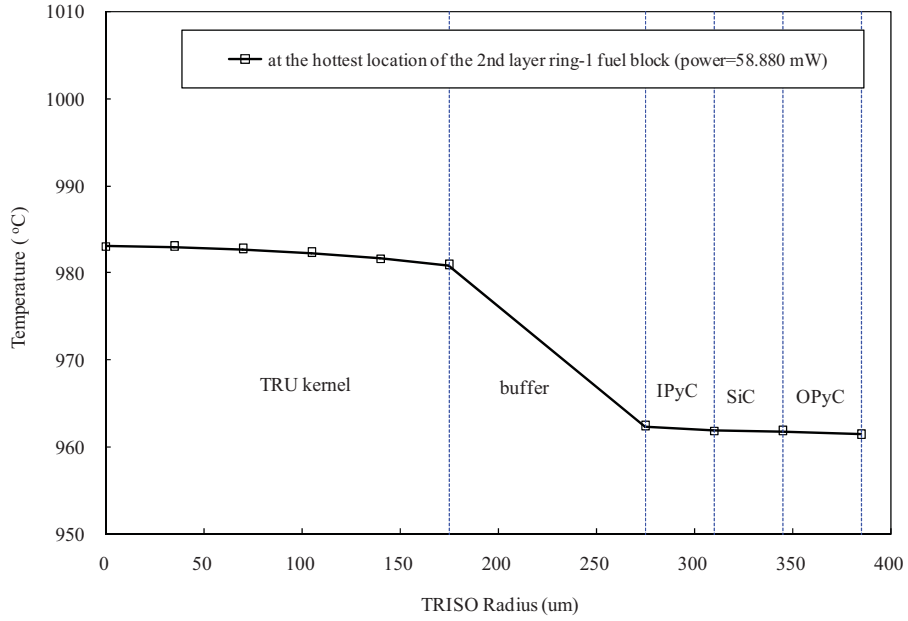

Figure 131. Internal temperature profile of TRISO particle.

6.4.2 Transient Results of LPCC Analysis

6.4.2.1 LPCC Event

The DB-HTR core system must be able to remove the residual heat after shutdown and keep the temperature of all core components (such as the fuel and RPV) below safety design limits during accidents. The accidents assume no credit of the active cooling system like the GT-HTR shutdown cooling system, which has a blower and gas/water heat exchanger with water circulation in the secondary circuit.

In this study, the LPCC event is initiated by rapid coolant loss due to a break in the primary pressure boundary. The LPCC event assumes that the outlet pressure decreases from 7.0 to 0.1 MPa in 10 seconds, and that the reactor trip signal occurs when the pressure is less than 6.24 MPa. The decay power load and the VCS flow isolation start after 1 second on the reactor trip signal. Under these assumptions, the reactor trip signal occurred at 1.1 seconds after the outlet pressure started to decrease, and the decay power load and the VCS flow isolation started at 2.1 seconds. The RCS flow rapidly decreased in a second and then slowly reached zero in 15 seconds.

Figure 133 shows the heat removal process during LPCC event. The decay power remains higher than the RCCS removal heat for a long time. During this period, the excess power is accumulated in the main core components such as fuel block, reflector, RPV and CB, increasing their temperature. The temperature of the RCCS structures also increases due to the increase of heat transferred through the RPV. After the RCCS heat removal becomes greater than the core decay power, the temperatures begin to decrease slowly. The cross-time between the decay power curve and the RCCS heat removal curve is dependent on the core design and the decay power curve of the fuel compositions. Figure 133 is the result for a TRU of 0.2%UO_2+99.8%($PuO_{1.8}$+NpO_2) +0.6 mole SiC getter with 6.9% PF and for the use of B_4C as the BP.

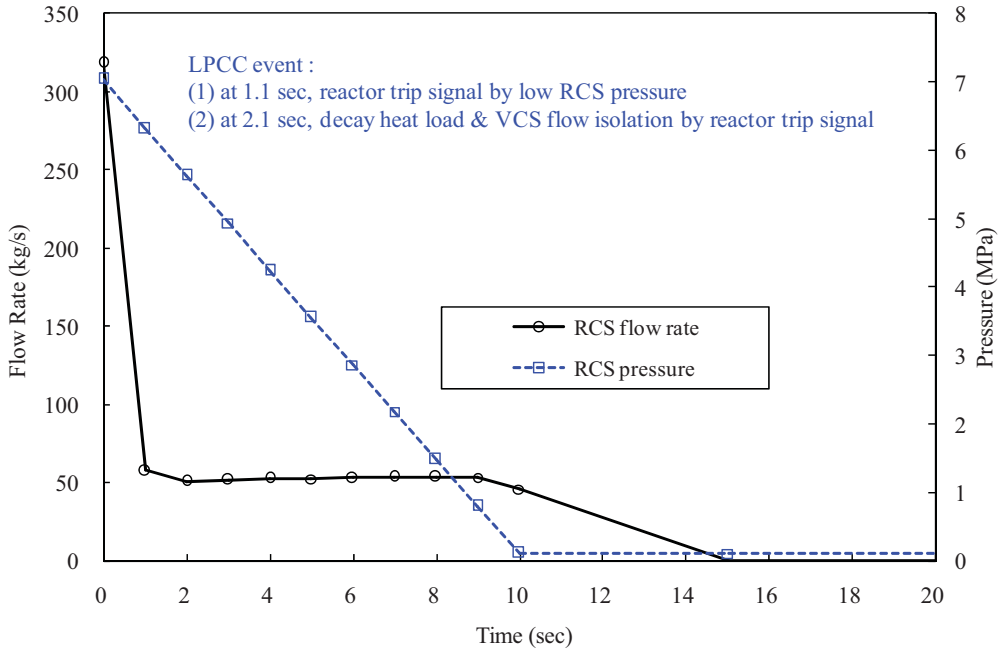

Figure 132. RCS flow rate and pressure changes during LPCC.

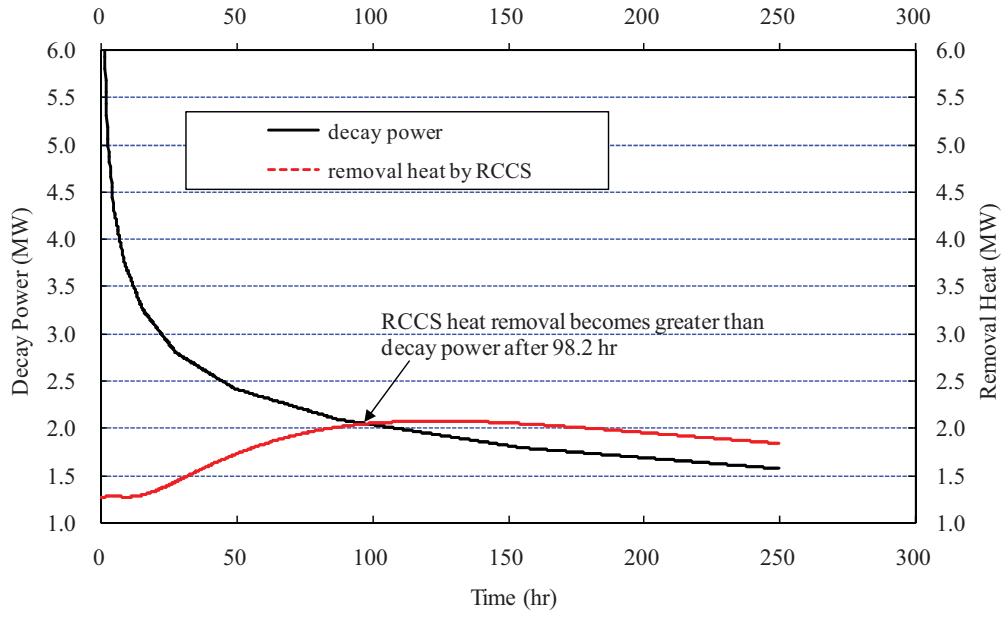

Figure 133. Heat removal process during LPCC.

6.4.2.2 Decay Heat Impact on Peak Fuel Temperature

Figure 134 shows the decay power impact on the peak fuel temperature of the various TRU fuel compositions in a DB-HTR core during LPCC event. As described in Section 6.3.4, the core power distribution and the decay power curve were applied for each TRU fuel composition. These results used the irradiated thermal conductivity of H451 graphite without considering the annealing effect as described in Section 6.3.3.

For a 0.2% UO_2 mixed TRU with the use of B_4C as a BP, the peak fuel temperatures are 1749°C (PF = 4.9%), 1844°C (PF = 5.9%) and 1903°C (PF = 6.9%) at about 105 hours. For a 30% UO_2 mixed TRU with the use of B_4C, the peak fuel temperatures are 1800°C (PF = 7.0%) and 1847°C (PF = 8.0%), which are relatively low due to a small decay power by the reduced amount of ($PuO_{1.8}$+NpO_2), compared to a 0.2% UO_2 mixed TRU. The peak fuel temperature for the use of Er_2O_3 as a burnable poison is much higher than that for the use of B_4C due to the axial power distribution.

Removing the initial Am isotopes and reducing the PF decreases the peak fuel temperature during LPCC event, compared to the TRU of 100%(PuO_2+NpO_2+Am) with 27% PF.[4] The peak fuel temperatures, however, are still higher than the transient fuel design limit of 1600°C[21] due to the lack of heat absorber volume in the central reflector.

Figure 135 shows the peak temperature behavior of the average core block and the RPV during LPCC event for a 0.2% UO_2 mixed TRU with the use of B_4C and 6.9% of PF. The peak temperature of the average core block is 1384°C at 105 hours. The peak temperature of the RPV is 515°C at 129 hours, which is less than the off-normal operation limits of RPV of SA508 steel. The SA533/SA508 steel[14] can be used for a temperature up to 538°C with the duration time limit of 1000 hours. Note that the 1000 hours limit accounts for a total exposure time during the life of a reactor.[13] Appendix B provides all peak temperature results of main core components such as central reflector, side reflector, top reflector, bottom reflector, and RPV for all TRU compositions. It also contains the results with considering the annealing effect of the irradiated thermal conductivity of H451 graphite, which is based on GA method or JAEA method as described in Section 6.3.3.

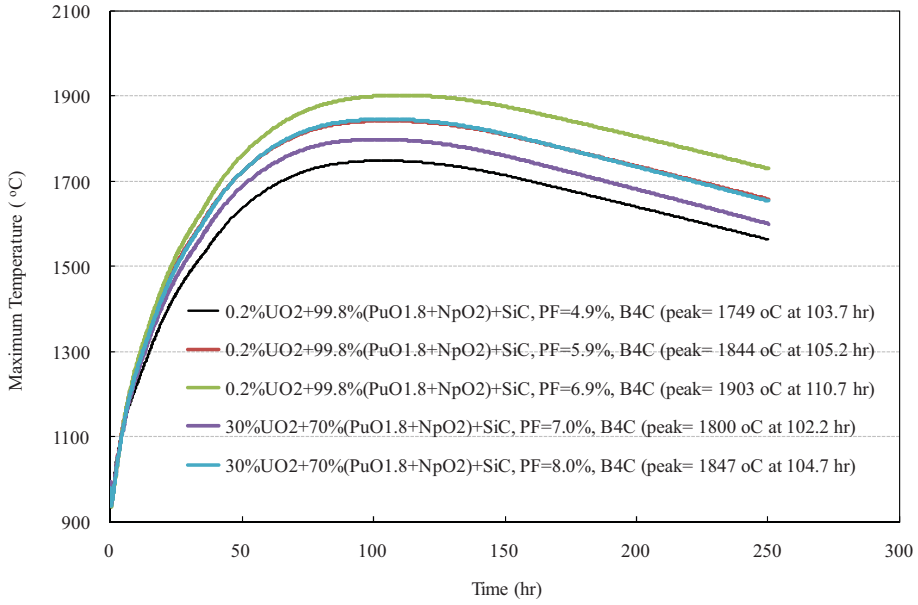

(a) For the use of B_4C as a burnable poison.

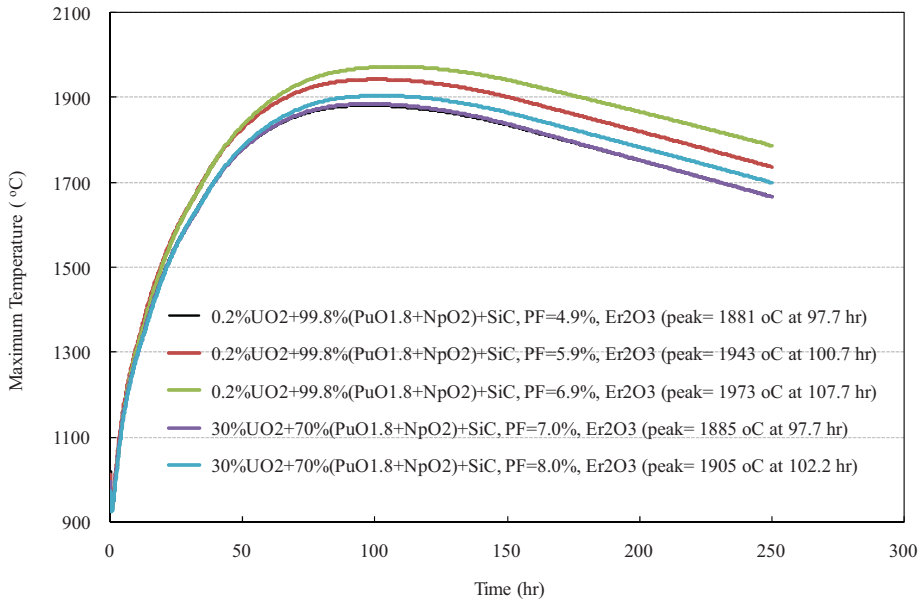

(b) For the use of Er_2O_3 as a burnable poison.

Figure 134. Decay heat impact on peak fuel temperature of the various TRU fuel compositions in a DB-HTR core during LPCC.

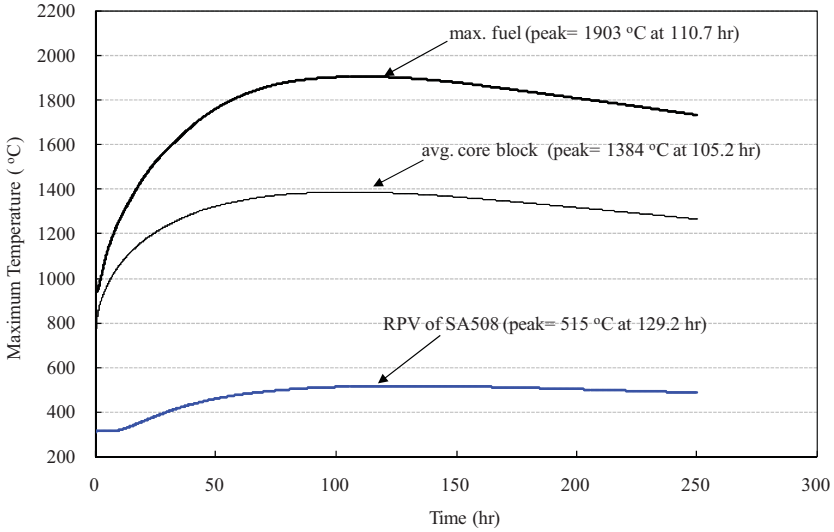

Figure 135. Peak temperatures of main core components during LPCC.

6.4.2.3 Annealing Effect of the Graphite on Peak Fuel Temperature

The effect of considering annealing of the irradiated graphite on the peak fuel temperature during LPCC is evaluated by using two kinds of correction factor for the graphite thermal conductivity, the GA method[8] and JAEA method[9] as described in Section 6.3.3. The results for all TRU compositions are listed in Subsection 6.7, and this section describes the results only for a TRU of 0.2%UO_2+99.8%($PuO_{1.8}$+ NpO_2)+0.6 mole SiC getter with 6.9% PF.

As shown in Figure 136, the peak fuel temperatures for the use of B_4C as a BP are estimated as 1903°C (No annealing), 1897°C (JAEA method), and 1685°C (GA method). The peak fuel temperatures for the use of Er_2O_3 as a burnable poison are also estimated as 1973°C (No annealing), 1953°C (JAEA method), and 1733°C (GA method). The decrease of peak fuel temperature for the application of JAEA annealing factor is about 6°C (B_4C) and 20°C (Er_2O_3), compared to the peak fuel temperature for the non-annealing effect. But, the decrease of peak fuel temperature for the application of GA annealing factor is about 212°C (B_4C) and 220°C (Er_2O_3).

It seems that the annealing effect of GA method is too high and is not realistic. In the simpler GA model, the temperature-dependent annealing correction factor begins to recover the thermal conductivity at 1000°C and reaches the un-irradiated thermal conductivity completely at 1300°C, and the thermal conductivity of all fuel blocks is almost completely recovered to the un-irradiated level during the LPCC event. As described in Section 6.3.3, GA method is useful only to low fast-neutron fluence and low-irradiation temperature condition. The irradiation temperature at the steady state is less than 1000°C, but it appears that the fast-neutron fluences for core ($3.0x10^{21}$ n/cm^2) and reflector graphites ($1.0x10^{21}$ n/cm^2) could be too high to apply the GA method.

Based on JAEA method, which is dependent on fast-neutron fluence, annealing temperature, and irradiation temperature, the peak fuel temperature is highly affected by the degradation of thermal conductivity due to the amount of fast-neutron fluence damage rather than the annealing temperature and the irradiation temperature. Thus, it seems that the detailed data of fast-neutron fluence distribution in DB-HTR core will be needed for more precise prediction of the peak fuel temperature.

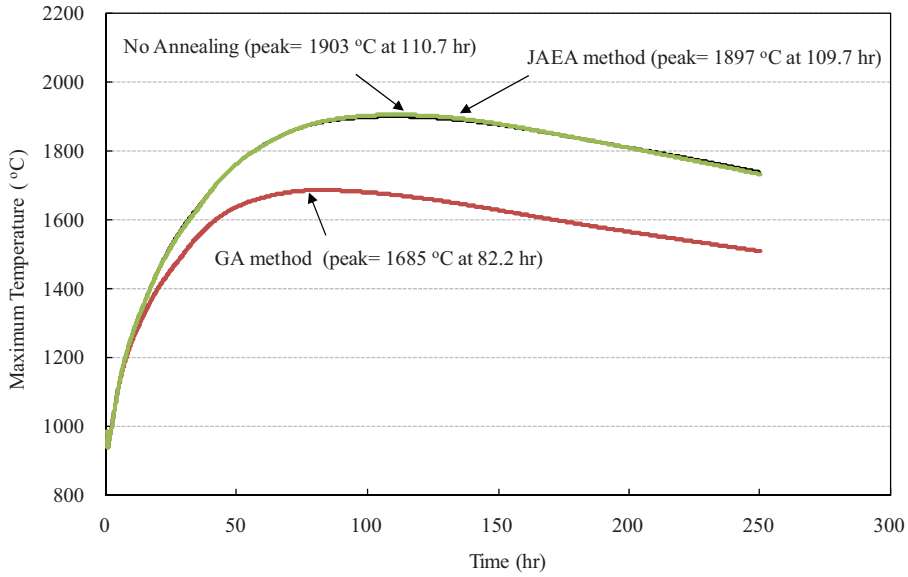

(a) For the use of B_4C as a burnable poison,

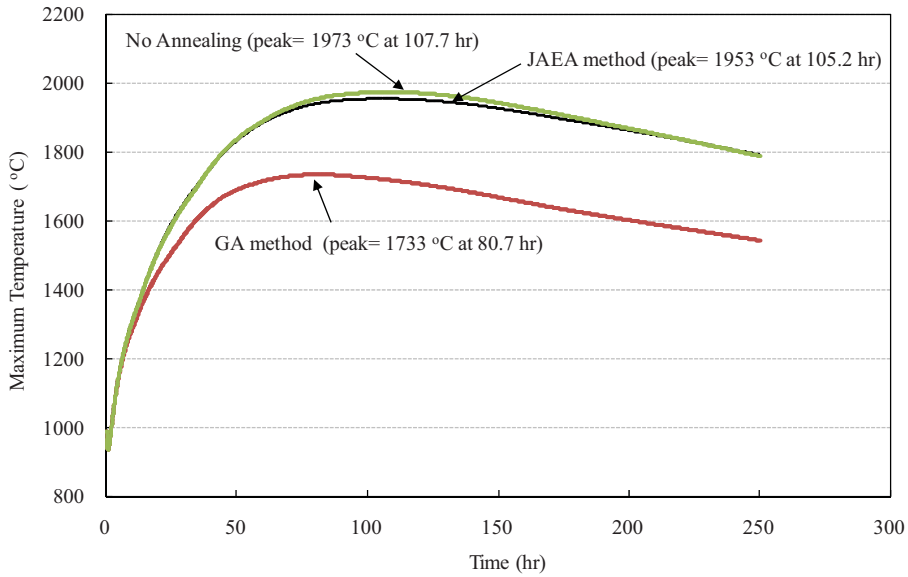

(b) For the use of Er_2O_3 as a burnable poison.

Figure 136. Annealing effect of the graphite on peak fuel temperature.

6.4.3 Power Level Optimization

6.4.3.1 The Maximum Power of 450 MW_{th} for a DB-HTR Core

Based on the above results of the various TRU fuel compositions, it is clear that the 600 MW_{th} DB-HTR core will not be satisfied with the design requirement of passive safety performance. The passive safety performance may be achieved by optimizing the DB-HTR core design through two possible design approaches. One is changing the geometry of the DB-HTR to keep the reactor power by increasing the diameters of the central reflector and core barrel. The other is decreasing the reactor power to keep the geometry of the reference DB-HTR. It seems that the modification of the geometry of the DB-HTR would require additional time to evaluate the new design. Thus, this report intends to provide the analysis results just for the allowable maximum power of DB-HTR core to the accident fuel design limit.

Based on the several sensitivity calculations, the allowable maximum power reactor is estimated to be a 450 MW_{th} for a TRU of 0.2%UO_2+99.8%($PuO_{1.8}$+NpO_2)+0.6 mole SiC getter (PF=6.9%) and a TRU of 30%UO_2+70%($PuO_{1.8}$+NpO_2)+0.6 mole SiC getter (PF=8.0%). The mixed of B_4C and Er_2O_3 is considered as the BP to avoid the positive power coefficient in low power level for the use of B_4C, and to get more the cycle length day than that for the use of Er_2O_3 as a BP.

Figure 137 and Figure 138 show the axial power distributions for 0.2% UO_2 mixed TRU (PF = 6.9%) and 30% UO_2 mixed TRU (PF = 8.0%), respectively. This analysis uses two kinds of the axial power distribution for each TRU fuel, using 18 axial nodes and 72 axial nodes, respectively. The axial power distribution for 18 nodes looks like smooth averaged profile due to two nodes for a FB. On the other hand, the axial power distribution for 72 nodes shows the detailed power peaking factor at the end of fuel block, where the local power becomes high due to high neutron moderating by the graphite zone as shown in Figure 106 (a). The ring-3 FA produces very sharp power peak, compared to the other rings. It is caused by the fact that the power difference in the adjacent fuel blocks is large because the ring-3 FA uses only the axial shuffling scheme. It is also caused by the fact that the effect of the FB graphite zone is relatively higher than other ring fuel blocks because the ring-3 FA is far away from the dominant reflector zone of central and side reflectors. This analysis intends to provide the impact of FB end-flux-peaking on the peak fuel temperature during LPCC event.

The peak fuel temperature is evaluated by using JAEA method because GA method of the annealing effect is not applicable to this analysis as described in Section 6.4.2.3.

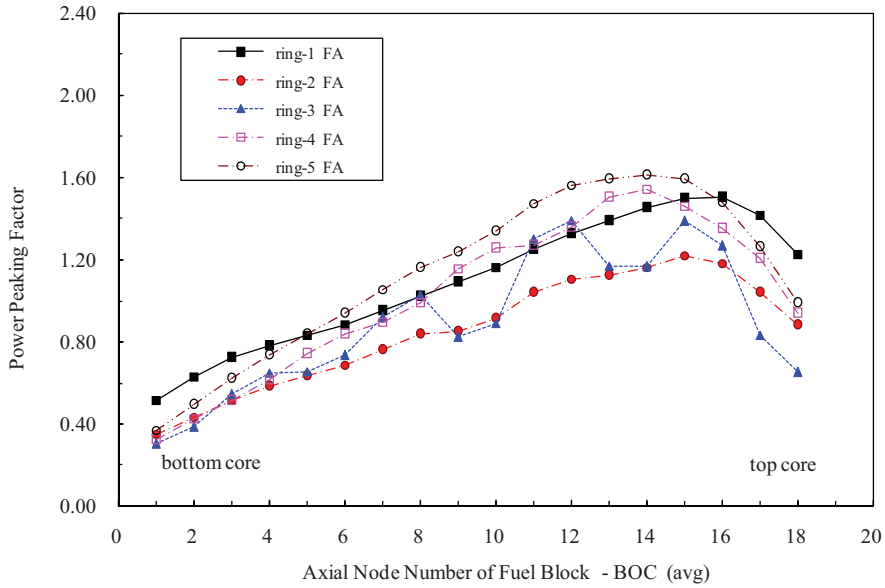

(a) For 18 nodes.

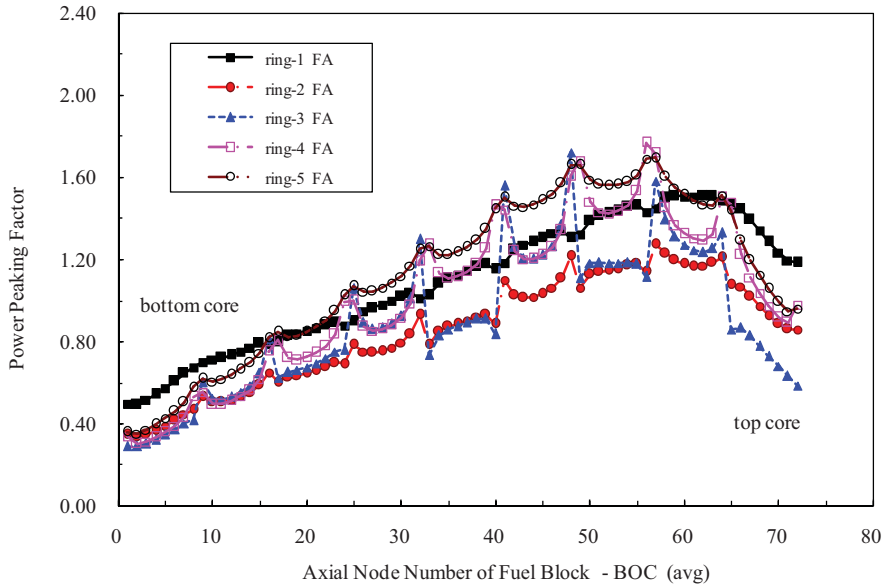

(b) For 72 nodes.

Figure 137. Axial power distribution of 450 MW_{th} DB-HTR core for 0.2% UO_2 mixed TRU (PF = 6.9%) using B_4C and Er_2O_3 as a burnable poison.

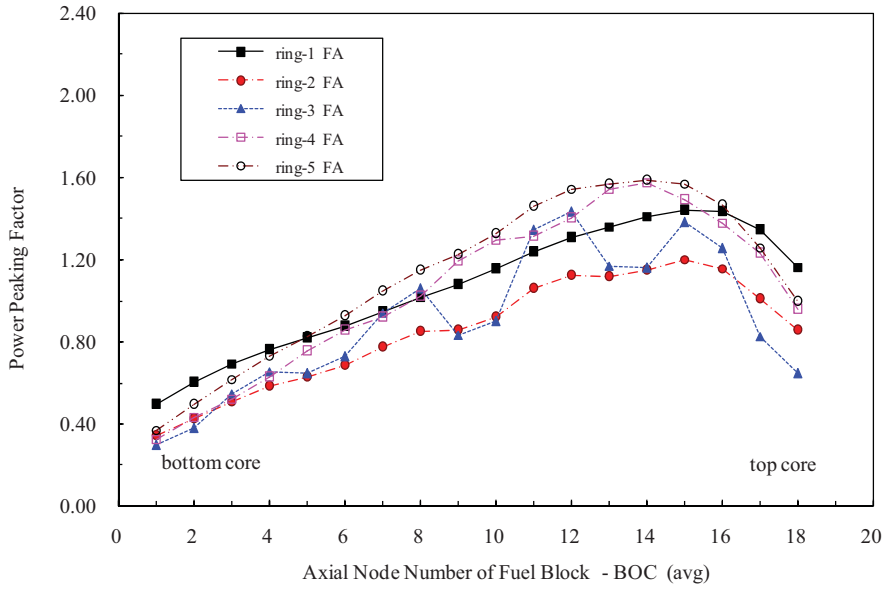

(a) For 18 nodes.

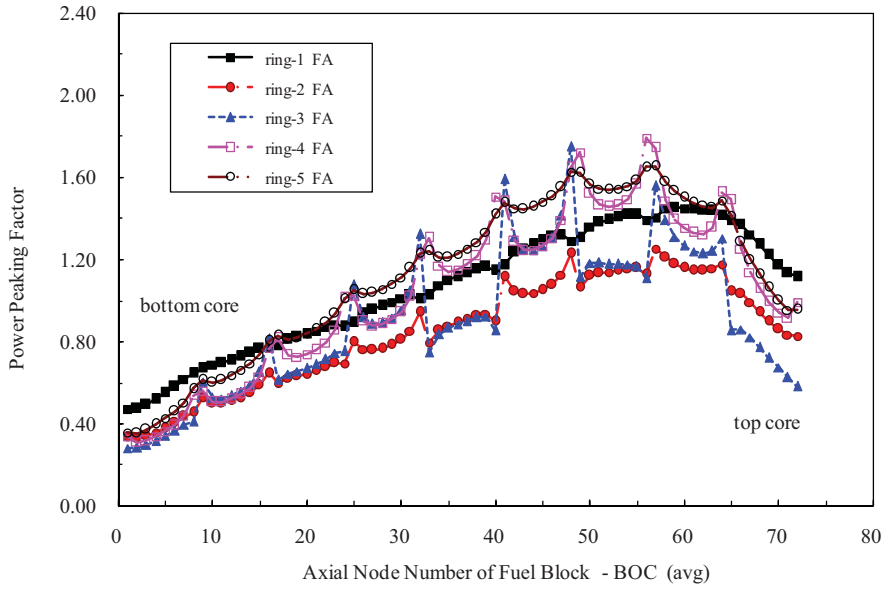

(b) for 72 nodes

Figure 138. Axial Power Distribution of 450 MW_{th} DB-HTR Core for 30%UO_2 mixed TRU (PF=8.0%) using B_4C and Er_2O_3 as a burnable poison

6.4.3.2 Peak Fuel Temperature for 450 MW_{th} DB-HTR Core

Figure 139 and Figure 140 show the peak fuel temperature behavior during LPCC event in 450 MW_{th} DB-HTR core for a 0.2% UO_2 mixed TRU (PF = 6.9%) and a 30% UO_2 mixed TRU (PF = 8.0%), respectively.

For a 0.2% UO_2 mixed TRU (PF = 6.9%), the peak fuel temperature is 1604°C for the use of 72 nodes and 1601°C for the use of 18 nodes without considering the annealing effect of the graphite thermal conductivity. Based on JAEA method of the annealing effect, the peak fuel temperature is estimated to be 1599°C for the use of 72 nodes and 1596°C for the use of 18 nodes. It shows that the estimated peak fuel temperatures are very close to the transient fuel design limit of 1600°C within ±4°C. The FB end-flux-peaking provides about 3°C higher peak fuel temperature.

For a 30% UO_2 mixed TRU (PF = 8.0%), the peak fuel temperature is 1557°C for the use of 72 nodes and 1553°C for the use of 18 nodes without considering the annealing effect of the graphite thermal conductivity. Based on JAEA method of the annealing effect, the peak fuel temperature is estimated to be 1553°C for the use of 72 nodes and 1549°C for the use of 18 nodes. In this case, all of the estimated peak fuel temperatures are less than the transient fuel design limit of 1600°C. It also provides about 4°C higher peak fuel temperature due to the FB end-flux-peaking.

Such a small impact of the FB end-flux-peaking is mainly caused by the fact that the peak fuel temperature is highly dependent on the axial power distribution of ring-1 FA where the hot spot occurs during LPCC event. As shown in Figure 137 and Figure 138, the FB end-flux-peaking of ring-1 FA is very small because the adjacent central reflector dominantly affects the power distribution, compared to the small part of the FB graphite zone.

Alternatively, the maximum fuel temperature of a 0.2% UO_2 mixed TRU (PF = 6.9%) at the steady state occurs at ring-5 FA and is decreased from 966°C for 18 nodes (Z = 3.569 m) to 961°C for 72 nodes (Z = 3.403 m). Based on the CFD calculations using the unit cell model,[22] it was evaluated that the hot spot fuel temperature at the steady state was increased by 21°C due to the impact of the sharp power peak such as the FB end-flux-peaking in the ring-3 FA.

Therefore, it can be expected that the impact of the FB end-flux-peaking on the peak fuel temperature is not significant and the calculation results using coarse mesh (18 nodes) are proper in this analysis.

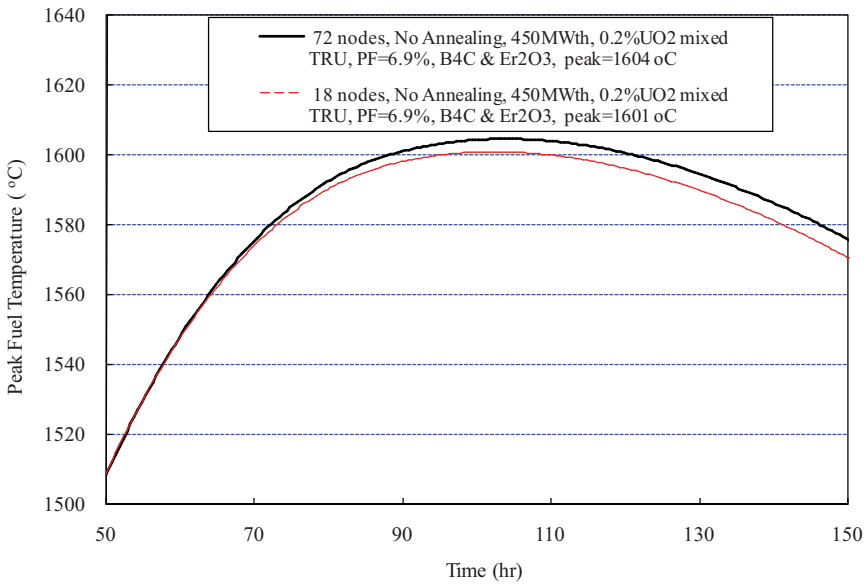

(a) For the use of no annealing method.

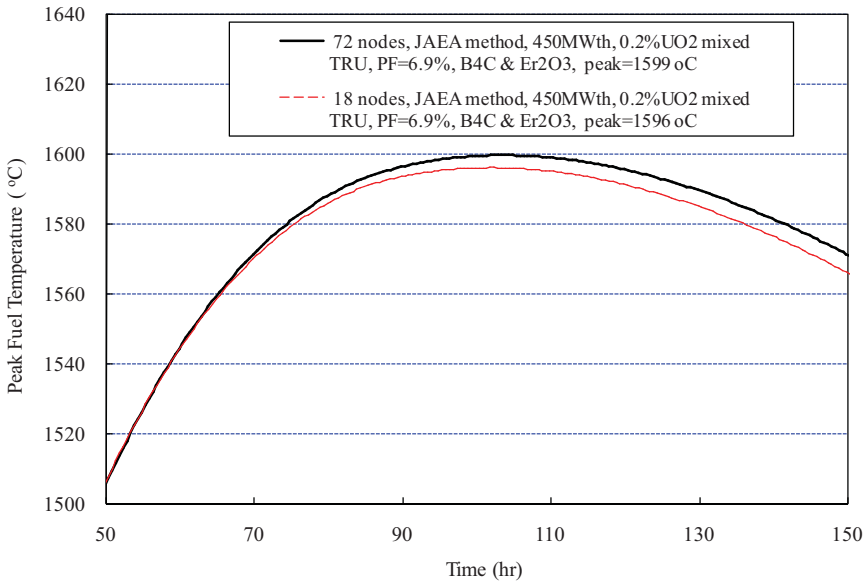

(b) For the use of JAEA method.

Figure 139. Peak fuel temperature of 0.2% UO_2 mixed TRU (PF = 6.9%) during LPCC event in 450 MW_{th} DB-HTR core.

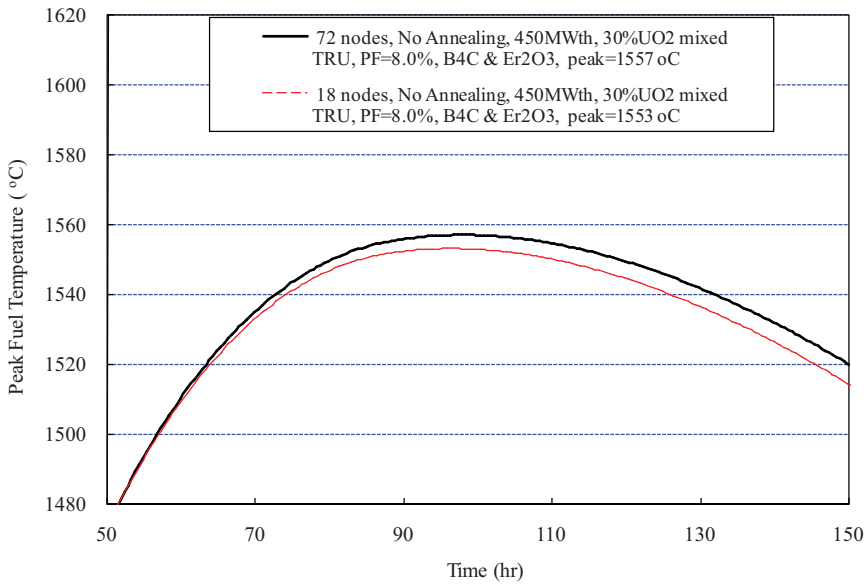

(a) For the use of no annealing method.

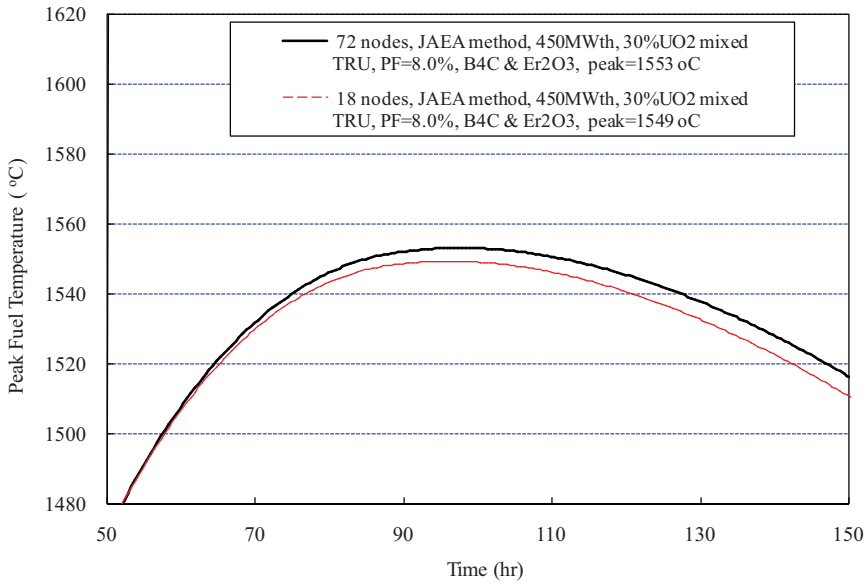

(b) For the use of JAEA method.

Figure 140. Peak fuel temperature of 30% UO_2 mixed TRU (PF = 8.0%) during LPCC event in 450 MW_{th} DB-HTR core.

6.5 Summary of the Results

- The thermal-fluid and safety of the 600 MW_{th} DB-HTR system was analyzed to investigate the feasibility of the DB-HTR being a candidate for a thermal-fluid design at the steady state, and achieving passive safety performance during an LPCC event by using the GAMMA+ code.
- Key design characteristics of the DB-HTR core are more fuel rings (five fuel-rings), less central reflectors (three rings) and the decay power curves due to the TRU fuel compositions that are different from the UO_2 fuel.
- At the steady state, average 88.7%, 7.1%, and 4.2% of total RCS flow go to the coolant channel, the CR/RSC hole and the FA bypass gap, respectively. It shows that the maximum fuel and RPV temperatures are less than the normal operation limit of 1250°C for TRISO fuel and the SA508 steel limit of 371°C, respectively.
- For a TRU of 100%(PuO_2+NpO_2+Am) with 27% PF, the peak fuel temperature during LPCC event is much higher than the transient fuel design limit of 1600°C, due to a lack of heat absorber in the central reflector as well as to the increased decay power of the TRU fuel compositions.
- For a 0.2% UO_2 mixed or a 30% UO_2 mixed TRU, the reduced decay power obtained by removing the initial Am isotopes and by reducing the PF decreases the peak fuel temperature. However, the peak fuel temperatures are still higher than 1600°C due to the lack of heat absorber volume in the central reflector.
- The 450 MW_{th} DB-HTR core is suggested as the optimization core design, which has the allowable maximum power reactor of a 450 MW_{th} to the accident fuel design limit for 0.2% UO_2 mixed TRU (PF = 6.9%) or 30% UO_2 mixed TRU (PF = 8.0%) using the mixed BP of B_4C and Er_2O_3.
- Based on JAEA method, the effect of graphite annealing on the peak fuel temperature is small. The GA method indicates a much larger impact, but it may not be applicable to the fluence and temperature conditions of the HTR. In addition, it shows that the impact of the FB end-flux-peaking on the peak fuel temperature is not significant.

6.6 All Figure Data of Core Temperature Distribution at the Steady State

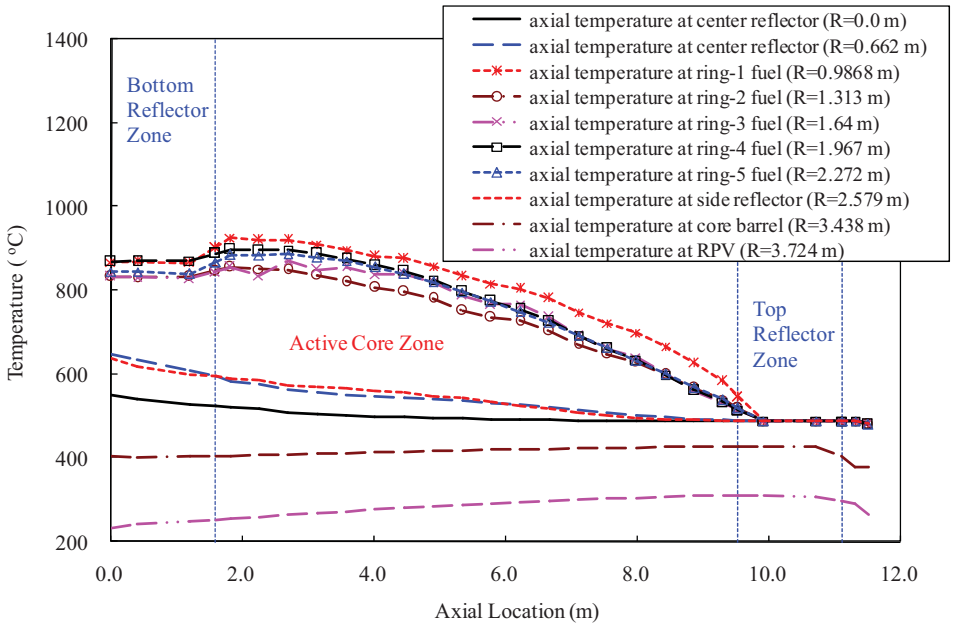

Figure 141. Axial temperature (PF = 4.9%, B_4C) for 0.2%UO_2 + 99.8%($PuO_{1.8}$, NpO_2) + 0.6 mole SiC getter.

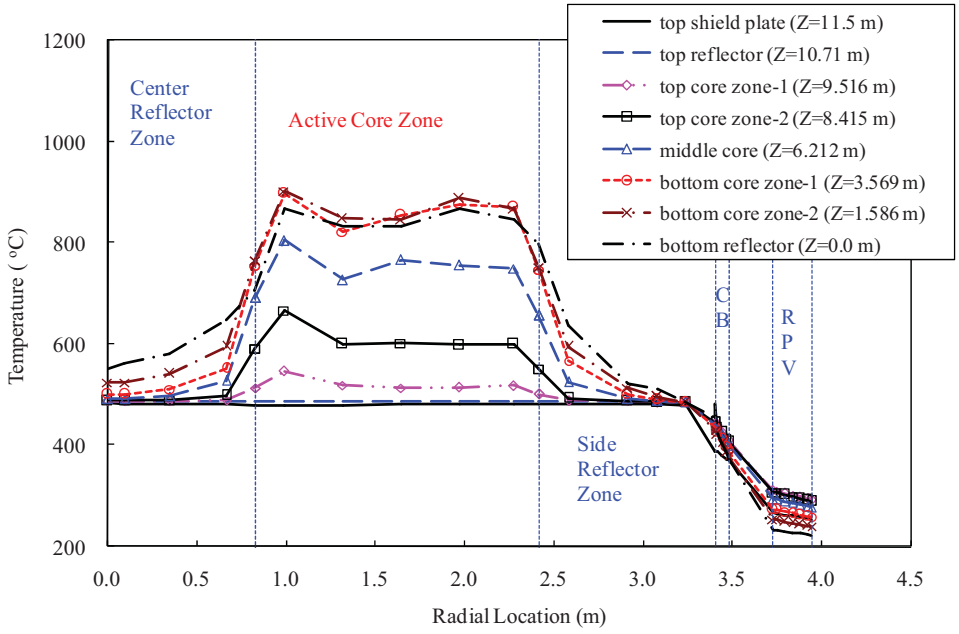

Figure 142. Radial temperature (PF = 4.9%, B_4C) for 0.2%UO_2 + 99.8%($PuO_{1.8}$, NpO_2) + 0.6 mole SiC getter.

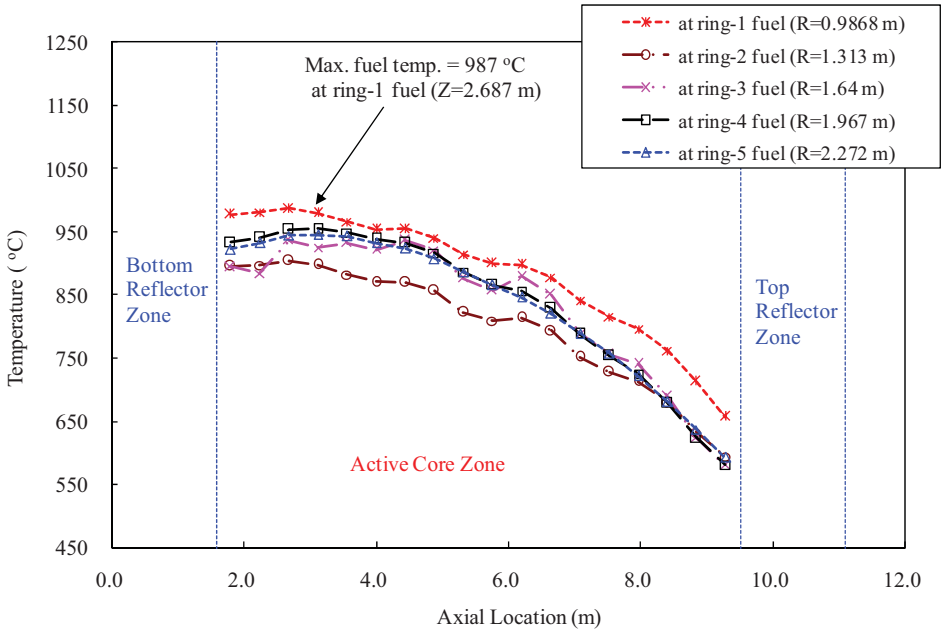

Figure 143. Maximum fuel temperature (PF = 4.9%, B_4C) for 0.2%UO_2 + 99.8%($PuO_{1.8}$, NpO_2) + 0.6 mole SiC getter.

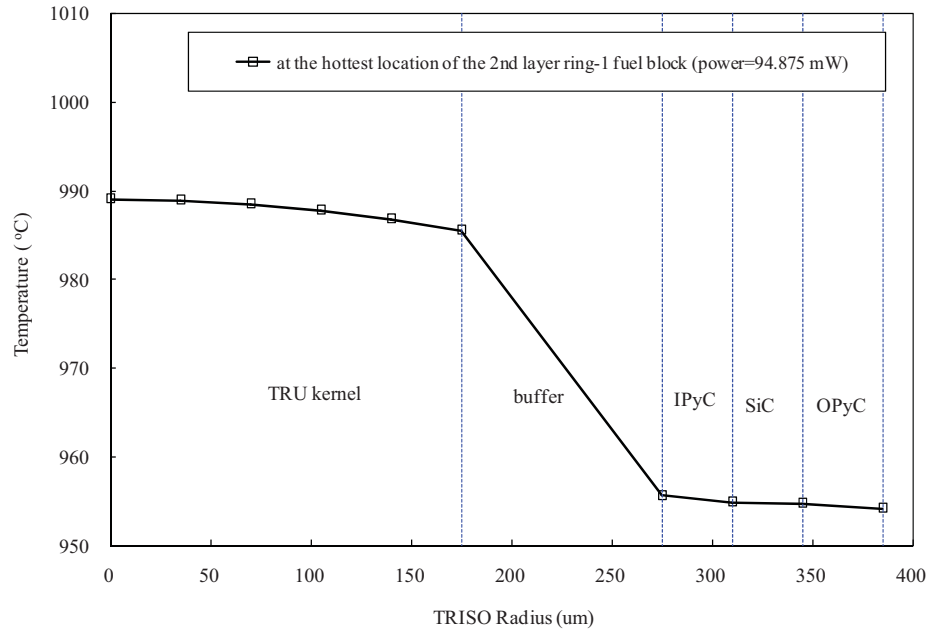

Figure 144. Internal temperature profile of TRISO particle (PF = 4.9%, B_4C) for 0.2%UO_2 + 99.8%($PuO_{1.8}$, NpO_2) + 0.6 mole SiC getter.

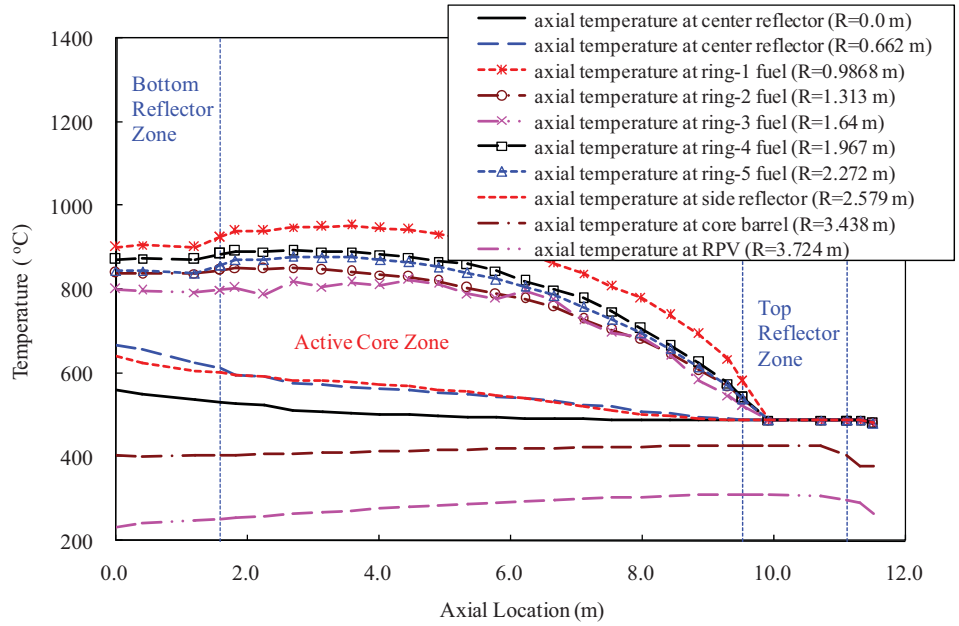

Figure 145. Axial temperature (PF = 4.9%, Er_2O_3) for 0.2%UO_2 + 99.8%($PuO_{1.8}$, NpO_2) + 0.6 mole SiC getter.

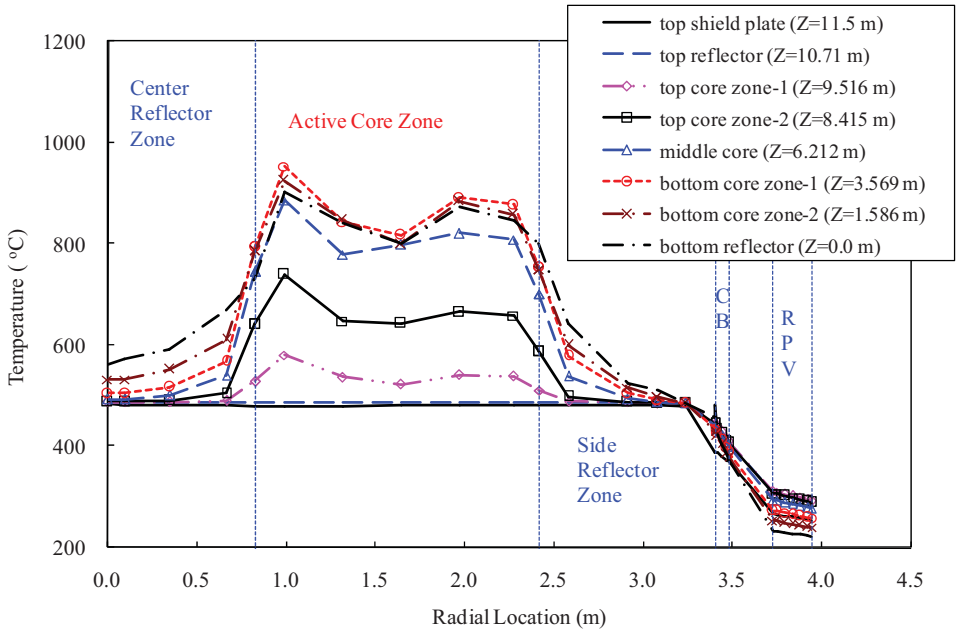

Figure 146. Radial temperature (PF = 4.9%, Er_2O_3) for 0.2%UO_2 + 99.8%($PuO_{1.8}$, NpO_2) + 0.6 mole SiC getter.

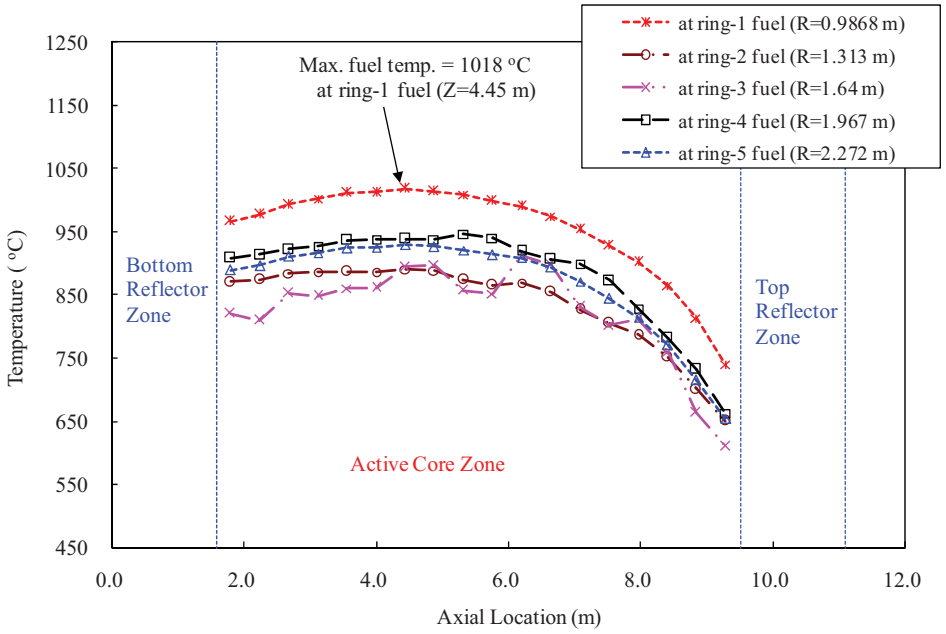

Figure 147. Maximum fuel temperature (PF = 4.9%, Er_2O_3) for 0.2%UO_2 + 99.8%($PuO_{1.8}$, NpO_2) + 0.6 mole SiC getter.

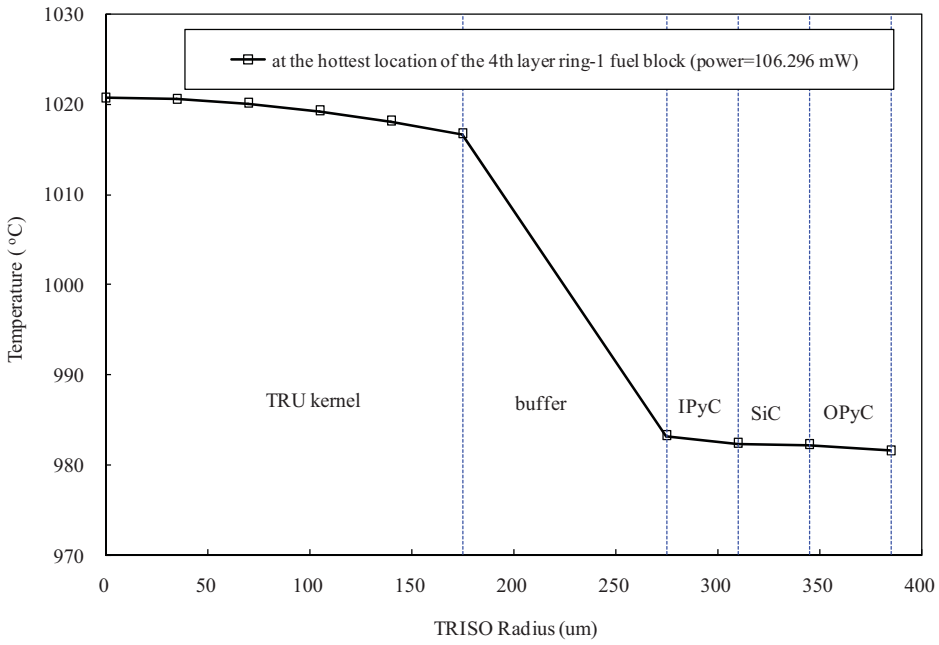

Figure 148. Internal temperature profile of TRISO particle (PF = 4.9%, Er_2O_3) for 0.2%UO_2 + 99.8%($PuO_{1.8}$, NpO_2) + 0.6 mole SiC getter.

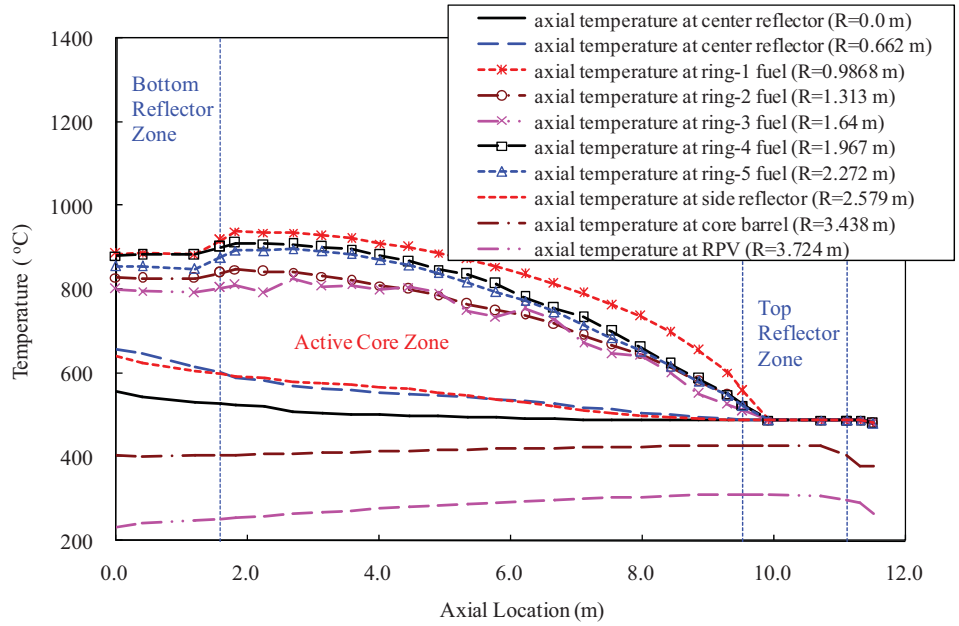

Figure 149. Axial temperature (PF = 5.9%, B_4C) for 0.2%UO_2 + 99.8%($PuO_{1.8}$, NpO_2) + 0.6 mole SiC getter.

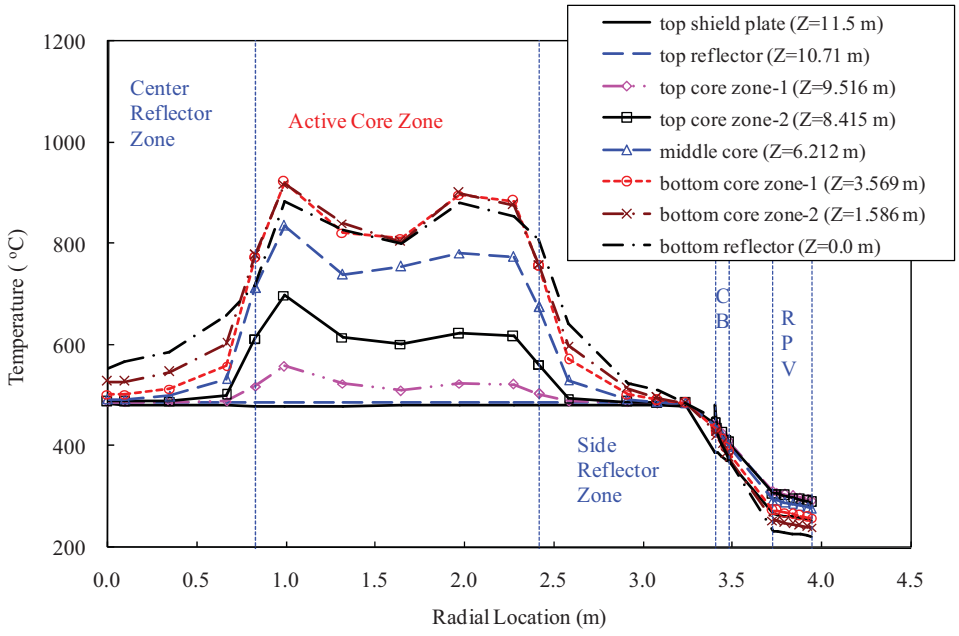

Figure 150. Radial temperature (PF = 5.9%, B_4C) for 0.2%UO_2 + 99.8%($PuO_{1.8}$, NpO_2) + 0.6 mole SiC getter.

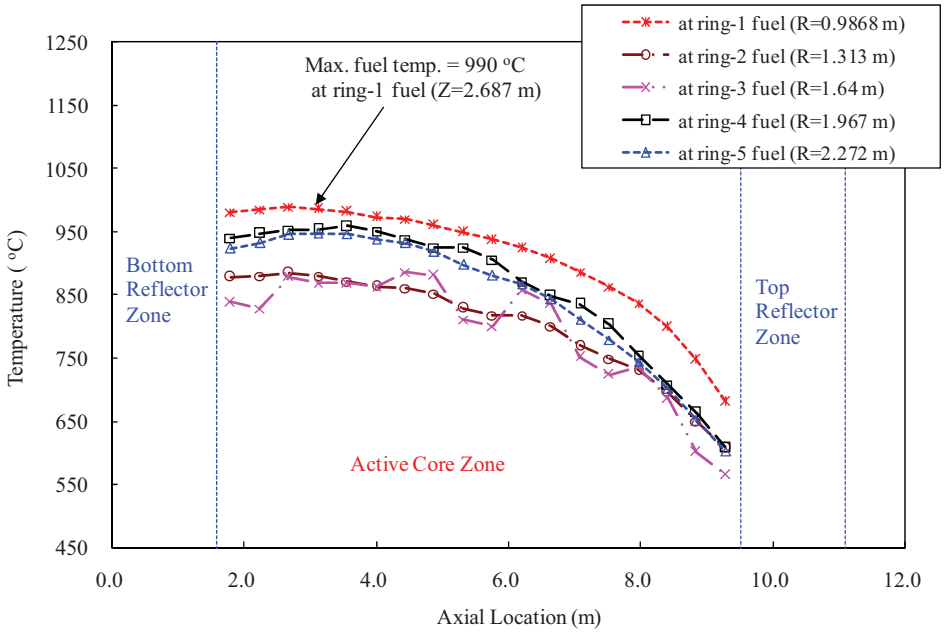

Figure 151. Maximum fuel temperature (PF = 5.9%, B_4C) for 0.2%UO_2 + 99.8%($PuO_{1.8}$, NpO_2) + 0.6 mole SiC getter.

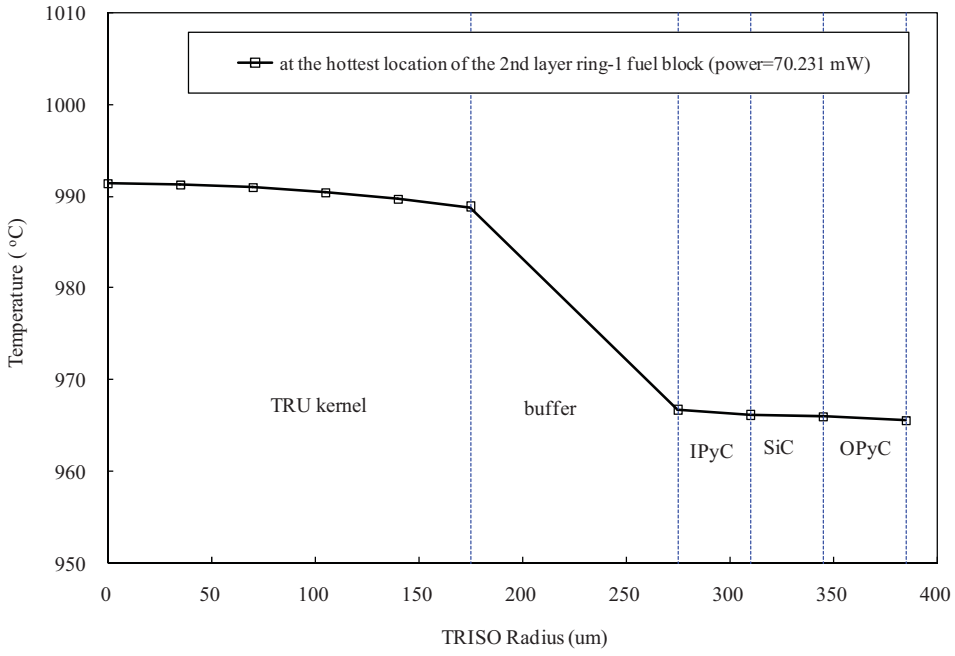

Figure 152. Internal temperature profile of TRISO particle (PF = 5.9%, B_4C) for 0.2%UO_2 + 99.8%($PuO_{1.8}$, NpO_2) + 0.6 mole SiC getter.

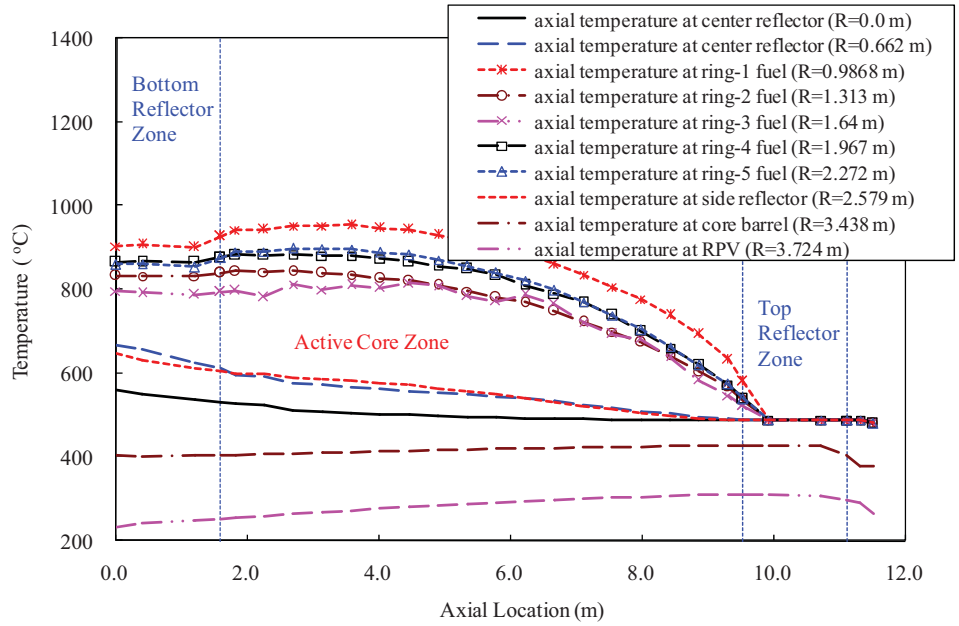

Figure 153. Axial temperature (PF = 5.9%, Er_2O_3) for 0.2%UO_2 + 99.8%($PuO_{1.8}$, NpO_2) + 0.6 mole SiC getter.

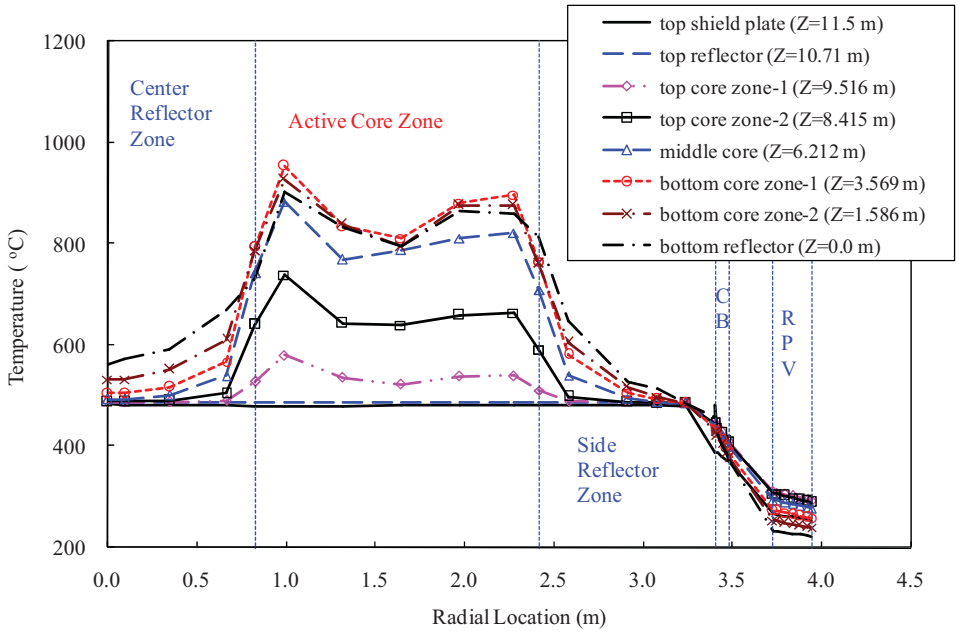

Figure 154. Radial temperature (PF = 5.9%, Er_2O_3) for 0.2%UO_2 + 99.8%($PuO_{1.8}$, NpO_2) + 0.6 mole SiC getter.

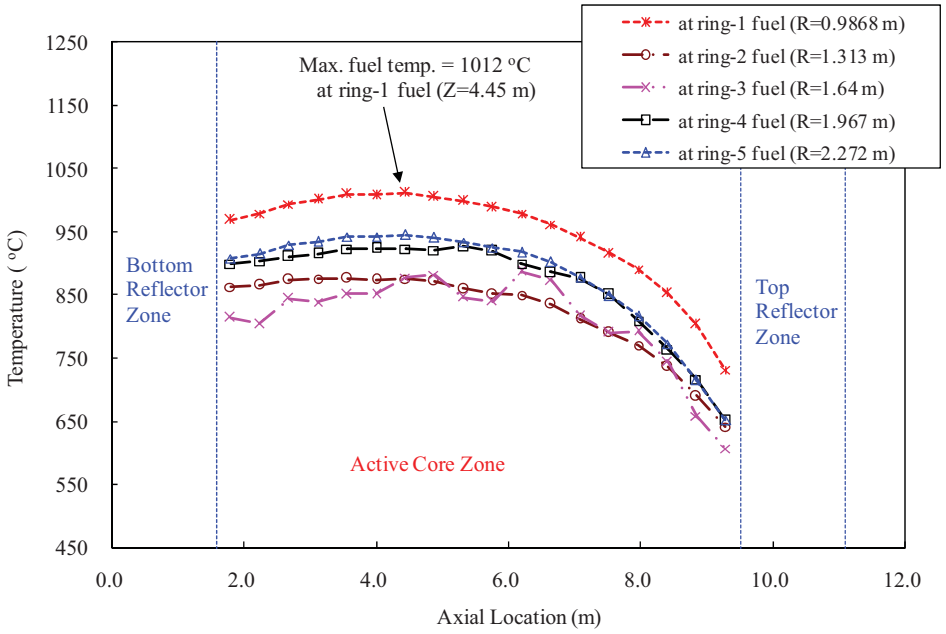

Figure 155. Maximum fuel temperature (PF = 5.9%, Er_2O_3) for 0.2%UO_2 + 99.8%($PuO_{1.8}$, NpO_2) + 0.6 mole SiC getter.

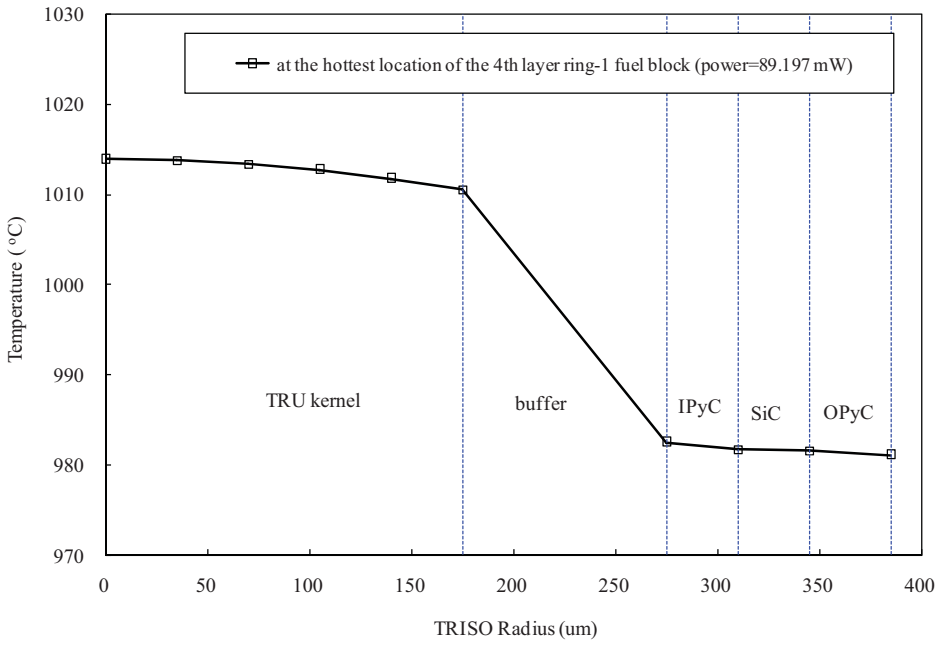

Figure 156. Internal temperature profile of TRISO particle (PF = 5.9%, Er_2O_3) for 0.2%UO_2 + 99.8%($PuO_{1.8}$, NpO_2) + 0.6 mole SiC getter.

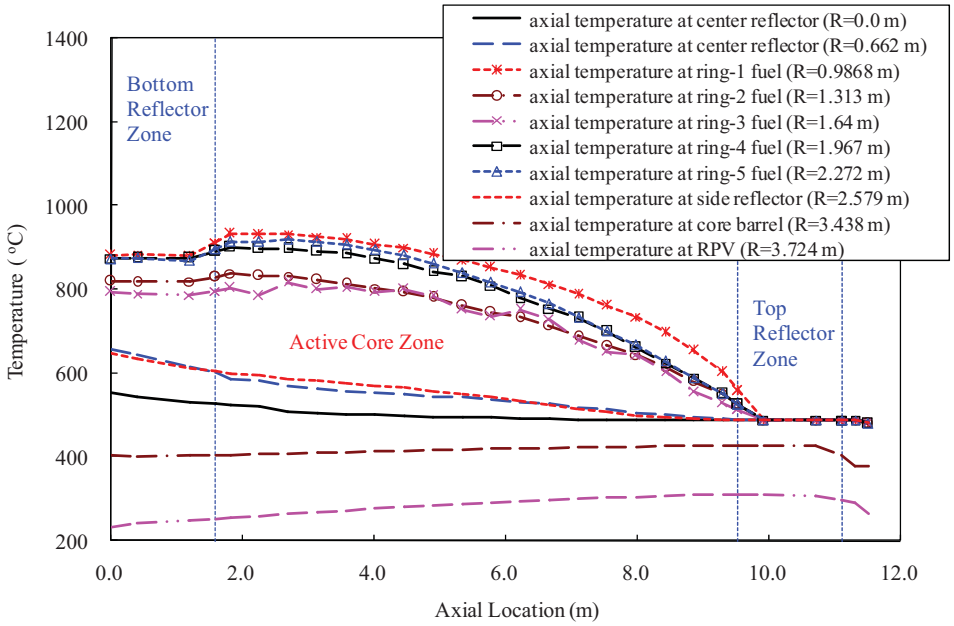

Figure 157. Axial temperature (PF = 6.9%, B_4C) for 0.2%UO_2 + 99.8%($PuO_{1.8}$, NpO_2) + 0.6 mole SiC getter.

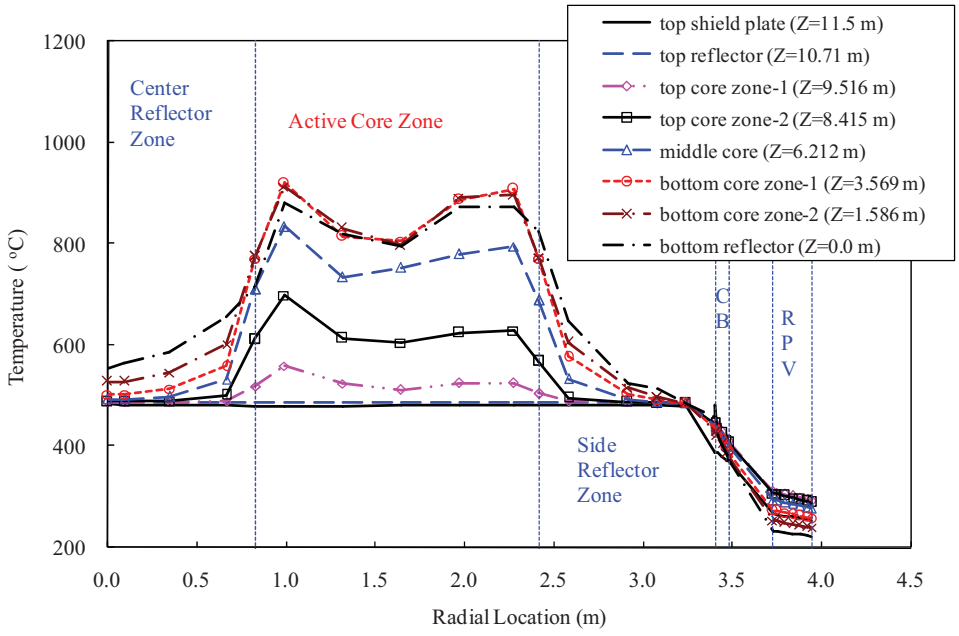

Figure 158. Radial temperature (PF = 6.9%, B_4C) for 0.2%UO_2 + 99.8%($PuO_{1.8}$, NpO_2) + 0.6 mole SiC getter.

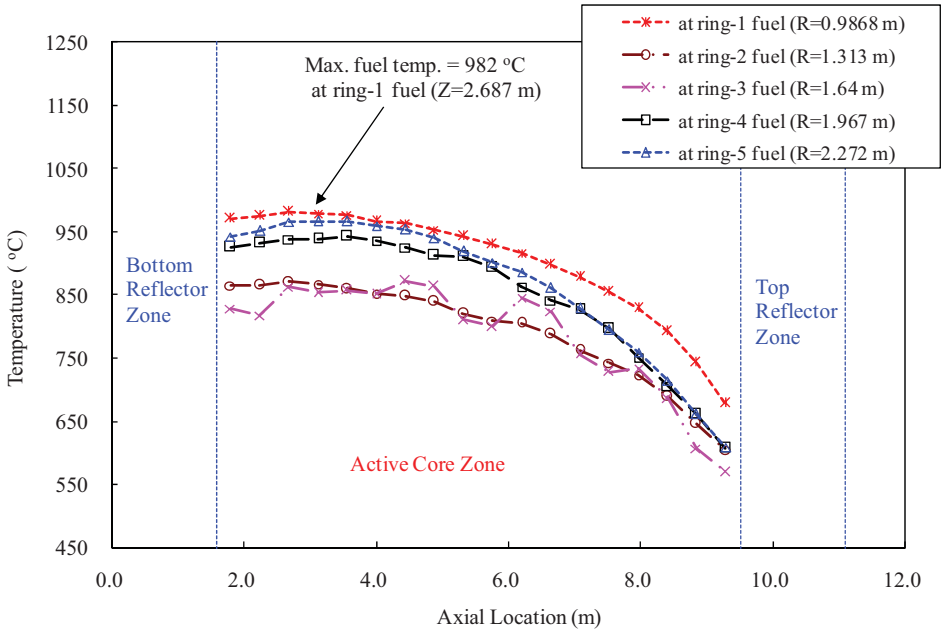

Figure 159. Maximum fuel temperature (PF = 6.9%, B_4C) for 0.2%UO_2 + 99.8%($PuO_{1.8}$, NpO_2) + 0.6 mole SiC getter.

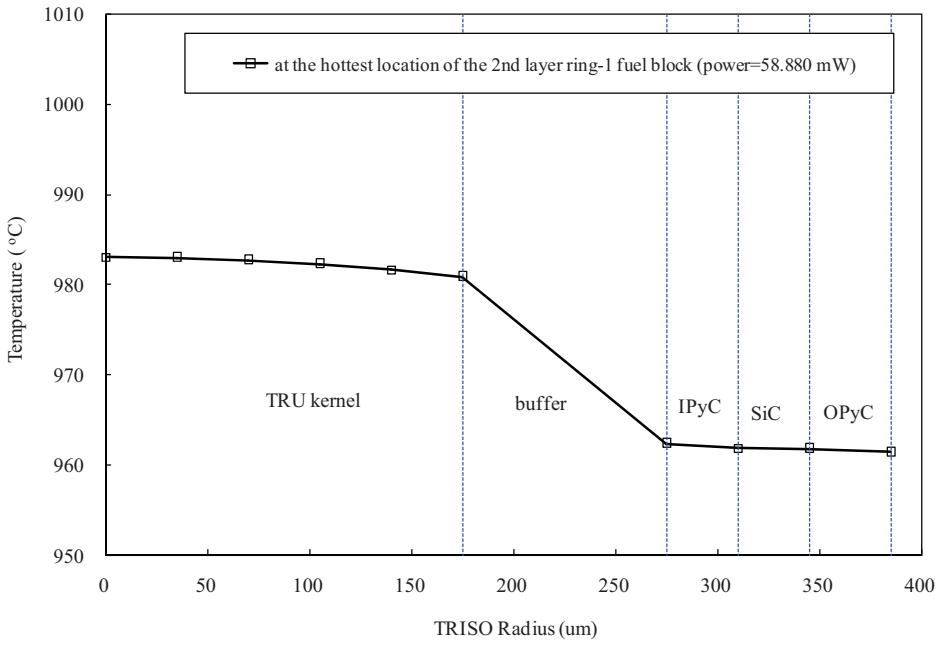

Figure 160. Internal temperature profile of TRISO particle (PF = 6.9%, B_4C) for 0.2%UO_2 + 99.8%($PuO_{1.8}$, NpO_2) + 0.6 mole SiC getter.

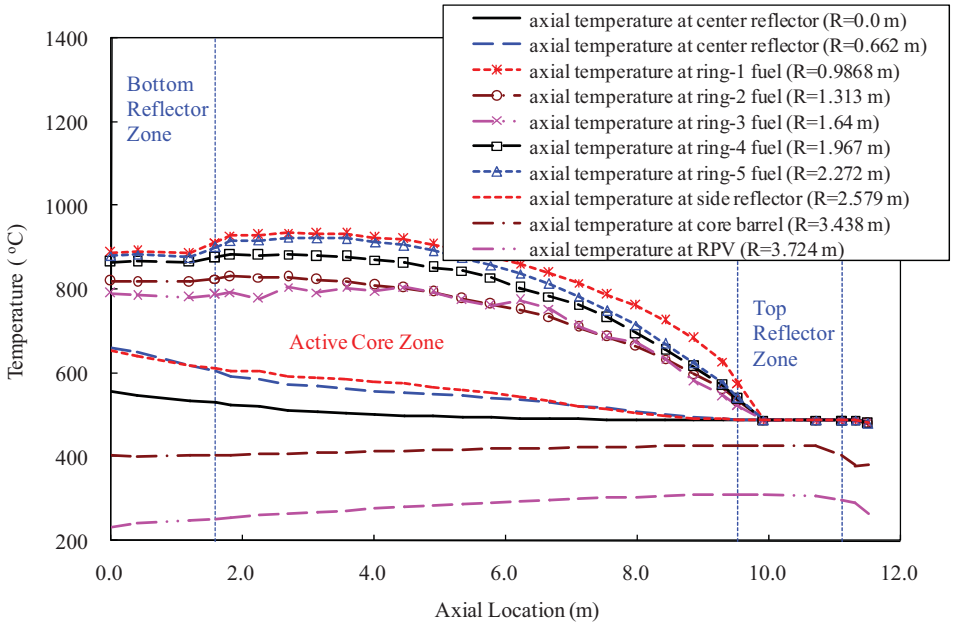

Figure 161. Axial temperature (PF = 6.9%, Er_2O_3) for 0.2%UO_2 + 99.8%($PuO_{1.8}$, NpO_2) + 0.6 mole SiC getter.

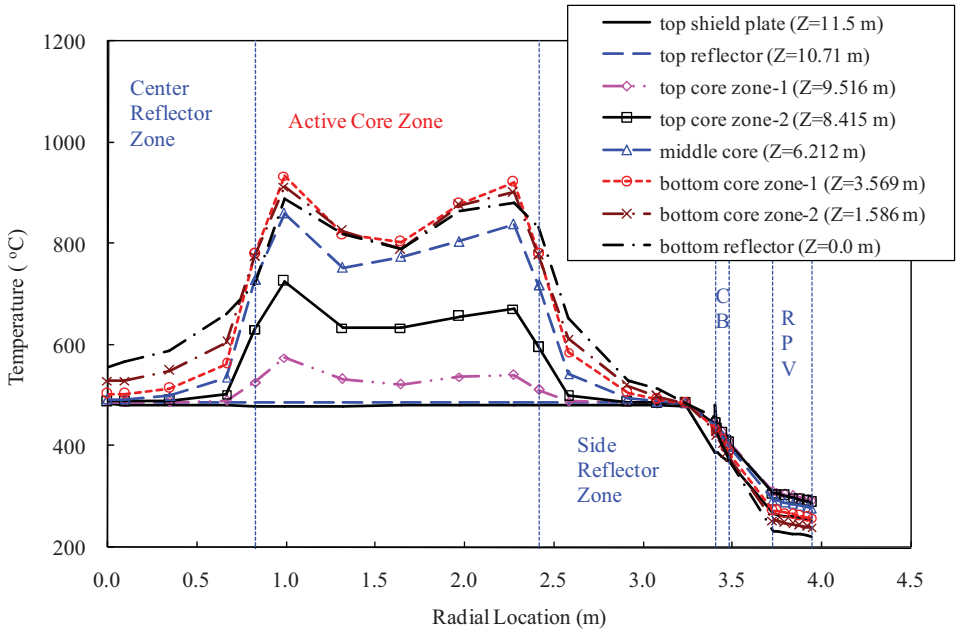

Figure 162. Radial temperature (PF = 6.9%, Er_2O_3) for 0.2%UO_2 + 99.8%($PuO_{1.8}$, NpO_2) + 0.6 mole SiC getter.

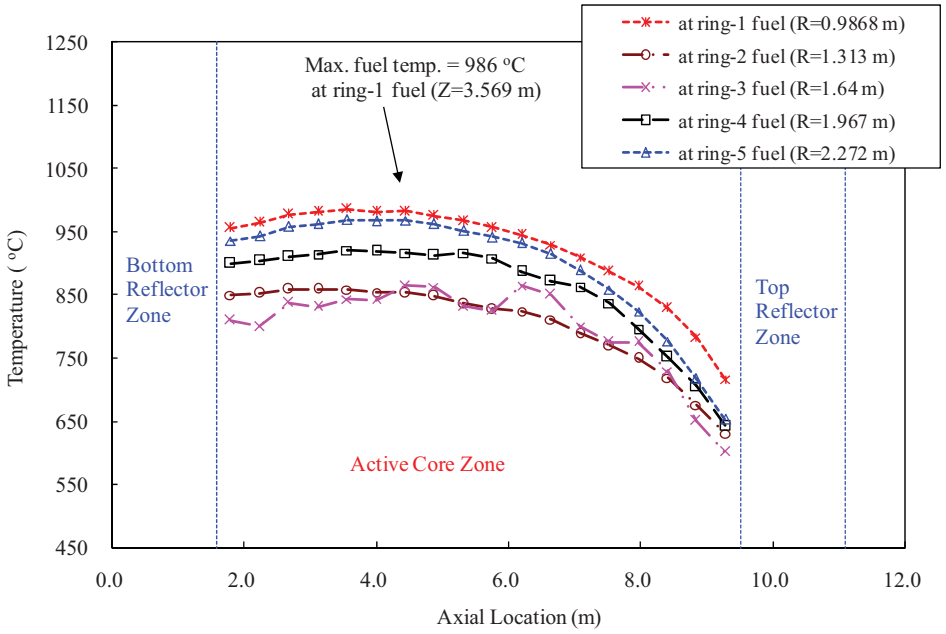

Figure 163. Maximum fuel temperature (PF = 6.9%, Er_2O_3) for 0.2%UO_2 + 99.8%($PuO_{1.8}$, NpO_2) + 0.6 mole SiC getter.

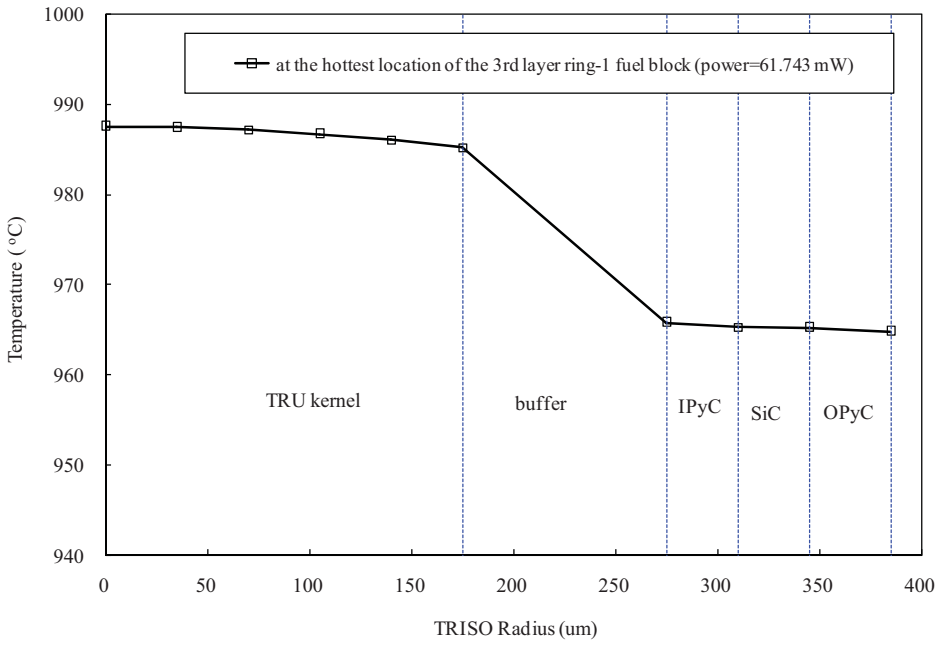

Figure 164. Internal temperature profile of TRISO particle (PF = 6.9%, Er_2O_3) for 0.2%UO_2 + 99.8%($PuO_{1.8}$, NpO_2) + 0.6 mole SiC getter.

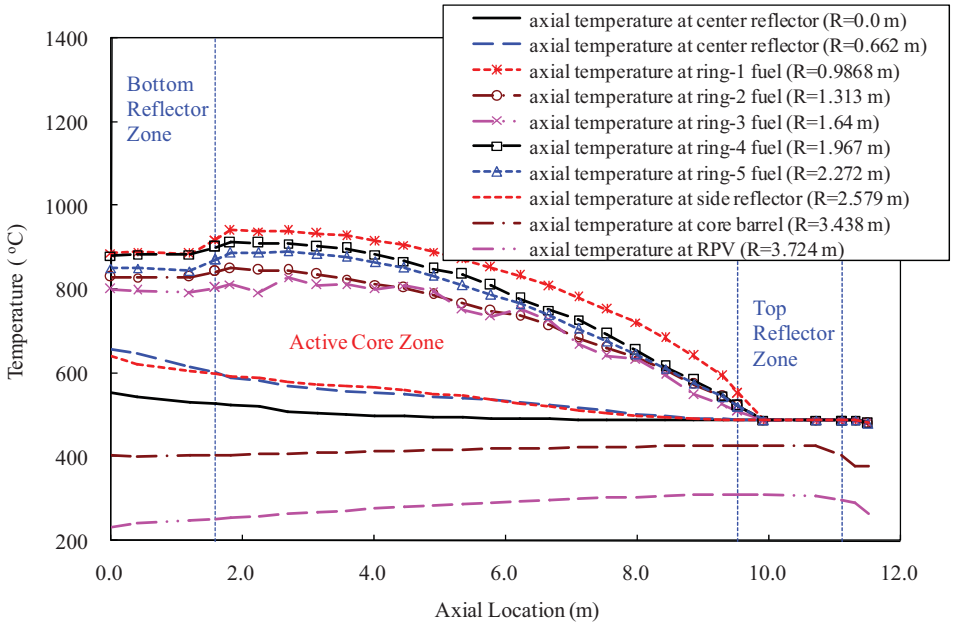

Figure 165. Axial temperature (PF = 7.0%, B_4C) for 30%UO_2 + 70%($PuO_{1.8}$, NpO_2) + 0.6 mole SiC getter.

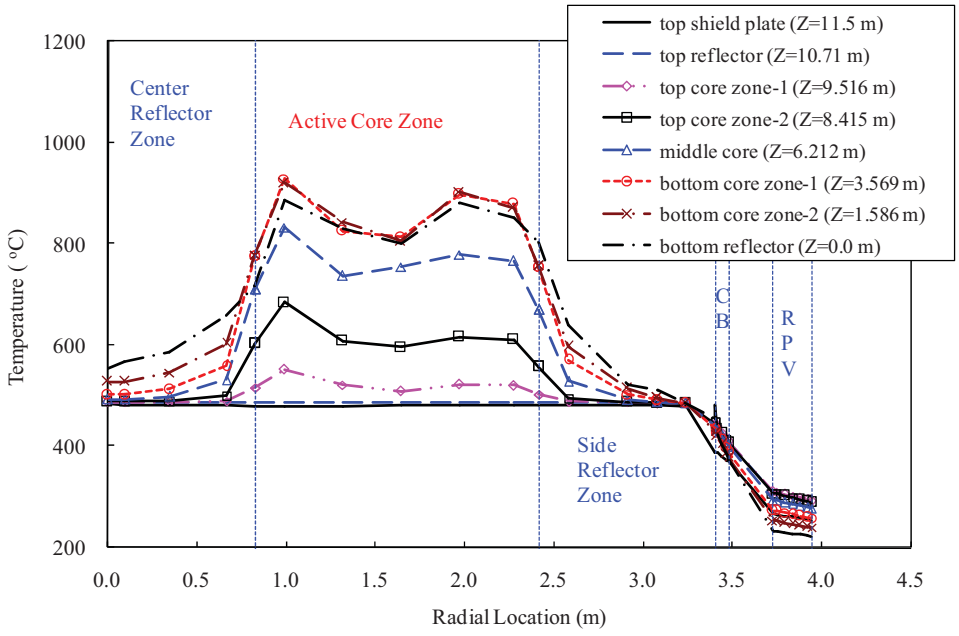

Figure 166. Radial temperature (PF = 7.0%, B_4C) for 30%UO_2 + 70%($PuO_{1.8}$, NpO_2) + 0.6 mole SiC getter.

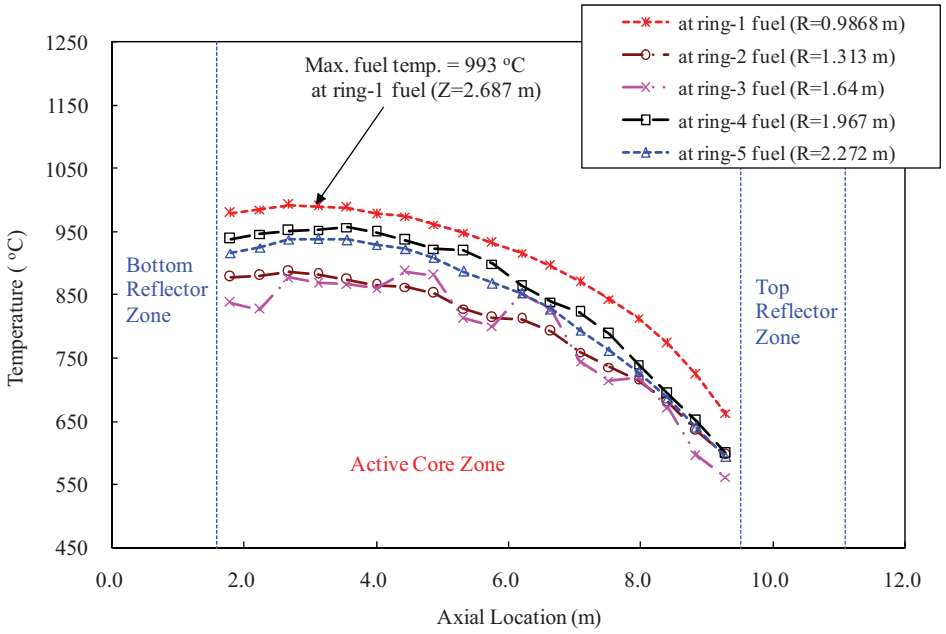

Figure 167. Maximum fuel temperature (PF = 7.0%, B_4C) for 30%UO_2 + 70%($PuO_{1.8}$, NpO_2) + 0.6 mole SiC getter.

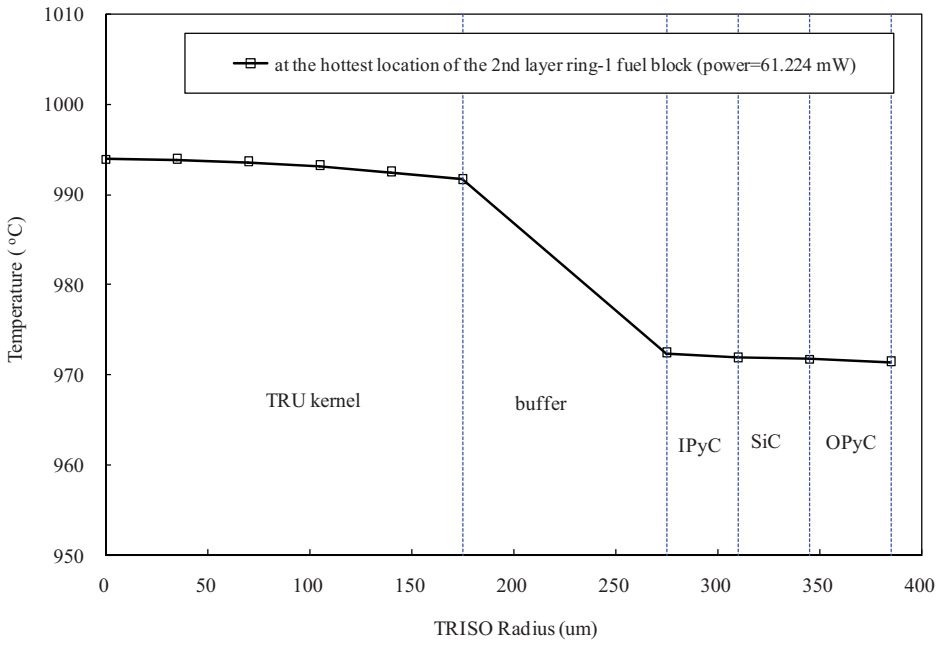

Figure 168. Internal temperature profile of TRISO particle (PF = 7.0%, B_4C) for 30%UO_2 + 70%($PuO_{1.8}$, NpO_2) + 0.6 mole SiC getter.

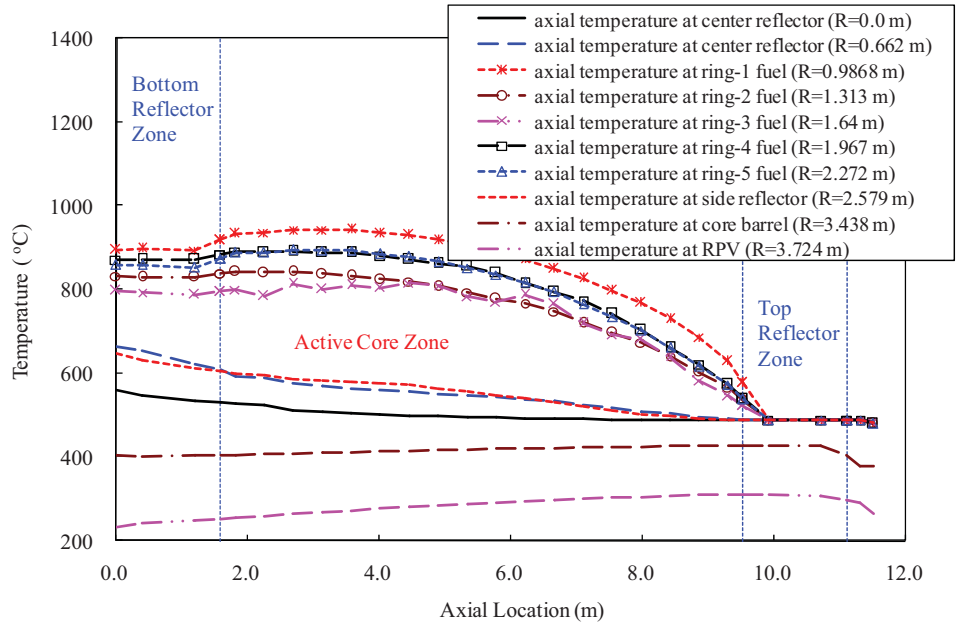

Figure 169. Axial temperature (PF = 7.0%, Er_2O_3) for 30%UO_2 + 70%($PuO_{1.8}$, NpO_2) + 0.6 mole SiC getter.

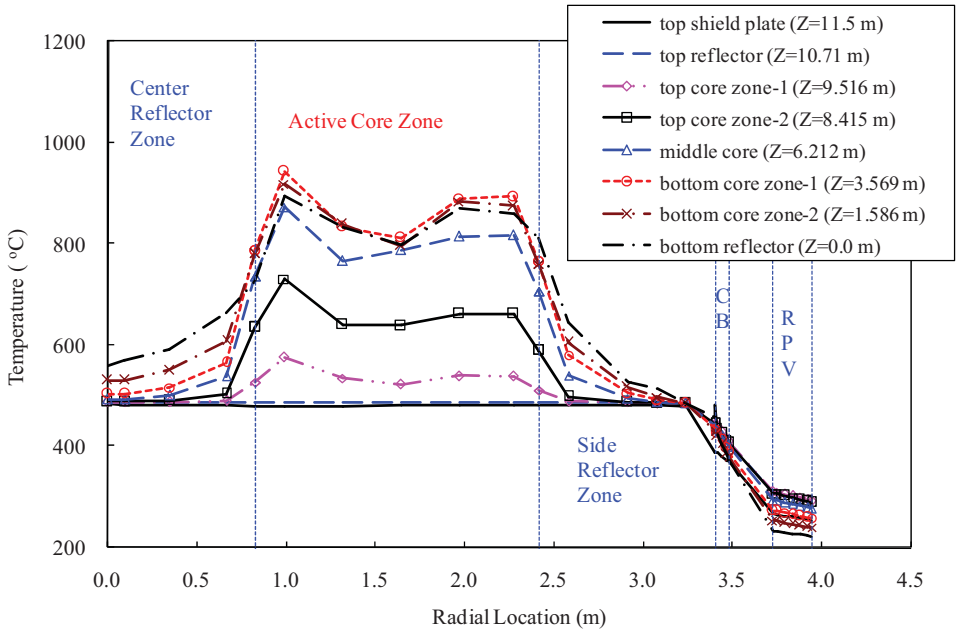

Figure 170. Radial temperature (PF = 7.0%, Er_2O_3) for 30%UO_2 + 70%($PuO_{1.8}$, NpO_2) + 0.6 mole SiC getter.

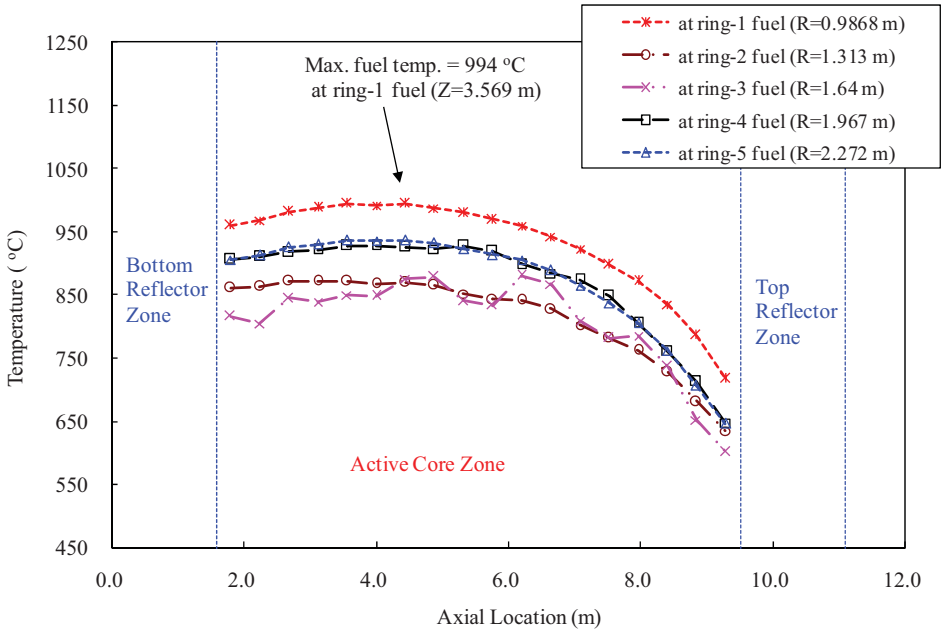

Figure 171. Maximum fuel temperature (PF = 7.0%, Er_2O_3) for 30%UO_2 + 70%($PuO_{1.8}$, NpO_2) + 0.6 mole SiC getter.

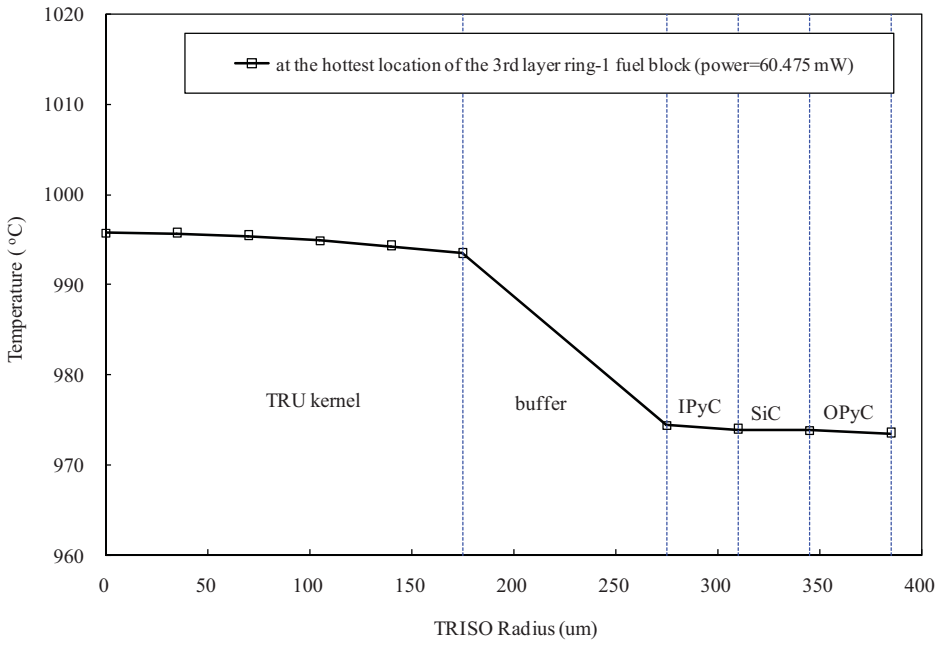

Figure 172. Internal temperature profile of TRISO particle (PF = 7.0%, Er_2O_3) for 30%UO_2 + 70%($PuO_{1.8}$, NpO_2) + 0.6 mole SiC getter.

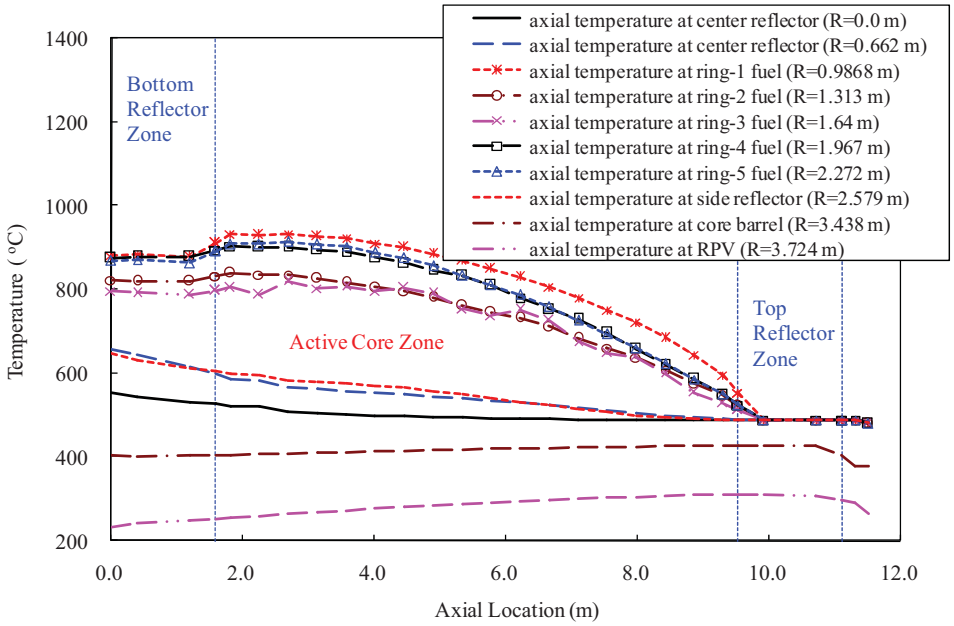

Figure 173. Axial temperature (PF = 8.0%, B_4C) for 30%UO_2 + 70%($PuO_{1.8}$, NpO_2) + 0.6 mole SiC getter.

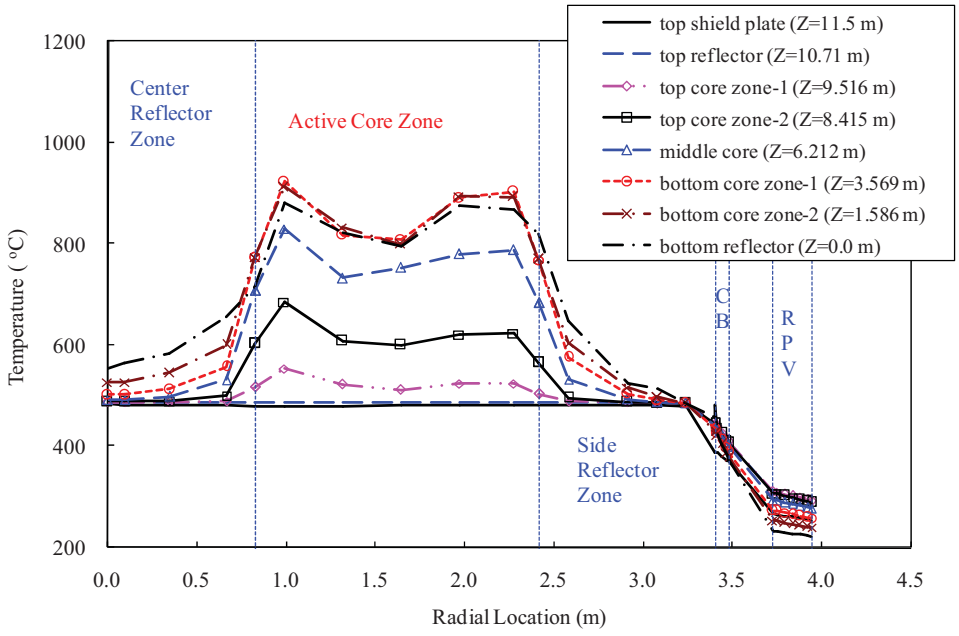

Figure 174. Radial temperature (PF = 8.0%, B_4C) for 30%UO_2 + 70%($PuO_{1.8}$, NpO_2) + 0.6 mole SiC getter.

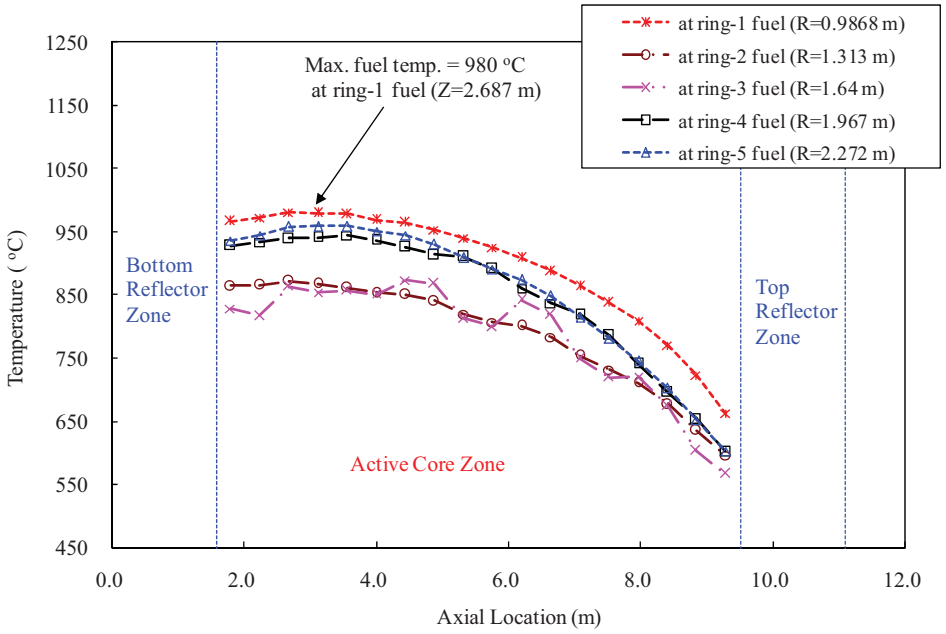

Figure 175. Maximum fuel temperature (PF = 8.0%, B_4C) for 30%UO_2 + 70%($PuO_{1.8}$, NpO_2) + 0.6 mole SiC getter.

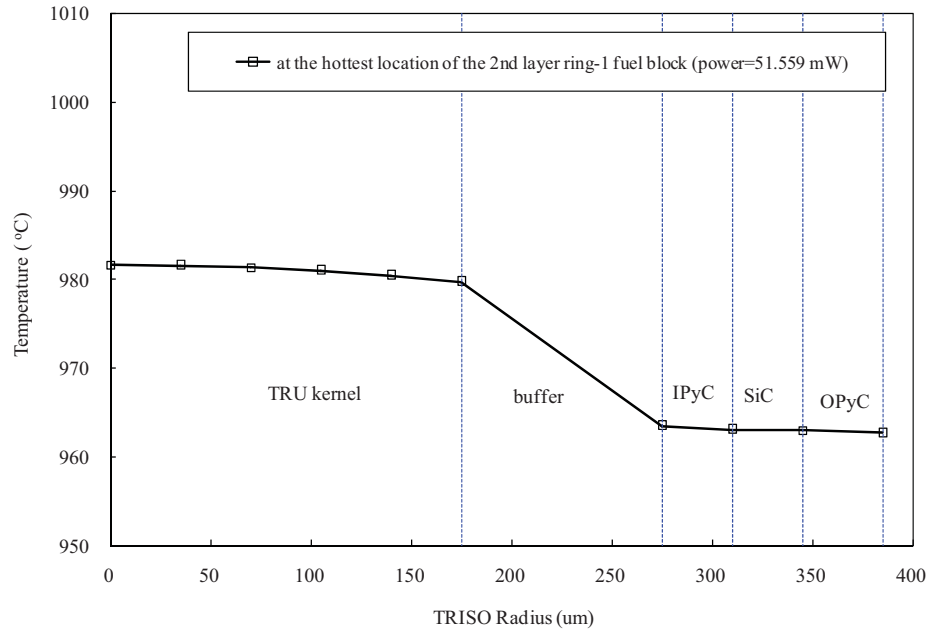

Figure 176. Internal temperature profile of TRISO particle (PF = 8.0%, B_4C) for 30%UO_2 + 70%($PuO_{1.8}$, NpO_2) + 0.6 mole SiC getter.

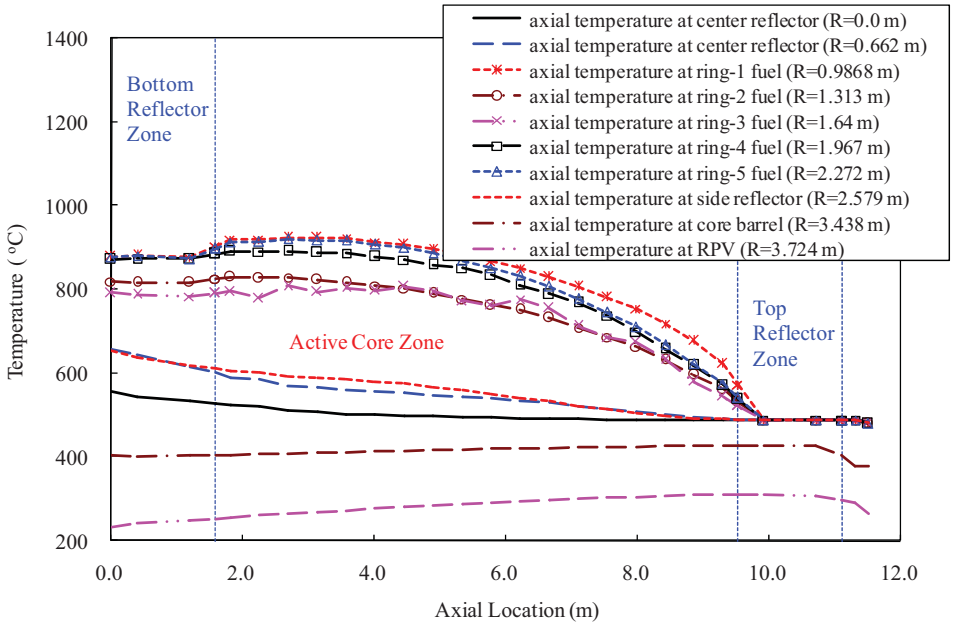

Figure 177. Axial temperature (PF = 8.0%, Er_2O_3) for 30%UO_2 + 70%($PuO_{1.8}$, NpO_2) + 0.6 mole SiC getter.

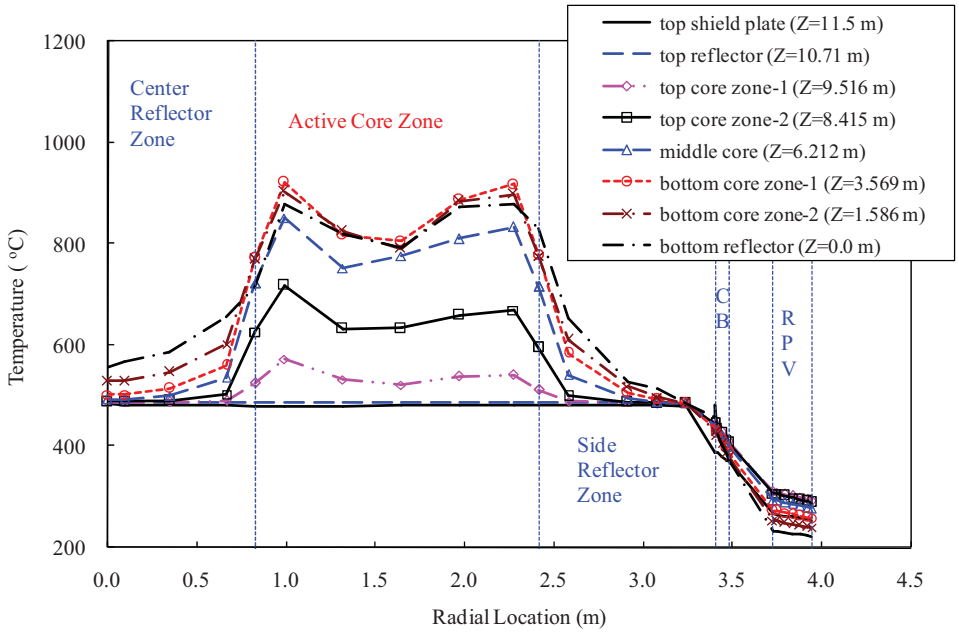

Figure 178. Radial temperature (PF = 8.0%, Er_2O_3) for 30%UO_2 + 70%($PuO_{1.8}$, NpO_2) + 0.6 mole SiC getter.

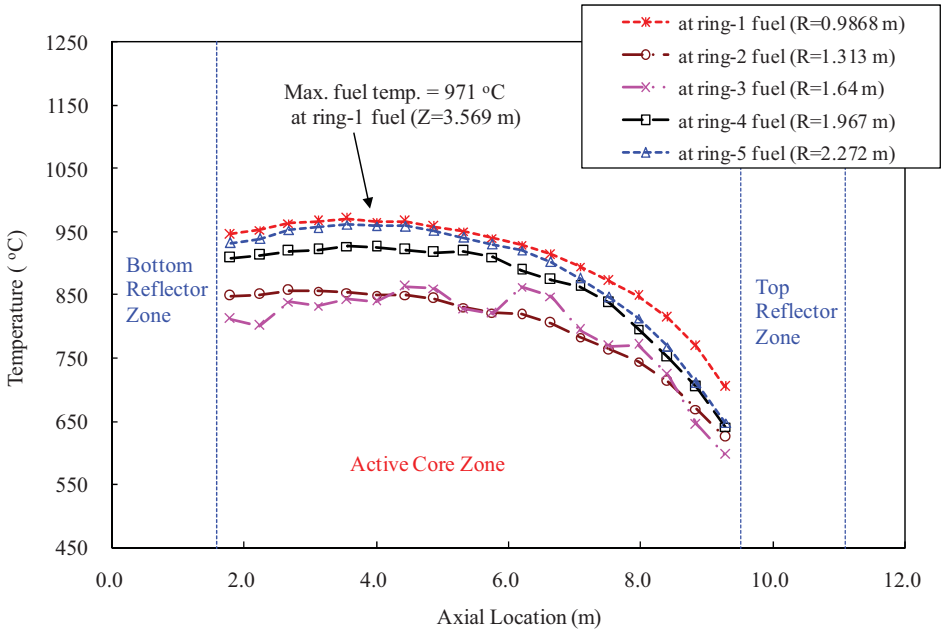

Figure 179. Maximum fuel temperature (PF = 8.0%, Er_2O_3) for 30%UO_2 + 70%($PuO_{1.8}$, NpO_2) + 0.6 mole SiC getter.

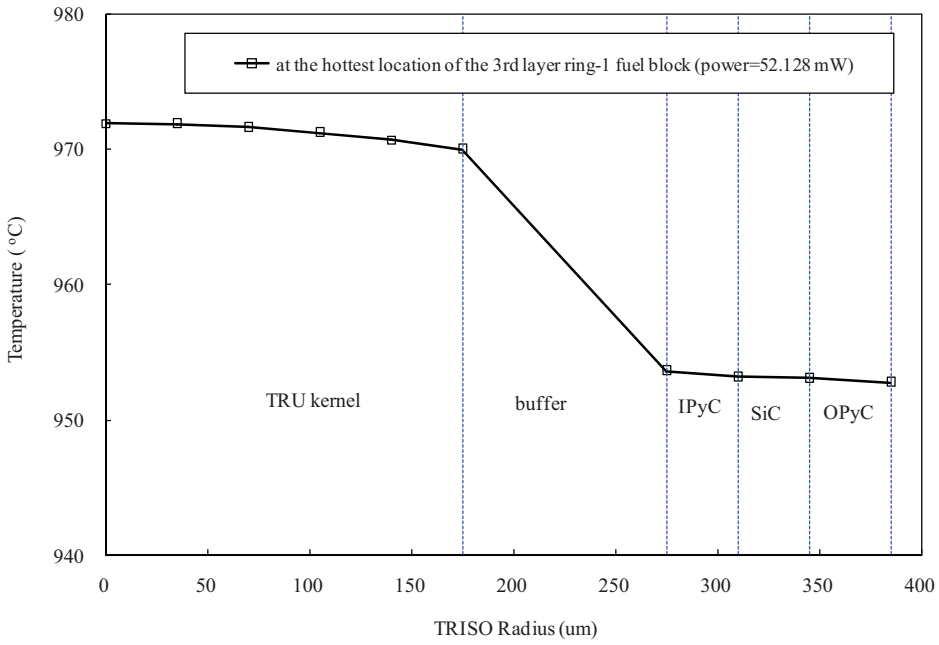

Figure 180. Internal temperature profile of TRISO particle (PF = 8.0%, Er_2O_3) for 30%UO_2 + 70%($PuO_{1.8}$, NpO_2) + 0.6 mole SiC getter.

6.7 All Peak Temperature Results Of Main Core Components During LPCC Event

Table 20. Peak temperatures of main core components during LPCC.

Peak Temperature (°C) for		0.2% UO_2 mixed TRU (PF = 4.9%)		0.2% UO_2 mixed TRU (PF = 5.9%)		0.2% UO_2 mixed TRU (PF = 6.9%)		30% UO_2 mixed TRU (PF= 7.0%)		30% UO_2 mixed TRU (PF = 8.0%)	
Core Components		BP		BP		BP		BP		BP	
	Conductivity	B_4C	Er_2O_3	B_4C	Er_2O_3	B_4C	Er_2O_3	B_4C	Er_2O_3	B_4C	Er_2O_3
TRISO Fuel	GA Method	1580	1671	1644	1715	1685	1733	1617	1674	1647	1687
	JAEA method	1755	1875	1844	1928	1897	1953	1803	1879	1847	1897
	No Annealing	1749	1881	1844	1943	1903	1973	1800	1885	1847	1905
Core Block Average	GA Method	1262	1254	1295	1288	1321	1314	1274	1266	1295	1286
	JAEA method	1309	1308	1354	1352	1391	1386	1326	1321	1354	1346
	No Annealing	1303	1302	1348	1346	1384	1380	1320	1316	1348	1341
Central Reflector	GA Method	1566	1652	1628	1695	1669	1714	1603	1655	1633	1668
	JAEA method	1737	1852	1824	1906	1878	1932	1784	1856	1827	1875
	No Annealing	1734	1858	1825	1919	1884	1949	1782	1862	1828	1882
Side Reflector	GA Method	1067	1119	1111	1151	1142	1173	1091	1126	1117	1144
	JAEA method	1059	1120	1108	1157	1146	1185	1085	1127	1115	1148
	No Annealing	1057	1117	1105	1155	1143	1182	1083	1125	1112	1146
Top Reflector	GA Method	942	1099	1022	1127	1059	1143	982	1100	1017	1110
	JAEA method	917	1078	995	1109	1033	1126	954	1077	989	1080
	No Annealing	914	1070	990	1099	1026	1115	951	1069	984	1080
Bottom Reflector	GA Method	900	906	888	907	885	891	890	898	884	882
	JAEA method	884	906	888	907	884	891	890	898	884	882
	No Annealing	883	906	888	907	884	891	890	898	884	882
Core Barrel	GA Method	636	658	658	676	675	688	647	663	661	673
	JAEA method	628	648	648	665	664	678	637	652	651	662
	No Annealing	629	650	649	666	665	679	639	653	652	663
RPV	GA Method	488	508	508	524	523	535	498	512	511	508
	JAEA method	481	499	499	514	514	527	489	502	501	511
	No Annealing	482	500	500	515	515	527	490	503	502	512

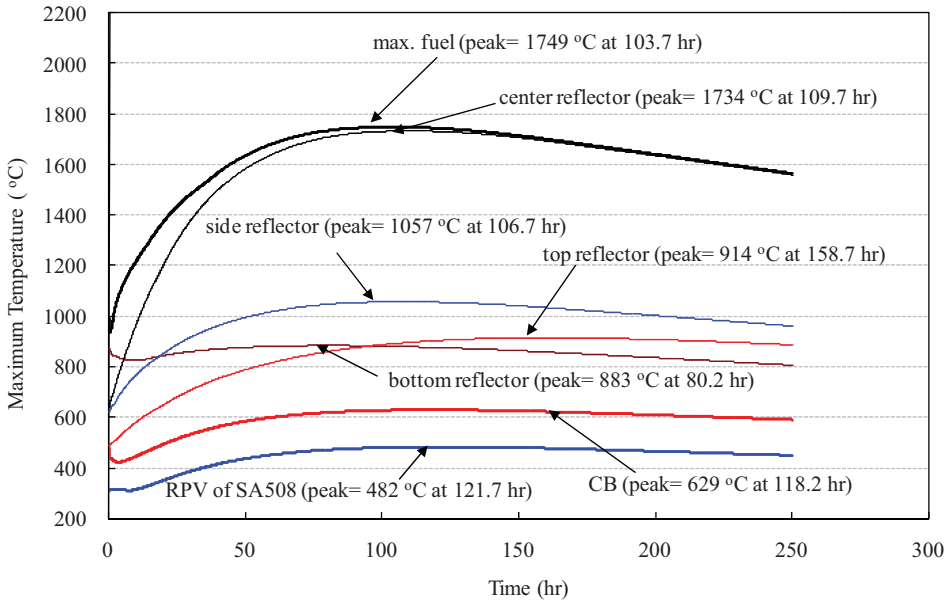

Figure 181. Peak temperature behavior (PF = 4.9%, B_4C, No Annealing) for 0.2% UO_2 + 99.8%($PuO_{1.8}$, NpO_2) + 0.6 mole SiC getter.

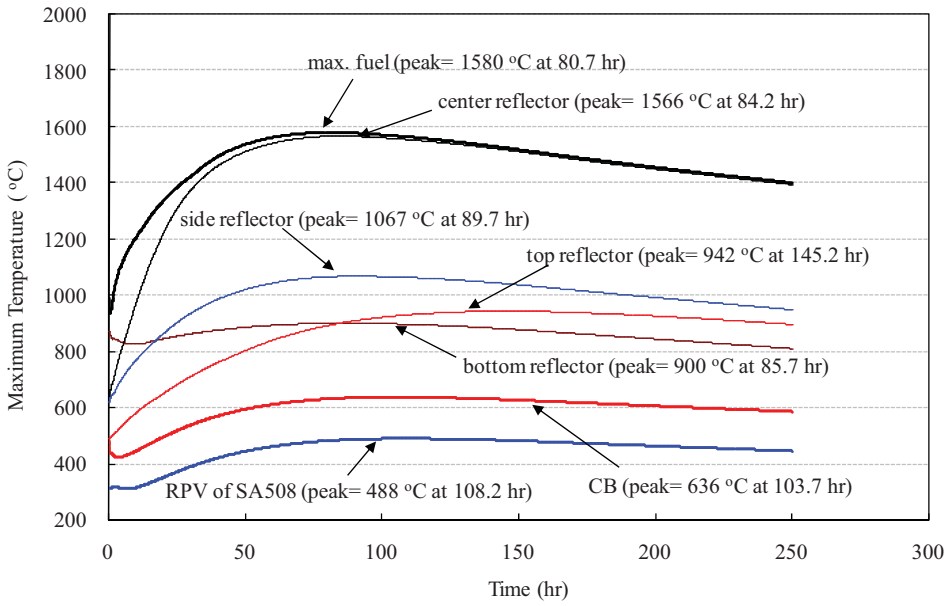

Figure 182. Peak Temperature behavior (PF = 4.9%, B_4C, GA method) for 0.2% UO_2 + 99.8%($PuO_{1.8}$, NpO_2) + 0.6 mole SiC getter.

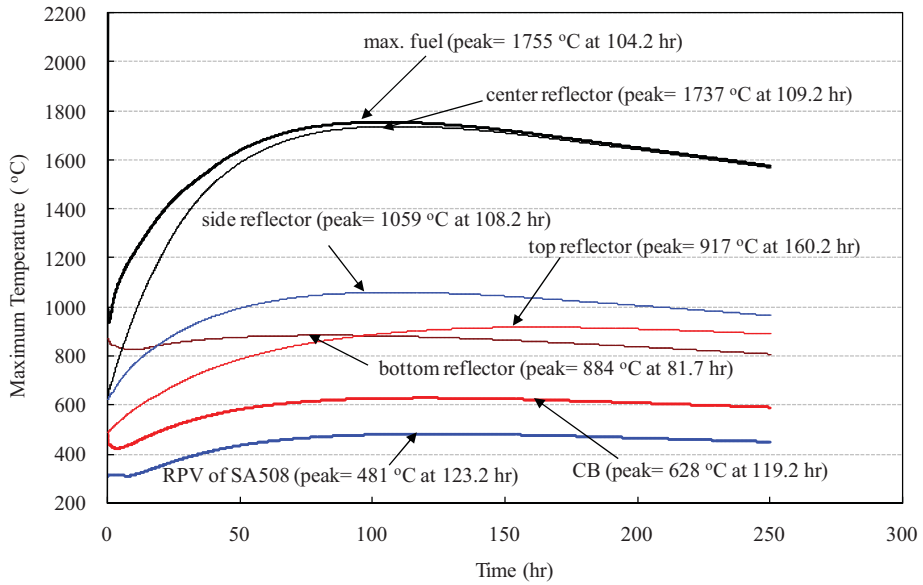

Figure 183. Peak temperature behavior (PF = 4.9%, B_4C, JAEA method) for 0.2%UO_2 + 99.8%($PuO_{1.8}$, NpO_2) + 0.6 mole SiC getter.

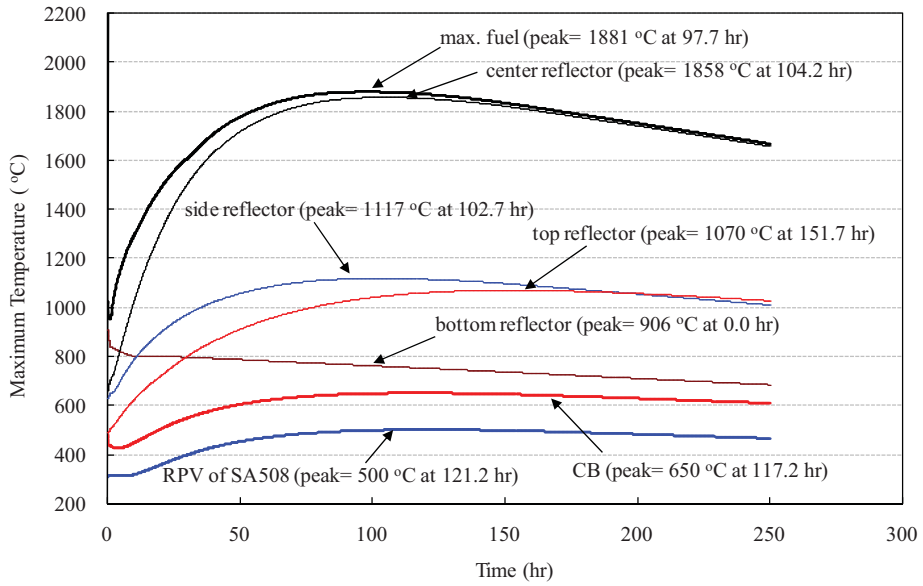

Figure 184. Peak temperature behavior (PF = 4.9%, Er_2O_3, No Annealing) for 0.2%UO_2 + 99.8%($PuO_{1.8}$, NpO_2) + 0.6 mole SiC getter.

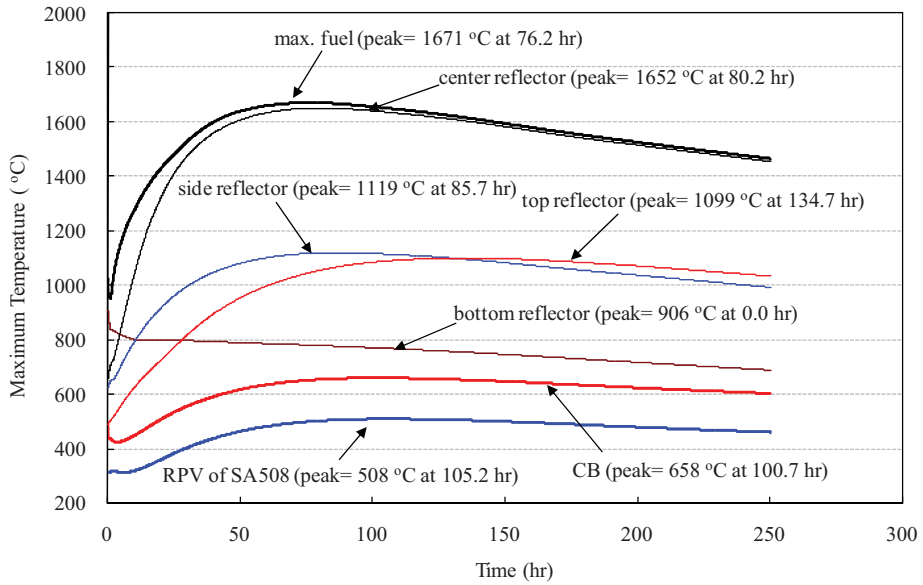

Figure 185. Peak temperature behavior (PF = 4.9%, Er_2O_3, GA method) for 0.2%UO_2 + 99.8%($PuO_{1.8}$, NpO_2) + 0.6 mole SiC getter.

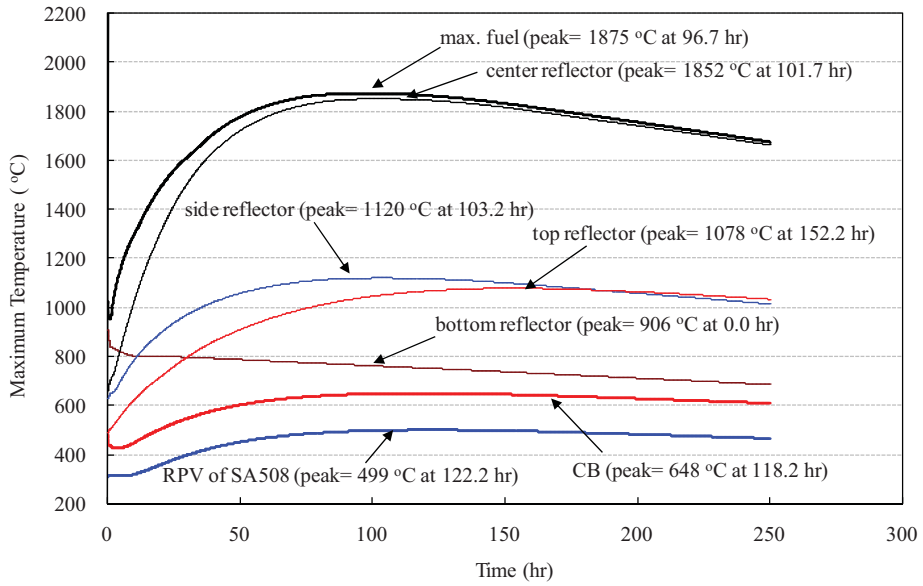

Figure 186. Peak temperature behavior (PF = 4.9%, Er_2O_3, JAEA method) for 0.2%UO_2 + 99.8%($PuO_{1.8}$, NpO_2) + 0.6 mole SiC getter.

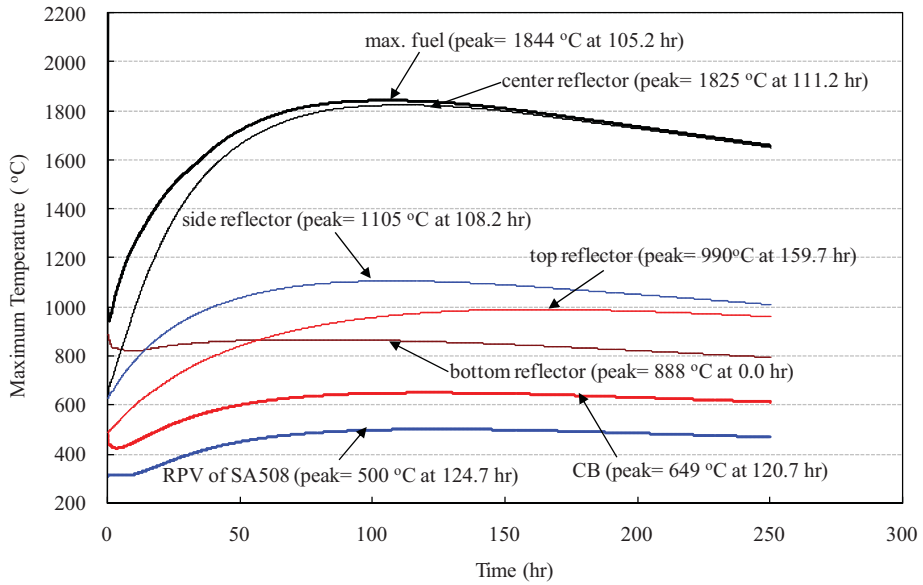

Figure 187. Peak temperature behavior (PF = 5.9%, B_4C, No Annealing) for 0.2%UO_2 + 99.8%($PuO_{1.8}$, NpO_2) + 0.6 mole SiC getter.

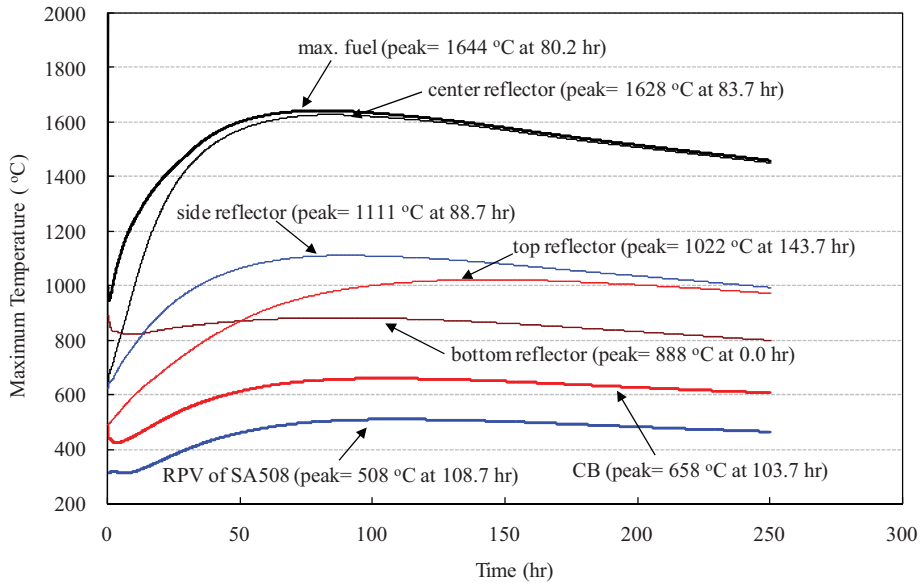

Figure 188. Peak temperature behavior (PF = 5.9%, B_4C, GA method) for 0.2%UO_2 + 99.8%($PuO_{1.8}$, NpO_2) + 0.6 mole SiC getter.

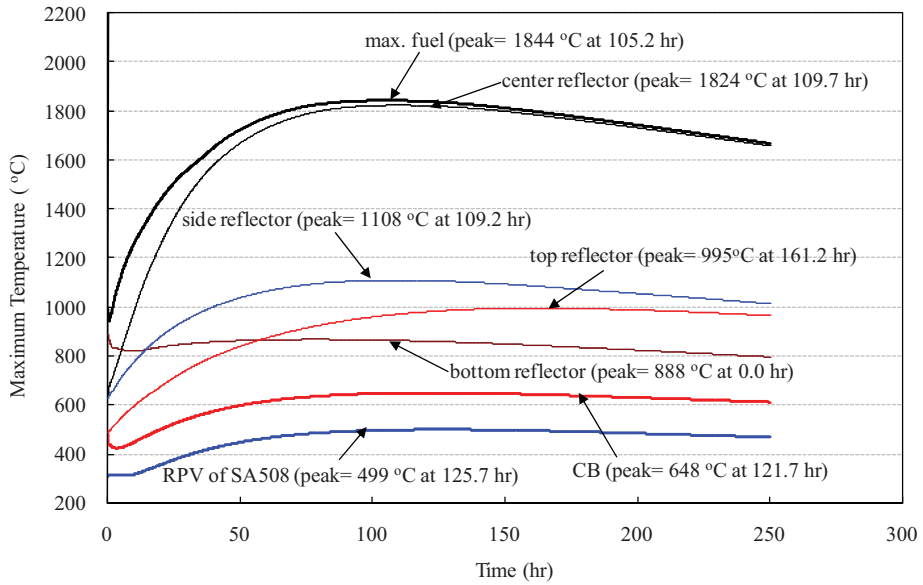

Figure 189. Peak temperature behavior (PF = 5.9%, B_4C, JAEA method) for 0.2%UO_2 + 99.8%($PuO_{1.8}$, NpO_2) + 0.6 mole SiC getter.

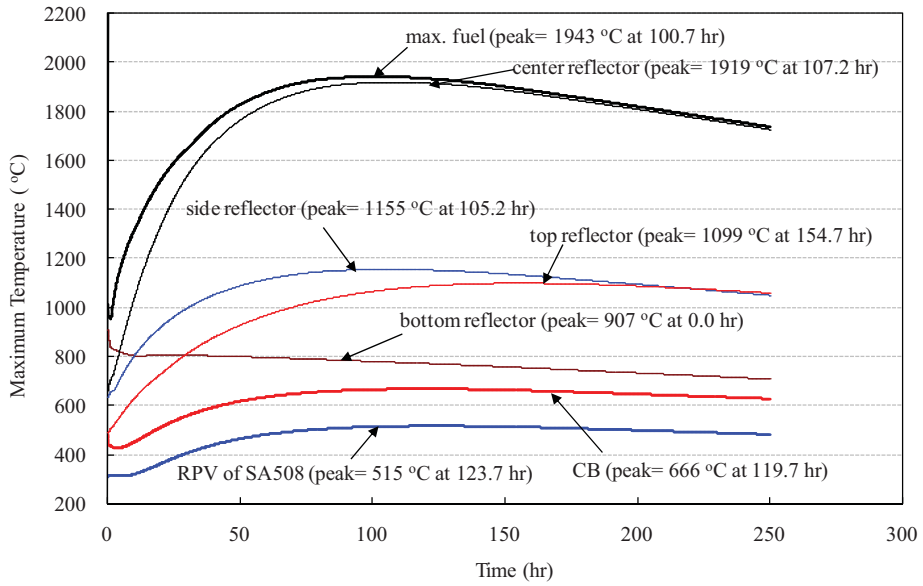

Figure 190. Peak temperature behavior (PF = 5.9%, Er_2O_3, No Annealing) for 0.2%UO_2 + 99.8%($PuO_{1.8}$, NpO_2) + 0.6 mole SiC getter.

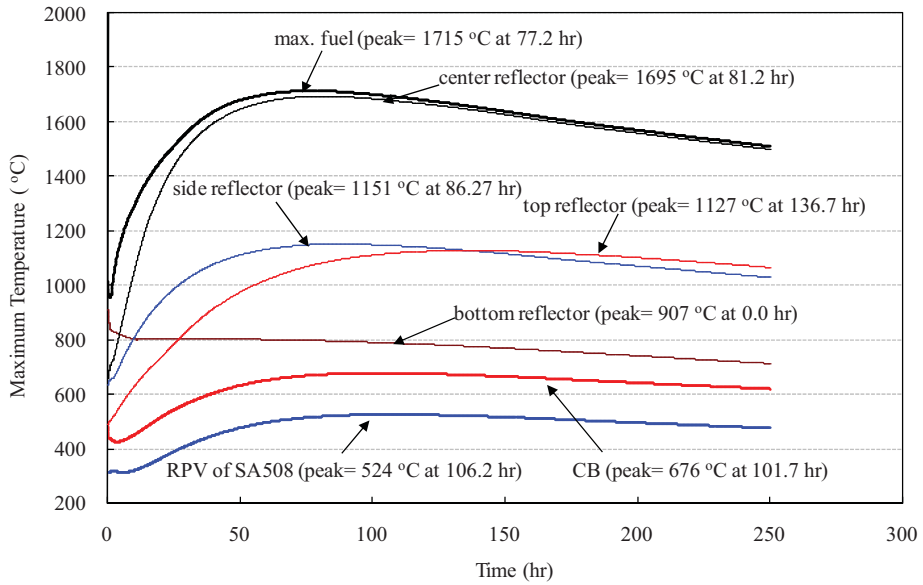

Figure 191. Peak temperature behavior (PF = 5.9%, Er_2O_3, GA Method) for 0.2%UO_2 + 99.8%($PuO_{1.8}$, NpO_2) + 0.6 mole SiC getter.

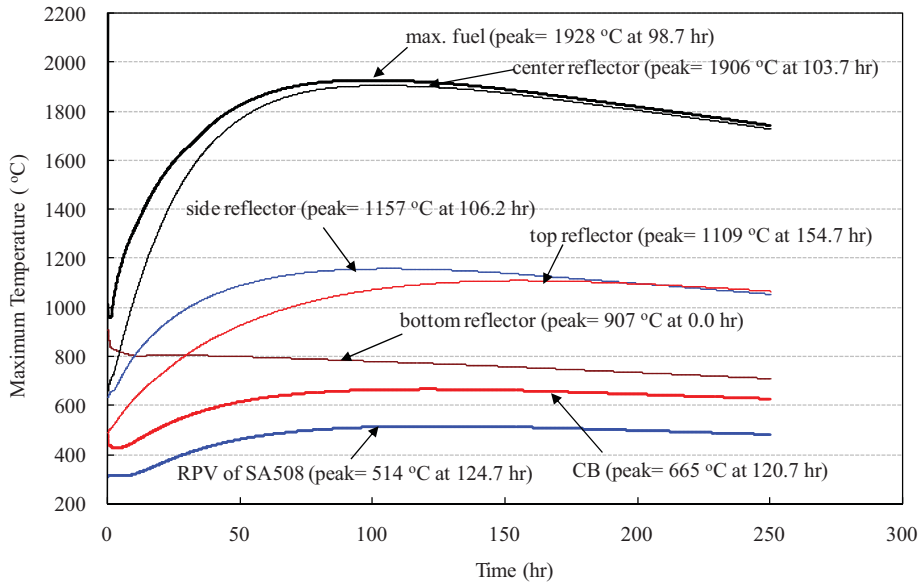

Figure 192. Peak temperature behavior (PF = 5.9%, Er_2O_3, JAEA Method) for 0.2%UO_2 + 99.8%($PuO_{1.8}$, NpO_2) + 0.6 mole SiC getter.

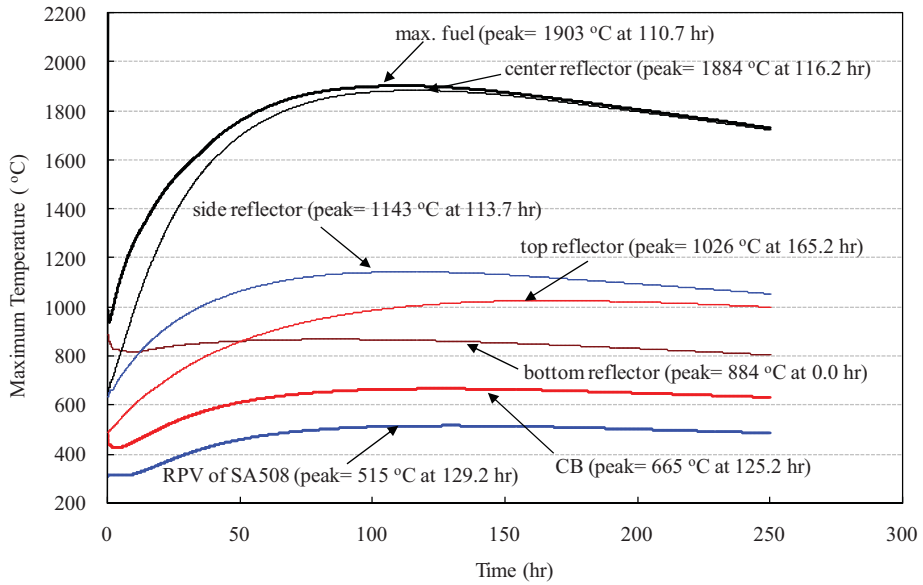

Figure 193. Peak temperature behavior (PF = 6.9%, B_4C, No Annealing) for 0.2%UO_2 + 99.8%($PuO_{1.8}$, NpO_2) + 0.6 mole SiC getter.

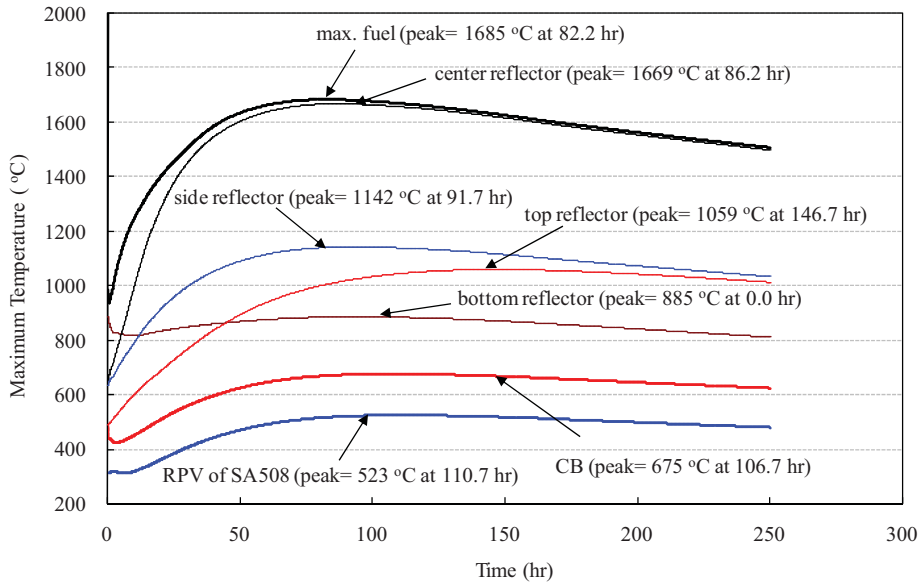

Figure 194. Peak temperature behavior (PF = 6.9%, B_4C, GA method) for 0.2%UO_2 + 99.8%($PuO_{1.8}$, NpO_2) + 0.6 mole SiC getter.

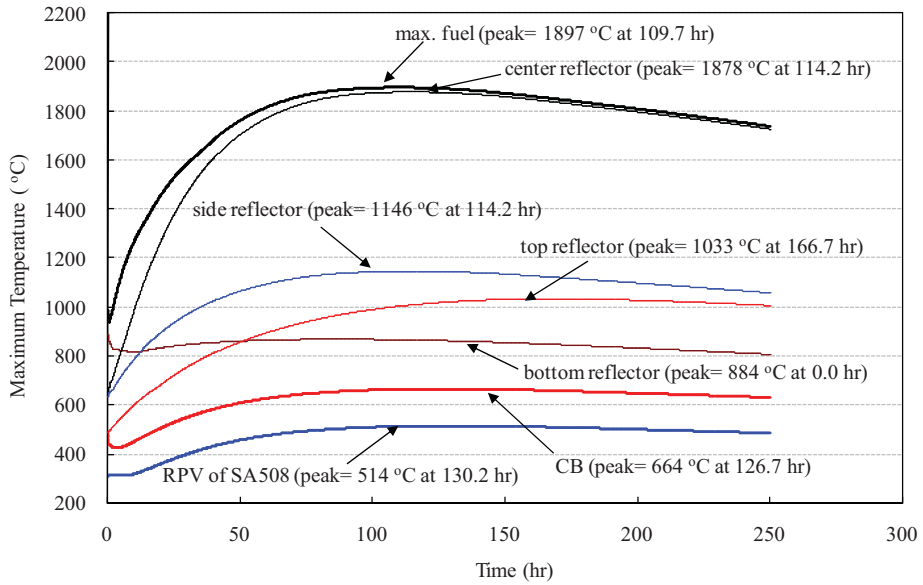

Figure 195. Peak temperature behavior (PF = 6.9%, B_4C, JAEA method) for 0.2%UO_2 + 99.8%($PuO_{1.8}$, NpO_2) + 0.6 mole SiC getter.

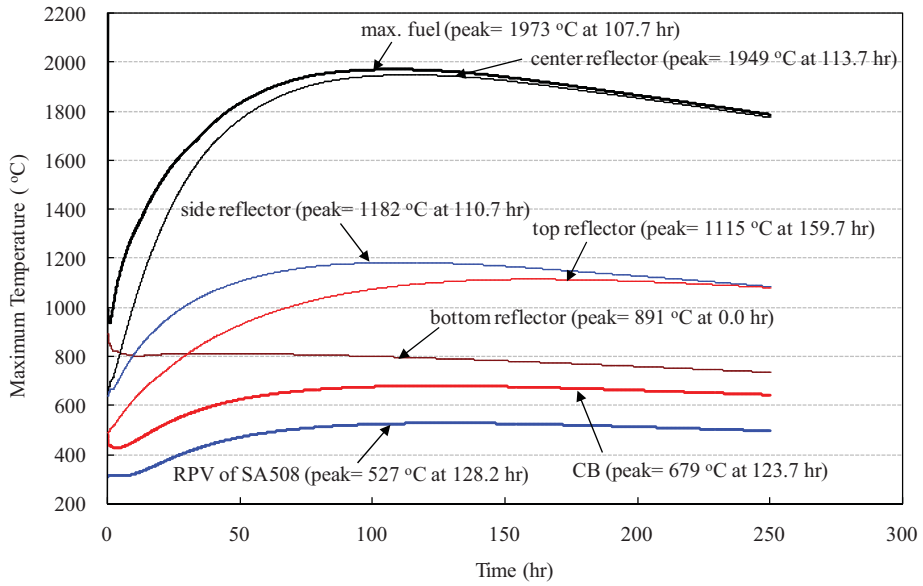

Figure 196. Peak temperature behavior (PF = 6.9%, Er_2O_3, No Annealing) for 0.2%UO_2 + 99.8%($PuO_{1.8}$, NpO_2) + 0.6 mole SiC getter.

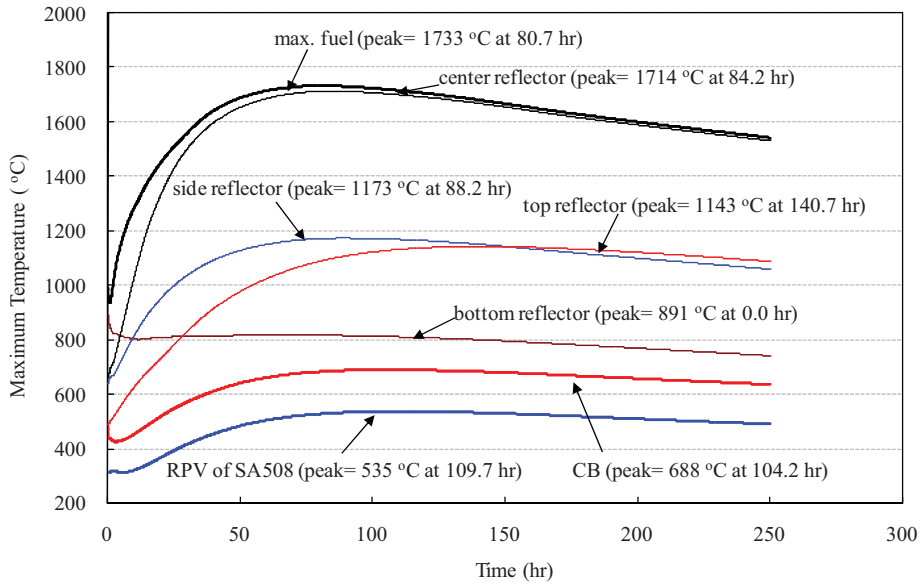

Figure 197. Peak temperature behavior (PF = 6.9%, Er_2O_3, GA Method) for 0.2%UO_2 + 99.8%($PuO_{1.8}$, NpO_2) + 0.6 mole SiC getter.

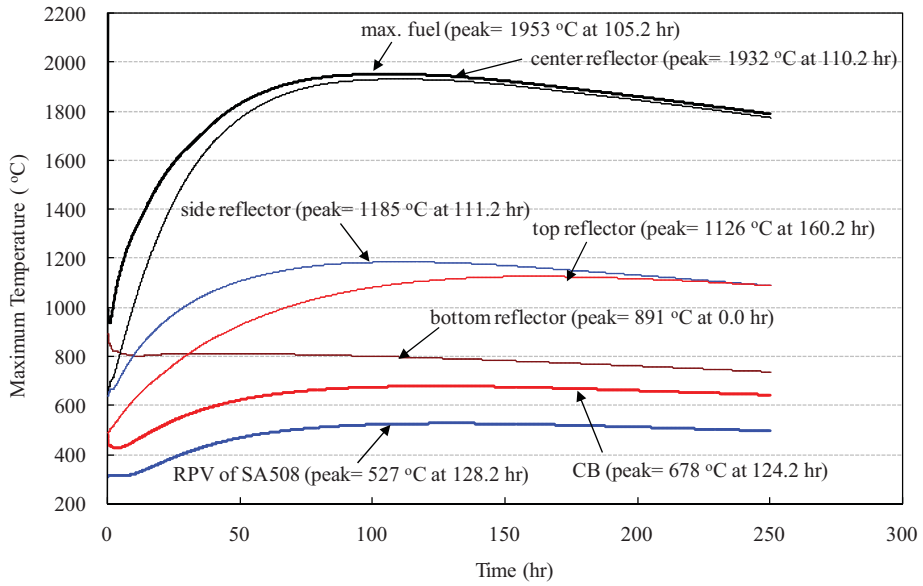

Figure 198. Peak temperature behavior (PF =6.9%, Er_2O_3, JAEA Method) for 0.2%UO_2 + 99.8%($PuO_{1.8}$, NpO_2) + 0.6 mole SiC getter.

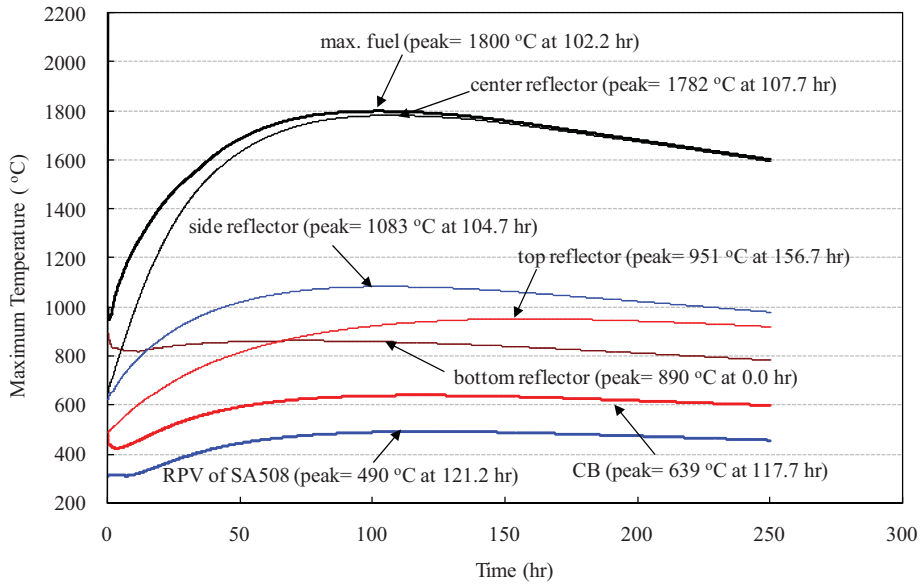

Figure 199. Peak temperature behavior (PF = 7.0%, B_4C, No Annealing) for 30%UO_2 + 70%($PuO_{1.8}$, NpO_2) + 0.6 mole SiC getter.

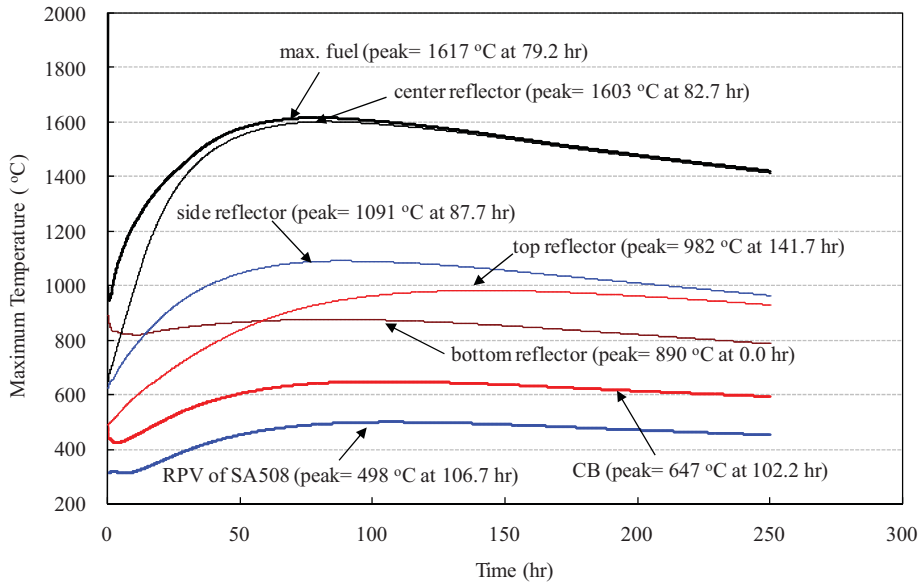

Figure 200. Peak temperature behavior (PF = 7.0%, B_4C, GA method) for 30%UO_2 + 70%($PuO_{1.8}$, NpO_2) + 0.6 mole SiC getter.

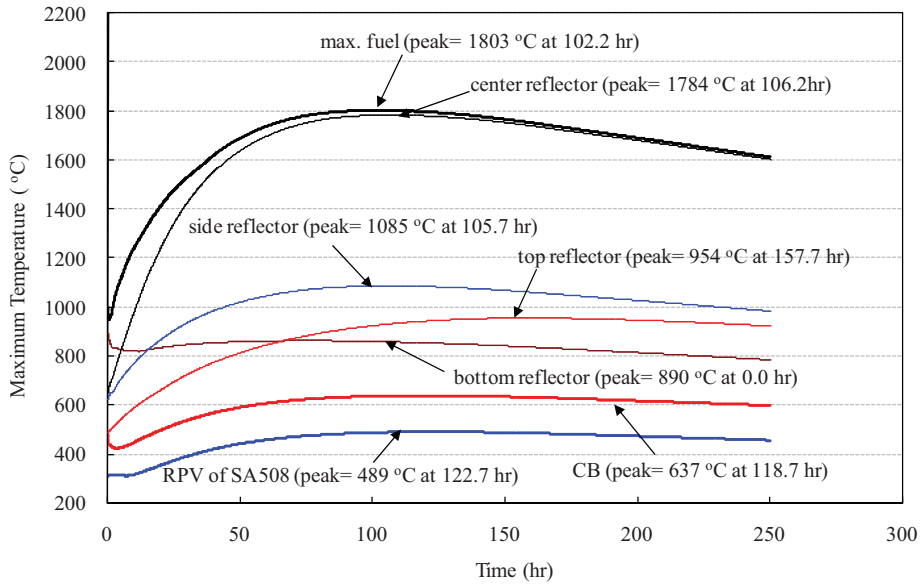

Figure 201. Peak temperature behavior (PF = 7.0%, B_4C, JAEA method) for 30%UO_2 + 70%($PuO_{1.8}$, NpO_2) + 0.6 mole SiC getter.

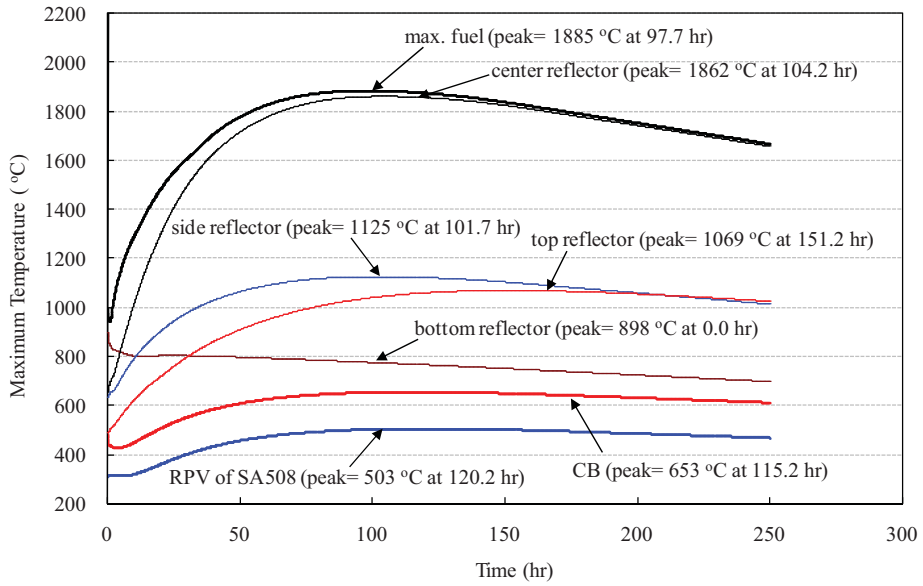

Figure 202. Peak temperature behavior (PF = 7.0%, Er_2O_3, No Annealing) for 30%UO_2 + 70%($PuO_{1.8}$, NpO_2) + 0.6 mole SiC getter.

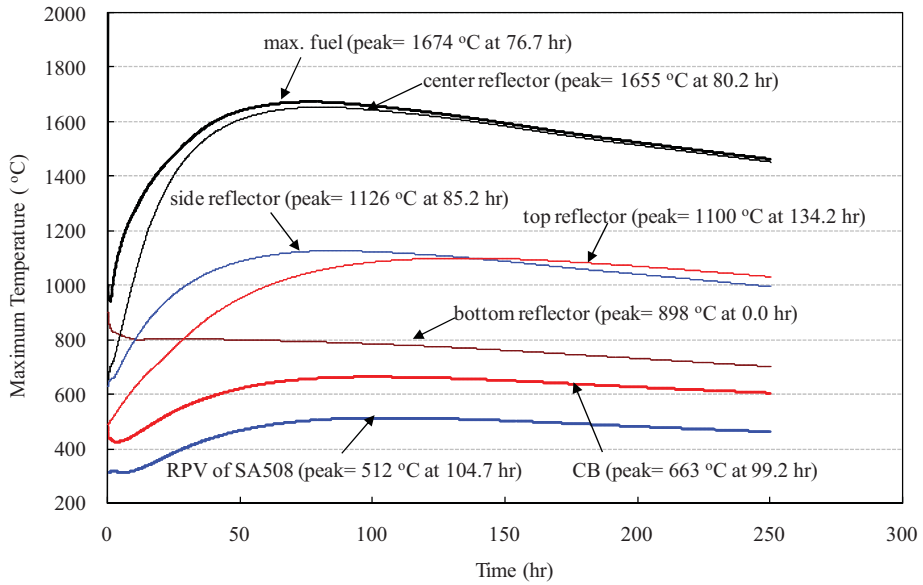

Figure 203. Peak temperature behavior (PF = 7.0%, Er_2O_3, GA method) for 30%UO_2 + 70%($PuO_{1.8}$, NpO_2) + 0.6 mole SiC getter.

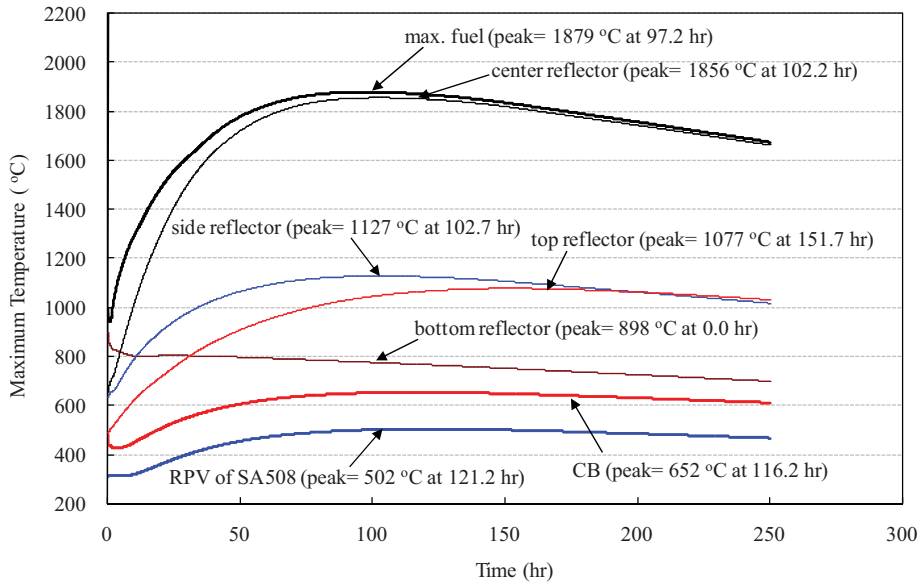

Figure 204. Peak temperature behavior (PF = 7.0%, Er_2O_3, JAEA method) for 30%UO_2 + 70%($PuO_{1.8}$, NpO_2) + 0.6 mole SiC getter.

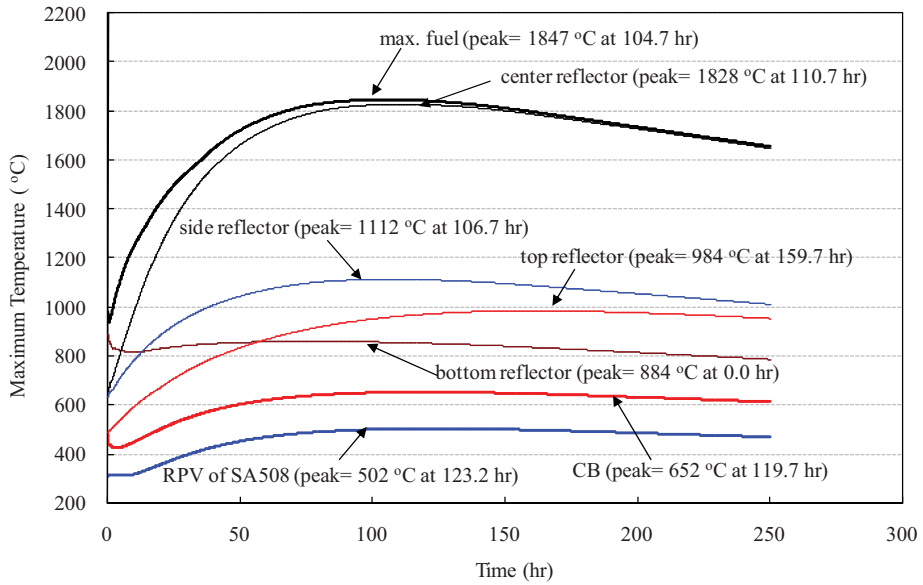

Figure 205. Peak temperature behavior (PF = 8.0%, B_4C, No Annealing) for 30%UO_2 + 70%($PuO_{1.8}$, NpO_2) + 0.6 mole SiC getter.

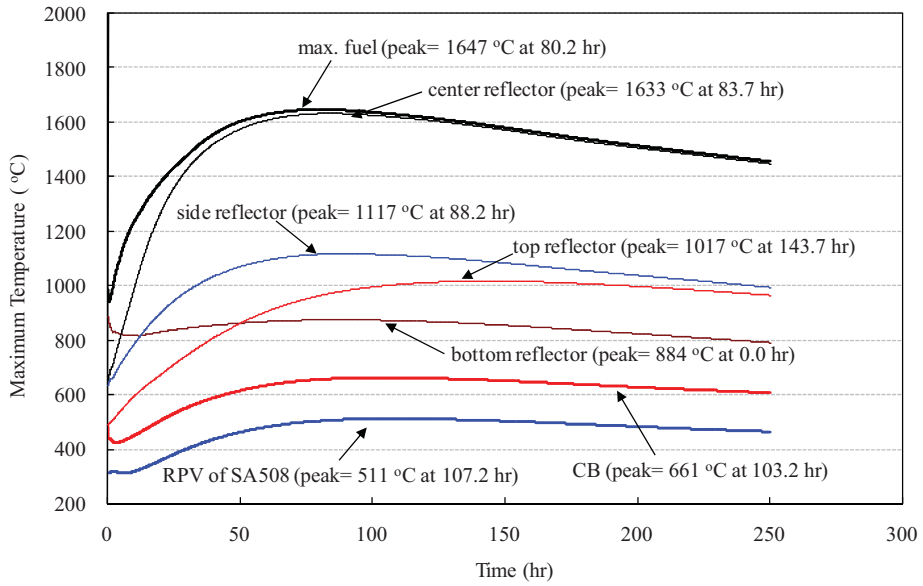

Figure 206. Peak temperature behavior (PF = 8.0%, B_4C, GA Method) for 30%UO_2 + 70%($PuO_{1.8}$, NpO_2) + 0.6 mole SiC getter.

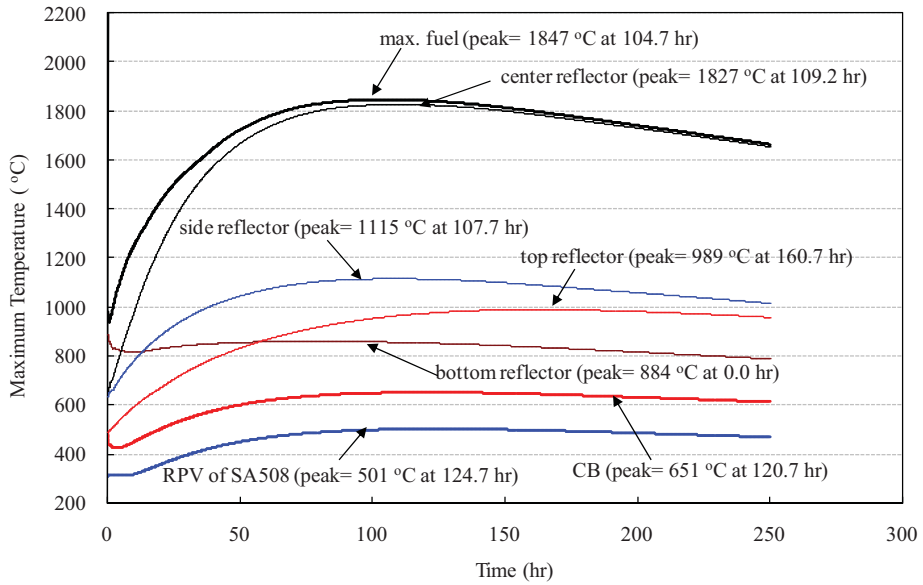

Figure 207. Peak temperature behavior (PF = 8.0%, B_4C, JAEA Method) for 30%UO_2 + 70%($PuO_{1.8}$, NpO_2) + 0.6 mole SiC getter.

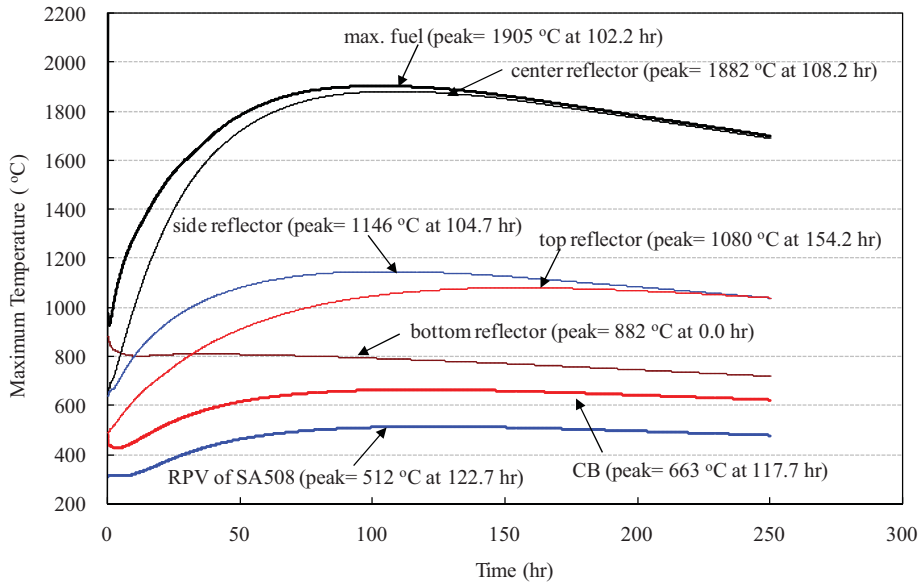

Figure 208. Peak temperature behavior (PF = 8.0%, Er_2O_3, No Annealing) for 30%UO_2 + 70%($PuO_{1.8}$, NpO_2) + 0.6 mole SiC getter.

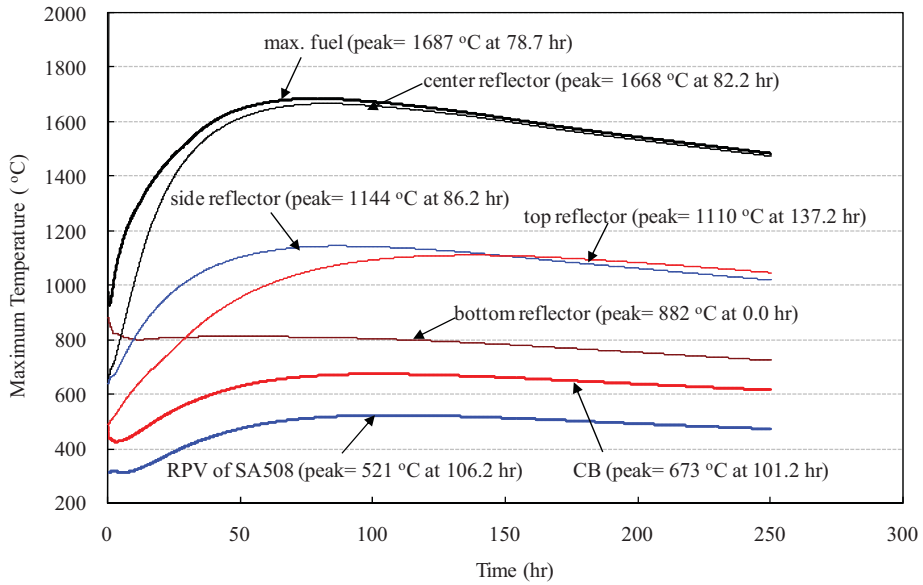

Figure 209. Peak temperature behavior (PF = 8.0%, Er_2O_3, GA Method) for 30%UO_2 + 70%($PuO_{1.8}$, NpO_2) + 0.6 mole SiC getter.

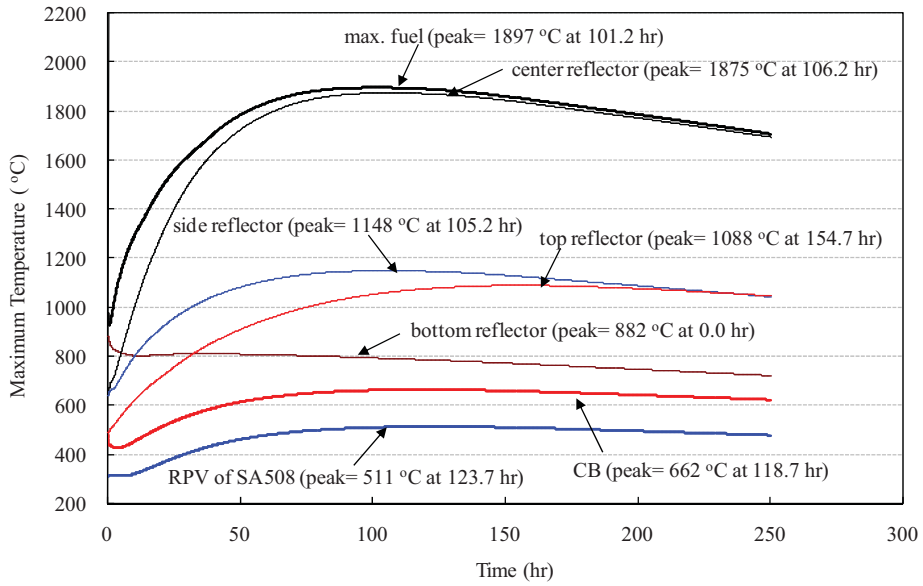

Figure 210. Peak temperature behavior (PF = 8.0%, Er_2O_3, JAEA Method) for 30%UO_2 + 70%($PuO_{1.8}$, NpO_2) + 0.6 mole SiC getter.

6.8 References

1. Potter and A. Shenoy, "Gas Turbine-Modular Helium Reactor (GTMHR) Conceptual Design Description Report," GA Report 910720, Revision 1, General Atomics, July 1996.
2. Yonghee Kim, "Physics Study on TRU Deep-Burn in MHRs," KAERI-GA-1-2006, February 3, 2007.
3. Yonghee Kim, Francesco Venneri, "Optimization of TRU Burnup in Modular Helium Reactor," Proceedings of ICAPP 2007 Nice, France, May 13–18, 2007.
4. Ji Su Jun, Hong Sik Lim, Jae Man Noh, "A Thermal-Fluid Analysis and Safety Analysis for the 600MW_{th} Deep-Burn MHR Core," NHDD-RD-CA-09-008, 2009.7.
5. Ji Su Jun, Hong Sik Lim, Chang Keun Jo, Francesco Venneri, "Thermal-Fluid and Safety Analysis of the TRU Deep-Burn MHR Core," Transactions of the Korean Nuclear Society Autumn Meeting, Gyeongju, Korea, October 29–30, 2009.
6. Ji Su Jun, Hong Sik Lim, Chang Keun Jo, Francesco Venneri, "Decay Heat Impact on the Maximum Transient Fuel Temperature of the various TRU Compositions in a Deep-Burn MHR Core," Transactions of the Korean Nuclear Society Spring Meeting, Pyeongchang, Korea, May 27–28, 2010.
7. Ji Su Jun, Hong Sik Lim, Chang Keun Jo, Jae Man Noh, Francesco Venneri, "Evaluation of the Transient Fuel Temperature in a DB-MHR Core," 5th International Conference on High Temperature Reactor Technology HTR 2010, Prague, Czech, October 18–20, 2010.
8. General Atomics, "Graphite Design Handbook," DOE-HTGR-8811, Rev. 0, September 1988.
9. Junya Sumita, Taiju Shibata, Shigeaki Nakagawa, Tatsuo Iyoku, Kazuhiro Sawa, "Investigation of Design Curve of Annealing Effect on Thermal Conductivity for Graphite Components of HTGR," JAEA-Research 2008-007, Japan Atomic Energy Agency, March 2008.
10. Theodore M. Besmann, "Thermochemical Assessment of Oxygen Gettering by SiC or ZrC in PuO_{2-x} TRISO Fuel," *Journal of Nuclear Materials*, 2010.
11. Hong Sik Lim, Hee Cheon No, "GAMMA Multidimensional Multicomponent Mixture Analysis to Predict Air Ingress Phenomena in an HTGR," *Nuclear Science and Engineering*, Vol. 152, 2006.
12. D.A. Nield, A. Bejan, "Convection in Porous Media," Springer-Verlag, New York, 1999.
13. Min Hwan Kim, Hong Sik Lim, Won Jae Lee, "A Thermal-Fluid Assessment of a Cooled-Vessel Concept for a VHTR," *Nuclear Engineering and Design*, Vol. 238, 2008.12.
14. ASME, "Use of SA-533 Grade B, Class 1 Plate and SA-508 Class 3 Forgings and their Weldments for Limited Elevated Temperature Services, Section III, Division 1, Case N-499-2," ASME, 2001.
15. B. O. Cho, et al., "MASTER-3.0: Multi-purpose Analyzer for Static and Transient Effects of Reactors," KAERI/TR-2061/2002, Korea Atomic Energy Research Institute, 2002.
16. H. J. Shim, et al., "Numerical Experiment on Variance Biases and Monte Carlo Neutronic Analysis with Thermal Hydraulic Feedback," International Conference on Supercomputing in Nuclear Applications, SNA 2003, Paris, France, September 22–24, 2003.
17. A. G. Croff, "ORIGEN-2 : A Versatile Computer Code for Calculating the Nuclide Compositions and Characteristics of Nuclear Materials," *Journal of Nuclear Technology*, 62, 335, 1983.

18. Hyun Chul Lee, Chang Keun Jo, Hyung Jin Sim, Yonghee Kim, Jae Man Noh, "Decay Heat Analysis of VHTR Cores by Monte Carlo Core Depletion Calculation," *Annals of Nuclear Energy*, Accepted Paper to be Published, 2010.

19. Hyun Chul Lee, Chang Keun Jo, Yonghee Kim, Jae Man Noh, "Decay Heat Analysis of a TRU-fueled Deepburn VHTR Core," Transactions of the Korean Nuclear Society Autumn Meeting, Gyeongju, Korea, October 29–30, 2009.

20. Chang Keun Jo, Yonghee Kim, Francesco Venneri, Jae Man Noh, "Deep-Burn MHR Neutronic Analysis with a SiC-gettered TRU Kernel," Transactions of the Korean Nuclear Society Spring Meeting, Pyeongchang, Korea, May 27–28, 2010.

21. GA, "VHTR Technology Course," Nuclear Training Center, KAERI, 2005.12.

22. Nam-il Tak, Min Hwan Kim, Jae Man Noh, "CFD Analysis for the Hot Spot Fuel Temperature of 600MW_{th} Deep-Burn MHR Core," NHDD-RD-CA-09-009 Rev. 0, 2009. 9.

7. FUEL PERFORMANCE ANALYSIS OF THE DEEP BURN PRISMATIC BLOCK REACTOR

7.1 Introduction

The DB-HTR was conceived to convert the TRU radionuclides, recovered from spent LWR fuel, into shorter-lived FPs.[1] It can reduce the long-term storage requirements for the high-level waste generated from currently operating nuclear power plants.

In October 2008, U.S. Department of Energy started sponsoring the Deep Burn (DB) Project, a feasibility study of transuranic management in the HTR.[2] The DB Project consists of seven tasks: project management, core and fuel analysis, spent fuel management, fuel cycle integration, TRU fuel modeling, TRU fuel qualification, and HTR fuel recycle. The task "core and fuel analysis" includes the TRISO fuel microanalysis as one of its subtasks. KAERI, as a subcontractor, conducted analyses of neutronics, thermal-hydraulics, and safety for the 600 MW_{th} prismatic-core DB-HTR, which is one of the candidate reactors. It is necessary to check, using the above analysis results, if the CFP fuel in a DB-HTR core maintains its integrity during its lifetime.

This report describes the microanalysis for two types of fuels that are charged in 600 and 450 MW_{th} DB-HTRs. The microanalysis covers the gas pressure buildup in a coated fuel particle including helium production, thermo-mechanical behavior of a CFP, failure probabilities of CFPs, temperature distribution in a CPF, and the FP transport in a CFP and a graphite. The fuel performance analysis code of KAERI, COPA, is used in the microanalyses for the DB-HTR fuels.[3]

7.2 Design of a DB-HTR

A performance analysis for a DB-HTR fuel requires the material properties and design parameters for all fuel-related components in a DB-HTR. The CFP considered in this study is a TRISO, which consists of a kernel, a low-density pyrocarbon layer called a buffer, an inner high-density pyrocarbon (IPyC) layer, a silicon carbide (SiC) layer, and an outer high-density pyrocarbon (OPyC) layer. The considered DB-HTR kernel materials are 0.2% UO_2 + 99.8% (5% NpO_2 + 95% $PuO_{1.8}$) mixed with 0.6 moles of SiC per mole of heavy metal and 30% UO_2 + 70% (5% NpO_2 + 95% $PuO_{1.8}$) mixed with 0.6 moles SiC per mole of heavy metal. The SiC is mixed with the heavy metal oxide in order to capture the free oxygen, which is generated in a kernel during the irradiation. Two thermal powers of the DB-MHR, 600 and 450 MW_{th}, are taken into account.

Table 21 shows the average thicknesses and densities of the layers of the CFP. The thicknesses and densities of the layers of a CFP are assumed to have a normal distribution with 5% and 1% standard deviations, respectively, used for a stochastic analysis of the failure fraction of CFPs. Table 22 shows the design parameters of a reference compact of a DB-HTR fuel. The compact is a matrix graphite cylinder in which a very large number of CFPs are embedded. The compact length in Table 22 is the unit length of a compact for fuel performance analyses. The real compact length is 5.144 cm. Table 23 shows the thermal hydraulic parameters of a DB-HTR. The parameter values are used to calculate the thermal and FP transport behaviors of a DB-HTR fuel.

Table 21. Thicknesses and densities of the CFP layers for the DB-HTR.

Layers	Thickness (μm)	Density (g/cm^3)
OPyC	40±5%	1.9±1%
SiC	35±5%	3.2±1%
IPyC	35±5%	1.9±1%
Buffer	100 ±5%	1.05±1%
Kernel	350±5%[a]	9.46±1%
a. Diameter		

Table 22. Design parameters of a compact and a fuel block of a DB-HTR fuel.

Design parameters	Values
Compact material	H-451
Matrix density (g/cm^3)	1.75
Packing fraction of CFPs	0.069
Compact diameter (cm)	1.245
Compact length (cm)	1
Number of CFPs per compact	345
Diameter of a fuel hole (cm)	1.27
Pitch in a unit cell of a block (cm)	1.88
Diameter of a coolant hole (cm)	1.588

Table 23. Thermal hydraulic parameters for a prismatic DB-HTR.

Parameters	Values
Active core height/ inner diameter (m)	7.93/ 2.96
Thermal power (MW)	600 and 450
Average power density (W/cm^3)	4.66 for 600 MW_{th} 3.11 for 450 MW_{th}
Inlet/outlet temperature (°C)	490/850
Coolant mass flow rate (kg/s)	320
Primary coolant pressure (MPa) - Normal operation - LPCC accident	 7.0 0.101

7.3 Fuel Performance Analysis Method for a DB-HTR Fuel

7.3.1 Geometric Model

The fuel performance analyses are applied to the unit cell of a DB-HTR fuel block as shown in Figure 211. The fuel performance analyses consist of:

- Estimation of fuel burnup and depletion
- Thermal analyses on a unit cell and a CFP
- Gas pressure buildup in the void volume of the kernel and buffer in a CFP
- Thermo-mechanical analysis on a CFP
- Calculation of the failure fraction of a batch of CFPs
- FP transport from CFPs, through fuel compact and structural graphite, into a coolant.

The unit cell of a DB-HTR fuel block is approximated to be an equivalent cylinder in Figure 212 to apply the fuel performance analysis more easily to the unit cell.[4] The compact region in an equivalent cylinder is equivalent to two original compacts. The areas of the structural graphite in a unit cell and an equivalent cylinder are the same.

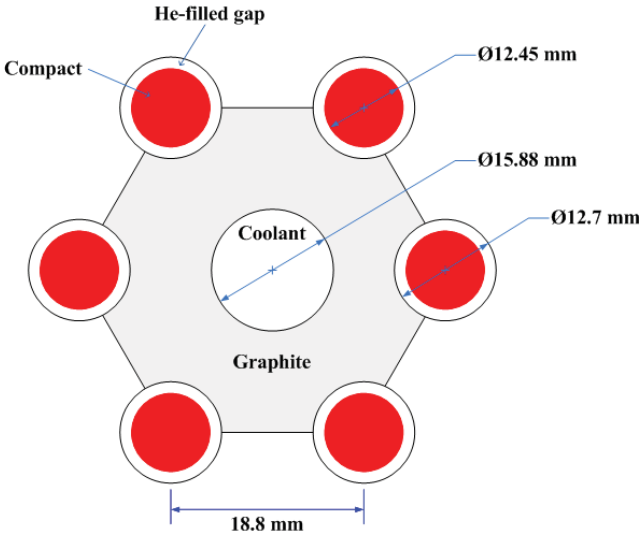

Figure 211. A unit cell in a DB-HTR fuel block.

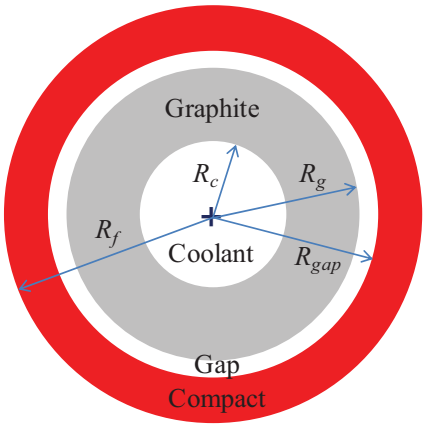

R_c = 7.94 mm
R_g = 14.55 mm
R_{gap} = 14.66 mm
R_f = 17.10 mm

Figure 212. Equivalent cylinder for a unit cell.

7.3.2 Operating Conditions/Fuel Burnup and Depletion

The GAMMA+ code generated the temperature of the coolant and the kernel power under the LPCC accident conditions.[5] The McCARD code[6] generated the burnup and depletion data for a reference compact in the DB-HTR fuel.

7.3.3 Thermal Analysis of Fuel Block and CFP

COPA calculates the temperature distribution in an equivalent cylinder and a CFP by using a one-dimensional finite element method. For an equivalent cylinder, the geometric elements of the numerical model are a compact, a gap between compact and the structural graphite, and the structural graphite. For a CFP, the geometric component parts of the numerical model are a kernel, a gap between kernel and buffer, a buffer, a gap between buffer and IPyC, an IPyC layer, a SiC layer, and an OPyC layer. The temperature distribution can be described by the following steady-state heat transfer equation:

$$\frac{1}{r^z}\frac{\partial}{\partial r}\left(kr^z\frac{\partial T}{\partial r}\right)+q'''=0 \quad , \tag{15}$$

where z is 1 for an equivalent cylinder and 2 for a CFP, r is the radial coordinate (m), T is the temperature (K), k is the thermal conductivity (W m^{-1} K^{-1}), and q''' is the volumetric heat generation rate (W/m^3).

The thermal current at the compact center in an equivalent cylinder is zero on the assumption of radial symmetry. The thermal current at the compact surface is the product of the heat conductance of the gap between compact and structural graphite and the temperature difference between the surface and the gap. The thermal current at the graphite surface facing the gap is the product of the heat conductance of the gap and the temperature difference between the graphite surface and the gap. The heat at the graphite surface facing the coolant is transferred to the helium coolant by convection. The thermal current at the kernel center in a CFP is zero on the assumption of radial symmetry. The temperature at the particle surface is equal to the temperature of the fuel element part where the particle is located.

The thermal conductivities of the structural components and the gases were extracted from published papers and reports.[4, 7,8,9] To get the same temperature drop across the compact region as that between the center and outer surface of an original compact, the thermal conductivity of the compact region in an equivalent cylinder of Figure 212 should be corrected as follows:

$$k_{eq} = k_c \left[\frac{\ln\left(\frac{R_{gap}}{R_f}\right)^2}{\left(\frac{R_{gap}}{R_f}\right)^2 - 1} - 1 \right], \quad (16)$$

where k_{eq} is the thermal conductivity of the compact region in an equivalent cylinder (W m^{-1} K^{-1}), and k_c is the thermal conductivity of the original compact in a unit cell (W m^{-1} K^{-1}).

7.3.4 Gas Pressure Buildup in the Void Volume of Kernel and Buffer

The generation of gas species in the kernel is calculated in the form of fission yield with the McCARD and HSC software.[10] The approximate expression obtained from the Booth model gives the release amount of gases from the kernel into the void volume in the kernel and the buffer.[11] The void volume is the open-pore volume in the kernel and the buffer. The solid and gaseous swelling of the kernel occurs with burnup, and it causes the buffer to become dense, and reduces the void volume. The gas pressure in the void volume can be estimated with the ideal gas law.

7.3.5 Thermo-mechanical Analysis of the CFP

COPA performs the thermo-mechanical analysis on the CFP by using a finite element method.[12] The material properties of the coating layers for the thermo-mechanical analysis were extracted from the CEGA report.[13] Under fast neutron irradiation, the layers in a CFP experience elastic deformation, thermal expansion, irradiation-induced dimensional change, and irradiation-induced creep. For each layer, the stress-strain relation, strain-displacement relationship, and equilibrium equation are set up. Gas pressure acts on the inner surface of the IPyC layer. The matrix graphite surrounding CFPs exerts ambient pressure on the surface of a CFP. There, contact stresses exist between two adjacent bonded layers. Through the finite element method, the displacement, strain and stress are sequentially calculated.

7.3.6 Failure Fraction of CFPs

COPA calculates the failure fractions of a batch of CFPs under reactor operation and heating accident conditions. The pressure vessel failure and the failure due to thermal decomposition are considered as failure mechanisms in the calculations of the failure probabilities of a batch of DB-HTR CFPs. Goodin[14] developed a stochastic model for the SiC failure due to the thermal decomposition. The COPA model for the failure due to the pressure vessel failure utilizes the Monte Carlo method for the random CFP sampling. The ultimate tensile strengths for PyC and SiC are expressed as Weibull distribution. The thicknesses, densities, and Bacon Anisotropy Factors (BAFs) of the coating layers of a CFP are characterized by normal distributions. The total failure fraction is given by:

$$\phi = 1 - (1 - \phi_{PVF})(1 - \phi_{TD}), \quad (17)$$

where ϕ is the total failure fraction, ϕ_{PVF} is the failure fraction due to the pressure vessel failure, and ϕ_{TD} is the failure fraction due to the thermal decomposition.

7.3.7 FP Transport

COPA analyzes the FP migration in the CFP, a pebble and a fuel block under reactor operational conditions, and during heating and irradiation tests.[15] It uses a finite element method to calculate the FP migration. The mechanism of the FP migration in the structural components is assumed to be diffusion only. In the CFP, the fission products are generated through nuclear fissions of nuclear materials in the kernel and a heavy metal contamination of the coating layers. They are also generated from adjacent layers through recoil. Partition factors are assumed at the layer interfaces. It is assumed that no retention of FPs occurs in a failed coating layer.

In the fuel block, the analysis of a FP migration is applied to an equivalent cylinder, which is an approximation to the unit cell in a fuel block. The vapor pressure in the gap between the compact and the structural graphite is assumed to be in the sorption isotherm with concentrations at the compact and graphite surfaces simultaneously. A mass balance is also applied to the gap. The concentration on the structural graphite surface facing a coolant is in the sorption isotherm equilibrium with the vapor pressure at the graphite side of the boundary layer which forms between the graphite surface and the bulk coolant. The mass transfer occurs through the boundary layer into the bulk coolant. The diffusivities and sorption isotherm parameters of FPs have been extracted from published reports.[16,17]

7.4 Fuel Performance for a TRU fuel of a 600 MWth DB-HTR

This DB-HTR kernel material is 0.2% UO_2 + 99.8% (5% NpO_2 + 95% $PuO_{1.8}$) mixed with 0.6 moles SiC per mole of heavy metal.

7.4.1 Nuclide Composition/Operating Conditions/Fuel Burnup and Depletion

Table 24 presents the nuclide composition in the CFP kernel in the DB-HTR fuel. It was assumed that the DB-HTR was operated at the coolant temperature of 864°C and the kernel power of 58.88 mW for three cycles having the average length of 426 effective full power days (EFPD), and then was subjected to a LPCC accident for 250 hours like Figure 213. The kernel power decreases rapidly during the LPCC event. The maximum coolant temperature is 1896.33°C at 109.72 hours. Figure 214 displays the burnup history. The final burnup and fast fluence are 519 GWd/tHM (51.31 %FIMA) and 4.054×10^{21} n/cm^2 (E > 0.1 MeV) at 1278 EFPD.

Table 24. Nuclide composition in the kernel (TRU fuel of a 600 MW_{th} DB-HTR).

Nuclides	Moles	Composition
U-235	1.030E-11	0.001%
U-238	1.443E-09	0.124%
Np-237	3.625E-08	3.119%
Pu-238	2.190E-08	1.884%
Pu-239	4.228E-07	36.379%
Pu-240	1.592E-07	13.696%
Pu-241	3.737E-08	3.215%
Pu-242	4.744E-08	4.082%
O-16	1.315E-06	113.149%
C-12	4.359E-07	37.500%
Si-28	4.022E-07	34.600%
Si-29	2.029E-08	1.746%
Si-30	1.342E-08	1.155%

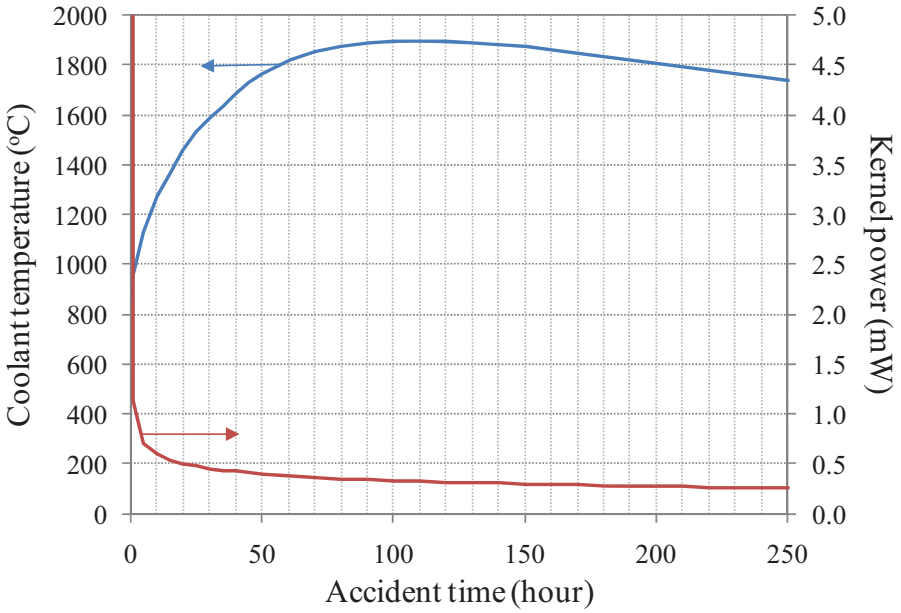

Figure 213. Coolant temperature and kernel power of the DB-HTR during an accident (TRU fuel of a 600 MW_{th} DB-HTR).

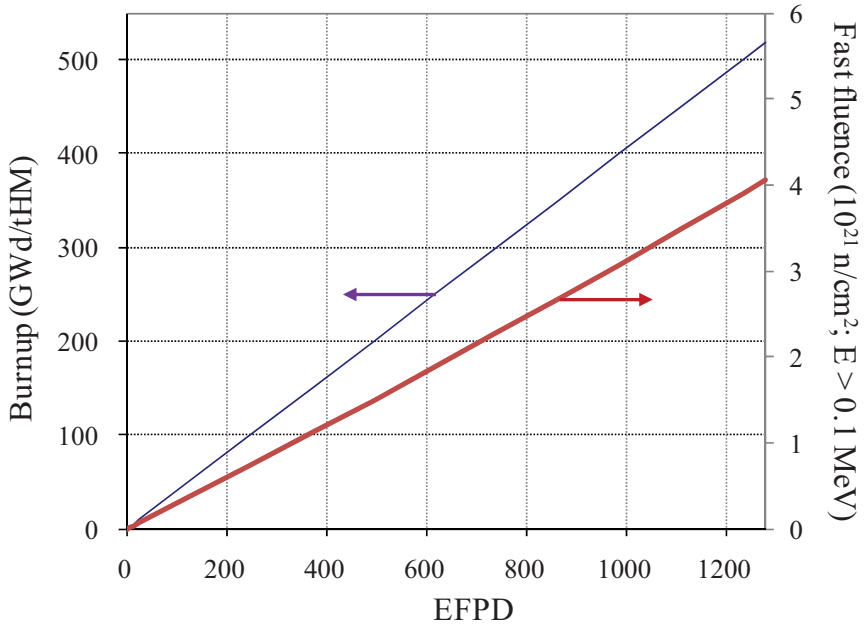

Figure 214. Fuel burnup history (TRU fuel of a 600 MW_{th} DB-HTR).

7.4.2 Thermal Analysis of Fuel Block and CFP

Figure 215 and Figure 216 show the temperature histories at the coolant, at the center of a compact, and at the center of a kernel located at the compact center during normal operation and accident, respectively. The temperature at the center of a kernel located at the compact center is about 925°C during normal operation. But it increases with the accident temperature of the coolant during an accident, when its

maximum is 1896.63°C. In Figure 216, the temperatures at coolant, compact, and kernel during an accident are nearly the same because the power is negligible during the LPCC, as shown in Figure 213.

Figure 217 represents the temperature distribution in an equivalent cylinder. During normal operation, the temperature jumps down at the gap between compact and structural graphite due to the relatively low thermal conductivity of helium in the gap. During an accident, the temperature distribution in the equivalent cylinder is nearly constant. Figure 218 displays the temperature distribution in a CFP. The thermal conductivity of the buffer was assumed to be 0.5 W/(m K). During normal operation, a relatively large temperature drop occurs across the buffer because its thermal conductivity is much lower than those of other layers. At 2.46 days, the temperature gradients are 12.60°C/mm across the kernel and 182.11°C/mm across the buffer. The temperature within the CFP is nearly constant during an accident.

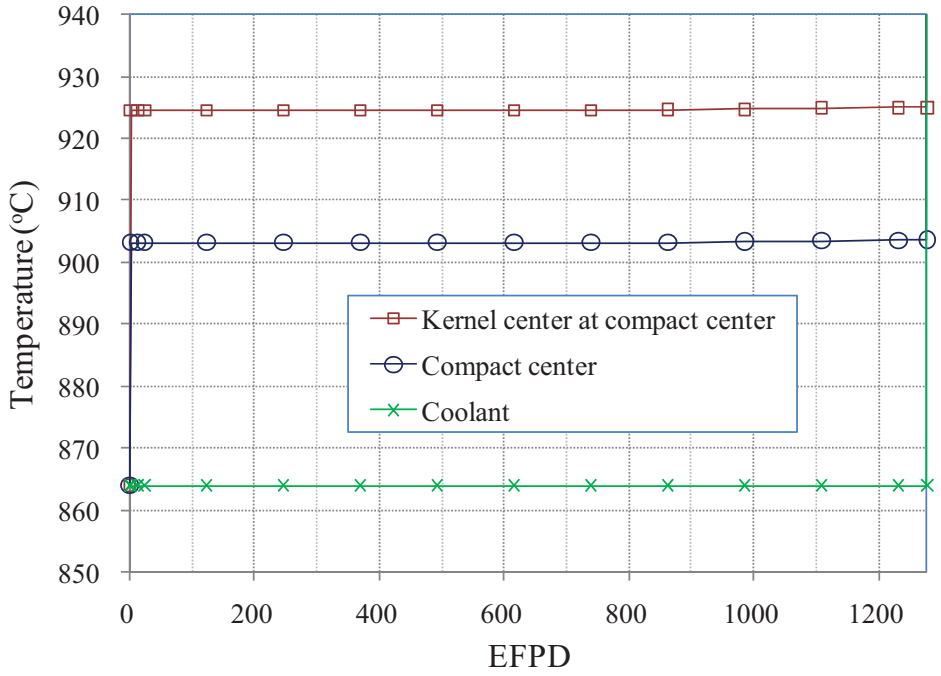

Figure 215. Temperature history during normal operation (TRU fuel of a 600 MW_{th} DB-HTR**).**

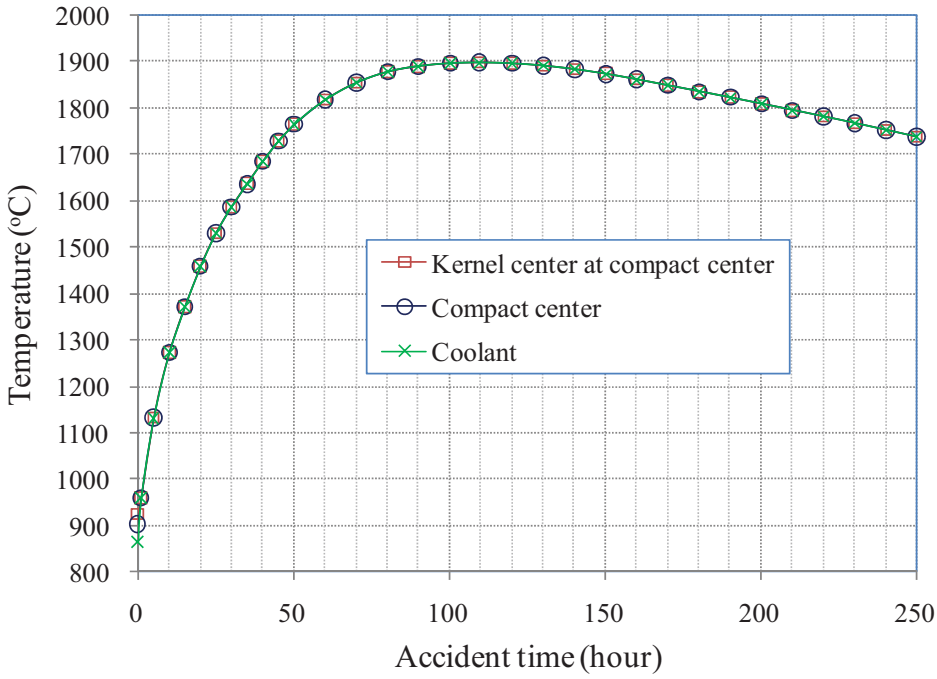

Figure 216. Temperature variation during an accident (TRU fuel of a 600 MW_{th} DB-HTR).

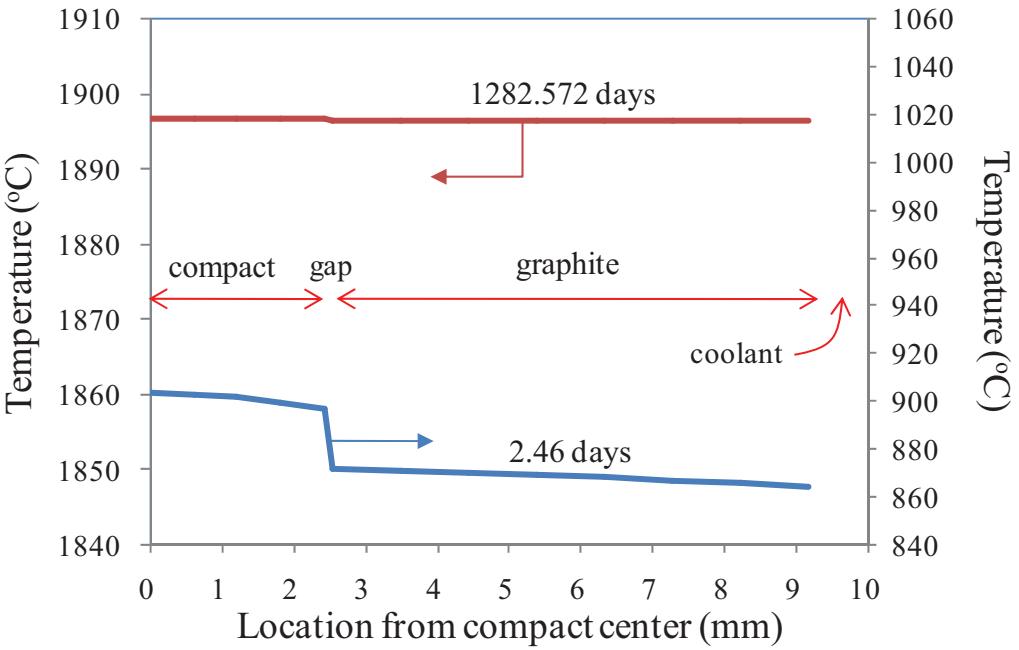

Figure 217. Temperature distribution across the compact and structural graphite (TRU fuel of a 600 MW_{th} DB-HTR).

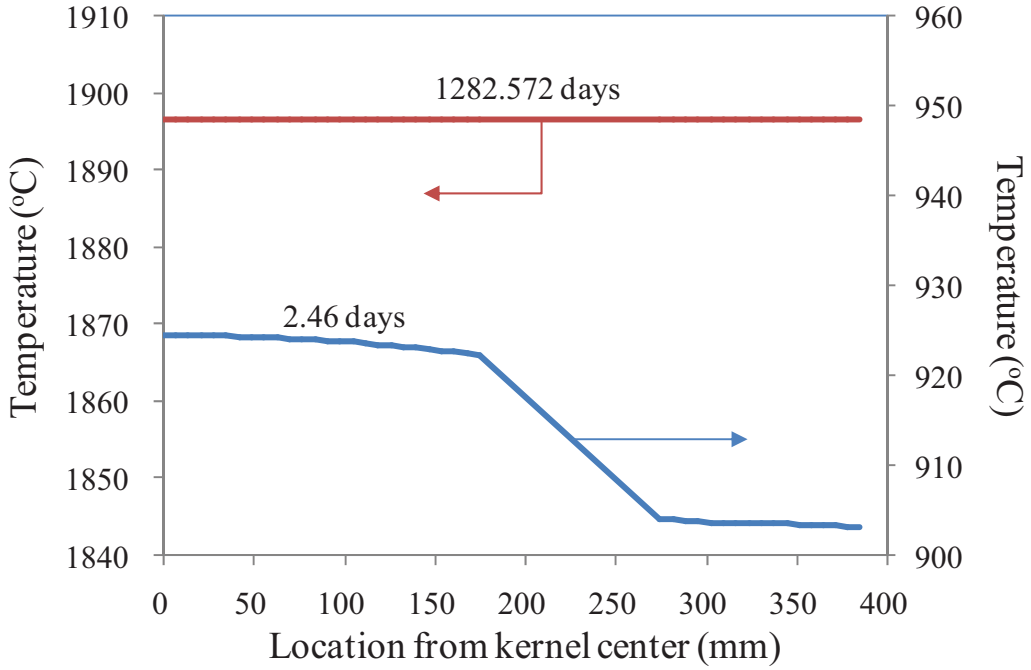

Figure 218. Temperature distribution in a CFP located at the center of the compact in a unit cell (TRU fuel of a 600 MW_{th} DB-HTR).

7.4.3 Gas Pressure Buildup in the Void Volume of Kernel and Buffer

Figure 219 and Figure 220 show the gas pressure in the void volume during normal operation and in accident conditions, respectively. Xenon, cesium, helium, and krypton are major gas species during normal operations, but carbon monoxide and silicon monoxide are additionally generated under the accident condition. The total gas pressure is 31.82 MPa at 1278 EFPD and 200.35 MPa at 109.72 hours after an accident.

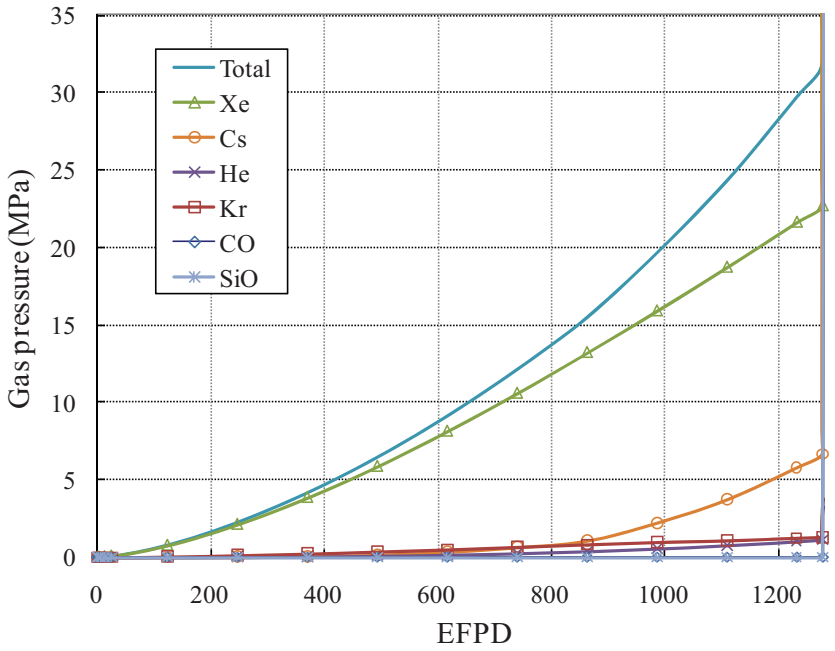

Figure 219. Gas pressure in the void volume during normal operation (TRU fuel of a 600 MW_{th} DB-HTR).

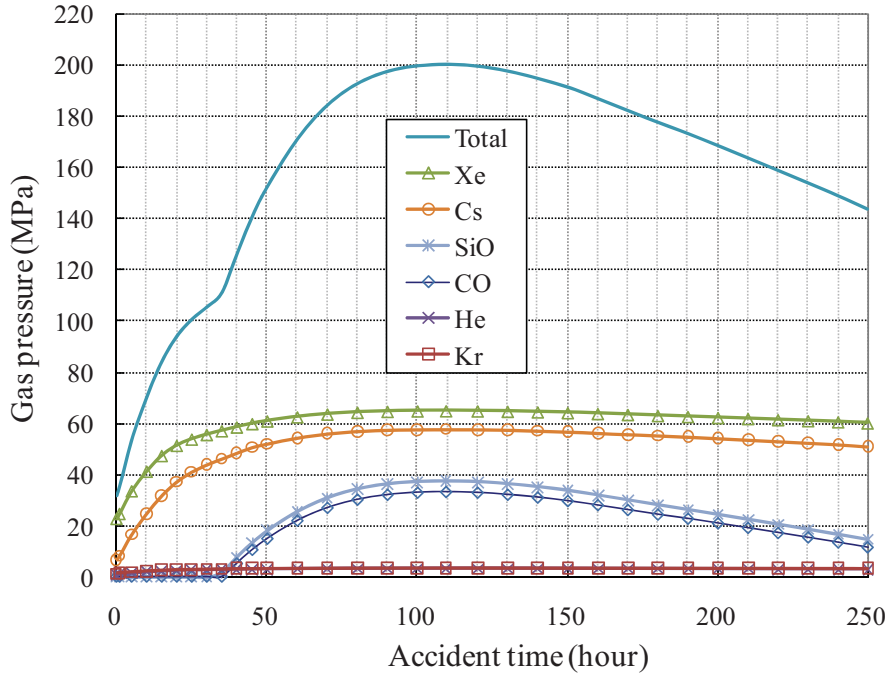

Figure 220. Gas pressure in the void volume in accident conditions (TRU fuel of a 600 MW_{th} DB-HTR).

7.4.4 Thermo-mechanical Analysis of the CFP

Figure 221 and Figure 222 display the tangential stresses at the inner surfaces of the IPyC, SiC, and OPyC layers during irradiation. The maximum tensile tangential stress at the inner surface of the IPyC layer is 310.24 MPa at 369.71 EFPD, when the fast fluence is about 1.12×10^{21} n/cm^2 (E > 0.1 MeV). The tangential stress at the inner surface of the SiC layer approaches -89.56 MPa at 1278 EFPD, and increases greatly in the period of the accident. Its maximum value is 446.05 MPa at 109.72 hours after the accident starts.

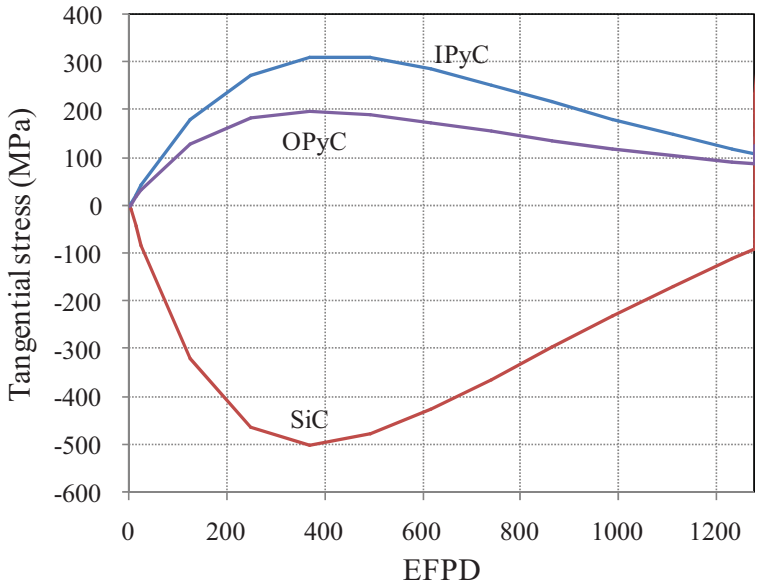

Figure 221. Stress evolutions during normal operation (TRU fuel of a 600 MW_{th} DB-HTR).

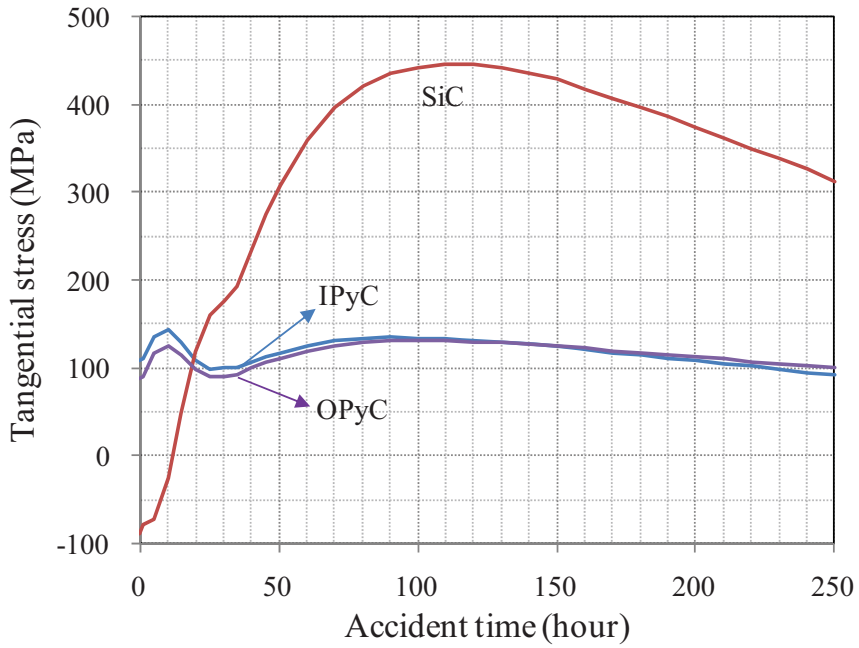

Figure 222. Stress evolutions during an accident (TRU fuel of a 600 MW_{th} DB-HTR).

7.4.5 Failure Fraction of CFPs

Figure 223 and Figure 224 show the failure fractions for 10^8 CFPs. The SiC failure fraction is 5.00×10^{-8} at 1278 EFPD. The thermal decomposition does not contribute to the failure of CFPs during normal operation. The pressure vessel failure is a major failure mechanism until about 40 hours after an accident. The thermal decomposition of the CFPs starts to occur significantly at 20 hours after the accident, and becomes a major failure mechanism after 60 hours after an accident. All the CFPs are broken at about 90.22 hours after the LPCC accident. These results indicate unacceptable levels of core damage during the LPCC.

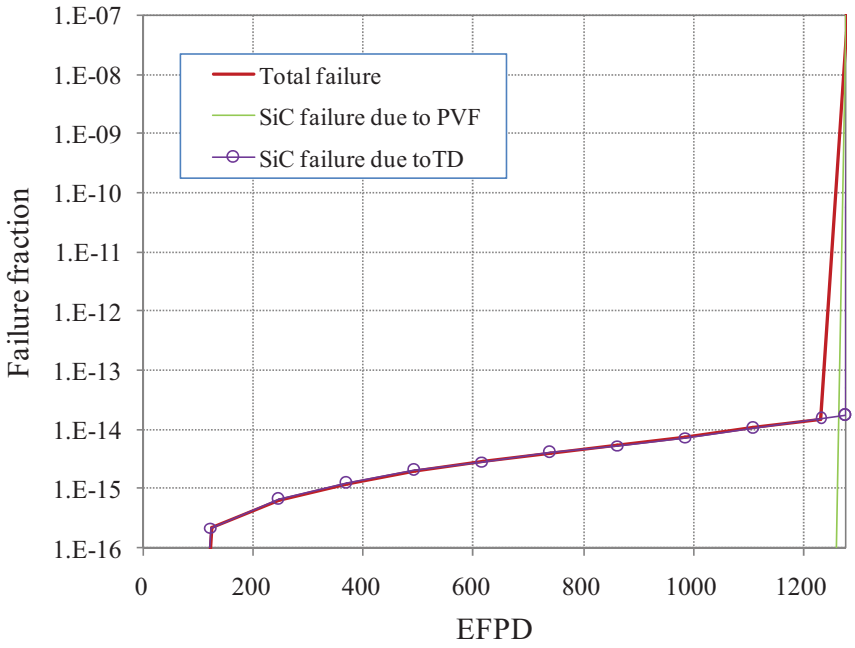

Figure 223. Variation of failure fraction of CFPs (TRU fuel of a 600 MW_{th} DB-HTR).

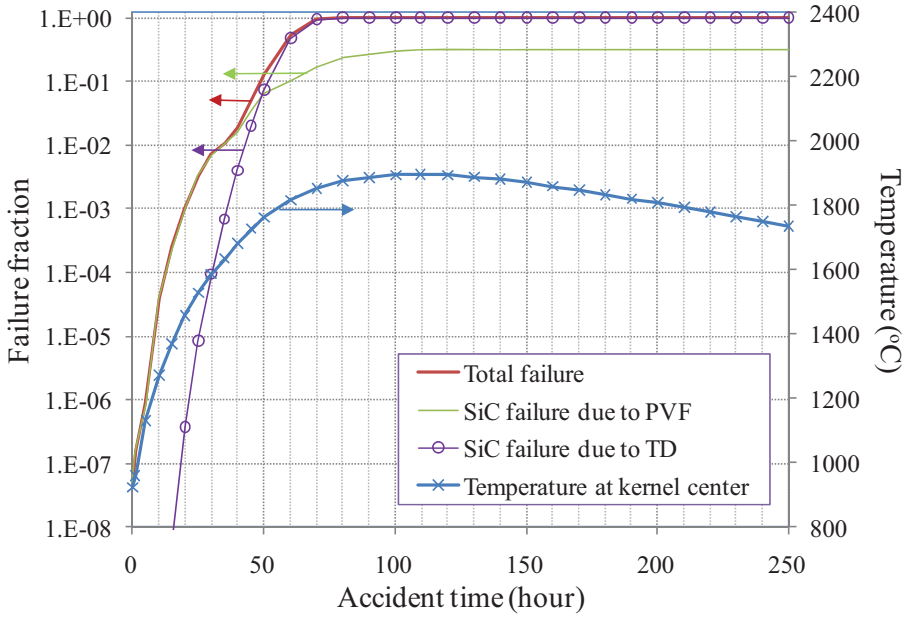

Figure 224. Variation of failure fraction of CFPs during a loss of coolant accident (TRU fuel of a 600 MW_{th} DB-HTR).

7.4.6 FP Transport

Figure 225 and Figure 226 display the fractional releases of Ag-110m, Cs-137, Sr-90 and Kr-85 into the coolant during normal reactor operation and during an accident, respectively. For metallic FPs, the fractional releases are large, of the same order as for cesium, silver, and strontium. The fractional releases of the metallic FPs increase with irradiation. The fractional release of krypton is nearly constant during normal operation because of the very low failure fraction and the constant coolant temperature of 864°C. During the LPCC, the fractional release of silver increases most rapidly among the fission products considered. At 109.72 hours after an accident, the fractional releases of silver, cesium, strontium, and krypton are 1.000, 1.000, 0.111, and 0.999, respectively. All species except strontium are completely released in accident conditions.

Table 25 and Table 26 present the fractional distributions of silver, cesium, strontium, and krypton at the reactor operation time of 1278 EFPD and at 109.72 hours after an accident, respectively. The SiC failure fraction is 5.00×10^{-8} at 1278 EFPD during normal operation and 1 at 109.73 hours after an accident, respectively. Among the FP amounts existing at 1278 EFPD, the intact CFPs contain 99.9% of silver, about 100% of cesium, 99.7% of strontium, and nearly all krypton. Strontium is better retained in the graphite matrix than silver and cesium. At 109.72 hours after an accident, the fractional releases in intact CFPs are all zero because the failure fraction is one at that time. Nearly all silver, cesium, and krypton are released into the coolant. In the case of strontium, about 85.0% stays in the matrix graphite, 3.9% in the structural graphite, and 11.1% is released.

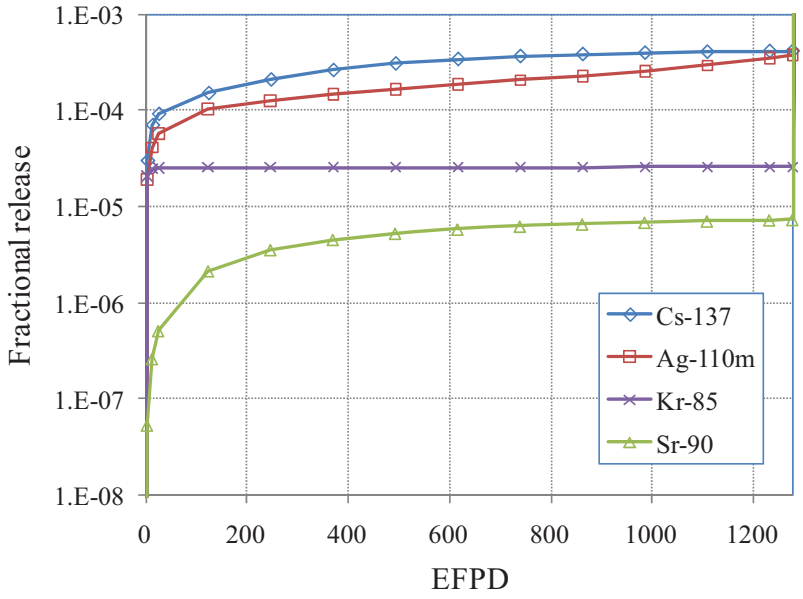

Figure 225. Fractional releases of silver, cesium, strontium, and krypton during normal operation (TRU fuel of a 600 MW_{th} DB-HTR).

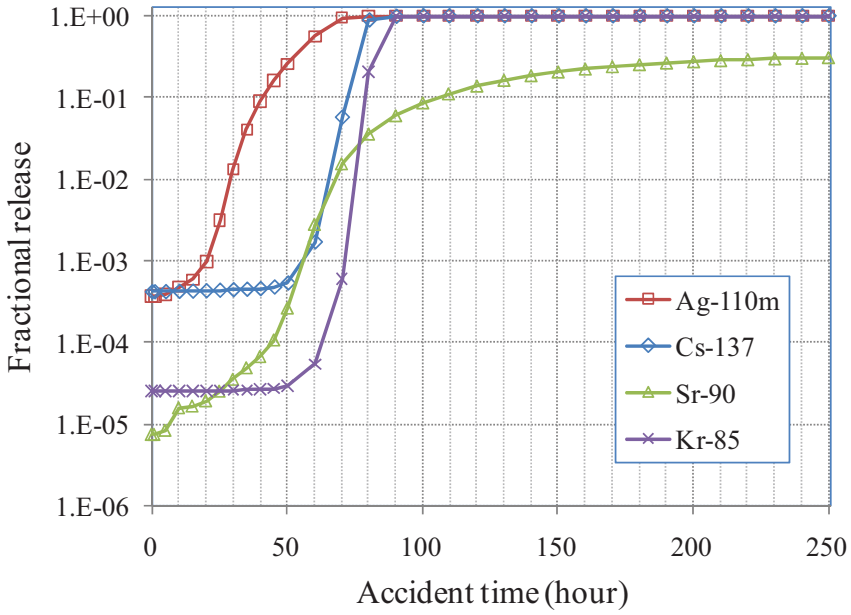

Figure 226. Fractional releases of silver, cesium, strontium, and krypton during an accident (TRU fuel of a 600 MW_{th} DB-HTR).

Table 25. Fractional distributions of silver, cesium, strontium, and krypton at 1278 EFPD (TRU fuel of a 600 MW_{th} DB-HTR).

	Ag-110m	Cs-137	Sr-90	Kr-85
Intact CFPs	9.99E-01	~1	9.97E-01	~1
Failed CFPs	8.30E-13	1.71E-13	1.71E-09	1.30E-13
Matrix graphite	3.90E-04	2.09E-05	2.45E-03	4.36E-12
Gap	4.99E-14	2.82E-15	1.48E-20	0
Structural graphite	2.03E-04	1.27E-05	2.63E-04	8.31E-11
Accumulated release	3.75E-04	4.18E-04	7.37E-06	2.58E-05

Table 26. Fractional distributions of silver, cesium, strontium, and krypton at 109.72 hours after an accident (TRU fuel of a 600 MW_{th} DB-HTR).

	Ag-110m	Cs-137	Sr-90	Kr-85
Intact CFPs	0	0	0	0
Failed CFPs	1.17E-07	3.03E-06	3.16E-08	5.61E-04
Matrix graphite	8.69E-07	4.96E-04	8.50E-01	1.75E-06
Gap	1.64E-11	9.73E-09	5.12E-08	0
Structural graphite	1.25E-08	7.54E-06	3.87E-02	7.20E-07
Accumulated release	~1	9.99E-01	1.11E-01	9.99E-01

7.4.7 Summary

The microanalysis of the 600 MW_{th} DB-HTR fuel has been done, including the determination of the gas pressure buildup in the void volume of a CFP, the thermal analyses for a DB-HTR fuel, the thermo-mechanical analyses for a CFP, and the estimation of the failure fractions of a batch of CFPs and the FP releases into a coolant. It was assumed that the DB-HTR was operated at constant temperature and power for 1278 EFPD and was subjected to an LPCC accident event for 250 hours.

- The temperature at the kernel center of the compact center was about 925°C during normal operation, but it increased to more than 1600°C, about 35 hours after the LPCC. During normal operation, temperature gradients are 12.60°C/mm across the kernel, and 182.11°C/mm across the buffer, respectively.
- The gas species that most significantly contribute to gas pressure during normal operation are xenon, cesium, helium, and krypton. Total gas pressure is about 31.82 MPa at 1278 EFPD. The silicon monoxide and carbon monoxide are generated during an accident. The maximum pressure is 200.35 MPa at 109.72 hours after an accident.
- The tangential stress at the inner surface of the SiC layer approaches -89.56 MPa at the end of normal operation, but greatly enlarges to about 446.05 MPa during an accident period. The maximum tensile tangential stress of IPyC inner surface is 310.24 MPa at a fast fluence of about 1.12×10^{21} n/cm^2 ($E > 0.1$ MeV).
- The total failure fraction is 5.00×10^{-8} at the end of normal operation. The pressure vessel failure predominantly contributes to the CFP failure until about 40 hours after an accident, at which the failure fraction is 0.019. The thermal decomposition starts to cause the CFPs to break at 20 hours after an accident, and becomes a major failure mechanism after 60 hours after an accident. Whole particle

failure occurs at about 90.22 hours after the LPCC accident. This indicates that active core cooling systems must be used to prevent excessive temperatures in the event of a loss of primary cooling.

- For metallic FPs, the fractional releases are large, of the same order as for cesium, silver, and strontium during normal operation. At the elevated temperatures of an accident condition, all of silver, cesium, and krypton are released. 85.0% of strontium is contained in the matrix graphite of a compact. 11.1% of strontium is released into a coolant, which is very high. These high fractional releases resulted from the high failure fraction of CFPs.
- The failure fraction is one during the LPCC. In order to secure the integrity of CFPs during the LPCC accident in a 600 MW_{th} DB-HTR loaded with the TRU fuel, it is necessary to prevent the excessive temperature conditions and to reduce the gas pressure in a CFP. Thus, it is necessary to decrease the power generation and to increase the buffer size of the CFP.

7.5 Fuel Performance for a U+TRU Fuel of a 600 MWth DB-HTR

This DB-HTR kernel material is 30% UO_2 + 70% (5% NpO_2 + 95% $PuO_{1.8}$) mixed with 0.6 moles SiC per mole of heavy metal.

7.5.1 Nuclide Composition/Operating Conditions/Fuel Burnup and Depletion

Table 27 presents the nuclide composition in the CFP kernel in the DB-HTR fuel. It was assumed that the DB-HTR was operated at the coolant temperature of 864°C and the kernel power of 51.56 mW for three cycles having the average length of 355 EFPD, and then was subjected to a LPCC accident for 250 hours, as shown in Figure 227. The kernel power decreases rapidly during an LPCC event. The maximum coolant temperature is 1846.28°C at 104.72 hours. Figure 228 displays the burnup history. The final burnup and fast fluence are 432 GWd/tHM (42.08 %FIMA) and 3.422×10^{21} n/cm^2 (E > 0.1 MeV) at 1065 EFPD.

Table 27. Nuclide composition in the kernel (U+TRU fuel of a 600 MW_{th} DB-HTR).

Nuclides	Moles	Composition
U-235	1.527E-09	0.133%
U-238	2.138E-07	18.617%
Np-237	2.513E-08	2.187%
Pu-238	1.518E-08	1.322%
Pu-239	2.931E-07	25.516%
Pu-240	1.103E-07	9.606%
Pu-241	2.591E-08	2.255%
Pu-242	3.289E-08	2.863%
O-16	1.340E-06	116.687%
C-12	4.307E-07	37.500%
Si-28	3.974E-07	34.599%
Si-29	2.005E-08	1.746%
Si-30	1.327E-08	1.155%

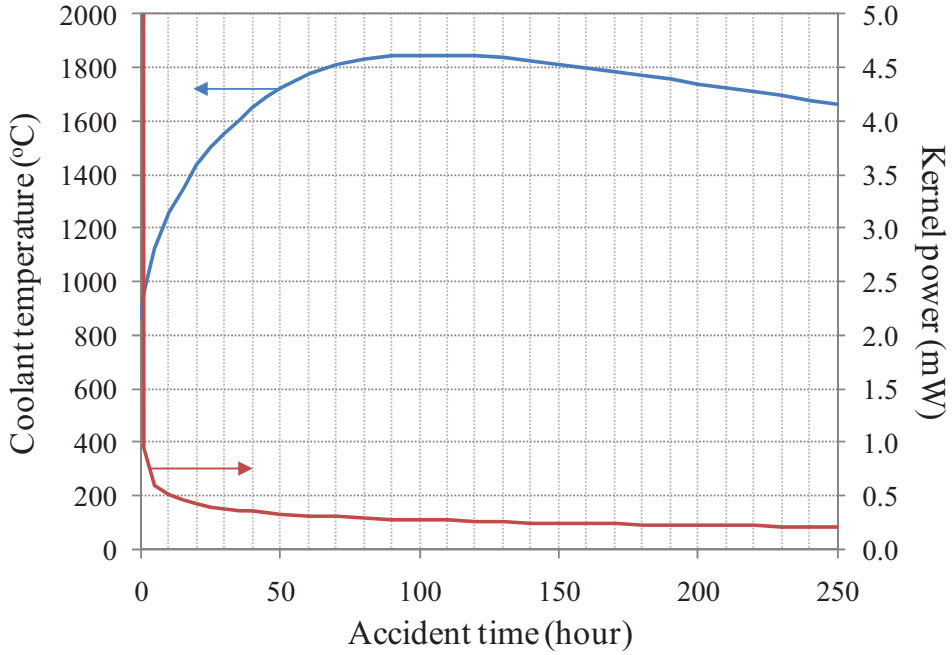

Figure 227. Coolant temperature and kernel power of the DB-HTR during an accident (U+TRU fuel of a 600 MW_{th} DB-HTR).

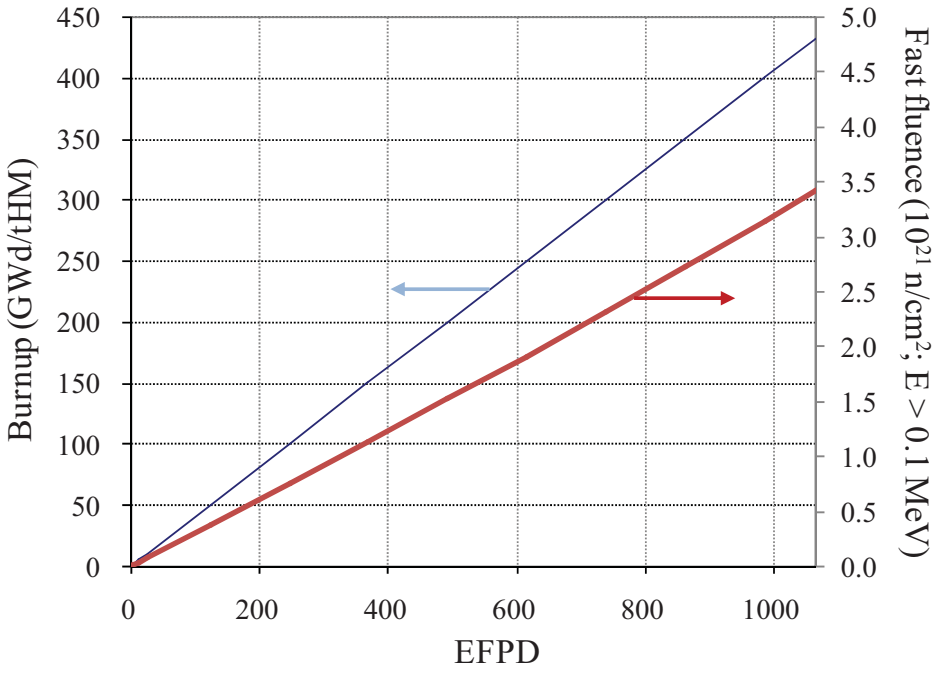

Figure 228. Fuel burnup history (U+TRU fuel of a 600 MW_{th} DB-HTR).

7.5.2 Thermal Analysis of Fuel Block and CFP

Figure 229 and Figure 230 show the temperature histories at the coolant, at the center of a compact, and at the center of a kernel located at the compact center during normal operation and accident, respectively. The temperature at the center of a kernel located at the compact center is about 923°C during normal operation. But it increases with the accident temperature of the coolant during an accident, when its maximum is 1846.55°C. In Figure 230, the temperatures at coolant, compact, and kernel during an accident are nearly the same because the power is negligible during the LPCC, as shown in Figure 227.

Figure 231 represents the temperature distribution in an equivalent cylinder. During normal operation, the temperature jumps down at the gap between compact and structural graphite due to the relatively low thermal conductivity of helium in the gap. During an accident, the temperature distribution in the equivalent cylinder is nearly constant. Figure 232 displays the temperature distribution in a CFP. The thermal conductivity of the buffer was assumed to be 0.5 W/(m K). During normal operation, a relatively large temperature drop occurs across the buffer because its thermal conductivity is much lower than those of other layers. At 2.46 days, the temperature gradients are 11.03°C/mm across the kernel and 159.47°C/mm across the buffer. The temperature within the CFP is nearly constant during an accident.

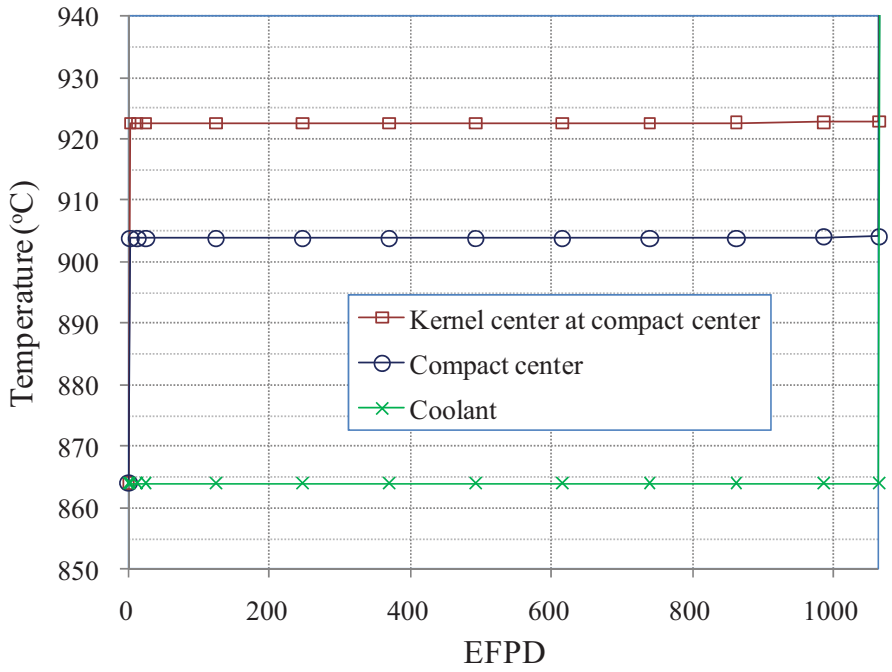

Figure 229. Temperature history during normal operation (U+TRU fuel of a 600 MW_{th} DB-HTR).

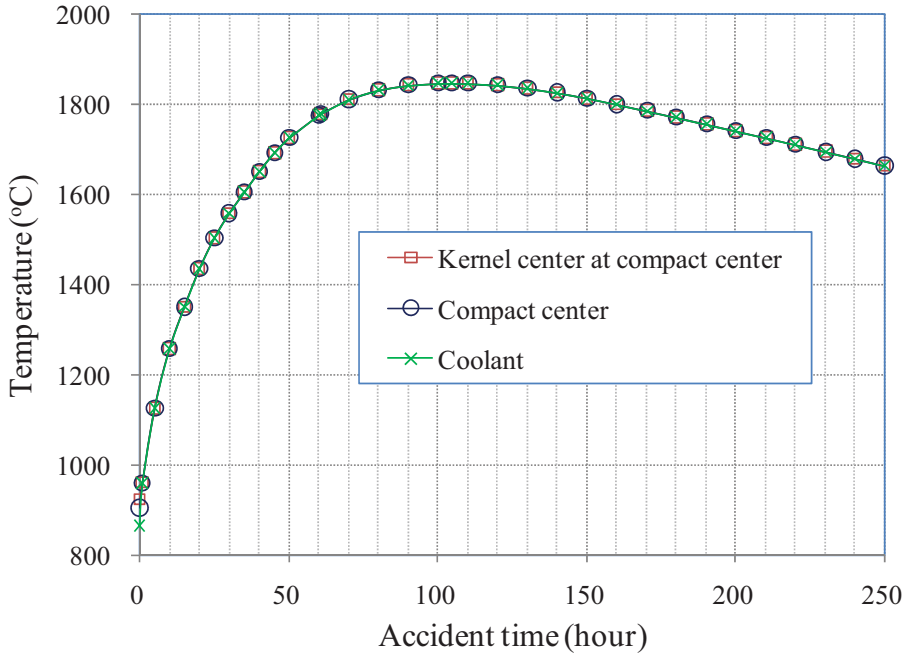

Figure 230. Temperature variation during an accident (U+TRU fuel of a 600 MW_{th} DB-HTR).

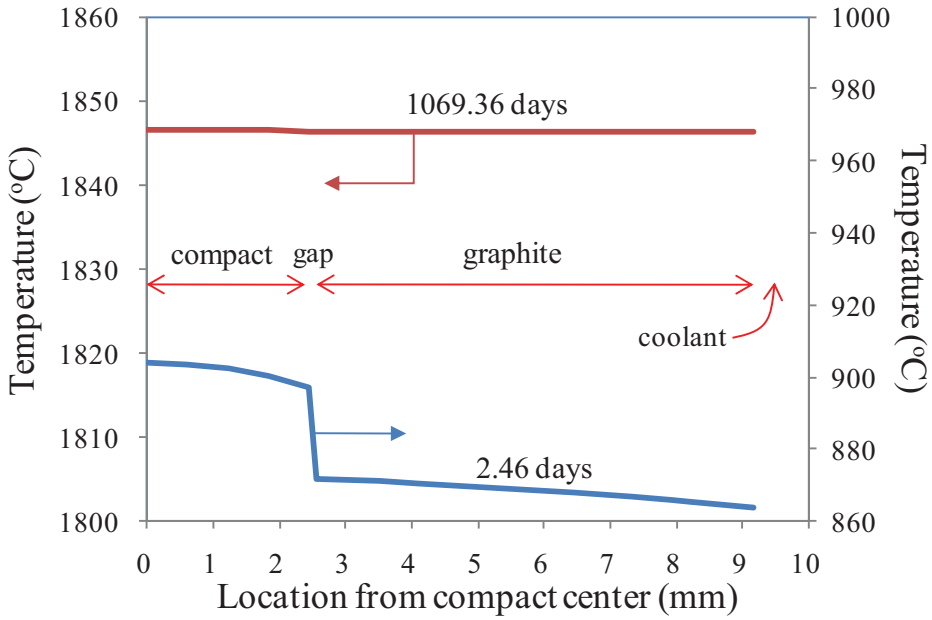

Figure 231. Temperature distribution across the compact and structural graphite (TRU fuel of a 600 MW_{th} DB-HTR).

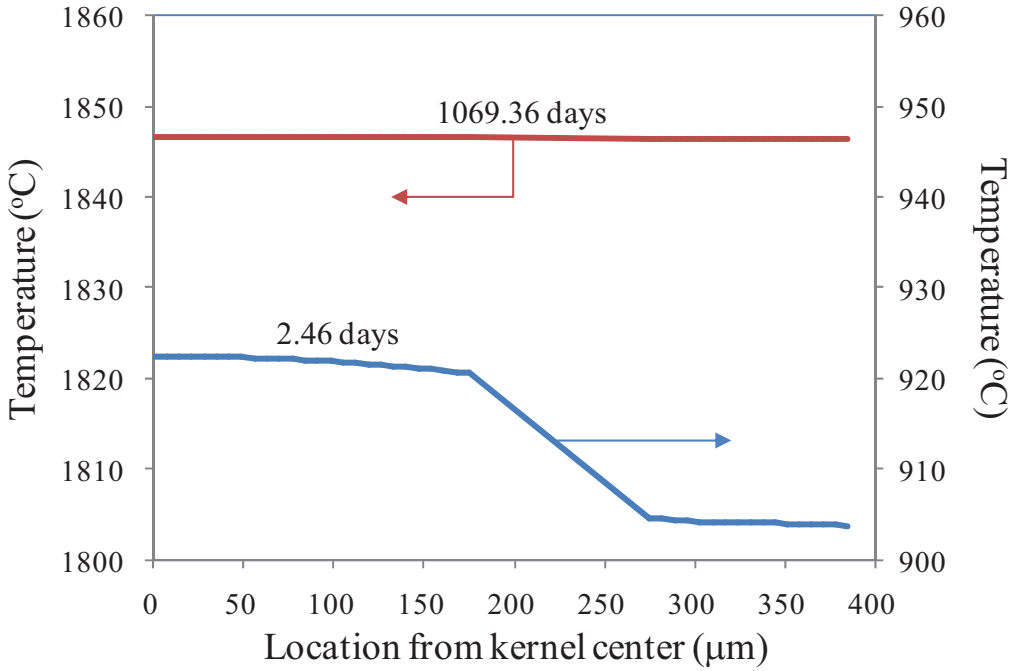

Figure 232. Temperature distribution in a CFP located at the center of the compact in a unit cell (U+TRU fuel of a 600 MW_{th} DB-HTR).

7.5.3 Gas Pressure Buildup in the Void Volume of Kernel and Buffer

Figure 233 and Figure 234 show the gas pressure in the void volume during normal operation and in accident conditions, respectively. Xenon, cesium, helium, and krypton are major gas species during normal operations, but carbon monoxide and silicon monoxide are additionally generated under the accident condition. The total gas pressure is 24.99 MPa at 1065 EFPD and 150.92 MPa at 104.72 hours after an accident.

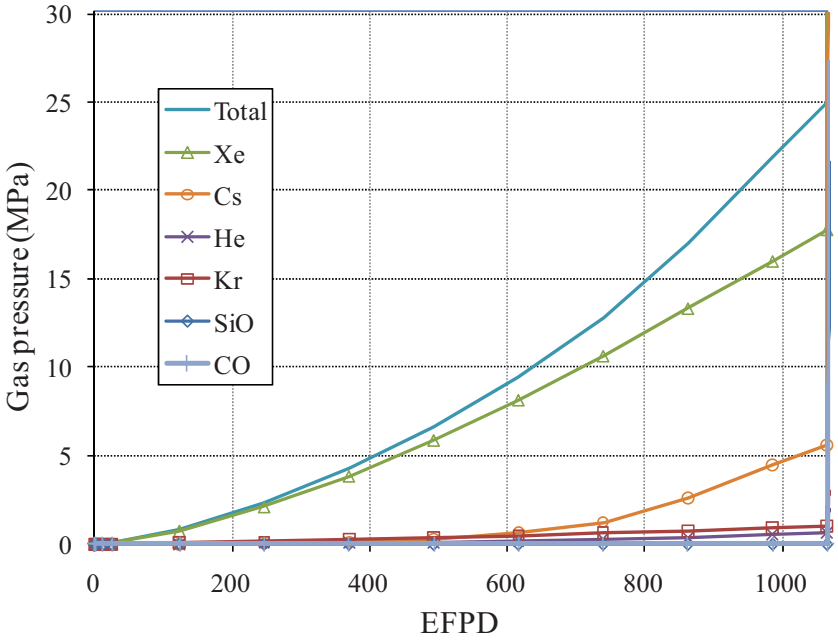

Figure 233. Gas pressure in the void volume during normal operation (U+TRU fuel of a 600 MW_{th} DB-HTR).

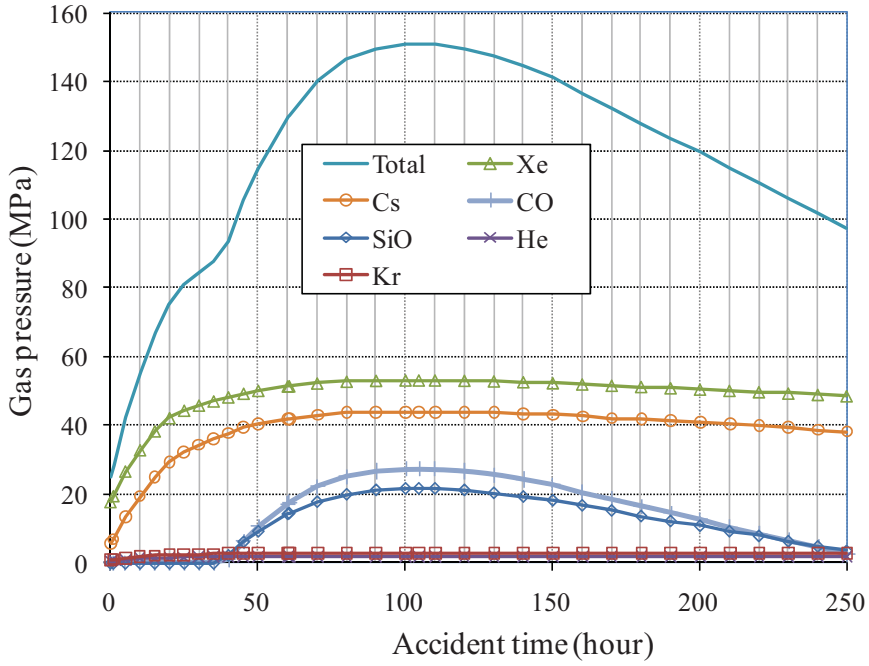

Figure 234. Gas pressure in the void volume in accident conditions (U+TRU fuel of a 600 MW_{th} DB-HTR).

7.5.4 Thermo-mechanical Analysis of the CFP

Figure 235 and Figure 236 display the tangential stresses at the inner surfaces of the IPyC, SiC, and OPyC layers during irradiation. The maximum tensile tangential stress at the inner surface of the IPyC layer is 311.60 MPa at 369.71 EFPD, when the fast fluence is about 1.13×10^{21} n/cm^2 (E > 0.1 MeV). The tangential stress at the inner surface of the SiC layer approaches -174.07 MPa at 1065 EFPD, and increases greatly in the period of the accident. Its maximum value is 257.29 MPa at 104.72 hours after the accident starts.

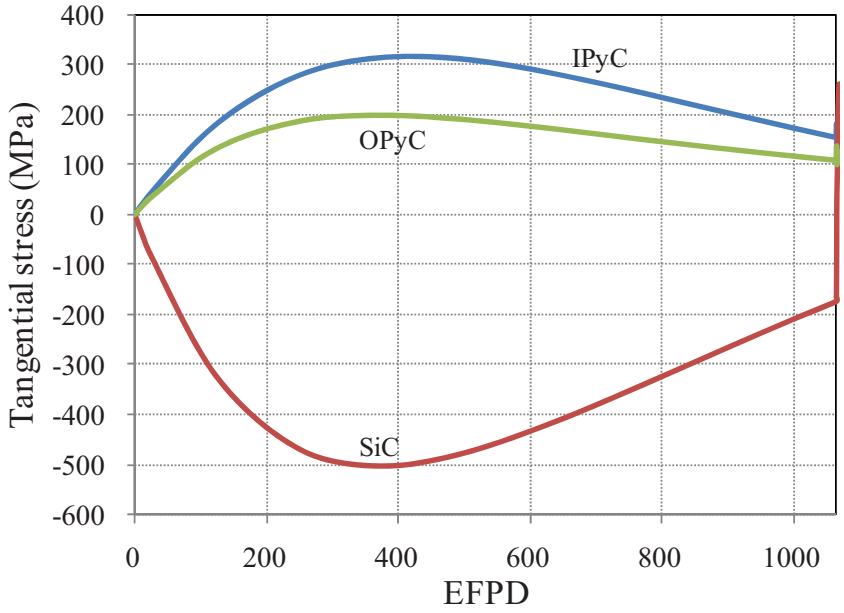

Figure 235. Stress evolutions during normal operation (U+TRU fuel of a 600 MW_{th} DB-HTR).

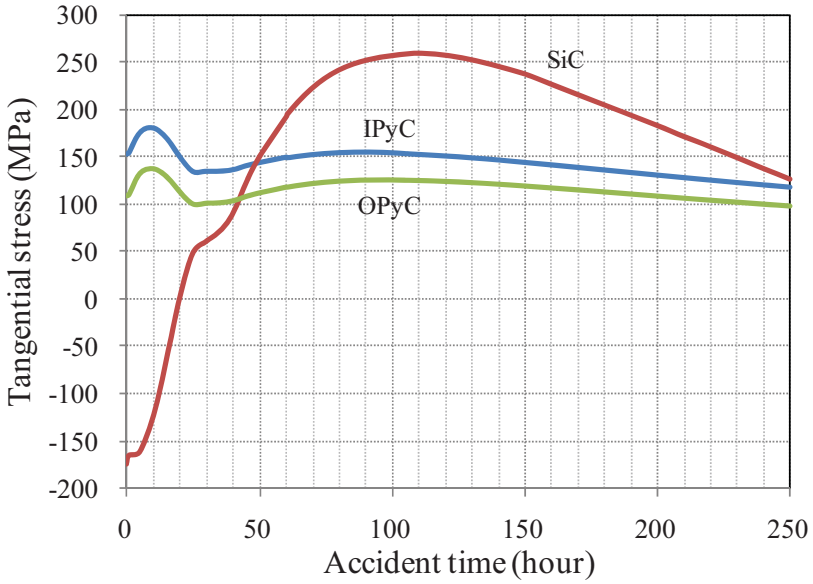

Figure 236. Stress evolutions during an accident (U+TRU fuel of a 600 MW_{th} DB-HTR).

7.5.5 Failure Fraction of CFPs

Figure 237 and Figure 238 show the failure fractions for 10^8 CFPs. The SiC failure fraction is 7.77×10^{-15} at 1065 EFPD. Both the pressure vessel failure and the thermal decomposition do not contribute to the failure of CFPs during normal operation. The pressure vessel failure is a major failure mechanism until about 35 hours after an accident. The thermal decomposition of the CFPs starts to occur significantly at 20 hours after the accident, and becomes a major failure mechanism after 60 hours after an accident. All the CFPs are broken at about 120.22 hours after the LPCC accident. These results indicate unacceptable levels of core damage during the LPCC.

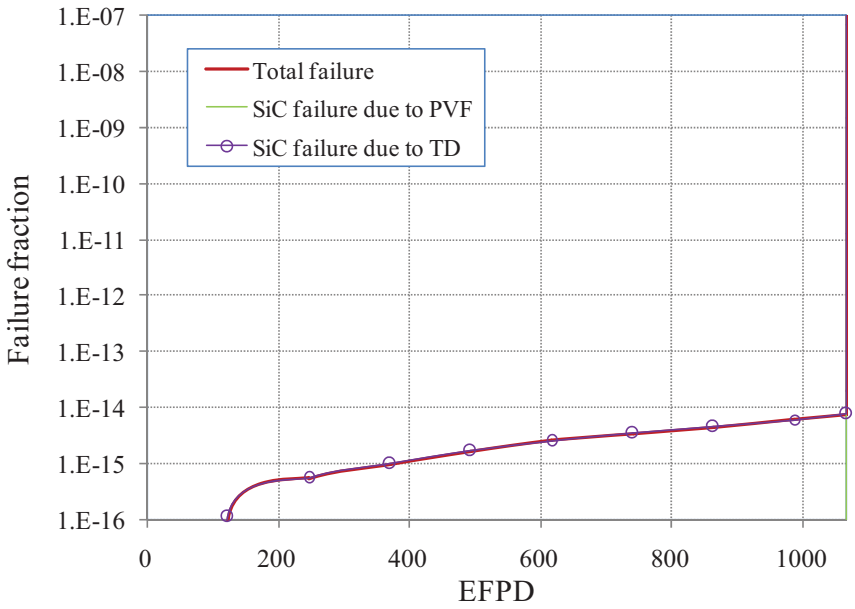

Figure 237. Variation of failure fraction of CFPs (U+TRU fuel of a 600 MW_{th} DB-HTR).

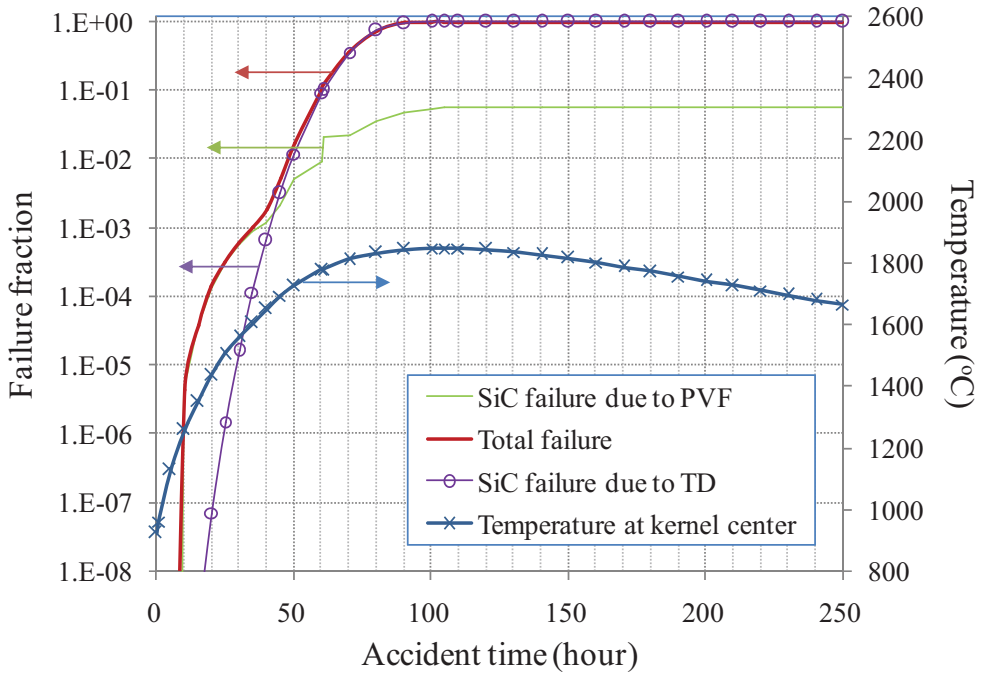

Figure 238. Variation of failure fraction of CFPs during a loss of coolant accident (U+TRU fuel of a 600 MW_{th} DB-HTR).

7.5.6 FP Transport

Figure 239 and Figure 240 display the fractional releases of Ag-110m, Cs-137, Sr-90, and Kr-85 into the coolant during normal reactor operation and during an accident, respectively. For metallic FPs, the fractional releases are large, of the order of cesium, silver, and strontium. The fractional releases of the metallic FPs increase with irradiation. The fractional release of krypton is nearly constant during normal operation because of the very low failure fraction and the constant coolant temperature of 864°C. During the LPCC, the fractional release of silver increases most rapidly among the fission products considered. At 104.72 hours after an accident, the fractional releases of silver, cesium, strontium, and krypton are 0.999, 0.891, 0.052, and 0.625, respectively.

Table 28 and Table 29 present the fractional distributions of silver, cesium, strontium, and krypton at the reactor operation time of 1065 EFPD and at 104.72 hours after an accident, respectively. The SiC failure fraction is 7.77×10^{-15} at 1065 EFPD during normal operation and 0.999 at 104.72 hours after an accident, respectively. Among the FP amounts existing at 1065 EFPD, the intact CFPs contain 99.9% of silver, about 100% of cesium, 99.9% of strontium, and nearly all krypton. Strontium is better retained in the graphite matrix than silver and cesium. At 104.72 hours after an accident, about 91.2% of strontium stays in the matrix graphite, 3.6% in the structural graphite, and 5.2% is released.

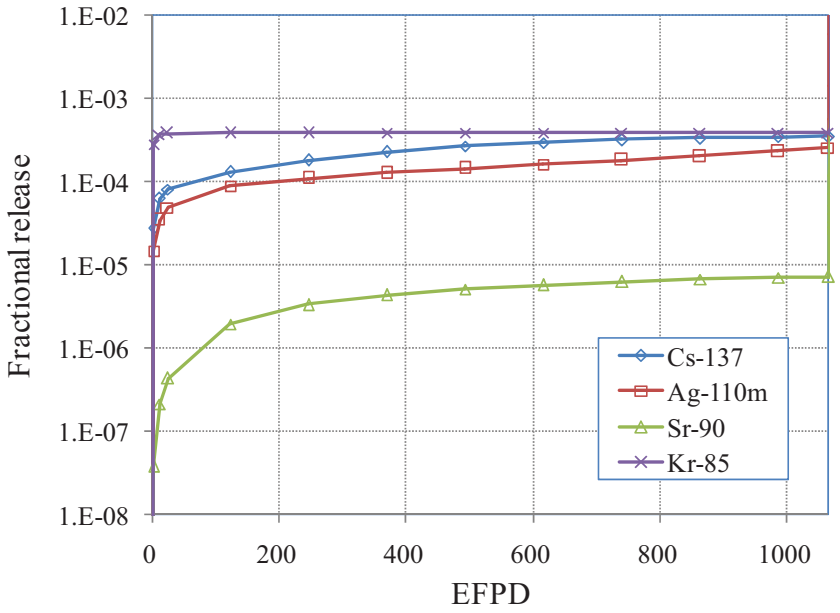

Figure 239. Fractional releases of silver, cesium, strontium, and krypton during normal operation (U+TRU fuel of a 600 MW_{th} DB-HTR).

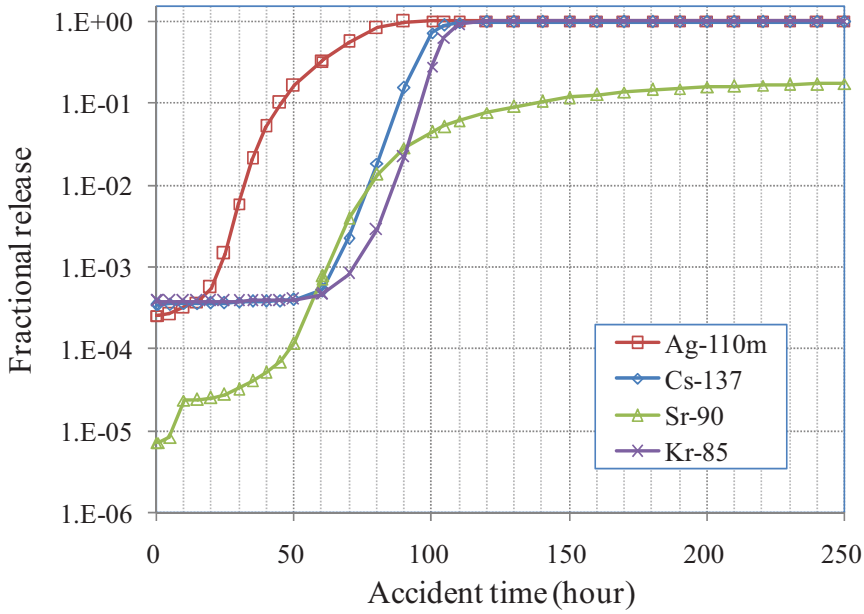

Figure 240. Fractional releases of silver, cesium, strontium, and krypton during an accident (U+TRU fuel of a 600 MW_{th} DB-HTR).

Table 28. Fractional distributions of silver, cesium, strontium, and krypton at 1065 EFPD (U+TRU fuel of a 600 MW_{th} DB-HTR).

	Ag-110m	Cs-137	Sr-90	Kr-85
Intact CFPs	9.99E-01	~1	9.99E-01	~1
Failed CFPs	1.32E-19	3.08E-20	3.26E-16	2.31E-20
Matrix graphite	2.69E-04	2.45E-05	1.20E-03	1.33E-11
Gap	3.48E-14	3.34E-15	8.88E-21	0
Structural graphite	1.26E-04	1.29E-05	2.10E-04	1.63E-11
Accumulated release	2.56E-04	3.52E-04	7.31E-06	3.87E-04

Table 29. Fractional distributions of silver, cesium, strontium, and krypton at 104.72 hours after an accident (U+TRU fuel of a 600 MW_{th} DB-HTR).

	Ag-110m	Cs-137	Sr-90	Kr-85
Intact CFPs	3.70E-04	7.06E-02	9.66E-05	3.74E-01
Failed CFPs	1.70E-05	2.13E-04	5.18E-06	1.11E-03
Matrix graphite	1.64E-04	3.75E-02	9.12E-01	1.81E-05
Gap	2.25E-09	5.37E-07	2.93E-08	0
Structural graphite	2.71E-06	6.48E-04	3.56E-02	1.90E-05
Accumulated release	9.99E-01	8.91E-01	5.20E-02	6.25E-01

7.5.7 Summary

The microanalysis of the 600 MW_{th} DB-HTR fuel has been done, including the determination of the gas pressure buildup in the void volume of a CFP, the thermal analyses for a DB-HTR fuel, the thermo-mechanical analyses for a CFP, and the estimation of the failure fractions of a batch of CFPs and the FP releases into a coolant. It was assumed that the DB-HTR was operated at constant temperature and power for 1065 EFPD and was subjected to an LPCC accident event for 250 hours.

- The temperature at the kernel center of the compact center was about 923°C during normal operation, but it increased to more than 1600°C about 35 hours after the LPCC. During normal operation, temperature gradients are 11.03°C/mm across the kernel and 159.47°C/mm across the buffer, respectively.
- The gas species that most significantly contributes to gas pressure during normal operation are xenon, cesium, helium, and krypton. Total gas pressure is about 24.99 MPa at 1065 EFPD. The silicon monoxide and carbon monoxide are also generated during an accident. The maximum pressure is 150.92 MPa at 104.72 hours after an accident.
- The tangential stress at the inner surface of the SiC layer approaches -174.07 MPa at the end of normal operation, but greatly enlarges to about 257.29 MPa during an accident period. The maximum tensile tangential stress of IPyC inner surface is 311.60 MPa at a fast fluence of about 1.13×10^{21} n/cm^2 (E > 0.1 MeV).
- The total failure fraction is nearly zero at the end of normal operation. The pressure vessel failure dominantly contributes to the CFP failure until about 35 hours after an accident. The thermal decomposition starts to cause the CFPs to break significantly at 20 hours after an accident, and becomes a major failure mechanism after 60 hours after an accident. Whole particle failure occurs at

about 120.22 hours after the LPCC accident. This indicates that active core cooling systems must be used to prevent excessive temperatures in the event of a loss of primary cooling.

- For metallic FPs, the fractional releases are large, of the same order as for cesium, silver, and strontium during normal operation. At the elevated temperatures of an accident condition, nearly all of silver, cesium, and krypton are released. These high fractional releases resulted from the high failure fraction of CFPs. At 104.72 hours after an accident, 91.2% of strontium is contained in the matrix graphite of a compact, and 5.2% of strontium is released into a coolant.
- The failure fraction is one during the LPCC. To secure the integrity of CFPs during the LPCC accident in a 600 MW_{th} DB-HTR loaded with the mixed fuel of uranium and TRU, it is necessary to prevent the excessive temperature conditions and to reduce the gas pressure in a CFP. It is thus necessary to decrease the power generation and to increase the buffer size of the CFP.

7.6 Fuel Performance for a TRU fuel of a 450 MW_{th} DB-HTR

This DB-HTR fuel kernel is 0.2% UO_2 + 99.8% (5% NpO_2 + 95% $PuO_{1.8}$) mixed with 0.6 moles SiC per mole of heavy metal.

7.6.1 Nuclide Composition/Operating Conditions/Fuel Burnup and Depletion

Table 30 presents the nuclide composition in the CFP kernel in the DB-HTR fuel. It was assumed that the DB-HTR was operated at the coolant temperature of 862°C and the kernel power of 45.84 mW for three cycles having the average length of 554 EFPD, and then was subjected to an LPCC accident for 250 hours, as shown in Figure 241. The kernel power decreases rapidly during the LPCC. The maximum coolant temperature is 1595.39°C at 100.22 hours. Figure 242 displays the burnup history. The final burnup and fast fluence are 554 GWd/tHM (54.72 % FIMA) and 3.991×10^{21} n/cm^2 (E > 0.1 MeV) at 1662 EFPD.

Table 30. Nuclide composition in the kernel (TRU fuel of a 450 MW_{th} DB-HTR).

Nuclides	Moles	Composition
U-235	1.030E-11	0.001%
U-238	1.443E-09	0.124%
Np-237	3.625E-08	3.119%
Pu-238	2.190E-08	1.884%
Pu-239	4.228E-07	36.379%
Pu-240	1.592E-07	13.696%
Pu-241	3.737E-08	3.215%
Pu-242	4.744E-08	4.082%
O-16	1.315E-06	113.149%
C-12	4.359E-07	37.500%
Si-28	4.022E-07	34.600%
Si-29	2.029E-08	1.746%
Si-30	1.342E-08	1.155%

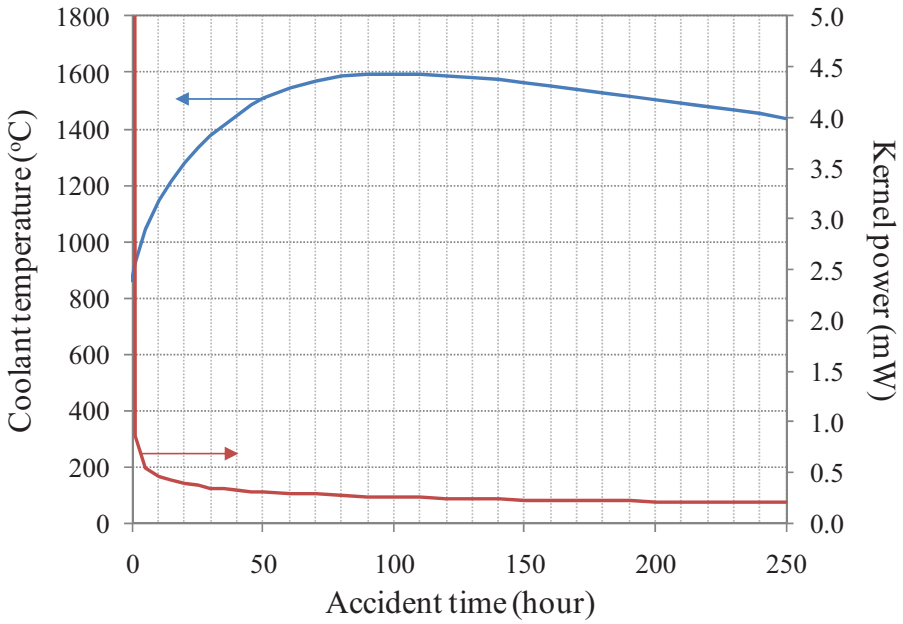

Figure 241. Coolant temperature and kernel power of the DB-HTR during an accident (TRU fuel of a 450 MW_{th} DB-HTR).

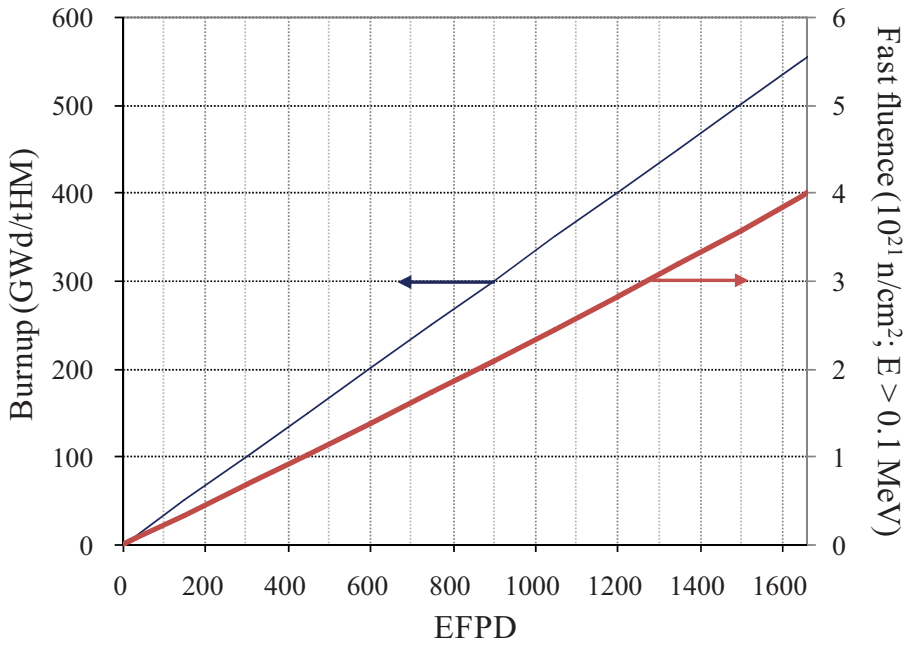

Figure 242. Fuel burnup history (TRU fuel of a 450 MW_{th} DB-HTR).

7.6.2 Thermal Analysis of Fuel Block and CFP

Figure 243 and Figure 244 show the temperature histories at the coolant, at the center of a compact, and at the center of a kernel located at the compact center during normal operation and accident, respectively. The temperature at the center of a kernel located at the compact center is between 909 and 910°C during normal operation. But it increases with the accident temperature of the coolant during an accident, when its maximum is 1595.63°C. In Figure 244, the temperatures at coolant, compact, and kernel during an accident are nearly the same because the power is negligible during the LPCC, as shown in Figure 241.

Figure 245 represents the temperature distribution in an equivalent cylinder. During normal operation, the temperature jumps down at the gap between compact and structural graphite due to the relatively low thermal conductivity of helium in the gap. During an accident, the temperature distribution in the equivalent cylinder is nearly constant. Figure 246 displays the temperature distribution in a CFP. The thermal conductivity of the buffer was assumed to be 0.5 W/(m K). During normal operation, a relatively large temperature drop occurs across a buffer because its thermal conductivity is much lower than those of other layers. At 3.00 days, the temperature gradients are 9.79°C/mm across the kernel and 141.77°C/mm across the buffer. The temperature within the CFP is nearly constant during an accident.

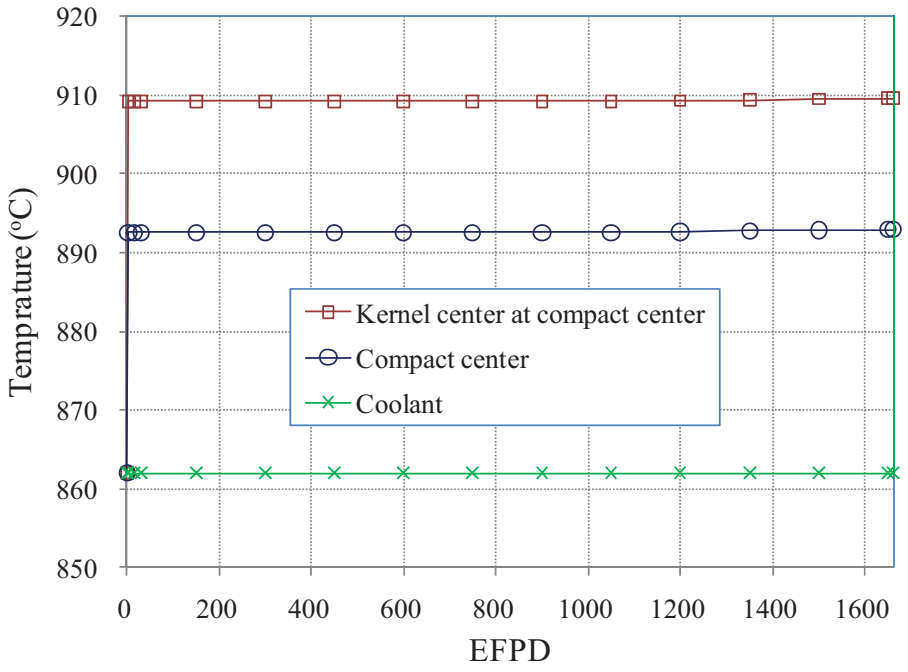

Figure 243. Temperature history during normal operation (TRU fuel of a 450 MW_{th} DB-HTR).

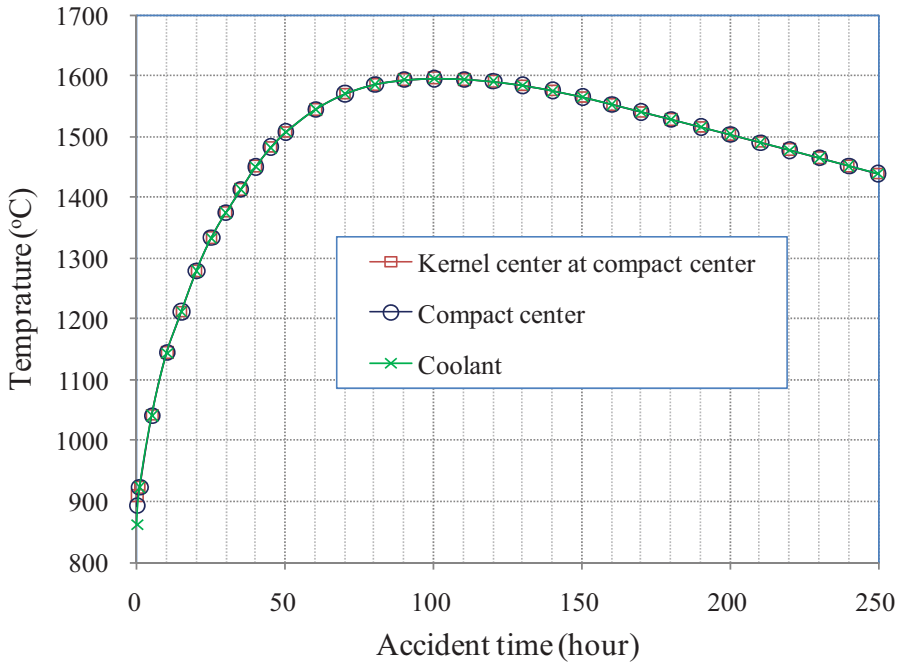

Figure 244. Temperature variation during an accident (TRU fuel of a 450 MW_{th} DB-HTR).

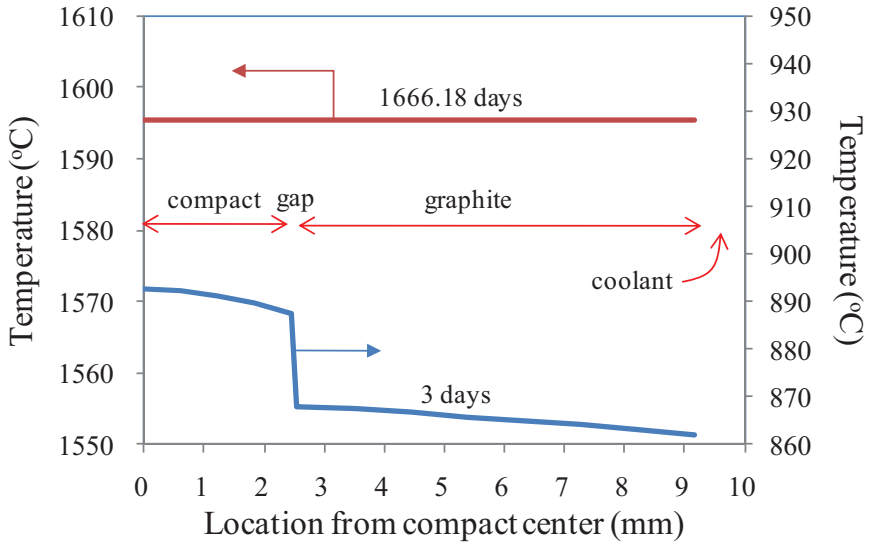

Figure 245. Temperature distribution across the compact and structural graphite (TRU fuel of a 450 MW_{th} DB-HTR).

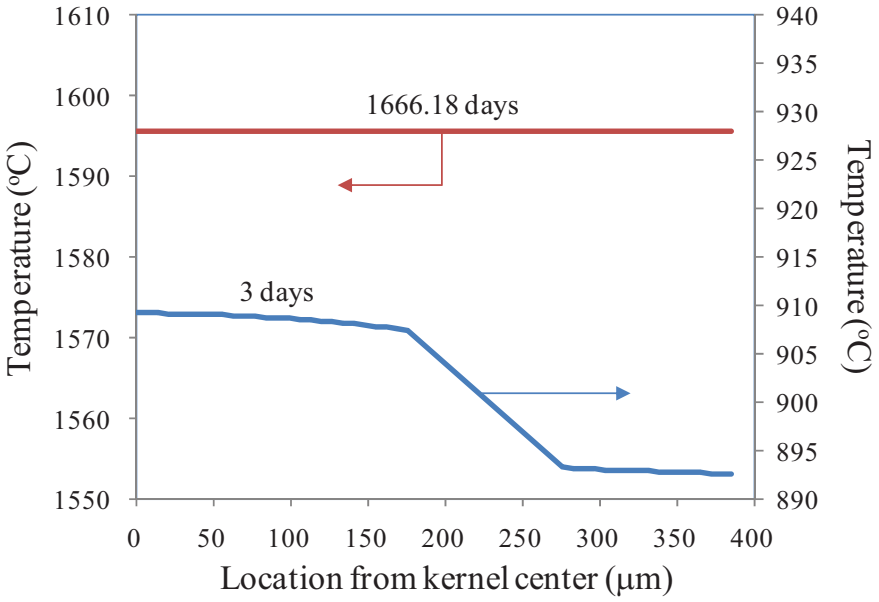

Figure 246. Temperature distribution in a CFP located at the center of the compact in a unit cell (TRU fuel of a 450 MW_{th} DB-HTR).

7.6.3 Gas Pressure Buildup in the Void Volume of Kernel and Buffer

Figure 247 and Figure 248 show the gas pressure in the void volume during normal operation and in accident conditions, respectively. Xenon, cesium, helium, and krypton are major gas species during normal operations and in accident conditions. Carbon monoxide and silicon monoxide are not generated in the accident conditions. The total gas pressure is 32.58 MPa at 1662 EFPD and 116.15 MPa at 100.22 hours after an accident.

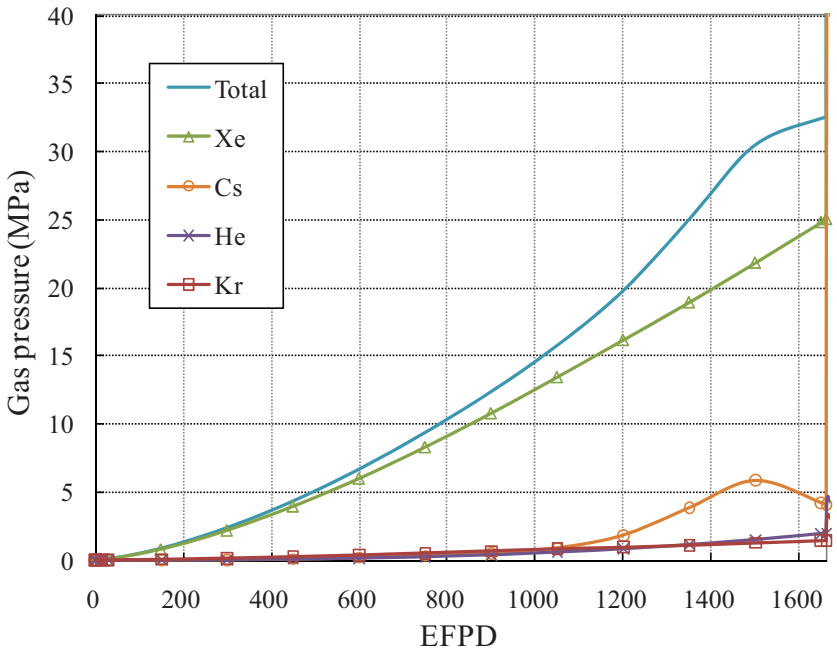

Figure 247. Gas pressure in the void volume during normal operation (TRU fuel of a 450 MW_{th} DB-HTR).

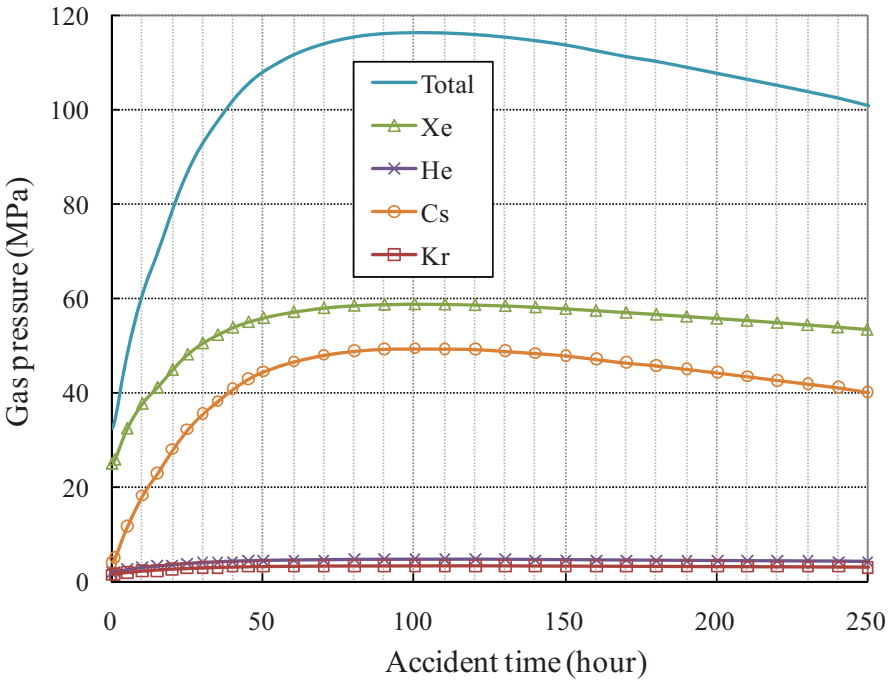

Figure 248. Gas pressure in the void volume in accident conditions (TRU fuel of a 450 MW_{th} DB-HTR).

7.6.4 Thermo-mechanical Analysis of the CFP

Figure 249 and Figure 250 display the tangential stresses at the inner surfaces of the IPyC, SiC, and OPyC layers during irradiation. The maximum tensile tangential stress at the inner surface of the IPyC layer is 320.77 MPa at 600.11 EFPD, when the fast fluence is about 1.37×10^{21} n/cm^2 (E > 0.1 MeV). The tangential stress at the inner surface of the SiC layer approaches -98.01 MPa at 1662 EFPD, and increases greatly in the period of the accident. Its maximum value is 202.57 MPa at 100.22 hours after the accident starts.

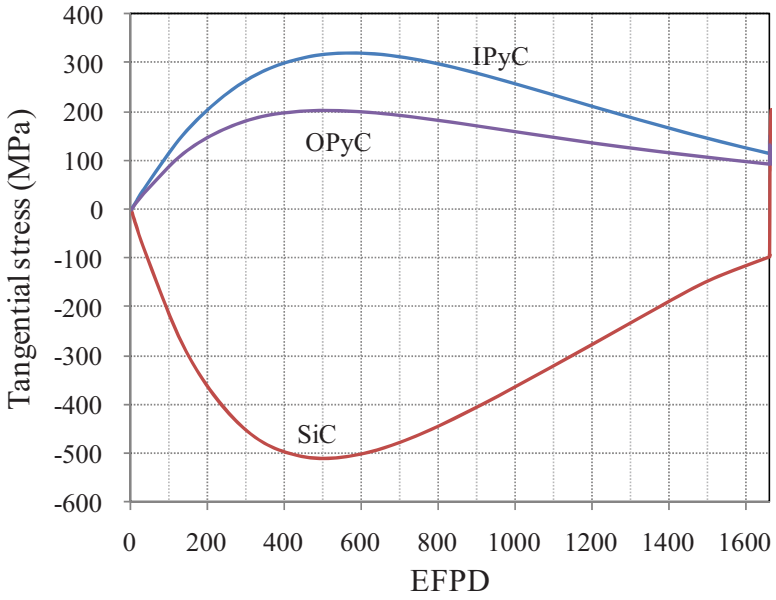

Figure 249. Stress evolutions during normal operation (TRU fuel of a 450 MW_{th} DB-HTR).

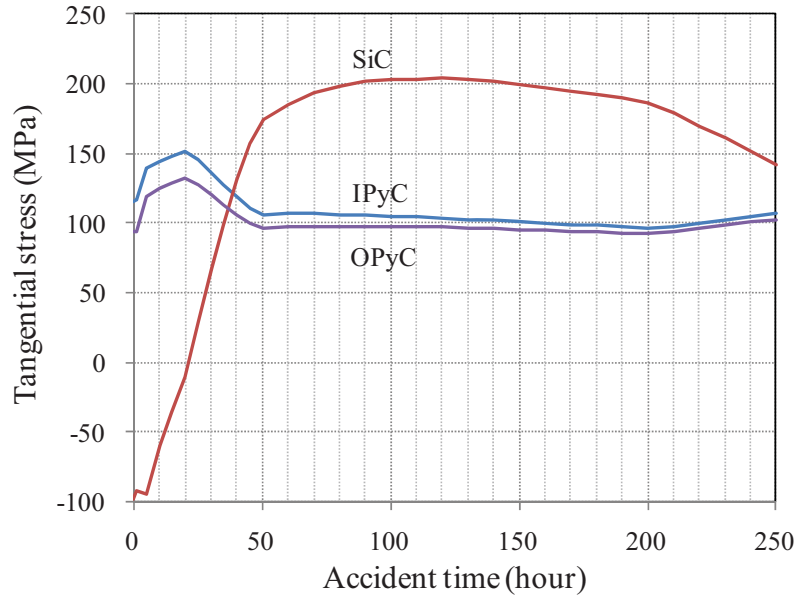

Figure 250. Stress evolutions during an accident (TRU fuel of a 450 MW_{th} DB-HTR).

7.6.5 Failure Fraction of CFPs

Figure 251 and Figure 252 show the failure fractions for 10^8 CFPs. The SiC failure fraction is 3.30×10^{-7} at 1662 EFPD. The thermal decomposition does not contribute to the failure of CFPs during normal operation. The pressure vessel failure is a major failure mechanism until about 100 hours after the accident. The thermal decomposition of the CFPs starts to occur significantly at 30 hours after the accident. The two failure mechanisms contribute, in nearly same degree, to the CFP failure from 150 hours after the accident on. The failure fraction is 5.03×10^{-2} at 250 hours after the LPCC accident.

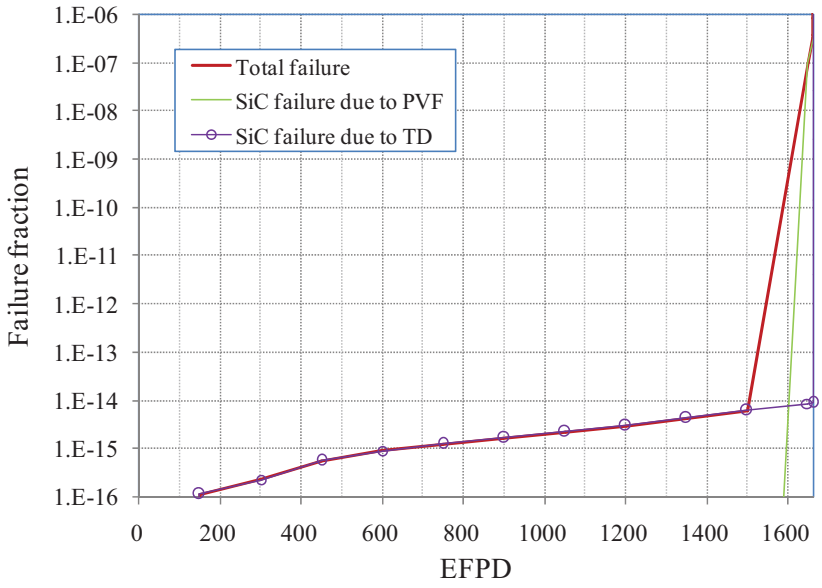

Figure 251. Variation of failure fraction of CFPs (TRU fuel of a 450 MW_{th} DB-HTR).

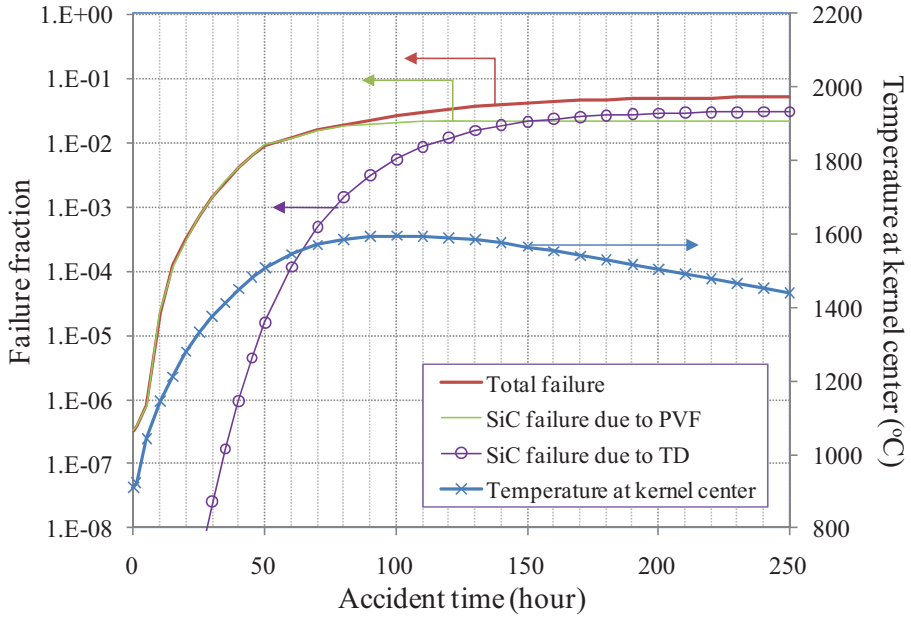

Figure 252. Variation of failure fraction of CFPs during a loss of coolant accident (TRU fuel of a 450 MW_{th} DB-HTR).

7.6.6 FP Transport

Figure 253 and Figure 254 display the fractional releases of Ag-110m, Cs-137, Sr-90 and Kr-85 into the coolant during normal operation and accident, respectively. For metallic FPs, the fractional releases are large, of the same order as for cesium, silver, and strontium. The fractional releases of the metallic FPs increase with irradiation. The fractional release of krypton is nearly constant during a normal operation because of the low failure fraction and the constant coolant temperature of 862°C. At 100.22 hours after an accident, the fractional releases of cesium, silver, strontium, and krypton are 4.88×10^{-4}, 2.59×10^{-1}, 1.30×10^{-4}, and 2.65×10^{-5}, respectively.

Table 31 and Table 32 present the fractional distributions of silver, cesium, strontium, and krypton at the reactor operation time of 1662 EFPD and at 100.22 hours after an accident, respectively. The SiC failure fraction is 3.30×10^{-7} at 1662 EFPD during normal operation and 2.58×10^{-2} at 100.22 hours after an accident, respectively. Among the FP amounts existing at 1662 EFPD, the intact CFPs contain 99.9% of silver, about 100% of cesium, 99.7% of strontium, and nearly all krypton. Strontium is better retained in the graphite matrix than silver and cesium. At 100.22 hours after an accident, 25.9% of silver, 0.005% of cesium, and 2.65×10^{-3} % of krypton are released into the coolant. In the case of strontium, 79.8% is in retention in intact CFPs, 19.8% stays in the matrix graphite, 0.3% in the structural graphite, and 1.30×10^{-2} % is released.

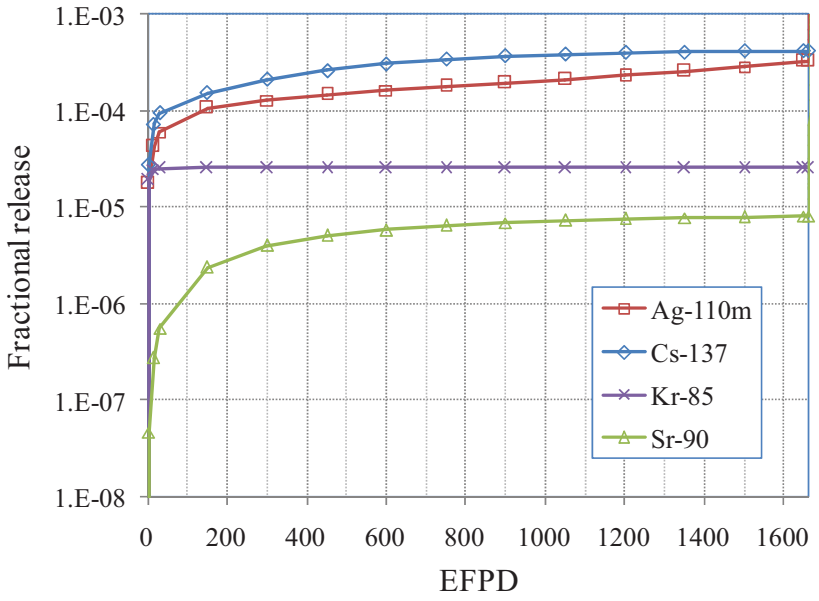

Figure 253. Fractional releases of silver, cesium, strontium, and krypton during normal operation (TRU fuel of a 450 MW_{th} DB-HTR).

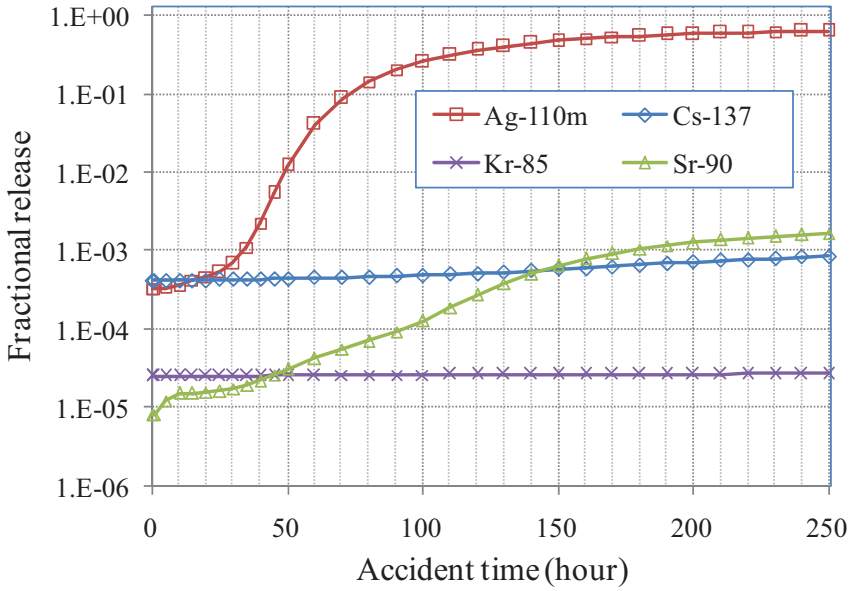

Figure 254. Fractional releases of silver, cesium, strontium, and krypton during an accident (TRU fuel of a 450 MW_{th} DB-HTR).

Table 31. Fractional distributions of silver, cesium, strontium, and krypton at 1662 EFPD (TRU fuel of a 450 MW_{th} DB-HTR).

	Ag-110m	Cs-137	Sr-90	Kr-85
Intact CFPs	9.99E-01	~1	9.97E-01	~1
Failed CFPs	6.27E-12	9.22E-13	1.26E-08	6.69E-13
Matrix graphite	3.34E-04	1.97E-05	2.89E-03	3.39E-12
Gap	3.47E-14	2.15E-15	1.20E-20	0
Structural graphite	1.53E-04	1.01E-05	2.62E-04	6.45E-11
Accumulated release	3.32E-04	4.22E-04	8.23E-06	2.58E-05

Table 32. Fractional distributions of silver, cesium, strontium, and krypton at 100.22 hours after an accident (TRU fuel of a 450 MW_{th} DB-HTR).

	Ag-110m	Cs-137	Sr-90	Kr-85
Intact CFPs	7.28E-01	9.99E-01	7.98E-01	1.00E+00
Failed CFPs	2.18E-07	4.89E-08	6.04E-08	5.36E-08
Matrix graphite	1.33E-02	1.13E-05	1.98E-01	1.71E-10
Gap	2.84E-08	2.51E-11	1.63E-10	0
Structural graphite	4.15E-04	3.75E-07	3.05E-03	1.33E-10
Accumulated release	2.59E-01	4.88E-04	1.30E-04	2.65E-05

7.6.7 Summary

The microanalysis of the 450 MW_{th} DB-HTR fuel has been done, including the determination of the gas pressure buildup in the void volume of a CFP, the thermal analyses for a DB-HTR fuel, the

thermo-mechanical analyses for a CFP, and the estimation of the failure fractions of a batch of CFPs and the FP releases into a coolant. It was assumed that the DB-HTR was operated at constant temperature and power for 1662 EFPD and was subjected to an LPCC accident event for 250 hours.

- The temperature at the kernel center of the compact center was about 910°C during normal operation, and was below 1600°C throughout the LPCC. During normal operation, temperature gradients are 9.8°C/mm across the kernel and 141.77°C/mm across the buffer, respectively.
- The gas species that most significantly contributes to gas pressure during normal operation and in accident conditions are xenon, cesium, helium, and krypton. Total gas pressure is about 32.58 MPa at 1662 EFPD. The maximum pressure is 116.15 MPa at 102.22 hours after an accident.
- The tangential stress at the inner surface of the SiC layer approaches -98.01 MPa at the end of normal operation, but greatly enlarges to about 202.57 MPa during an accident period. The maximum tensile tangential stress of IPyC inner surface is 320.77 MPa at a fast fluence of about 1.37×10^{21} n/cm^2 (E > 0.1 MeV).
- The total failure fraction is 3.30×10^{-7} at the end of normal operation. The pressure vessel failure is a major failure mechanism until about 100 hours after an accident. The pressure vessel failure and the thermal decomposition contribute, in nearly same degree, to the CFP failure after 150 hours after the accident. The failure fraction is 5.03×10^{-2} at 250 hours after the LPCC accident.
- For metallic FPs, the fractional releases are large, of the same order as for cesium, silver, and strontium during normal operation. At 100.22 hours after an accident, 25.9% of silver, 0.005% of cesium, and 2.65×10^{-3} % of krypton are released into the coolant. In the case of strontium, 79.8% is in retention in intact CFPs, 19.8% stays in the matrix graphite, 0.3% in the structural graphite, and 1.30×10^{-2} % is released.
- It is judged that the failure fractions due to the pressure vessel failure and the thermal decomposition are still high. To secure the integrity of CFPs during the LPCC accident in a 450 MW_{th} DB-HTR charged with the TRU fuel, it is necessary to decrease the accident temperature and to reduce the gas pressure in a CFP. It is thus necessary to decrease the power generation and to increase the buffer size of the CFP.

7.7 Fuel Performance for a U+TRU Fuel of a 450 MW_{th} DB-HTR

This DB-HTR kernel material is 30% UO_2 + 70% (5% NpO_2 + 95% $PuO_{1.8}$) mixed with 0.6 moles SiC per mole of heavy metal.

7.7.1 Nuclide Composition/Operating Conditions/Fuel Burnup and Depletion

Table 33 presents the nuclide composition in the CFP kernel in the DB-HTR fuel. It was assumed that the DB-HTR was operated at the coolant temperature of 858°C and the kernel power of 39.02 mW for three cycles having the average length of 465 EFPD, and then was subjected to an LPCC accident for 250 hours, as shown in Figure 255. The kernel power decreases rapidly during an LPCC event. The maximum coolant temperature is 1548.70°C at 95.72 hours. Figure 256 displays the burnup history. The final burnup and fast fluence are 415 GWd/tHM (39.52 %FIMA) and 3.353×10^{21} n/cm^2 (E > 0.1 MeV) at 1395 days.

Table 33. Nuclide composition in the kernel (U+TRU fuel of a 450 MW_{th} DB-HTR).

Nuclides	Moles	Composition
U-235	1.527E-09	0.133%
U-238	2.138E-07	18.617%
Np-237	2.513E-08	2.187%
Pu-238	1.518E-08	1.322%
Pu-239	2.931E-07	25.516%
Pu-240	1.103E-07	9.606%
Pu-241	2.591E-08	2.255%
Pu-242	3.289E-08	2.863%
O-16	1.340E-06	116.687%
C-12	4.307E-07	37.500%
Si-28	3.974E-07	34.599%
Si-29	2.005E-08	1.746%
Si-30	1.327E-08	1.155%

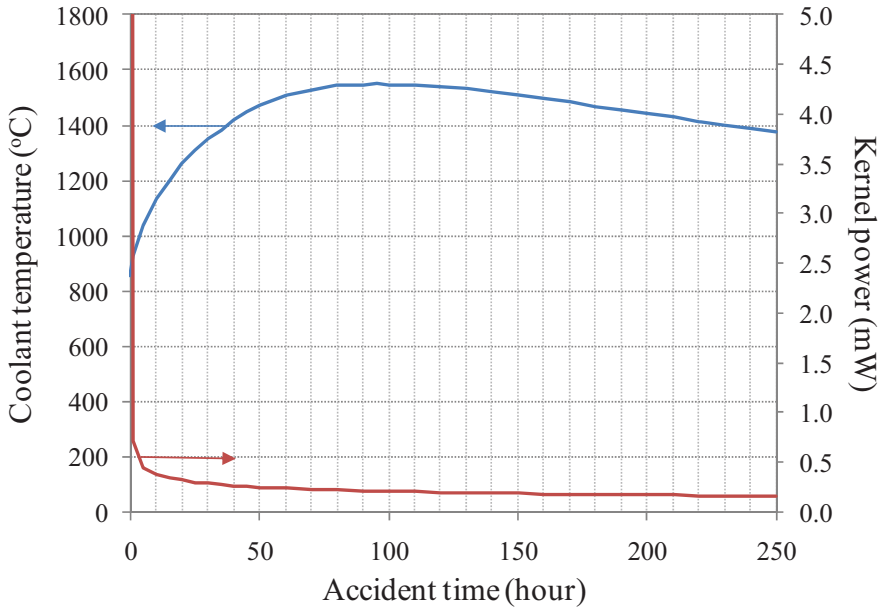

Figure 255. Coolant temperature and kernel power of the DB-HTR during an accident (U+TRU fuel of a 450 MW_{th} DB-HTR).

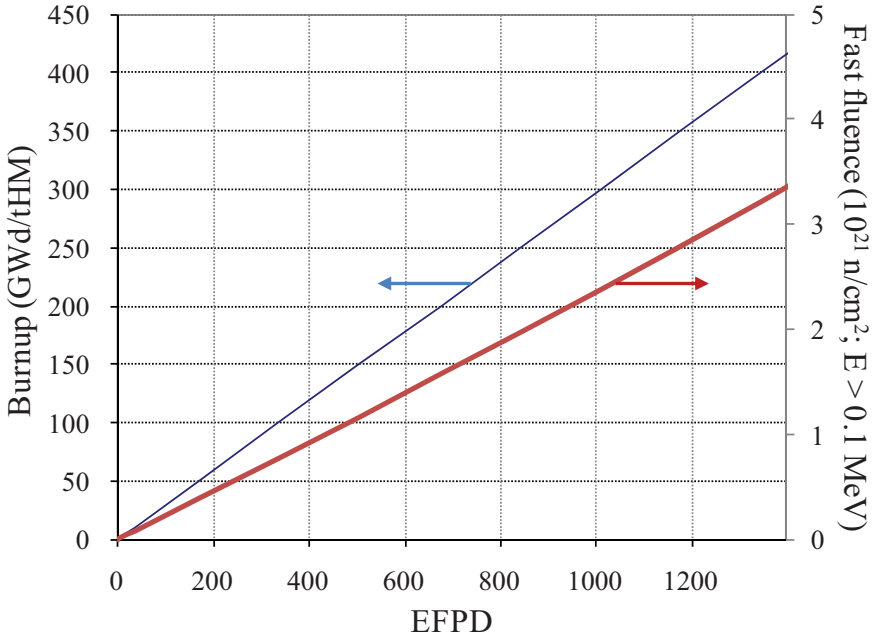

Figure 256. Fuel burnup history (U+TRU fuel of a 450 MW_{th} DB-HTR).

7.7.2 Thermal Analysis of Fuel Block and CFP

Figure 257 and Figure 258 show the temperature histories at the coolant, at the center of a compact, and at the center of a kernel located at the compact center during normal operation and accident, respectively. The temperature at the center of a kernel located at the compact center is about 902°C during normal operation. But it increases with the accident temperature of the coolant during an accident, when its maximum is 1548.91°C. In Figure 258, the temperatures at coolant, compact, and kernel during an accident are nearly the same because the power is negligible during the LPCC, as shown in Figure 255.

Figure 259 represents the temperature distribution in an equivalent cylinder. During normal operation, the temperature jumps down at the gap between compact and structural graphite due to the relatively low thermal conductivity of helium in the gap. During an accident, the temperature distribution in the equivalent cylinder is nearly constant. Figure 260 displays the temperature distribution in a CFP. The thermal conductivity of the buffer was assumed to be 0.5 W/(m K). During normal operation, a relatively large temperature drop occurs across the buffer because its thermal conductivity is much lower than those of other layers. At 3.36 days, the temperature gradients are 8.33°C/mm across the kernel and 120.67°C/mm across the buffer. The temperature within the CFP is nearly constant during an accident.

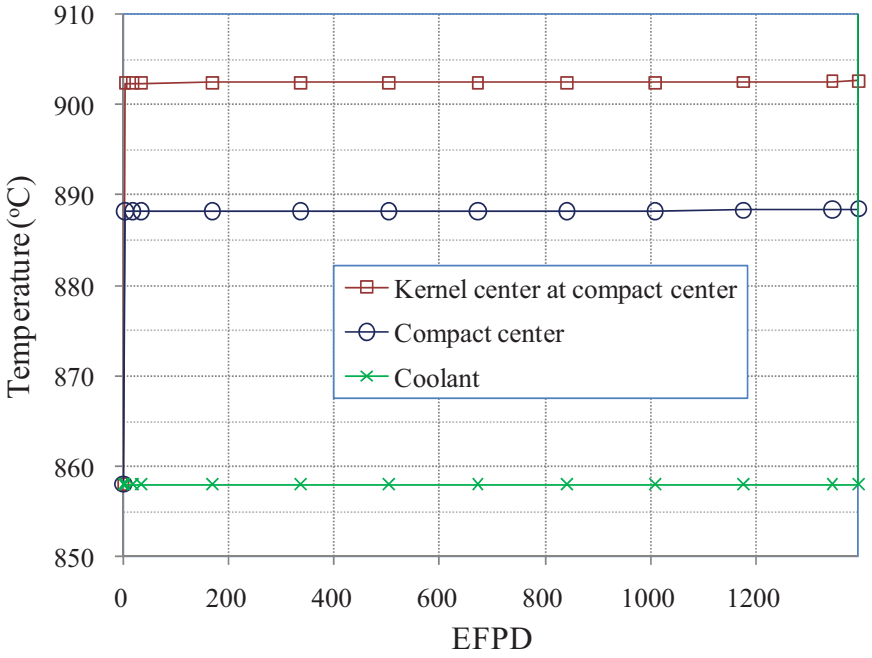

Figure 257. Temperature history during normal operation (U+TRU fuel of a 450 MW_{th} DB-HTR).

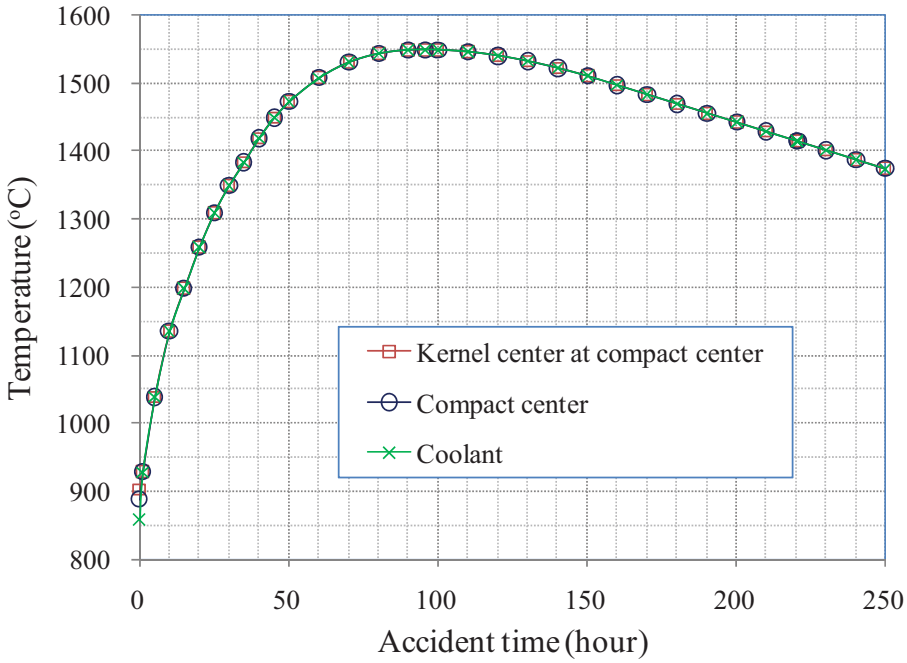

Figure 258. Temperature variation during an accident (U+TRU fuel of a 450 MW_{th} DB-HTR).

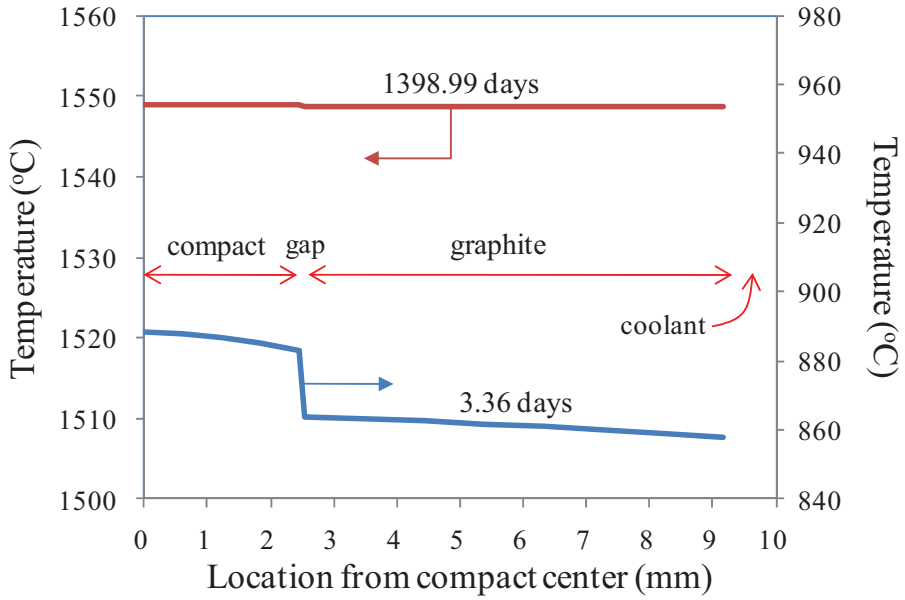

Figure 259. Temperature distribution across the compact and structural graphite (TRU fuel of a 450 MW_{th} DB-HTR).

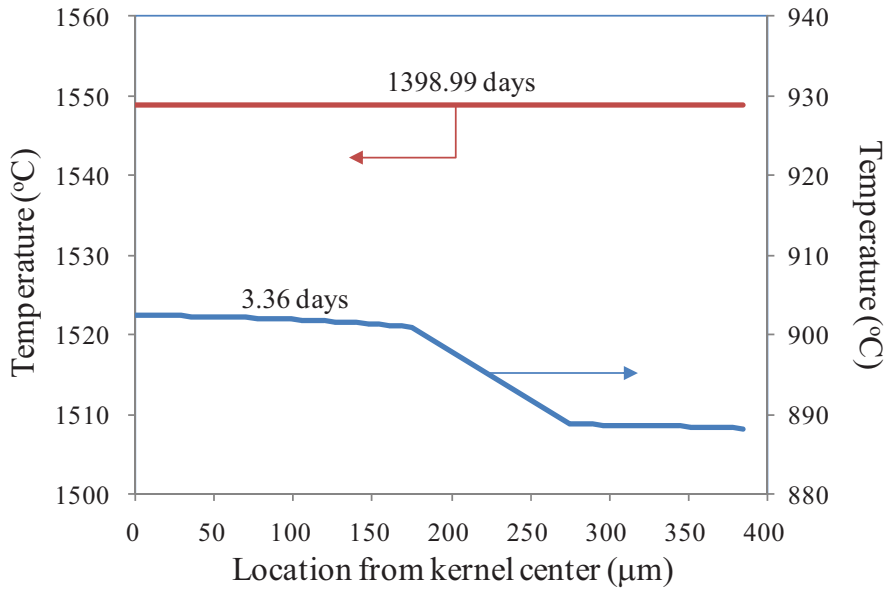

Figure 260. Temperature distribution in a CFP located at the center of the compact in a unit cell (U+TRU fuel of a 450 MW_{th} DB-HTR).

7.7.3 Gas Pressure Buildup in the Void Volume of Kernel and Buffer

Figure 261 and Figure 262 show the gas pressure in the void volume during normal operation and in accident conditions, respectively. Xenon, cesium, helium, and krypton are major gas species during normal operation and accident. The total gas pressure is 27.00 MPa at 1395 EFPD and 90.49 MPa at 95.72 hours after an accident.

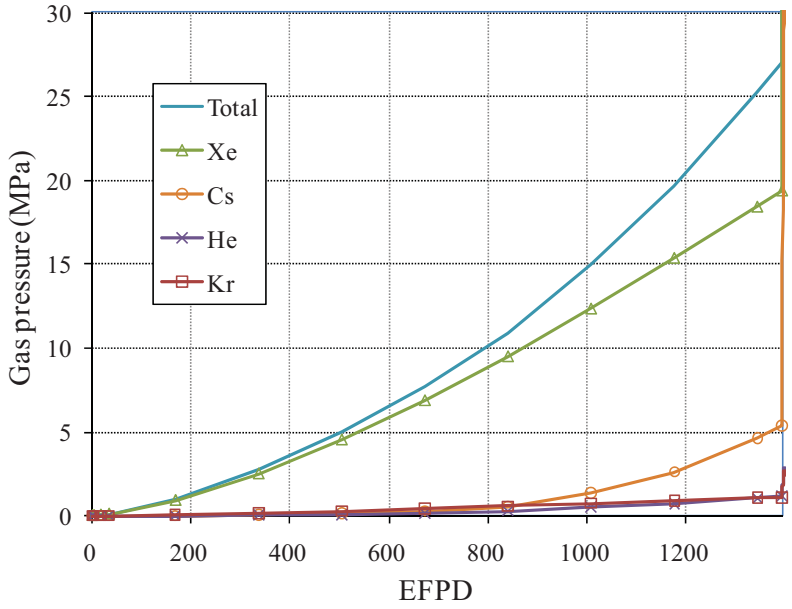

Figure 261. Gas pressure in the void volume during normal operation (U+TRU fuel of a 450 MW_{th} DB-HTR).

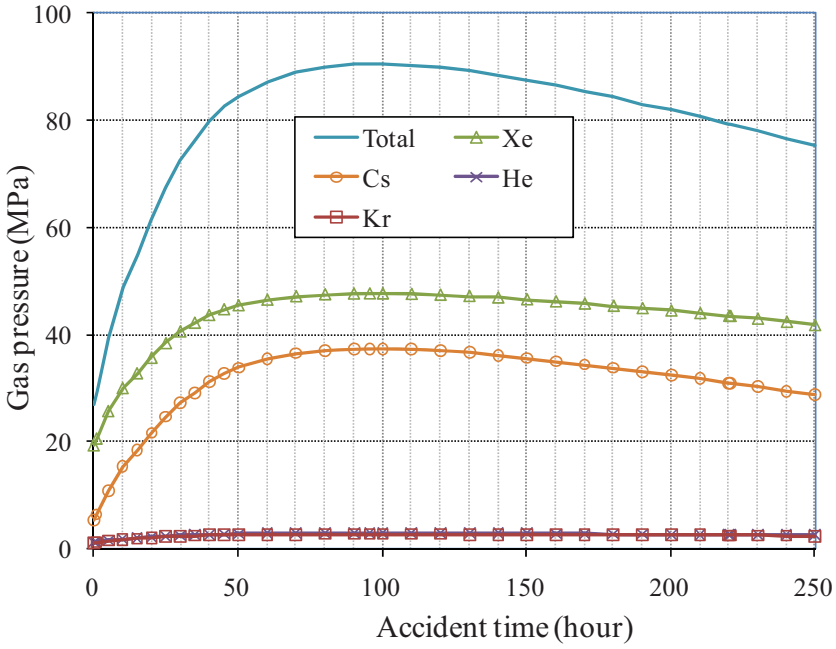

Figure 262. Gas pressure in the void volume in accident conditions (U+TRU fuel of a 450 MW_{th} DB-HTR).

7.7.4 Thermo-mechanical Analysis on a CFP

Figure 263 and Figure 264 display the tangential stresses at the inner surfaces of the IPyC, SiC, and OPyC layers during irradiation. The maximum tensile tangential stress at the inner surface of the IPyC layer is 322.41 MPa at 504.31 EFPD, when the fast fluence is about 1.17×10^{21} n/cm^2 (E > 0.1 MeV). The tangential stress at the inner surface of the SiC layer approaches -189.76 MPa at 1395 EFPD, and increases greatly in the period of the accident. Its maximum value is 64.37 at 95.72 hours after the accident starts.

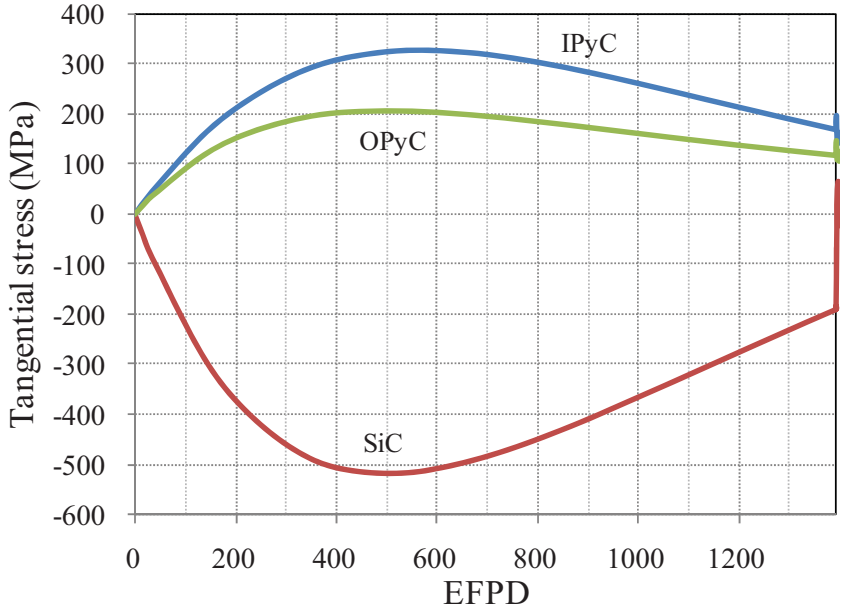

Figure 263. Stress evolutions during normal operation (U+TRU fuel of a 450 MW_{th} DB-HTR).

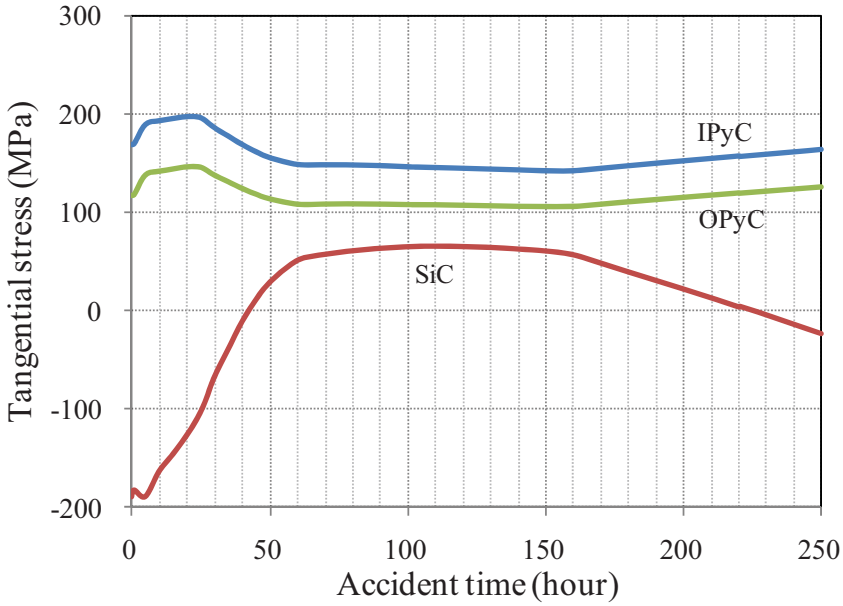

Figure 264. Stress evolutions during an accident (U+TRU fuel of a 450 MW_{th} DB-HTR).

7.7.5 Failure Fraction of CFPs

Figure 265 and Figure 266 show the failure fractions for 10^8 CFPs. The SiC failure fraction is 2.22×10^{-15} at 1395 EFPD. It can be said that the failure of CFPs does not happen during normal operation. The significant failure due to the pressure vessel failure starts to occur at 5 hours after the accident. The pressure vessel failure is a major failure mechanism until about 130 hours after the accident. The thermal decomposition of the CFPs starts to occur significantly at 35 hours after the accident. The two failure mechanisms contribute, in nearly same degree, to the CFP failure from 150 hours after the accident on. The failure fraction is 3.30×10^{-3} at 250 hours after the LPCC accident.

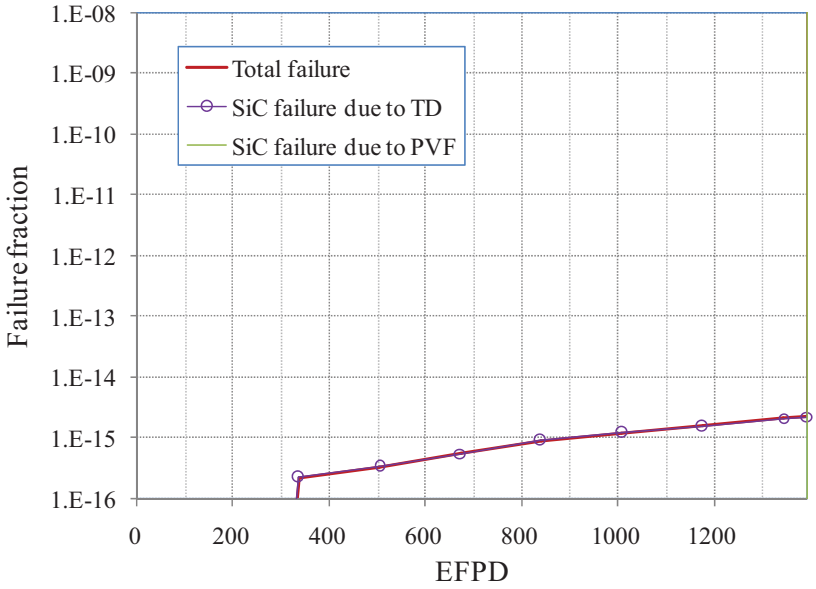

Figure 265. Variation of failure fraction of CFPs (U+TRU fuel of a 450 MW_{th} DB-HTR).

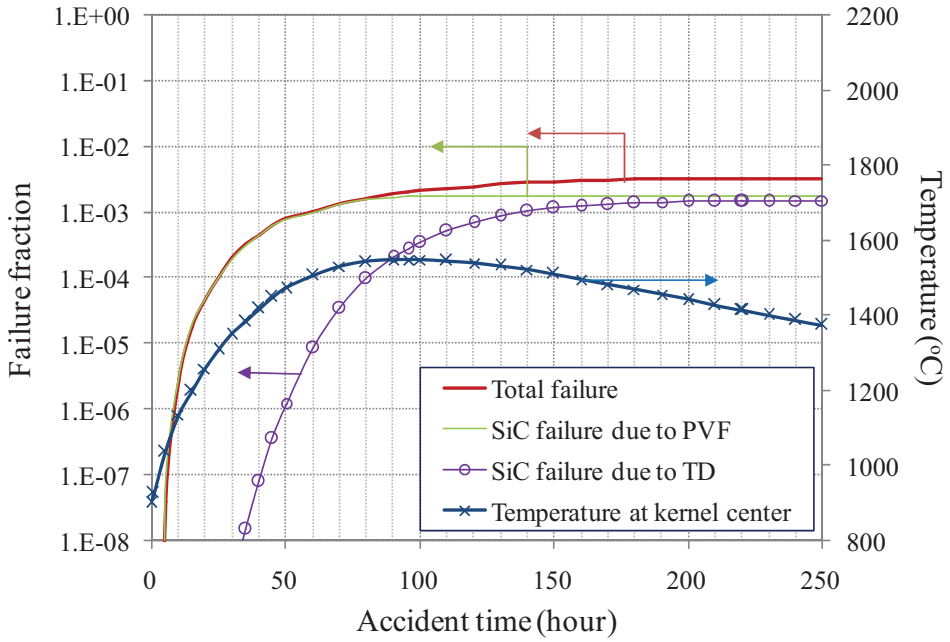

Figure 266. Variation of failure fraction of CFPs during a loss of coolant accident (U+TRU fuel of a 450 MW_{th} DB-HTR).

7.7.6 FP Transport

Figure 267 and Figure 268 display the fractional releases of Ag-110m, Cs-137, Sr-90, and Kr-85 into the coolant during normal reactor operation and in accident conditions, respectively. For metallic FPs, the fractional releases are large, of the same order as for cesium, silver, and strontium. The fractional release of krypton is nearly constant during normal operation because of the very low failure fraction of nearly zero and the constant coolant temperature of 858°C. During an accident, the releases of silver and strontium increase with the accident temperature. The releases of krypton and cesium, however, do not increase.

Table 34 and Table 35 present the fractional distributions of silver, cesium, strontium, and krypton at the reactor operation time of 1395 EFPD and at 95.72 hours after an accident, respectively. The SiC failure fraction is nearly zero at 1395 EFPD during normal operation and 2.05×10^{-3} at 95.72 hours after an accident, respectively. Among the FP amounts existing at 1395 EFPD, the intact CFPs contain 99.9% of silver, about 100% of cesium, 99.9% of strontium, and about 100% of krypton. Strontium is better retained in the graphite matrix than silver and cesium. At 95.72 hours after an accident, 13.9% of silver, 3.93×10^{-2} % of cesium, and 3.90×10^{-2} % of krypton are released into the coolant. In the case of strontium, 89.3% is in retention in intact CFPs, 10.6% stays in the matrix graphite, 0.1% in the structural graphite, and 6.67×10^{-3} % is released.

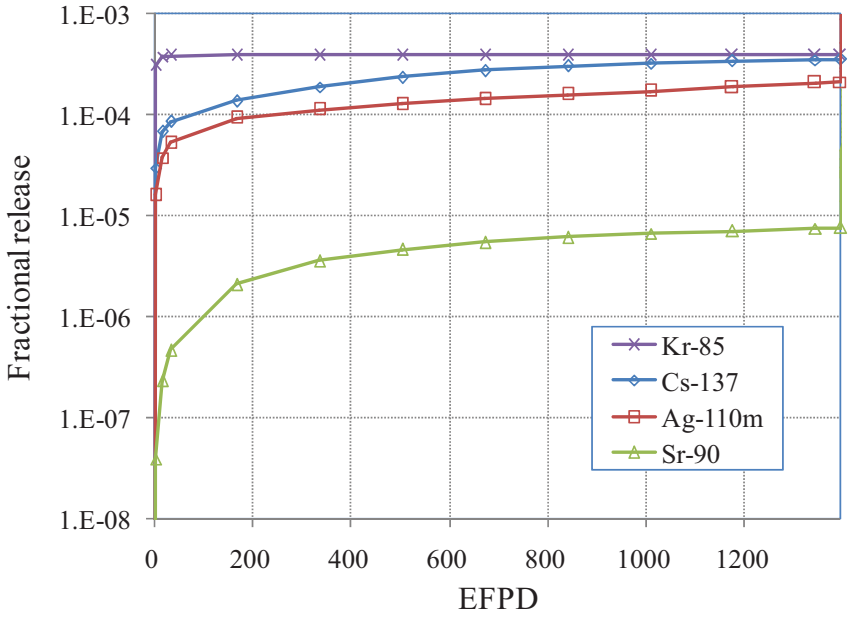

Figure 267. Fractional releases of silver, cesium, strontium, and krypton during normal operation (U+TRU fuel of a 450 MW_{th} DB-HTR).

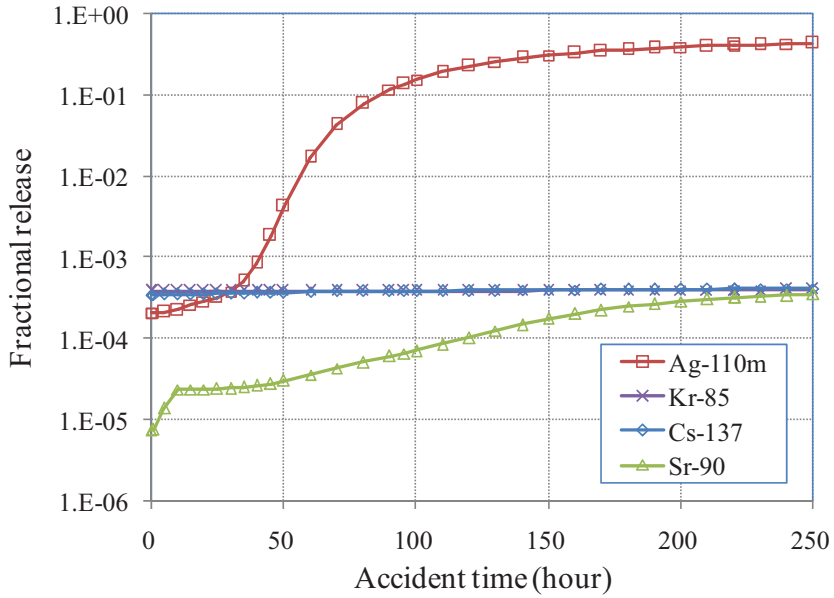

Figure 268. Fractional releases of silver, cesium, strontium, and krypton during an accident (U+TRU fuel of a 450 MW_{th} DB-HTR).

Table 34. Fractional distributions of silver, cesium, strontium, and krypton at 1395 EFPD (U+TRU fuel of a 450 MW_{th} DB-HTR).

	Ag-110m	Cs-137	Sr-90	Kr-85
Intact CFPs	9.99E-01	~1	9.99E-01	~1
Failed CFPs	4.65E-20	7.62E-21	1.20E-16	5.24E-21
Matrix graphite	2.17E-04	2.62E-05	1.12E-03	1.06E-11
Gap	2.06E-14	2.59E-15	4.80E-21	0
Structural graphite	8.95E-05	1.13E-05	2.09E-04	1.29E-11
Accumulated release	2.11E-04	3.52E-04	7.57E-06	3.87E-04

Table 35. Fractional distributions of silver, cesium, strontium, and krypton at 95.72 hours after an accident (U+TRU fuel of a 450 MW_{th} DB-HTR).

	Ag-110m	Cs-137	Sr-90	Kr-85
Intact CFPs	8.48E-01	~1	8.93E-01	1.00E+00
Failed CFPs	1.71E-08	4.48E-09	6.22E-09	4.84E-09
Matrix graphite	1.32E-02	2.30E-06	1.06E-01	9.00E-11
Gap	1.88E-08	3.41E-12	3.92E-11	0
Structural graphite	4.56E-04	8.47E-08	1.33E-03	9.62E-11
Accumulated release	1.39E-01	3.93E-04	6.67E-05	3.90E-04

7.7.7 Summary

The microanalysis of the 450 MW_{th} DB-HTR fuel has been done, including the determination of the gas pressure buildup in the void volume of a CFP, the thermal analyses for a DB-HTR fuel, the thermo-mechanical analyses for a CFP, and the estimation of the failure fractions of a batch of CFPs and the FP releases into a coolant. It was assumed that the DB-HTR was operated at constant temperature and power for 1395 EFPD and was subjected to an LPCC accident event for 250 hours.

- The temperature at the kernel center of the compact center was about 902°C during normal operation, and was below 1600°C throughout the LPCC. During normal operation, temperature gradients are 8.3°C/mm across the kernel and 120.7°C/mm across the buffer, respectively.
- The gas species that most significantly contributes to gas pressure during normal operation and in accident conditions are xenon, cesium, helium, and krypton. Total gas pressure is about 27.00 MPa at 1395 EFPD. The maximum gas pressure is 90.49 MPa at 90.72 hours after an accident.
- The tangential stress at the inner surface of the SiC layer approaches -189.76 MPa at the end of normal operation, but greatly enlarges to about 64.37 MPa during an accident period. The maximum tensile tangential stress of IPyC inner surface is 322.41 MPa at a fast fluence of about 1.17×10^{21} n/cm^2 (E > 0.1 MeV).
- The total failure fraction is nearly zero at the end of normal operation. The pressure vessel failure is a major failure mechanism until about 130 hours after the accident. The thermal decomposition of the CFPs starts to occur at 35 hours after the accident. The two failure mechanisms contribute, in nearly same degree, to the CFP failure from 150 hours after the accident on. The failure fraction is 3.30×10^{-3} at 250 hours after the LPCC accident.

- For metallic FPs, the fractional releases are large, of the same order as for cesium, silver, and strontium during normal operation. During an accident, the releases of silver and strontium increase with the accident temperature, but the releases of krypton and cesium do not increase. At 95.72 hours after an accident, 13.9% of silver, 3.93×10^{-2} % of cesium, 3.90×10^{-2} % of krypton, and 6.67×10^{-3} % of strontium are released into the coolant.
- The fractional releases due to the pressure vessel failure and the thermal decomposition are in the order of minus three. It is judged that the failure fractions are not sufficiently low. To secure more sufficiently the integrity of CFPs during the LPCC accident in a 450 MW_{th} DB-HTR loaded with the mixed fuel of uranium and TRU, it is necessary to decrease the accident temperature and to reduce the gas pressure in a CFP. It is thus necessary to decrease the power generation and to increase the buffer size of the CFP.

7.8 Comparisons of the Microanalysis Results

Figure 269 presents the temperature at the center of the kernel located at the compact center. In 600 MW_{th} DB-HTRs, the temperatures are above 1600°C after about 30 hours after the accident. In 450 MW_{th} DB-HTRs, the temperatures are below 1600°C throughout the accident.

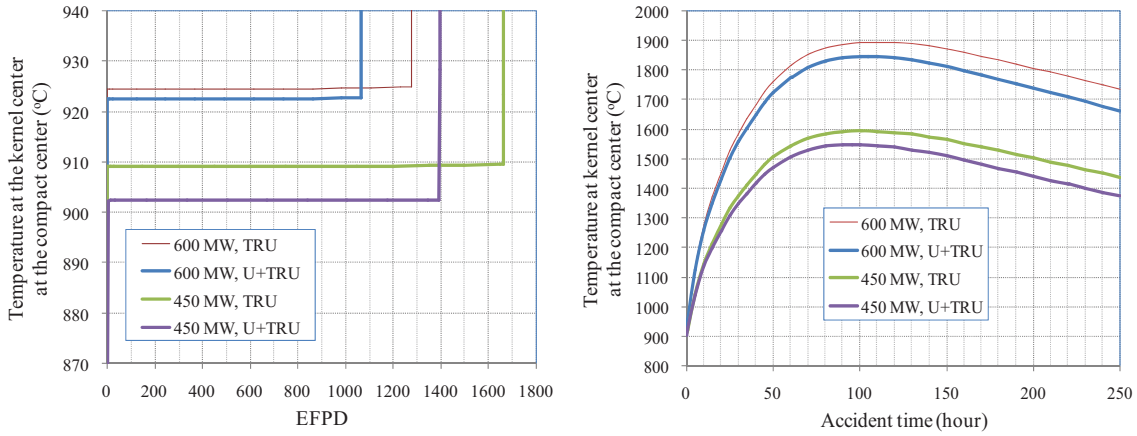

Figure 269. Temperatures at the center of the kernel located at the compact center.

Figure 270 shows the gas pressures accumulated in the void volume of the kernel and buffer during normal operation and LPCC accident. The gas pressures in the DB-HTRs charged with the TRU fuel are higher than those in the DB-HTRs loaded with the mixed fuel of uranium and TRU. The maximum gas pressures during the accident are between 90 and 200 MPa, which are judged to be very high. Major gas species during normal operation are xenon, cesium, helium and krypton. Silicon monoxide and carbon monoxide are generated during an accident in the 600 MW_{th} DB-MHRs. It was estimated that silicon monoxide and carbon monoxide are produced at the elevated temperatures more than 1600°C.

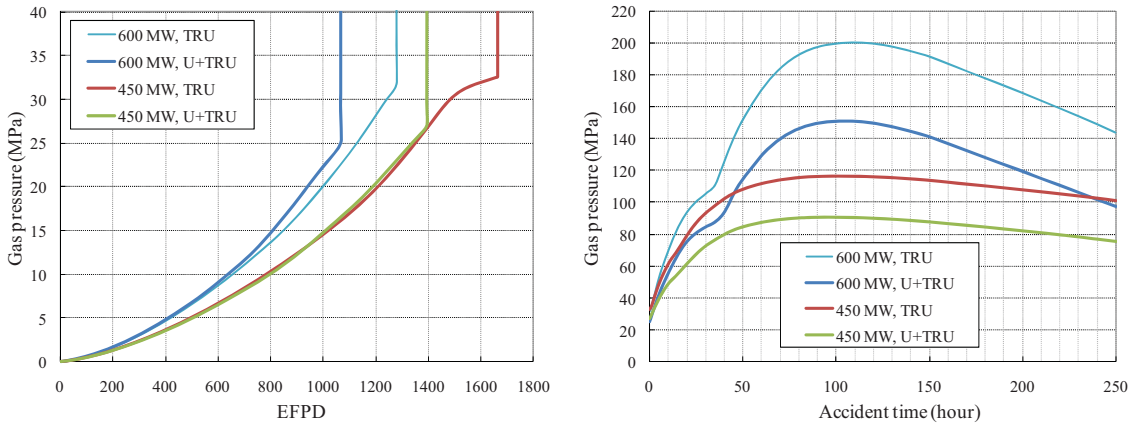

Figure 270. Total gas pressures during normal operation and accident.

Figure 271 displays the tangential stresses at the inner surfaces of the SiC layers in the nominal CFP. During normal operation, the stresses are all in the range of compression. The stress behavior during the accident depends on the behaviors of the gas pressure in the accident conditions, as shown in Figure 270. The maximum tangential stresses of the SiC layers are between 65 and 446 MPa during the accident.

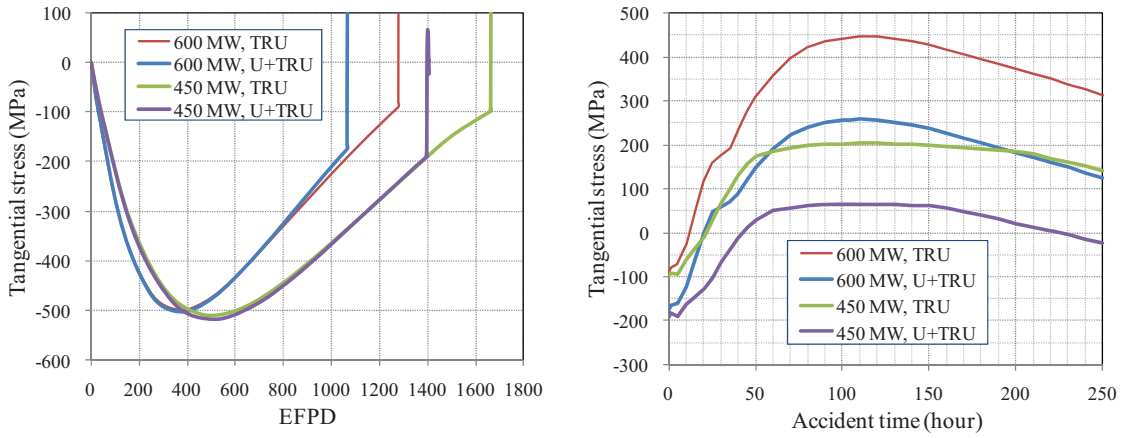

Figure 271. Tangential stresses at the inner surfaces of the SiC layers.

Figure 272 shows the SiC failure fractions during normal operation and in accident conditions. Figure 273 represents the SiC failure fractions during the accident according to two failure mechanisms, the pressure vessel failure and the thermal decomposition. Only the failure fractions due to the pressure vessel failure in the DB-HTRs loaded with the TRU fuel are significant during normal operation. That is because the gas pressure is higher in the TRU fuel than in the mixed fuel of uranium and TRU. During normal operation, the failure fraction in the 450 MW_{th} DB-HTR loaded with the TRU is highest because the reactor burnup was most extended. All CFPs in the 600 MW_{th} DB-HTRs break during an accident. The thermal decomposition breaks all the CFP failure during an accident in the 600 MW_{th} DB-HTR. Both the pressure vessel failure and the thermal decomposition play dominant roles in the failure of CFPs during an accident in the DB-HTRs. The failure fractions in the 450 MW_{th} DB-HTR with the uranium and TRU-loaded are the lowest among those in the other types of DB-HTRs, although it is necessary to scrutinize whether the fractional releases are acceptable or not.

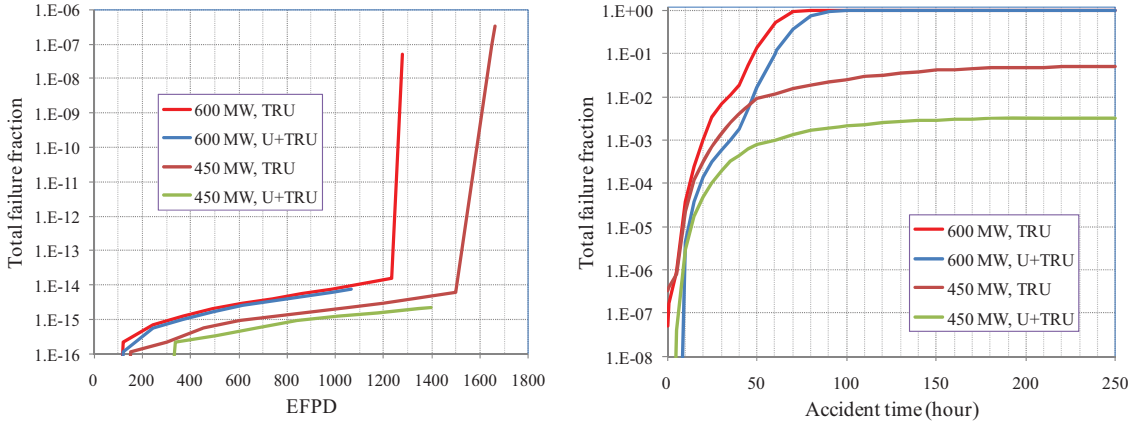

Figure 272. SiC failure fractions in accident conditions.

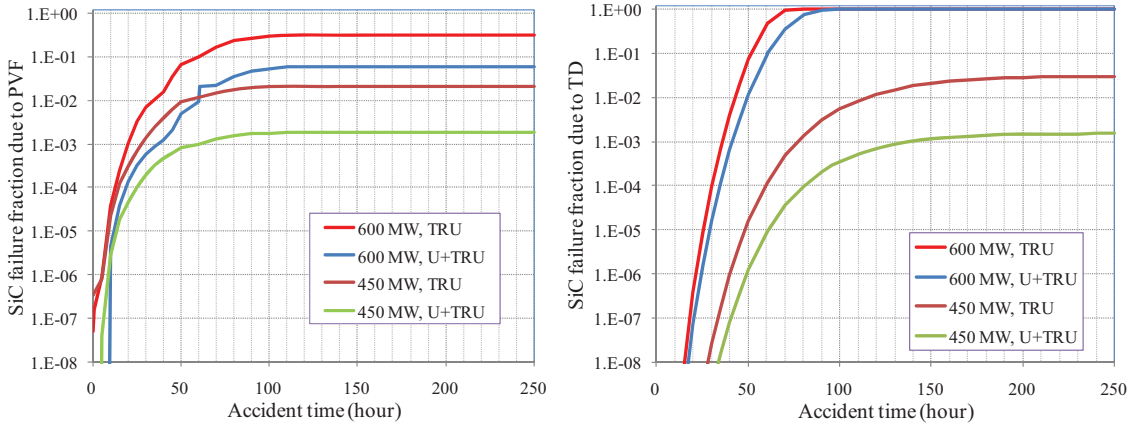

Figure 273. SiC failure fractions due to PVF and TD in accident conditions.

Figure 274 presents the fractional releases of the fission products at the ends of normal operation and accident. The fractional releases of all the fission products considered are below 0.001 during normal operation. They should be scrutinized through the environmental impact if they are acceptable. More than 40% of silver is released during an accident. Silver is known to be effectively captured on the metallic surface of the reactor components through the sorption phenomena, so it is necessary to take some measures to prevent occupational dose from silver. The fractional releases of cesium, strontium and krypton are above 10% during an accident in the 600 MW_{th} DB-HTRs, which are very high. On the other hand, they are below 0.001 during an accident in the 450 MW_{th} DB-HTRs except the fractional release of strontium in the 450 MW_{th} DB-HTR loaded with the TRU fuel, 1.66×10^{-3}.

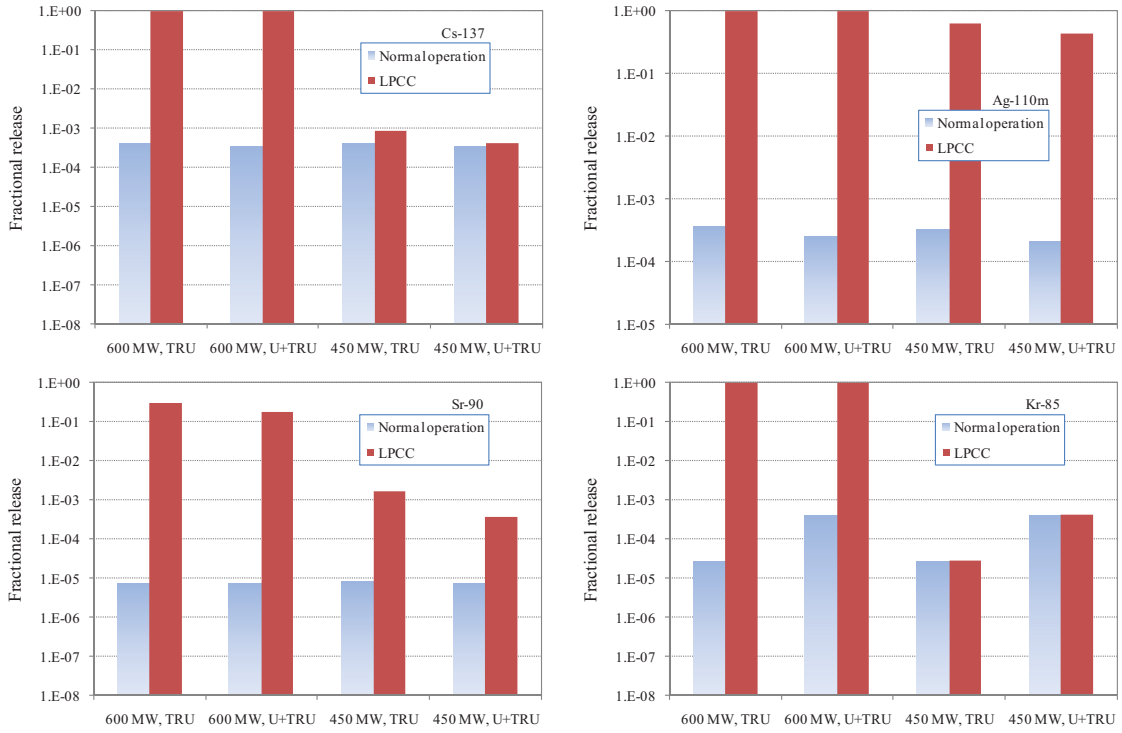

Figure 274. Fractional releases of the fission products at the ends of normal operation and accident.

7.9 Conclusions

The fuel performance analysis for four types of the DB-HTRs has been done.

- Major gas species are xenon, cesium, helium and krypton during normal operation. Carbon monoxide and silicon monoxide are additionally generated at elevated temperatures above 1600°C.
- All the fuels of the DB-HTRs had good mechanical and thermal integrity during normal operation. During the LPCC, however, all CFPs in the 600 MW_{th} DB-HTRs are broken. The failure fractions due to the pressure vessel failure are between 5.8 and 31.3 %. These high failure fractions indicate that it is necessary to reduce the gas pressure in a CFP during the LPCC. The gas pressure can be reduced by increasing the buffer size of the CFP or by reducing the accident temperature. The failure fraction due to the thermal decomposition is unity, which indicates that active core cooling systems must be used to prevent excessive temperatures in the event of a LPCC.
- In the 450 MW_{th} DB-HTRs, the failure fraction due the pressure vessel failure are between 1.79×10^{-3} and 2.09×10^{-2}, and the failure fraction due the thermal decomposition are between 1.51×10^{-3} and 3.00×10^{-2}. It is necessary to scrutinize if these failure fractions are acceptable. The DB-HTR loaded with the mixed fuel of uranium and TRU is most favored in the aspect of fuel integrity.
- The fractional releases of all the fission products considered are below 0.001 during normal operation. They should be scrutinized through the environmental impact if they are acceptable. More than 40% of silver is released during an accident regardless of the rector power and the fuel types. Some measures should be taken in order to prevent excessive occupational doses of silver. The fractional releases of cesium, strontium and krypton are above 10% during an accident in the 600 MW_{th} DB-HTRs, which are very high. Alternatively, they are below 0.001 during an accident in

the 450 MW_{th} DB-HTRs except the fractional release of strontium in the 450 MW_{th} DB-HTR loaded with the TRU fuel, 1.66×10^{-3}.

- It is desirable in the aspect of HTR safety that the CFPs sufficiently survive some accident conditions of a HTR. Therefore, the 600 MW_{th} DB-HTR is not appropriate for burning TRU. It is judged that the failure fractions in the 450 MW_{th} DB-HTRs are not sufficiently low. It thus is necessary to decrease the thermal power more and increase the buffer size of a CFP.

7.10 References

1. S. J. Ball, "Deep-Burn Modular Helium Reactor Fuel Development Plan," ORNL/TM-2002/135, GA-224-0-TRT-000167, Oak Ridge National Laboratory and General Atomics, 2002.
2. "Deep Burn: Development of Transuranic Fuel and Fuel Cycles for High Temperature Gas-Cooled Reactor," unnumbered document, 2009.
3. Y. M. Kim, M. S. Cho, Y. W. Lee and W. J. Lee, "Development of a Fuel Performance Analysis Code COPA," Paper 58040, Proc. HTR 2008, Washington D.C., USA, September28–October 1, 2008.
4. INEEL, CEA, MIT, "Development of Improved Models and Designs for Coated-Particle Gas Reactor Fuels," INEEL/EXT-05-02615, 2004.
5. J. S. Jun, H. S. Lim, C. K. Jo, J. M. Noh, and F. Venneri, "Evaluation of the Transient TRU Fuel Temperature in a DB-HTR Core," Paper 232, Proc. HTR 2010, Prague, Czech Republic, 18 October 18–20, 2010.
6. H. J. Shim and C. H. Kim, "Error Propagation Module Implemented in the McCARD Monte Carlo Code," *Transactions of the American Nuclear Society*, 86, p. 325 (2002).
7. D. T. Hagrman, editor, *SCDAP/RELAP5/MOD3.1 Code Manual Volume 4: MATPRO – A Library of Materials Properties for Light-Water-Reactor Accident Analysis*, NUREG/CR-6150 (1993).
8. J. J. Carbajo, G. L. Yoder, S. G. Popov, V. K. Ivanov, "A Review of the Thermophysical Properties of MOX and UO_2 Fuels," *J. Nucl. Mater.*, 299, p. 181, 2001.
9. L. L. Snead, T. Nozawa, Y. Katoh, T.-S. Byun, S. Kondo, and D. Petti, "Handbook of SiC Properties for Fuel Performance Modeling," *J. Nucl. Mater.*, 371, p. 329, 2007.
10. Outokumpu HSC Chemistry® for Windows, Version 5.1, Outokumpu Research Oy, 2002.
11. S. D. Beck, *The Diffusion of Radioactive Fission Products from Porous Fuel Elements*, BMI-1433, 1960.
12. Y. M. Kim and M. S. Cho, "A Stress Analysis for a Coated Fuel Particle of a HTGR using a Finite Element Method," *Nucl. Eng. Technol.*, 41(8), p. 1087, 2009.
13. *NP-MHTGR Material Models of Pyrocarbon and Pyrolytic Silicon Carbide*, CEGA-002820, Rev. 1, CEGA Corporation, 1993.
14. D. T. Goodin, *US/FRG Accident Condition Performance Models*, DOE/HTGR-85107, 1989.
15. Y. M. Kim and M. S. Cho, "Development of the Fission Product Release Analysis Code COPA-FPREL," *Nucl. Technol.*, 170, p. 231, 2010.
16. *Fuel Performance and Fission Product Behaviour in Gas Cooled Reactors*, IAEA-TECDOC-978, 1997.

17. R. C. Martin, "Compilation of Fuel Performance and Fission Product Transport Models and Database for MHTGR Design," ORNL/NPR-91/6, Oak Ridge National Laboratory, 1993.

8. TRU Self-Cleaning of the Prismatic Block Reactor

8.1 Introduction

Deep burning (DB) of LWR TRUs in DB-MHR (Modular Helium Reactor) has been studied for an efficient transmutation of the LWR spent fuel. Previous studies have shown that an over 60% deep-burning is feasible in a single-pass DB-MHR concept. In addition, the spent fuel of the DB-MHR core can be reused in an SFR for a completely closed fuel cycle.[1,2]

In this report, we consider an SC of TRUs in an HTR. An SC-HTR concept is based on a fuel cycle scenario in which current LWRs and future advanced light water reactors (ALWRs) retire sometime in the future. In this case, all of the TRU material generated by existing LWRs and future ALWRs will be consumed by DB-HTRs within a finite time and HTRs should be loaded with a low-enriched uranium, and the uranium-loaded MHR generates TRUs by itself. In an SC-HTR concept, the self-generated TRU material is recycled into the same HTR core after a reprocessing treatment (removal of uranium and FPs) in a single-pass deep-burn mode. Figure 275 shows a schematic fuel cycle of an SC-HTR. The spent TRU fuel of SC-HTRs can be fed synergistically into fast reactors for a closed fuel cycle or disposed of in a final repository.

A neutronic analysis of an SC-HTR core has been performed in this report. The equilibrium uranium-TRU-mixed core is determined by using the Monte Carlo depletion analysis and its characteristics and performances are presented in this section.

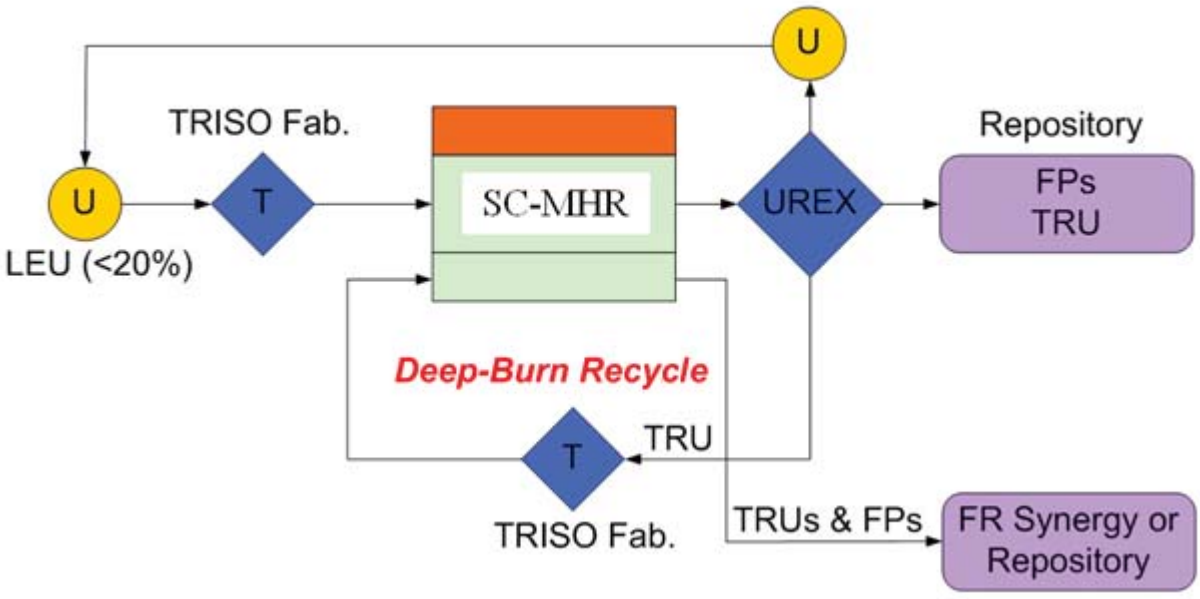

Figure 275. Fuel cycle concept in the SC-HTR.

8.2 Design Concepts of SC-HTR and Calculational Methodology

8.2.1 Design Concepts

Figure 276(a) and Figure 276(b) show the schematic configurations of the SC-HTR core considered in this study. The SC-HTR core was modified from the original GT-MHR of GA,[3] which has three fuel rings. In the modified SC-HTR cores, there are nine axial layers, while the original design has 10 axial layers. Case 1 in Figure 276(a) is composed of five fuel rings while the core in Case 2 has four fuel rings. Consequently, the number of fuel blocks of Case 1 and Case 2 are 1296 and 1134, respectively. In Table 36, major design parameters of the core are provided.

The fuel block configurations are shown in Figure 277. In the fuel block, dowels are not modeled. Burnable poison (BP) is not used in this study and the burnable poison holes are assumed to be filled with graphite. The 12 reserved shutdown control assemblies are considered at each core. And the 36 operating control rod holes are located in the outer reflector region at Case 1 and Case 2. Also, 12 and 18 startup control rod holes are located in inner reflector region in Case 1 and Case 2, respectively. Taking into account the blind fuel holes, it is assumed that each fuel block has a 2.9 cm-thick non-fuel graphite zone at both top and bottom.

The SC-HTR core in Case 1 is basically the same as in the previous DB-MHR core[4] except that both TRU and uranium fuels are simultaneously loaded. In this study, oxide fuel forms ($TRUO_2$, and UO_2) are utilized for both TRU and uranium fuels. In Case 1, the uranium fuel is loaded in 108 fuel columns and the TRU fuel is loaded in 36 fuel columns which are located in inner part of core. In the Case 2, the uranium fuel is loaded in 102 fuel columns and the TRU fuel is loaded in 24 fuel columns in the inner-most fuel ring.

In an equilibrium condition, all the TRU material needs to be recycled into the core. To find such a condition, repeated core depletion calculations should be done. The TRU loading scheme may affect the performance of an SC-HTR core in terms of the TRU discharge burnup and power distributions, and power peaking factor. However, the core design optimization is not currently done.

Table 36. Comparison of the feed TRU compositions (wt%).

Parameter	Value	
	Case 1	Case 2
Thermal power, MWt	600	
Coolant inlet/outlet temperature, K	1200	
No. of fuel columns	144	126
Active core height, cm	792.9	
Core radius, cm	340	
Top/bottom reflector thickness, cm	120/120	
No. of axial layers	9	
Average power density, W/cm^3	4.66	5.32
Graphite block density, g/cm^3	1.74	

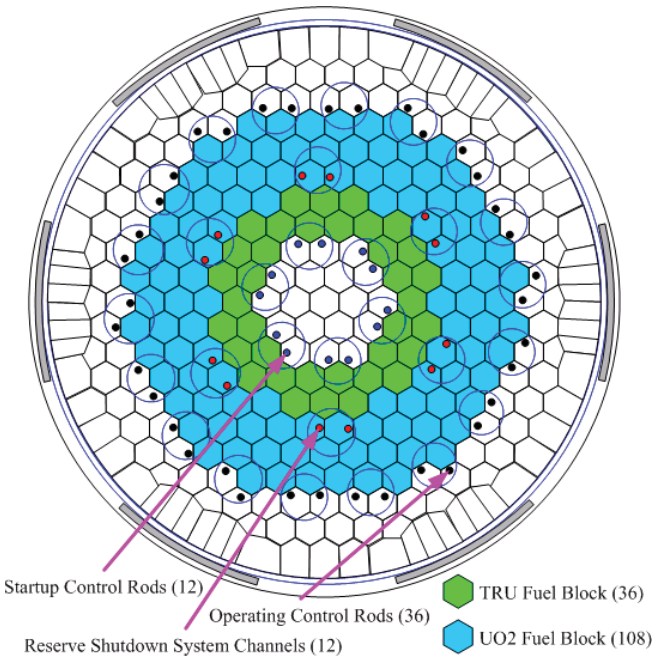

(a) Case 1: Five-ring SC-HTR core.

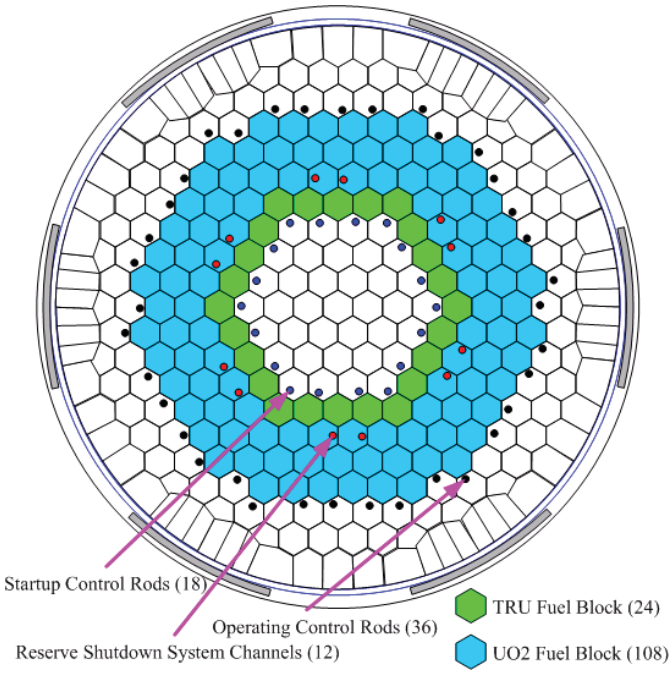

(b) Case 2: Four-ring SC-HTR core.

Figure 276. Two core configurations in SC-HTR.

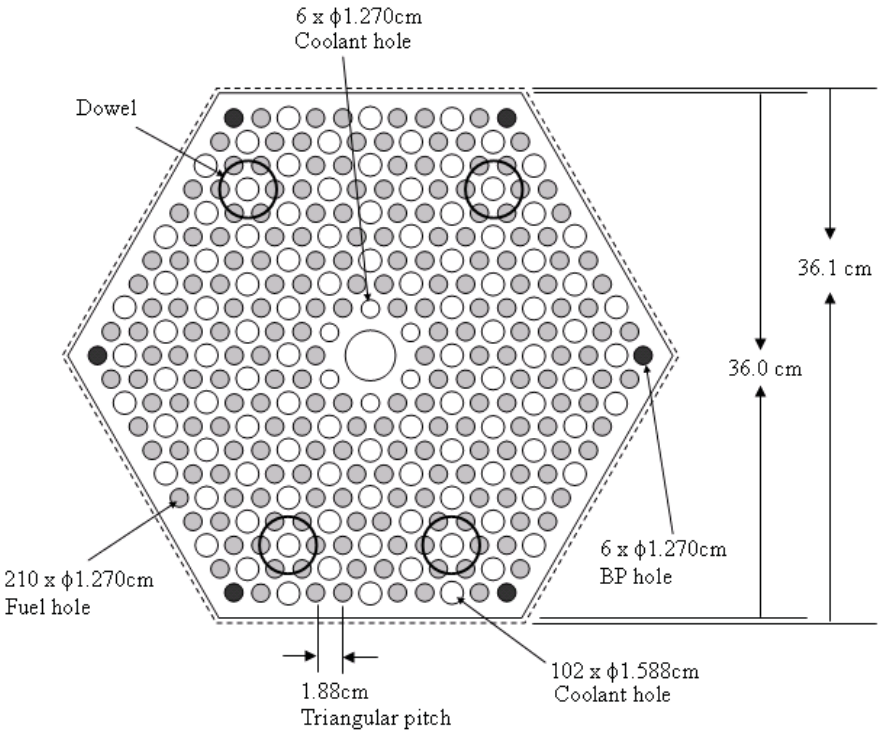

(a) Plane configuration.

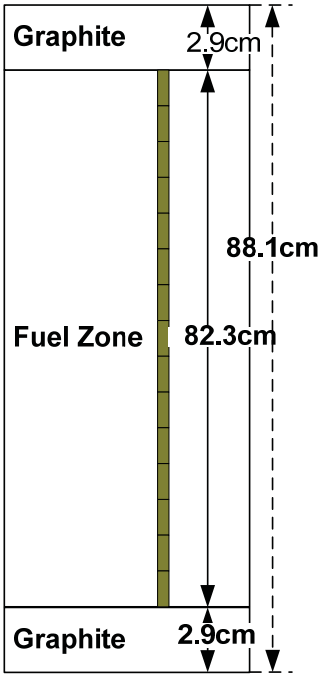

(b) Axial model.

Figure 277. Fuel block configuration of SC-HTR.

A three-batch fuel management scheme is used for the SC-HTR core with nine axial core layers. Figure 278 shows the block shuffling strategy employed in this work. Note that the axial shuffling scheme is not optimized and most-burned fuel blocks are loaded into boundary regions to minimize the axial neutron leakages.

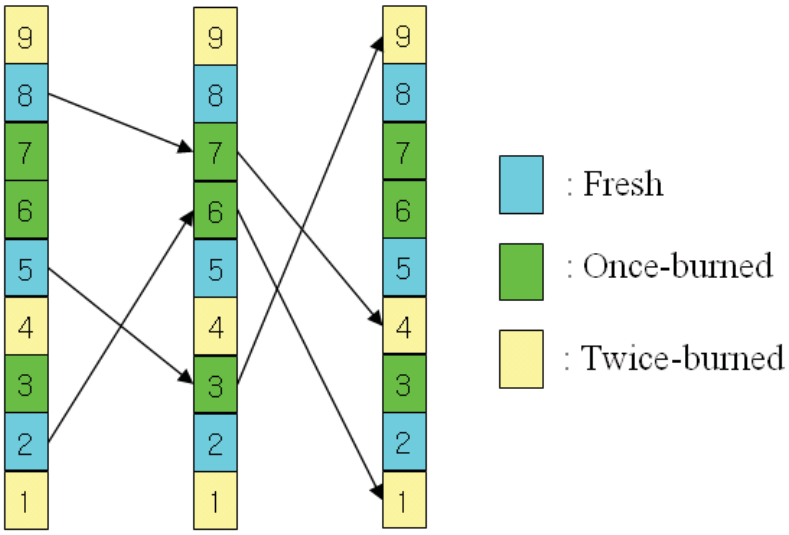

Figure 278. Axial block shuffling scheme in SC-HTR.

For the TRISO particles as shown in Figure 279, the following specific design parameters are used: the buffer thickness = 100μm, the inner PyC thickness = 35μm, the SiC thickness = 35μm, the outer PyC thickness = 40μm, density of carbon matrix = 1.70g/cm^3. Diameter of TRU kernel is 200μm and the diameter of UO_2 kernel is 500μm in this work.

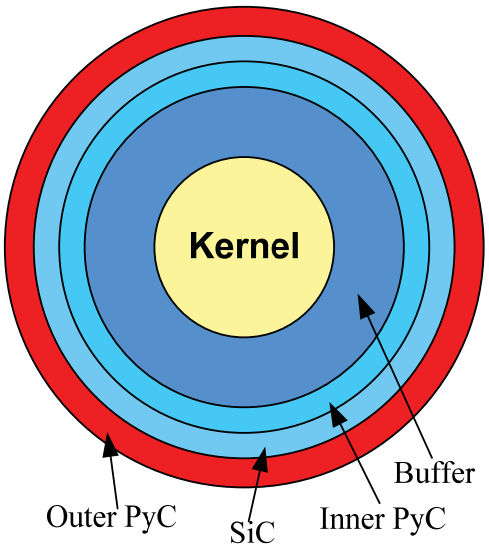

Figure 279. Configuration of a TRISO particle.

A packing fraction of 26% is used for the UO_2 fuel compact. Regarding UO_2 fuel, the conventional TRISO fuel with a concentrated kernel is utilized, which is given in Table 37. In the current evaluation of the SC-HTR cores, a relatively low uranium enrichment (12%) is used. The uranium fuel specifications are based on an optimization study of a UO_2-fueled HTR core. It was found that, through some design optimization, the required uranium enrichment can be lowered from the typical values of 14–15% in other designs.

Table 37. Design parameters of UO_2 TRISO fuel and compact.

TRISO fuel	
Fuel type	UO_2
Uranium enrichment, wt%	12
Kernel (diameter, μm/density, g/cm^3)	500/10.4
Buffer layer (thickness, μm/density, g/cm^3)	100/1.05
IPyC layer (thickness, μm/density, g/cm^3)	35/1.9
SiC layer (thickness, μm/density, g/cm^3)	35/3.18
OPyC layer (thickness, μm/density, g/cm^3)	40/1.9
Fuel compact	
Radius, cm	0.6225
Matrix density, g/cm^3	1.70
Packing fraction, %	26

8.2.2 Computational Methodology

A continuous energy Monte Carlo code McCARD[5] is used for the neutronic analysis of the SC-HTR cores. The McCARD code was developed at Seoul National University, Korea. It has a built-in depletion routine, thus it can be used in a stand-alone mode for the reactor depletion analysis. In a Monte Carlo depletion calculation, it is important to consider fission products as many as possible. In the current McCARD depletion calculation, all actinides and over 160 fission products nuclides are considered and the fission product poisoning can be accounted almost completely. The cross section libraries are generated from the ENDF-B/VI data.

It can directly handle the double-heterogeneous fuel used in HTRs. In particular, randomness of the TRISO fuel particles can also be taken into consideration: locations of TRISO fuels are randomly determined. The McCARD code can be run on parallel computers.

For an accurate analysis of a TRISO-fueled HTR core, the double-heterogeneity of the TRISO fuel should be correctly modeled. In particular, the double-heterogeneity effect is very large in a reactor-grade TRU-loaded HTR. Generally, a direct modeling of the TRISO fuel requires a huge memory requirement and an extremely long computing time for 3-D core depletion calculations. Therefore, in this work, the RPT[6,7,8] method is adopted to convert a double-heterogeneous fuel compact into a conventional single-heterogeneous material. With the aid of the RPT method, the HTR core can be analyzed very efficiently with a Monte Carlo depletion method.

8.3 Results of an Equilibrium Cycle Performance Analysis

Table 38 shows the fresh UO_2 and TRU fuel masses which are fed in each equilibrium cycle. They were determined by repeated core depletion calculations. The TRU fuel is self-generated from the UO_2 fuel in the same core. The TRU production in the Case 1 is about 51.6 kg/cycle and 48.2 kg/cycle in Case 2. It is observed that the fresh fuel masses of Case 1 are a little higher than those of Case 2 because the number of uranium fuel blocks in Case 1 is more than that of Case 2. Consequently, the cycle length of Case 1 is higher than that of Case 2 as shown in Table 38.

Table 39 shows the TRU compositions of Case 1 and Case 2 in the equilibrium cycle. In this study, it is assumed that self-generated Cm isotopes are not recycled in the TRU fuel since inclusion of Cm make the TRISO fuel fabrication process rather complicated and costly. It is noted that the Pu-239 fraction is substantially smaller and the Pu-241 fraction is relatively higher, compared with a TRU vector from LWRs. The fissile (Pu-239 and Pu-241) content in the vector is about 52% for the Case 1 and Case 2. Currently, TRU vectors in Table 39 were determined after 5-year cooling period of the spent fuel.

Table 38. Fresh feed fuel mass and cycle length.

Case	Fresh Feed Fuel Mass (kg)		Cycle Length (EFPD)
Case 1	Uranium	2582.0	487.0
	TRU	51.61	
Case 2	Uranium	2437.0	450.0
	TRU	48.23	

Table 39. Self-generated TRU vector (5-year cooling) in SC-HTR.

Nuclides	Fraction, wt%	
	Case 1	Case 2
Np-237	5.61	5.50
Pu-238	2.67	2.51
Pu-239	**38.12**	**38.54**
Pu-240	22.59	22.82
Pu-241	**14.34**	**14.39**
Pu-242	10.11	9.80
Am-241	4.79	4.75
Am-242m	0.044	0.041
Am-243	1.73	1.64

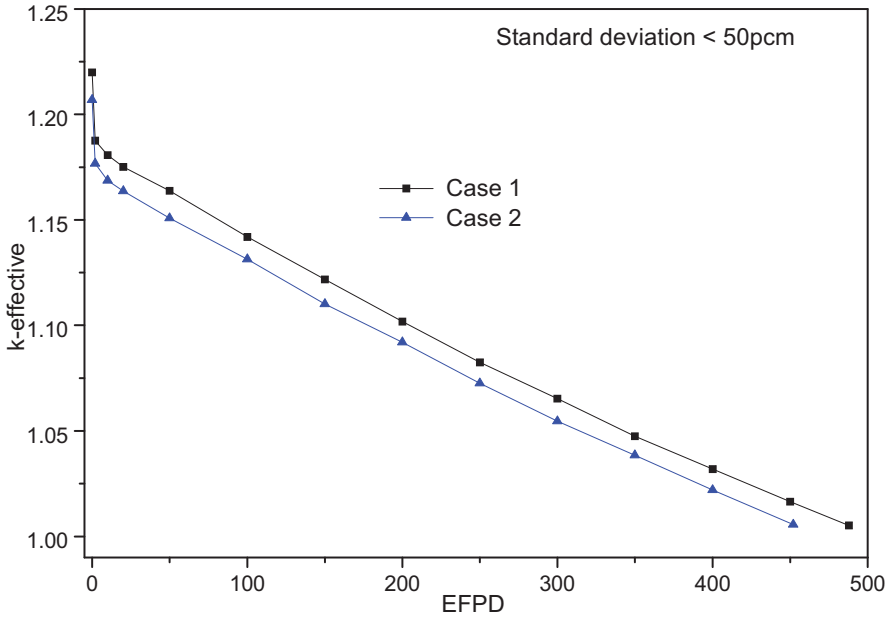

Figure 280. Evolution of equilibrium reactivity in SC-HTR.

With the axial shuffling scheme in Figure 278, consecutive eight cycles were simulated by the McCARD code and an equilibrium cycle was determined. Figure 280 shows the reactivity rundown curve during an equilibrium cycle for Case 1 and Case 2. In Figure 280, one can see that the core reactivity linearly decreases with burnup and its behavior is quite similar to that observed in a UO_2 HTR core. In the current evaluation, the EOC residual reactivity is relatively big, ~500 pcm. As shown in Figure 280 and Table 38, the equilibrium cycle lengths of Case 1 and Case 2 are 487 and 450 EFPDs, respectively. The cycle length of Case 2 is shorter than that of Case 1 because of the smaller UO_2 fuel mass and the larger neutron leakage.

In Table 40 and Table 41, burnups of the uranium and TRU fuels in Case 1 and Case 2 are summarized. The UO_2 burnups of Case 1 and Case 2 are 10.3% and 10.1%, respectively. And the TRU discharge burnups of Case 1 and Case 2 are 64.7% and 63.5%, respectively. Taking into the uranium enrichment of 12w/o, the UO_2 burn can be considered to be rather high. Also, the achieved discharge burnup of TRU should be considered extremely high. The high burnup is mainly ascribed to the additional transmutation by neutrons produced in the uranium fuel zone. This implies that the fuel burnup would be significantly higher than 10.3% in Case 1, if the core is solely loaded with UO_2 fuels.

Table 40. Burnup of uranium and TRU fuel in Case 1.

Fuel Type		HM mass (kg)		Burnup, %	
		BOC	EOC	BOC	EOC
UO_2	Fresh	2,582	2,462	0.0	4.6
	1-burned	2,462	2,371	4.6	8.2
	2-burned	2,371	2,316	8.2	10.3
	Total	7,415	7,149		
TRU	Fresh	51.61	28.60	0.0	44.6
	1-burned	28.67	20.90	44.4	59.5
	2-burned	20.91	18.23	59.5	64.7
	Total	101.19	67.73		

Table 41. Burnup of uranium and TRU fuel in Case 2.

Fuel Type		HM mass (kg)		Burnup, %	
		BOC	EOC	BOC	EOC
UO_2	Fresh	2,437	2,326	0.0	4.6
	1-burned	2,326	2,241	4.6	8.0
	2-burned	2,241	2,190	8.0	10.1
	Total	7,004	6,757		
TRU	Fresh	48.23	28.31	0.0	41.3
	1-burned	28.34	20.42	41.2	57.7
	2-burned	20.45	17.60	57.6	63.5
	Total	97.02	66.33		

Table 42. Axial power profiles in SC-HTR.

	Case 1		Case 2	
Layer	BOC	EOC	BOC	EOC
9 (Top)	0.51	0.57	0.57	0.59
8	1.59	1.31	1.72	1.32
7	1.04	1.06	1.20	1.08
6	1.17	1.09	1.29	1.11
5	1.93	1.40	1.91	1.41
4	0.65	0.74	0.66	0.75
3	0.66	0.95	0.56	0.94
2	1.09	1.32	0.81	1.26
1 (bottom)	0.35	0.57	0.27	0.56

Table 42 and Figure 281 show the axial and radial power distributions, respectively. As shown in Table 42, the axial power profile at BOC is top-skewed due to the axial shuffling scheme adopted.

However, it became a bottom-skewed one at EOC as is expected. From Figure 281, one can see that the power density of the TRU region is much lower than that of the UO_2 region in the all cases. Also, it is observed that the distribution of Case 2 is more flat than that of Case 1. The lower power density in TRU fuel is because the TRU burnup is very high and the heavy metal inventory in a TRU block is much lower than that in UO_2 fuel block. The radial power distribution indicates that some design measures needs to be introduced to flatten the overall power distribution.

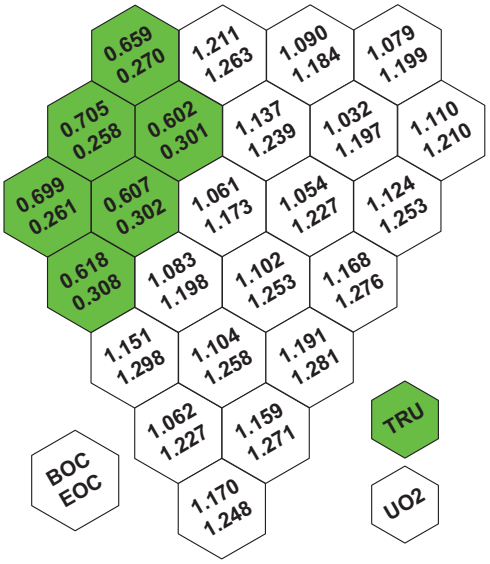

(a) Case 1

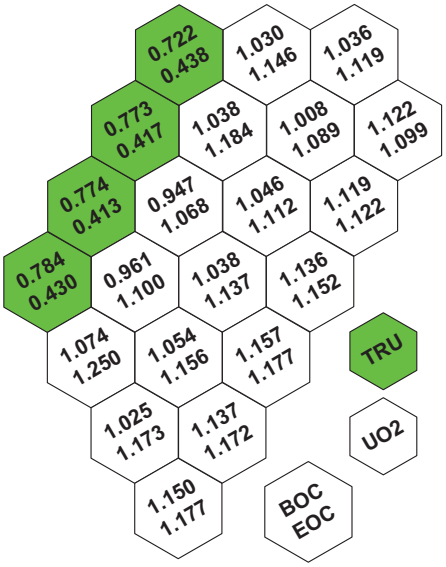

(b) Case 2

Figure 281. Normalized assembly power distribution.

In Table 43 and Table 44, the TRU composition changes after deep-burn are given. The burnup of plutonium and TRU of Case 1 is higher than that of Case 2 because the neutron leakage of the Case 1 is smaller than that of the Case 2. However, transmutation of Pu-239 in the two cases is near complete in SC-HTR. It is worthwhile to note that the transmutation rates of Pu-240 and Pu-241 is significantly higher than in the previous DB-MHR case.[4] Again, this is because the transmutation of TRU is boosted by the uranium fuel, as compared with a TRU-only DB-MTR case.

Decay heat of SC-HTR core is shown in Figure 282. Decay heat of Case 1 and Case 2 is very similar to the UO_2 only core with 23.5% packing fraction of TRISO and 12 w/o uranium enrichment, which is consisted of 108 columns and nine layers HTR core.

Table 43. TRU composition change after deep-burn of the Case 1.

	Charge		Discharge		
Nuclide	Mass (kg)	Fraction (%)	Mass (kg)	Fraction (%)	Consumption (%)
U-234			0.06	0.34	
U-235			0.01	0.05	
U-236			0.004	0.02	
Np-237	2.89	5.61	0.66	3.62	-77.2
Pu-238	1.38	2.67	2.16	11.86	57.0
Pu-239	19.66	38.09	0.24	1.29	**-98.8**
Pu-240	11.65	22.58	1.12	6.13	-90.4
Pu-241	7.41	14.35	0.61	3.36	**-91.7**
Pu-242	5.22	10.12	8.87	49.19	71.7
Am-241	2.47	4.79	0.03	0.17	-98.7
Am-242m	0.03	0.05	0.002	0.01	-94.6
Am-243	0.90	1.74	2.49	13.64	177.0
Cm-242			0.05	0.26	
Cm-243			0.004	0.02	
Cm-244			1.76	9.65	
Cm-245			0.05	0.28	
Cm-246			0.02	0.12	
Pu	45.32	87.81	13.09	71.83	**-71.1**
TRU	51.61	100.0	18.23	100.0	**-64.7**

Table 44. TRU composition change after deep-burn of the Case 2.

Nuclide	Charge		Discharge		
	Mass (kg)	Fraction (%)	Mass (kg)	Fraction (%)	Consumption (%)
U-234			0.05	0.31	
U-235			0.01	0.05	
U-236			0.003	0.02	
Np-237	2.65	5.50	0.71	4.02	-73.3
Pu-238	1.21	2.51	2.25	12.78	85.6
Pu-239	18.59	38.54	0.24	1.38	**-98.7**
Pu-240	11.00	22.82	1.30	7.41	-88.1
Pu-241	6.94	14.39	0.84	4.76	**-87.9**
Pu-242	4.73	9.80	8.12	46.13	71.8
Am-241	2.29	4.75	0.05	0.27	-97.9
Am-242m	0.02	0.05	0.002	0.01	-90.5
Am-243	0.79	1.64	2.30	13.05	190.9
Cm-242			0.07	0.38	
Cm-243			0.005	0.03	
Cm-244			1.58	8.98	
Cm-245			0.05	0.31	
Cm-246			0.02	0.11	
Pu	42.47	88.06	12.75	72.45	**-70.0**
TRU	48.23	100.0	17.60	100.0	**-63.5**

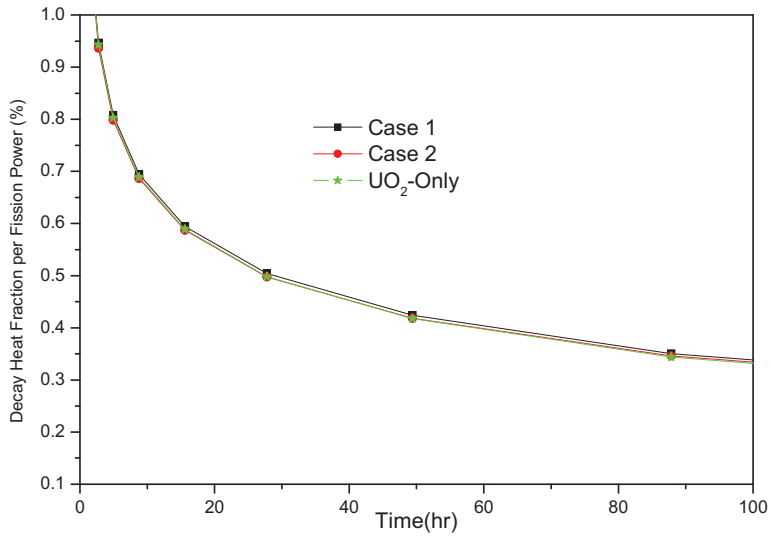

Figure 282. Decay heat of SC-HTR core.

8.4 Conclusions

Core characteristics and performances have been evaluated for an SC-HTR. It has been demonstrated that SC of self-generated TRUs is feasible and deep-burning of the self-generated TRU can be achieved in SC-HTR. The TRU discharge burnups in SC-HTR is shown to be over 63%. The fissile (Pu-239 and Pu-241) content of the self-generated TRU vector is about 52%. Also, it is observed that the power distribution is rather flat within the uranium fuel zone, but the power sharing of TRU fuel zone is significantly lower due to the very high TRU fuel burnup. It was found that transmutation of Pu-239 is near complete (~99%) in the SC-HTR core and that of Pu-241 is also extremely high. The decay heat of SC-HTR core is evaluated to be very similar to that of the conventional UO_2-only core. It is expected that the TRU deep-burn can be improved if the fuel management and core designs are optimized.

8.5 References

1. S. G. Hong, Y. Kim, F. Venneri, "Characterization of a Sodium-cooled Fast Reactor in an MHR-SFR synergy for TRU Transmutation," *Annals of Nuclear Energy*, 35, pp.1461–1470, 2008.
2. A. Talamo, W. Gudowski, F. Venneri, "The Burnup Capabilities of the Deep Burn Modular Helium Reactor Analyzed by the Monte Carlo Continuous Energy Code MCB," Annals of Nuclear Energy 31, pp.173–196, 2004.
3. Potter and A. Shenoy, "Gas Turbine-Modular Helium Reactor (GT-MHR) Conceptual Design Description Report," GA Report 910720, Revision 1, General Atomics, July 1996.
4. Y. Kim and F. Venneri, "Optimization of One-Pass Transuranic Deep Burn in a Modular Helium Reactor," *Nuclear Science and Engineering,* 160, 59–74, 2008.
5. H. J. Shim et al., "Numerical Experiment on Variance Biases and Monte Carlo Neutronic Analysis with Thermal Hydraulic Feedback," Int. Conf. On Supercomputing in Nuclear Applications, SNA 2003, September 22–24, 2003, Paris, France.
6. Y. Kim and M. Baek, "Elimination of Double-Heterogeneity through a Reactivity-Equivalent Physical Transformation," GLOBAL 2005, Tsukuba, Japan, October 9–13, 2005.
7. Y. Kim and W. S. Park, "Reactivity-Equivalent Physical Transformation for Elimination of Double-Heterogeneity," Transaction of Am. Nucl. Soc., 93, 959, 2005.
8. Y. Kim and J. M. Noh, "Physical Similarity in the Reactivity-equivalent Physical Transformation," Transaction of Am. Nucl. Soc., 94, 383, 2006.

Appendix A

Task 2.1 Contribution from INL

A-1. Highlights from INL Contribution to Subtask 2.1

- Studies were performed analyzing the effect of size of a DRAGON supercell on the homogenized cross sections produced for whole core diffusion calculations for Deep Burn Very High-Temperature Reactors (DB-VHTRs).
- Further work was performed to analyze the effects of lattice calculation assumptions on whole core calculations using the Idaho National Laboratory (INL) P_n code. Both single block calculations and 1/12 core calculations were performed in DRAGON and the power shapes compared in INSTANT using various energy group condensations.
- The following conference paper has been submitted: "Investigation of Supercells for Preparation of Homogenized Cross Sections for Prismatic Deep Burn VHTR Calculations," M.A. Pope, J. Ortensi, A.M. Ougouag, HTR 2010 Conference Prague, paper 207, Czech Republic, October 18–20, 2010.

A-2. Core Design Optimization in the HTR Prismatic Block Design (INL)

The traditional two-step method of neutronic analysis typically used for Light Water Reactors (LWRs) involves a transport calculation on a relatively small domain (usually one fuel assembly) in fine groups, followed by homogenization of the domain and condensation of cross sections to course energy groups for a whole core nodal diffusion code. Because LWRs have very short neutron mean free paths, the spectral influence of one assembly does not penetrate deep into its neighboring assemblies. Therefore, for most LWR applications, a single assembly with reflected boundary conditions is adequate to capture the correct spectrum and produce accurate few group cross sections. In more challenging scenarios, such as a partial core of mixed oxide fuel or surrounding a cruciform control rod in a boiling water reactor, colorsets are used, which include in the domain one-half of each of the surrounding fuel elements.

In VHTRs, the neutron mean free paths and resulting migration areas are significantly larger than those of LWRs. Thus the spectrum at any point in the reactor is more strongly influenced by other regions far from the point of interest. Therefore, infinite lattice transport calculations for the purpose of coarse group cross section preparation may not be adequate for all VHTR analysis. There are several types of dissimilarities between blocks that can affect the spectra of other blocks; fuel elements of different burnups or initial enrichments, placement of burnable poisons in adjacent blocks, control rod locations, and perhaps most importantly, the location of reflector regions on the inside and outside of the annular fuel region.

The particular case of the DB-VHTR introduces challenges additional to those faced in traditional enriched uranium VHTR analysis. The difference in neutron spectrum between fresh TRU-loaded fuel and the same element fully burned is substantial in comparison to the change that occurs during the life of a fuel block loaded with enriched uranium. Furthermore, more extensive use of burnable poisons in the DB-VHTR than in the traditional VHTR may also complicate the spectral communication between neighboring blocks.

During this quarter, work was performed at INL in further development and evaluation of methods used in preparing cross sections for use in prismatic DB-VHTR analysis. The reactor parameters used in this analysis represent a simplified prismatic DB-VHTR with core layout, fuel block design, and TRU compositions similar to those in Kim and Venneri's 2008 article.[1]

Figure A-1 shows the layout of the core with the shaded regions representing the fuel blocks and the white regions the reflector blocks. The dimensions are similar to the Next Generation Nuclear Plant (NGNP), but instead of the typical three rings of fuel, the DB-VHTR has five rings of fuel to give lower leakage, increasing fuel economy and the resulting discharge burnup over a three-ring design. The steel core barrel and vessel wall are shown in Figure A-1 as well, but are not of great neutronic significance in this analysis. These initial investigations were performed with the objective of capturing the effect of reflectors on the neutron spectrum in peripheral fuel blocks and the resulting cross sections and diffusion parameters generated for whole core diffusion code. As a test for the methods, a block on the outer periphery (shown with an arrow in Figure A-1) was selected as a fuel location whose proximity to reflector blocks would present a challenge for cross section preparation.

Table A-1 gives a list of parameters for the DB-VHTR core modeled in this work. The design has been simplified in several ways for this preliminary stage of work; all fuel blocks were assumed to be fresh TRU-loaded fuel, no burnable poisons or control rods were modeled, and axial effects were excluded from the analysis (i.e., 2-D core). The fuel kernels of DB-VHTR fuel have reduced diameters from that of a typical VHTR design. Here, 200 μm kernels were used containing stoichiometric TRU-O_2 of density 10.86 g/cm^3 and the isotopics given in Table A-2. The TRISO particle layers other than the fuel kernel are typical with the dimensions and densities given in Table A-3. Graphite in the compact matrix had a density of 1.70 g/cm^3 while block graphite had a density of 1.75 g/cm^3.

Figure A-2 shows a diagram of the simplified DB-VHTR fuel blocks used in this analysis. Note that the six corner locations, normally reserved for burnable poisons, have been filled in with graphite of the same density of the block. Fuel and coolant locations are indicated in the figure by dark and light circles, respectively. Fuel handling holes, along with control rod holes, have been omitted for further simplification of this preliminary analysis. Reflector blocks were assumed to be solid graphite with the same density of the fuel block graphite material.

A-2.1 Review of Challenges in Modeling Prismatic DB-VHTRs

The traditional two-step method of neutronic analysis typically used for LWRs involves a transport calculation on a relatively small domain (usually one fuel assembly) in fine groups, followed by homogenization of the domain and condensation of cross sections to course energy groups for a whole core nodal diffusion code. Because LWRs have very short neutron mean free paths, the spectral influence of one assembly does not penetrate deep into its neighboring assemblies. Therefore, for most LWR applications, a single assembly with reflected boundary conditions is adequate to capture the correct spectrum and produce accurate few group cross sections. In more challenging scenarios, such as a partial core of mixed oxide fuel or surrounding a cruciform control rod in a boiling water reactor, colorsets are used that include in the domain one-half of each of the surrounding fuel elements.

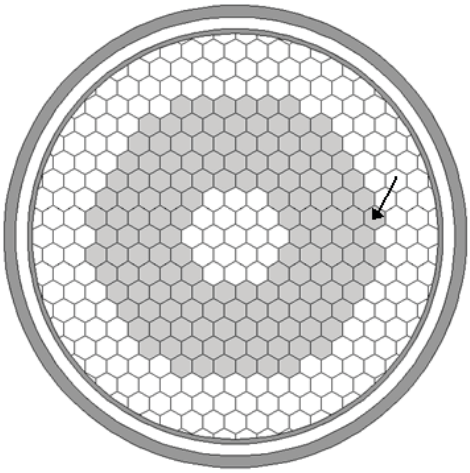

Figure A-1. Core map of simplified prismatic DB-VHTR with block of interest indicated with arrow.

Table A-1. Core and fuel block parameters.

Parameter	Value
Block flat-to-flat dimension (cm)	36.0
Block pitch (cm)	36.1
Large coolant channel diameter (cm)	1.588
Large coolant channels per block	102
Small coolant channel diameter (cm)	1.27
Small coolant channels per block	6
Fuel compact diameter (cm)	1.245
Fuel compact locations per block	210
Fuel hole diameter (cm)	1.27
Coolant/Fuel channel pitch (cm)	1.88
TRISO packing fraction (%)	17.5

Table A-2. Fuel composition in weight percent.

Nuclide	Weight Fraction (%)
Np-237	6.8
Pu-238	2.9
Pu-239	49.5
Pu-240	23.0
Pu-241	8.8
Pu-242	4.9
Am-241	2.8
Am-242m	0.02
Am-243	1.4

Table A-3. TRISO particle layer dimensions and densities.

Layer	Thickness (μm)	Density (g/cm^3)
Fuel Kernel	200	10.86
Buffer Layer	120	1.05
IPyC	40	1.9
SiC	35	3.18
OPyC	40	1.9

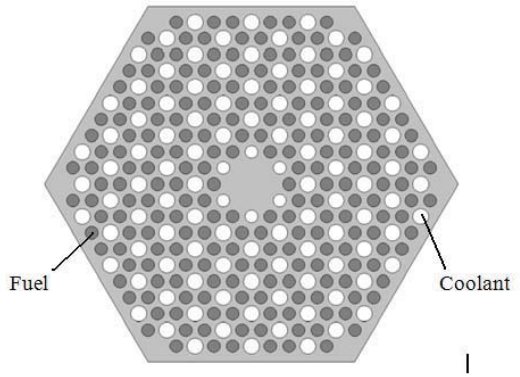

Figure A-2. Schematic of simplified fuel block used in this analysis.

In VHTRs, the neutron mean-free paths and resulting migration areas are significantly larger than those of LWRs. Thus the spectrum at any point in the reactor is more strongly influenced by other regions far from the point of interest. Therefore, infinite lattice transport calculations for the purpose of coarse group cross section preparation are not adequate in VHTR analysis. There are several types of dissimilarities between blocks that can affect the spectra of other blocks—fuel elements of different burnups or initial enrichments, placement of burnable poisons in adjacent blocks, control rod locations, and perhaps most importantly, the location of reflector regions on the inside and outside of the annular fuel region.

The particular case of the DB-VHTR introduces challenges additional to those faced in traditional enriched uranium VHTR analysis. The difference in neutron spectrum between fresh TRU-loaded fuel and the same element fully burned is substantial in comparison to the change that occurs during the life of a fuel block loaded with enriched uranium. Furthermore, more extensive use of burnable poisons in the DB-VHTR than in the traditional VHTR may also complicate the spectral communication between neighboring blocks.

A-2.2 Calculation Methods

A-2.2.1 DRAGON Supercell Models

The DRAGON[2] supercell models used here were constructed in a multi-step procedure starting with a small domain, which includes the 1/12 fuel block shown in Figure A-3. Collision probability calculations are performed on this domain treating the double-heterogeneity of the TRISO particles in the fuel compacts directly using the method by Hébert.[3] The cross section library used was ENDF/B-VII in the SHEM-281 energy group structure.[4] As is evident in Figure A-3, DRAGON is currently limited in

hexagonal geometry to building a hexagonal block from smaller hexagonal cells. Because of this, a single block is modeled by using an outer row of hexagons containing a reduced density of graphite to conserve the correct ratio of materials for the single block.

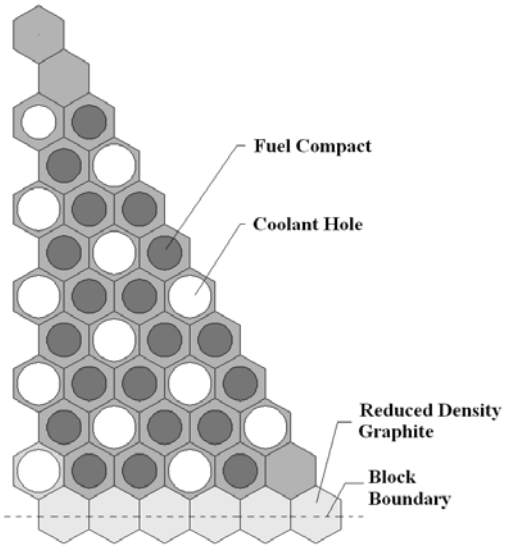

Figure A-3. 1/12 assembly DRAGON model.

Once the flux solution is obtained for the first step, each cell within the domain shown in Figure A-3 is homogenized and effective homogenized cross sections are written in the same 281-group structure for each cell type—fuel locations, coolant channels, and graphite. These new homogenized cells and their cross sections are then used to construct the supercell shown in Figure A-4. In this figure, various supercell sizes are shown with dark lines accompanied by the supercell size in centimeters. This size is defined as the distance past a flat side of the block of interest that the supercell domain extends. Starting with the block of interest alone (denoted by 0 cm), the supercell was extended to approximately 72 cm beyond the boundary of the block of interest. Collision probability calculations were performed for each domain size and homogenized parameters for the block of interest were tabulated.

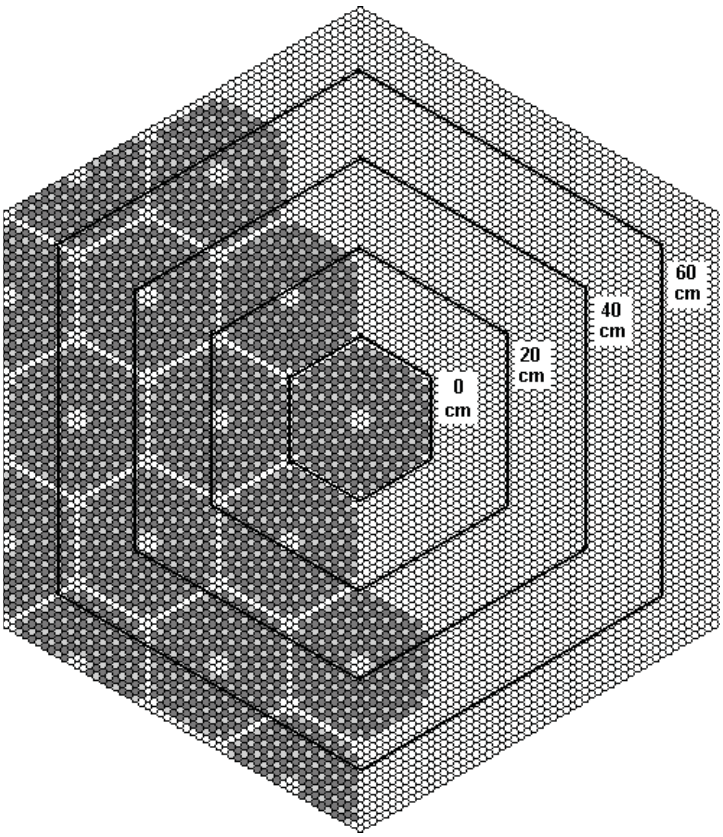

Figure A-4. Diagram of DRAGON supercell for peripheral block of interest with various domain sizes.

A-2.2.2 MCNP5 Model

In the absence of experimental data to validate the methods of cross section preparation evaluated in this work, a reference set of calculations must be used. In this work, several calculations were made using MCNP5[5] for comparison against the results from the DRAGON supercell calculations. The model used was the thin 1/12 core slice shown in Figure A-5. Top and bottom boundaries were modeled using reflective surfaces and the outer radial boundary beyond the reactor vessel was a void condition. Some labels are included on and around the block of interest that will be referred to below.

Since a truly random distribution of TRISO particles within each compact is not available in the current version of MCNP5, a lattice was constructed of matrix graphite cubes, each containing a TRISO particle, as is shown in Figure A-6. The location of each particle within its cubic lattice location is regenerated randomly each time a neutron enters the lattice element. While not a strictly true representation of a stochastic mixture of particles, this method has been shown to perform well in comparison to models containing random arrangements of TRISO particles.[6] The core model was only tall enough in the axial direction for one layer of TRISO particles.

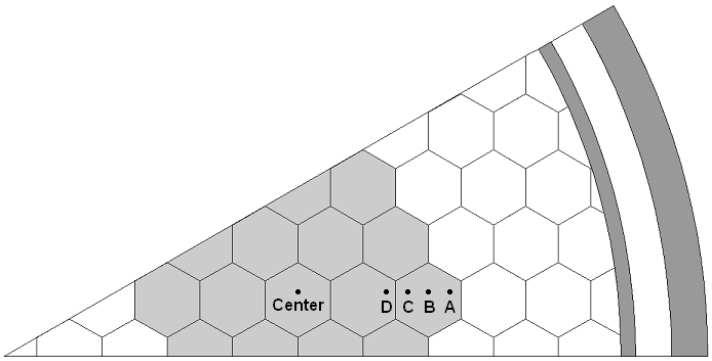

Figure A-5. View of MCNP5 model with locations of flux tallies shown in Figure A-7 and Figure A-8.

Figure A-7 shows the normalized neutron flux per unit lethargy versus energy in the tally locations shown in Figure A-5. From this, it can be observed that the spectrum change across the peripheral fuel assembly is quite extreme, with very thermal flux close to fuel/reflector interface due to the large number of thermal neutrons returning from the reflector. This is the cause of the large power peaking in fuel compacts near the reflector in an unpoisoned reactor. As the tally location moves farther from the fuel/reflector interface, the large thermal flux peak disappears and by the time the other side of the peripheral fuel assembly is reached (Tally Location C), the flux shape is approaching that of the center of the reactor. Figure A-8 shows the spectra from Tally Points C, D, and the core center. This shows that in the second row of fuel from the reflector, the flux shape is not changing drastically with increased distance from the fuel/reflector interface. This suggests that while infinite lattice calculations on a small domain may be acceptable for the interior fuel assemblies, this assumption would not be appropriate for those on the periphery. It should be noted that this simplified study only provides insight with respect to the spectral effect of distance from the reflector. Burnable poisons, dissimilar fuel, and control rods will complicate the process of cross section preparation, whether it be for a block on the interior of the fuel region or adjacent to an inner or outer reflector.

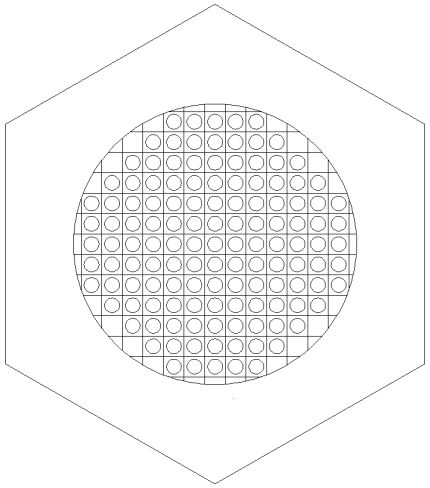

Figure A-6. Modeling of TRISO particles in fuel compacts in MCNP5.

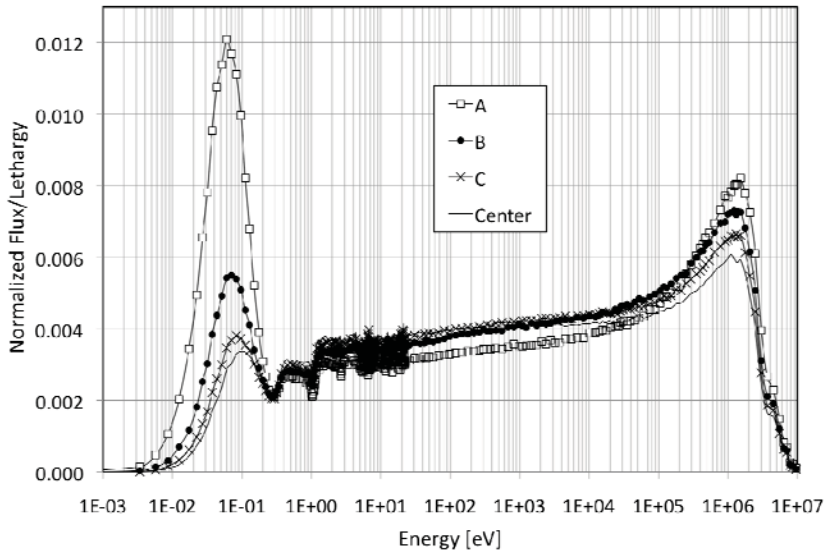

Figure A-7. Normalized flux per unit lethargy calculated in MCNP5 for locations shown in Figure A-5.

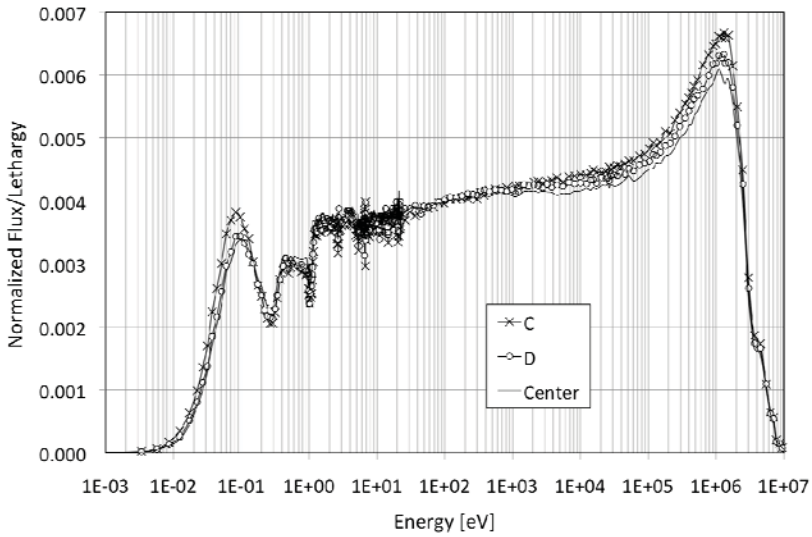

Figure A-8. Normalized flux per unit lethargy calculated in MCNP5 for locations in Figure A-5.

A-2.3 Evaluation of 1-Group Cross Sections

The supercell modeled in DRAGON and shown in Figure A-4 was used to examine the effect that this expanding domain has on the resulting homogenized parameters. One-group homogenized macroscopic cross sections for absorption (Σ_a) and fission ($\nu\Sigma_f$) were calculated along with the diffusion coefficient (D) for increasing domain size. Figure A-9 shows the percent change in each of these parameters versus the size of the supercell from 0 to 72 cm with a reflective outer boundary condition. As the supercell size is increased from the single block of interest, a sharp increase in all three parameters was observed. This is primarily due to the thermalization that takes place with the addition of the reflector material. After approximately 10–25 cm, all three parameters have begun to decrease gradually. Once the supercell

reaches 70 cm, the parameters are changing quite slowly with increase in domain, though they do not appear to have reached their final values.

Once a supercell is large enough to give the true spectrum that would exist in the block of interest (to be completely decoupled), it should be insensitive to the boundary condition used. To test this, the same calculations were performed, but with a void boundary condition instead of reflected. Figure A-10 shows one-group homogenized parameters Σ_a and $\nu\Sigma_f$ versus size of the supercell for both boundary conditions. Diffusion coefficient is omitted because currently DRAGON does not produce this for calculations using void boundary conditions. From this plot it shows that while the reflected and void cases are approaching each other, the cases have not yet totally converged in the largest supercell calculation performed. Thus the supercell is not totally decoupled, even after nearly two rows of neighboring blocks are included in the domain.

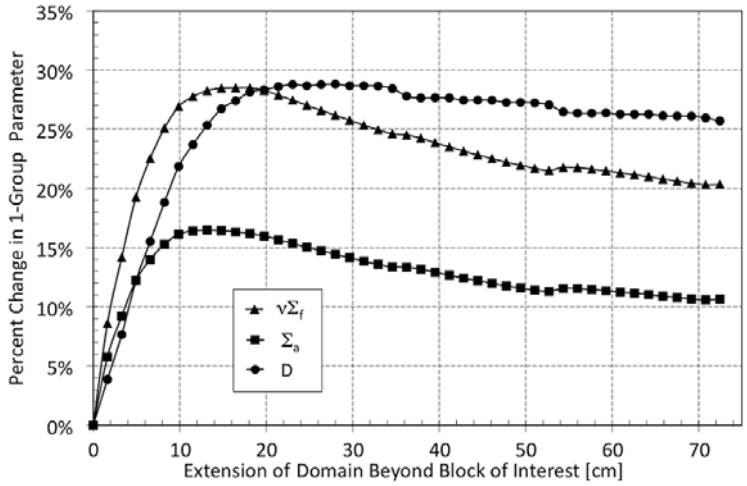

Figure A-9. Percent change in homogenized one-group parameter versus size of supercell with reflected boundary conditions.

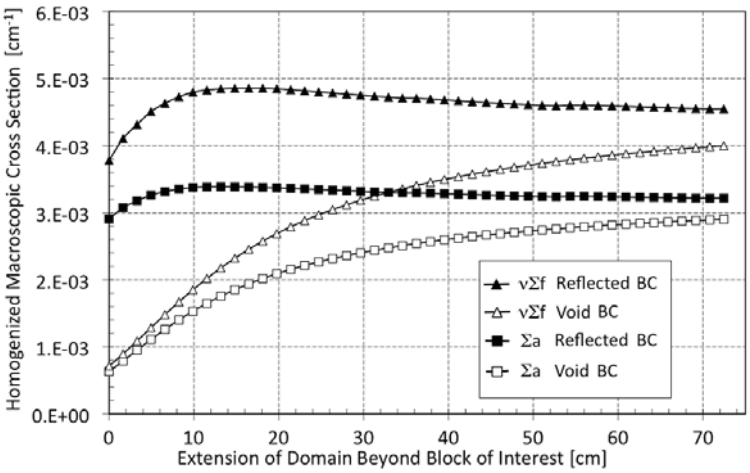

Figure A-10. Homogenized one-group cross sections versus size of supercell for reflected and void boundary conditions.

Figure A-11 shows the neutron spectrum in fuel kernels of the block of interest as calculated using the 72 cm DRAGON supercells with both reflected and void conditions, along with the value from MCNP5. The spectrum calculated using the large reflected supercell in DRAGON is closer to the MCNP5 value than the supercell with the void boundary condition. However, neither one exactly predicts this spectrum. The large regions of flux suppression are due to large low-lying resonances in the plutonium isotopes. These are extreme in this plot because the flux calculation was taken only within the kernels of the TRISO particles.

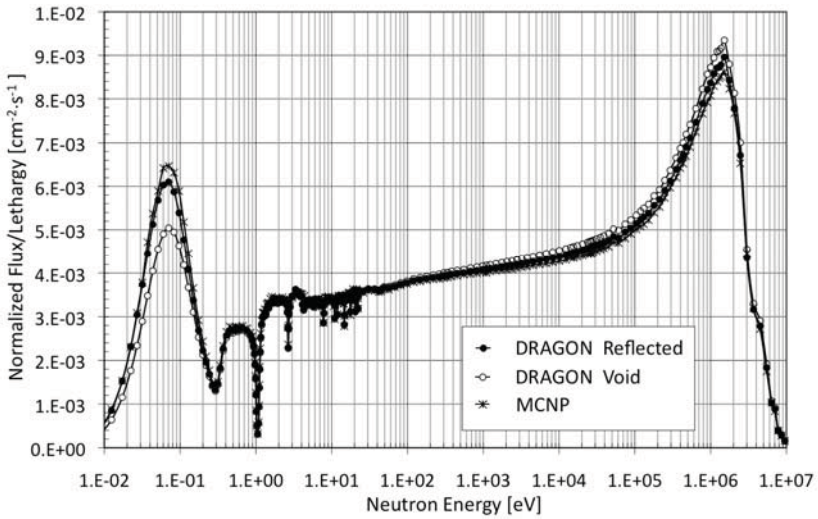

Figure A-11. Neutron energy spectrum for fuel kernels in block of interest calculated with MCNP5 and DRAGON.

A-2.4 Evaluation of Thermal Cross Sections

The homogenized cross sections resulting from the DRAGON supercell of varying size were then collapsed to two energy groups, fast and thermal, with the boundary at 2 eV. Figure A-12 shows the percent change of the homogenized thermal parameters for the block of interest versus size of the supercell with a reflected boundary condition. Here, the diffusion coefficient changes more drastically than in the case where cross sections were collapsed to one group, but the values calculated for Σ_a and $\nu\Sigma_f$ change less with size of supercell and appear to stabilize much more quickly. Figure A-13 shows Σ_a and $\nu\Sigma_f$ values calculated using the same DRAGON supercell, but with the two different boundary conditions, void and reflected. Again diffusion coefficient is omitted since DRAGON does not tabulate this for void boundary conditions. The void and reflected cases converge for the thermal group much more quickly than in the case of all energy groups collapsed to one as was shown above, though they never totally reach one another. This may indicate that for the most important energies, the approximations inherent in very large supercells show promise.

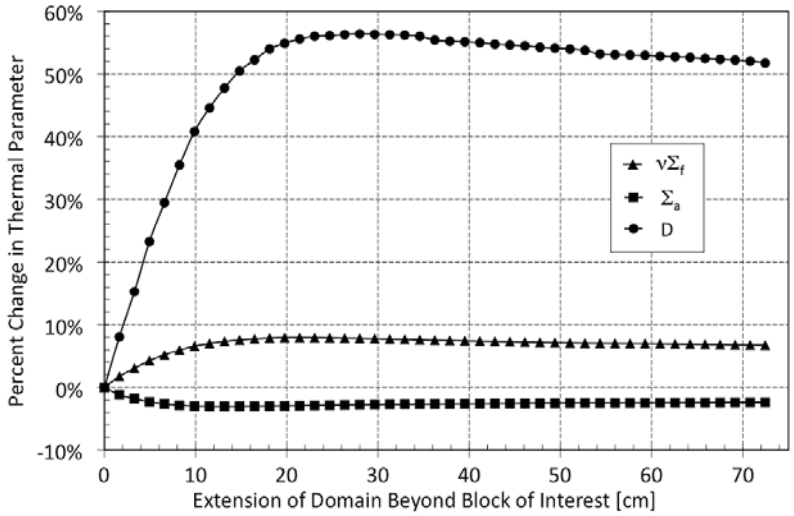

Figure A-12. Percent change in homogenized thermal group parameter versus size of supercell with reflected boundary conditions.

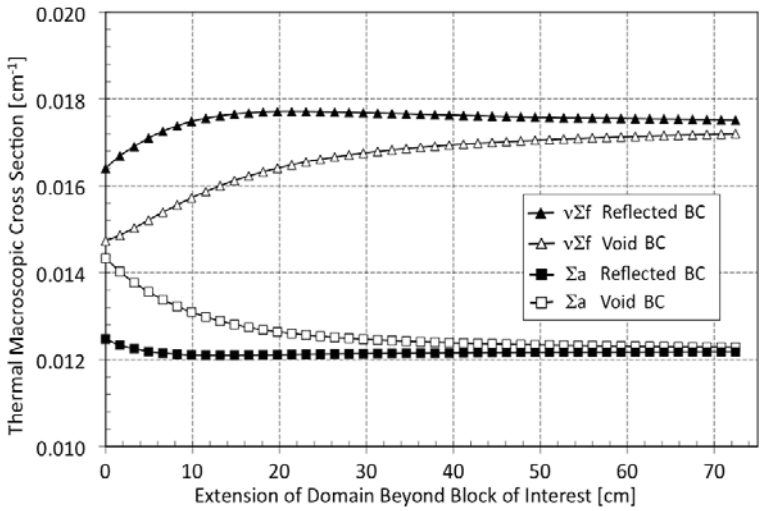

Figure A-13. Homogenized thermal group cross sections versus size of supercell for reflected and void boundary conditions.

A-2.5 Resolution of Power Shape By Supercell

Analysis of commercial LWRs currently requires calculation of individual pin powers. This is done by taking relative pin powers within each assembly from the lattice calculations and scaling them by the power calculated for that homogenized region in the whole-core code. If compact power estimates are required by regulators in prismatic VHTR analysis, it is of interest to examine how well a supercell can predict the power shape within an assembly.

As mentioned above, in an LWR, the short mean-free paths of neutrons allow the analyst to use infinite lattice calculations on single fuel blocks. Dissimilarities between adjacent bundles are not “felt” beyond a few centimeters from the assembly periphery, and so the pin powers within an assembly calculated on this domain can be relied upon in general. Unlike the case of the LWR assembly, performing infinite lattice

calculations on a single VHTR fuel block would not capture the bulk power shape across that block resulting from neighboring assemblies. The power shape across a block would come entirely from the whole core calculation. Using a supercell such as the one described in this work may help to provide this within-assembly information to then be scaled according to the block power calculated by the whole-core code.

To examine the performance of the supercell in predicting power shape in a peripheral fuel block, a radial traverse of fuel compacts across the center of the block of interest was selected. Power was calculated using the DRAGON supercell of variable size for each of the 10 compacts along this traverse for comparison to the MCNP5 model results. Figure A-14 shows relative compact power for these compacts versus their location measured in centimeters from the block center. The compacts to the left on the plot are those closer to the second row of fuel blocks and those on the right of the plot are adjacent to the reflector region. The domain sizes shown range from the single block alone to a supercell extending 64 cm beyond the block of interest. The single block calculation results are shown as darkened squares on the plot. The shape from this assumption is symmetric, though not flat due to the variation in the number of compacts and amount of graphite from one flat side of a fuel block to the other. As the domain increases to successively-larger supercells, a rather extreme variation in power from the side of the fuel adjacent to another fuel block to the side adjacent to reflector. The larger supercells begin to approach the results from the MCNP5 1/12 core model. Figure A-15 shows these values on the basis of their percent deviation from the MCNP5 result. The single block case was omitted to reduce the scale. The 64-cm supercell shows relative compact powers on this traverse differing from MCNP5 results by <3%.

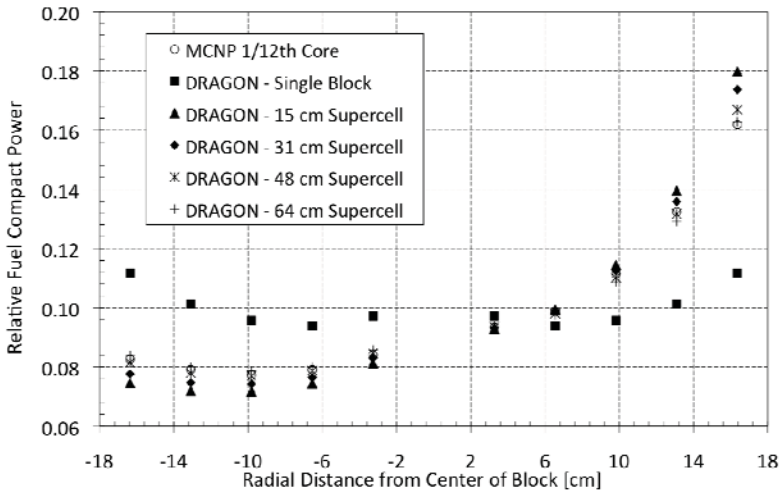

Figure A-14. Relative compact power versus radial distance from center of block of interest.

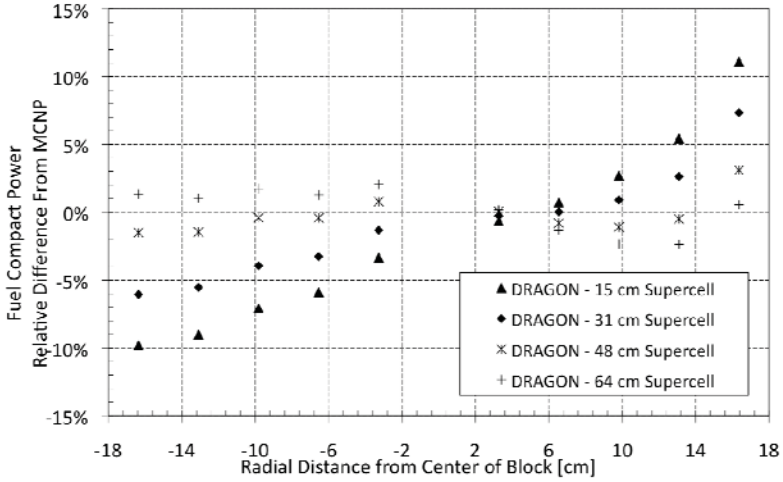

Figure A-15. Variation of compact power from MCNP5 result versus radial distance from center of block of interest.

A-2.6 Effect of Lattice Calculation Methods on Whole-Core Solutions using INSTANT

To investigate the effects of lattice calculation assumptions on whole core solutions, the Idaho National Laboratory code INSTANT.[7] This code uses the hybrid finite element method (FEM) for the spatial discretization and the P_N method for the angular discretization. The interior and interface shape functions used for the FEM are polynomials.

A-2.6.1 Method of Investigation

In this work, the same simplified deep burn core described in the preceding section was assumed. The lattice calculations in DRAGON were performed on a single block and an entire 1/12 core. In future work, supercells should be evaluated in a similar study as an intermediate domain to capture some of the effects of neighboring assemblies. As with the work described above, DRAGON was used as the lattice physics code with the 281-group SHEM group structure. Homogenized cross sections were collapsed from the lattice calculations to various coarse group structures for use in the INSTANT 1/6 core calculations. These were performed in 2-D only to observe effects of energy group structure and lattice calculation domain on the ability to resolve the effect of the inner and outer. As before, lattice calculations were performed in a two-step process wherein a single block calculation is performed and then individual cells are homogenized (e.g., fuel, coolant channels, and solid graphite) for use in the second step.

Figure A-16 shows the 2-D core map of the INSTANT model, with a center reflector cell, two rings of reflector, five rings of fuel blocks, and three rings of reflector blocks. The reactor barrel and vessel were not considered in our analysis because of the limitations in the software used. However, their influence on the reactor physics should be minimal compared to the inner and outer graphite.

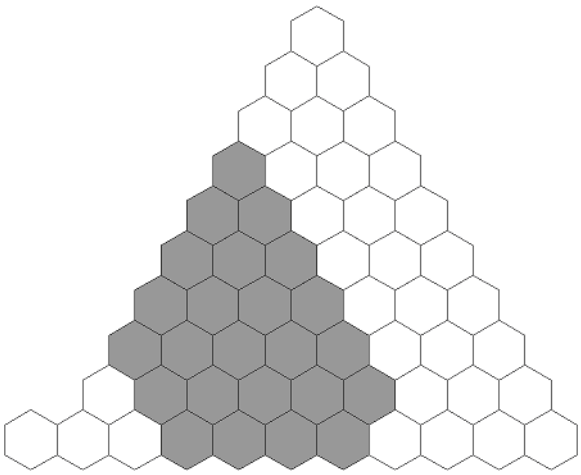

Figure A-16. 1/6 core layout modeled in INSTANT.

Table A-4. Energy boundaries (in eV) for group structures used in this study.

26-Group	23-Group	12-Group	6-Group	4-Group
7.408E+06	3.679E+06	1.8315E+05	1.8315E+05	1.111E+05
3.679E+06	1.353E+06	1.0140E+03	1.6745E+01	2.900E+01
6.721E+05	5.000E+05	1.6745E+01	2.1300E+00	1.860E+00
1.111E+05	1.110E+05	4.1293E+00	6.2501E-01	
1.931E+04	6.738E+04	2.1300E+00	1.1500E-01	
3.355E+03	9.118E+03	1.3050E+00		
1.585E+03	3.673E+02	7.9000E-01		
7.485E+02	4.000E+00	6.2501E-01		
2.754E+02	1.500E+00	3.9100E-01		
1.301E+02	1.097E+00	3.1450E-01		
6.144E+01	1.045E+00	1.1500E-01		
2.900E+01	9.700E-01			
1.370E+01	8.500E-01			
8.320E+00	5.000E-01			
5.040E+00	4.000E-01			
2.380E+00	3.500E-01			
1.290E+00	3.000E-01			
6.500E-01	2.500E-01			
3.500E-01	1.800E-01			
2.000E-01	1.400E-01			
1.120E-01	1.000E-01			
8.000E-02	5.000E-02			
5.000E-02				
2.000E-02				
1.000E-02				

The reflector block cross sections were generated once, and kept for every calculation, so that we can better isolate the change of the fuel cross-sections (mixtures 4 to 11). Details about the generation of cross-sections for the reflector will be provided further, while describing the single block lattice calculation. Based on convergence studies not described in detail here, P_3 was selected as the order of angular discretization to be used for all 1/6 core calculations with INSTANT.

A-2.6.2 DRAGON Single Block Models

The first scheme of calculation was done with the modeling of a single block (in fact 1/12 block symmetry was assumed) of fuel into DRAGON. This model was made up of 11 rows of hexagons plus the central hexagonal cell. Figure A-3 gives a representation of the geometry that was modeled. The dimensions and other details are given in Table A-1, Table A-2, and Table A-3.

As in the case described before, special attention must be given to the boundary cells. Indeed, DRAGON does not have the capability to include a portion of a hexagonal lattice into a larger hexagon. Thus, we are forced to terminate the lattice with a row of hexagons with particular graphite density. This density has been determined to conserve the average homogenized density of graphite material in the whole core calculation. This permits us to take directly the macroscopic cross section generated by DRAGON as input for INSTANT.

DRAGON single block calculations were performed in 281 energy groups, then we performed a homogenization of the whole cell and took the resulting mixture as the fuel mixture used in INSTANT.

The reflector graphite cross sections were calculated with a simplified 2D cylindrical model of the whole core. We first calculated the fuel parameters at 281 groups using the single block model, and then designed a cylindrical core geometry whose dimensions were determined so that we conserved the total surface of the real geometry for each region. These reflector cross sections were kept the same for the entire study. This was done so that we did not introduce a bias while recalculating them with different methods or different cross sections for the fuel ring. This study focuses on the preparation of the fuel homogenized cross sections only. In later work, it will be possible to define a more accurate method to produce cross sections for the reflector blocks.

A-2.6.3 Results from Single Block Calculations

This section describes results of whole core calculations whose cross section data was generated using single block lattice calculations. To provide a reference calculation against which to compare other condensations, a single-block DRAGON calculation was performed followed by homogenization but no condensation in energy. The resulting 281-group cross sections were then used in INSTANT calculations on the 1/6 core model. Figure A-17 shows a contour plot of the resulting power shape. This plot clearly shows the typical peaked power shape which is observed in an annular HTR without burnable poisons at the inner and outer reflector interfaces. Of course, in an actual design this power shape would be flattened by burnable poisons and shuffling schemes, but to resolve that flattening correctly, the peaks in the unpoisoned reactor would need to be resolved correctly.

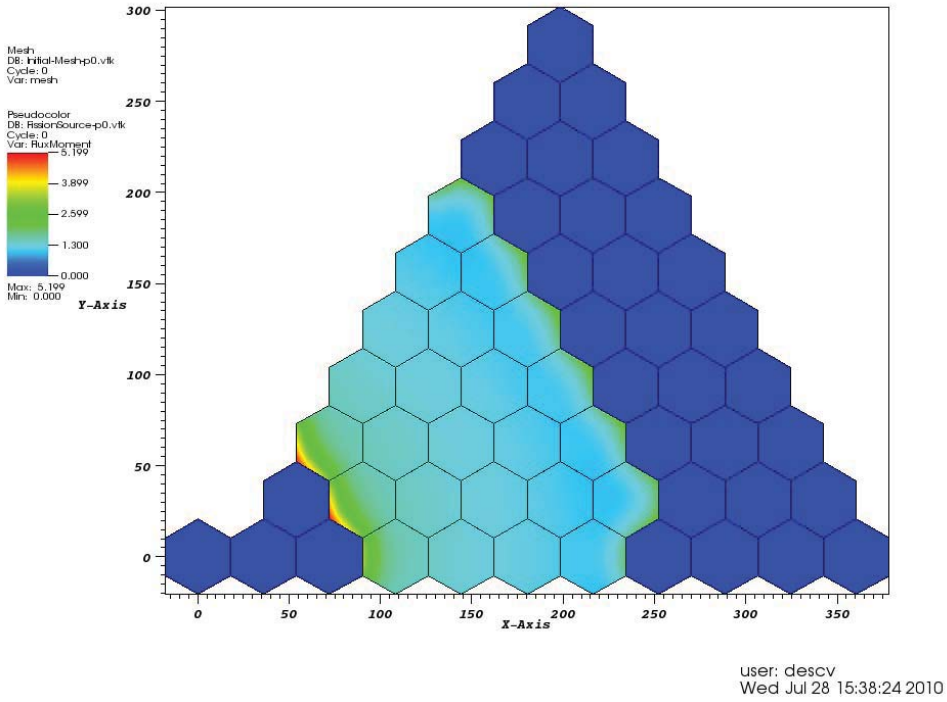

Figure A-17. Power density calculated by INSTANT in 281 energy groups from single block lattice calculations.

When at the homogenization stage, condensation in energy is performed as well, the expected decrease in accuracy was observed and quantified. Cross sections were collapsed to the 4, 12, 23, and 26 group structures shown in Table A-4. Then the percent differences in power relative to the reference case described above were taken and plotted in Figure A-18 through Figure A-22. From these plots, which are arranged in order of increasing number of coarse energy groups, it shows that in the cases where the number of energy groups is small, the percent error from the reference case can be quite large. In the case where the energy condensation is performed to the four-group structure, the error is as high as 28% locally. As the number of energy groups at the whole core level is increased, the peak local error decreases. In the case where the 26-group structure is used, this local error has been reduced to around 1%. Table A-5 shows the peak local power differences between each case and the reference. Another observation from these plots is that the largest errors between each case and the reference occur near the reflector where the flux and power are at their peak values. This is expected because these are the regions where the single block lattice calculations give a neutron spectrum which is the most erroneous in this reactor.

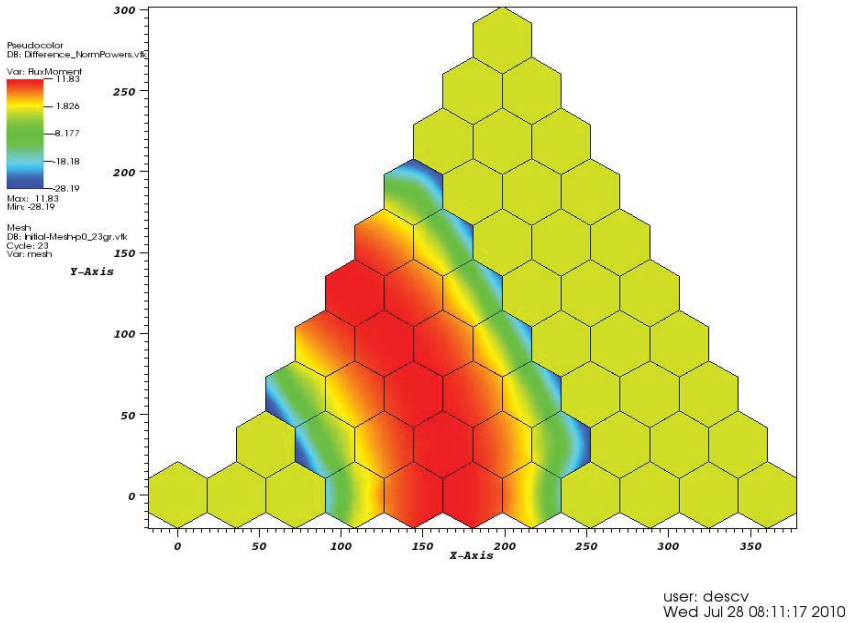

Figure A-18. Percent difference in power density between four-group and 281-group INSTANT calculations, both using single block DRAGON lattice calculations.

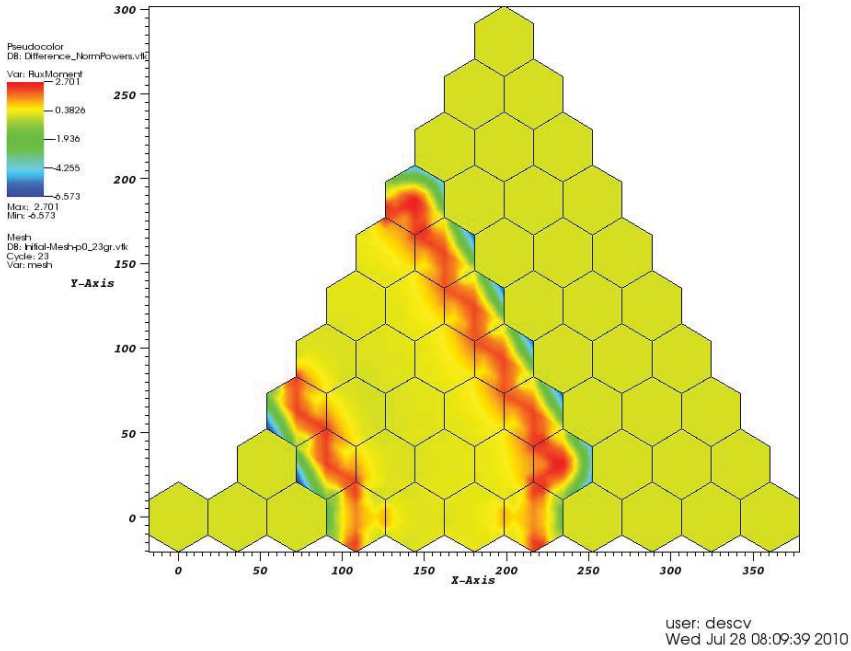

Figure A-19. Percent difference in power density between six-group and 281-group INSTANT calculations, both using single block DRAGON lattice calculations.

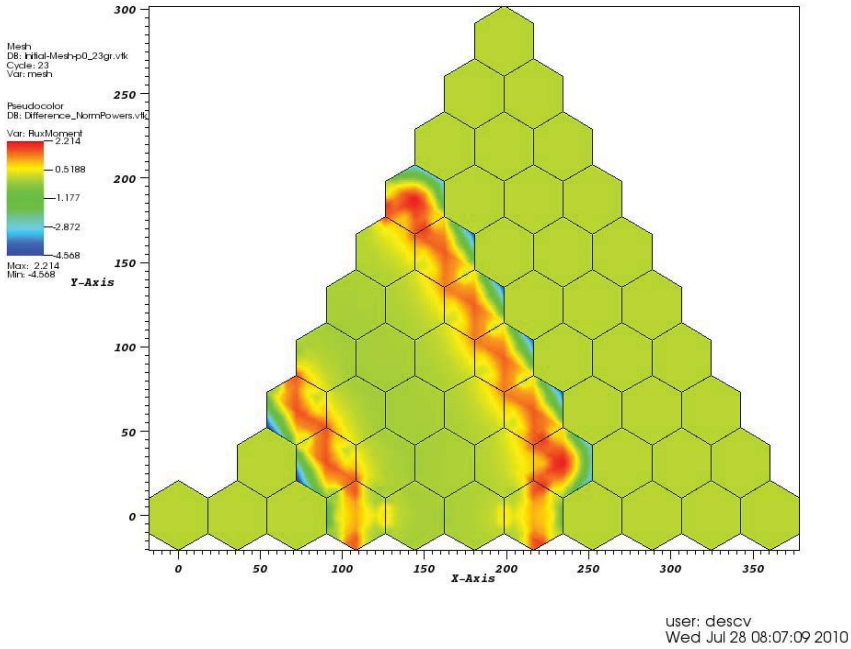

Figure A-20. Percent difference in power density between 12-group and 281-group INSTANT calculations, both using single block DRAGON lattice calculations.

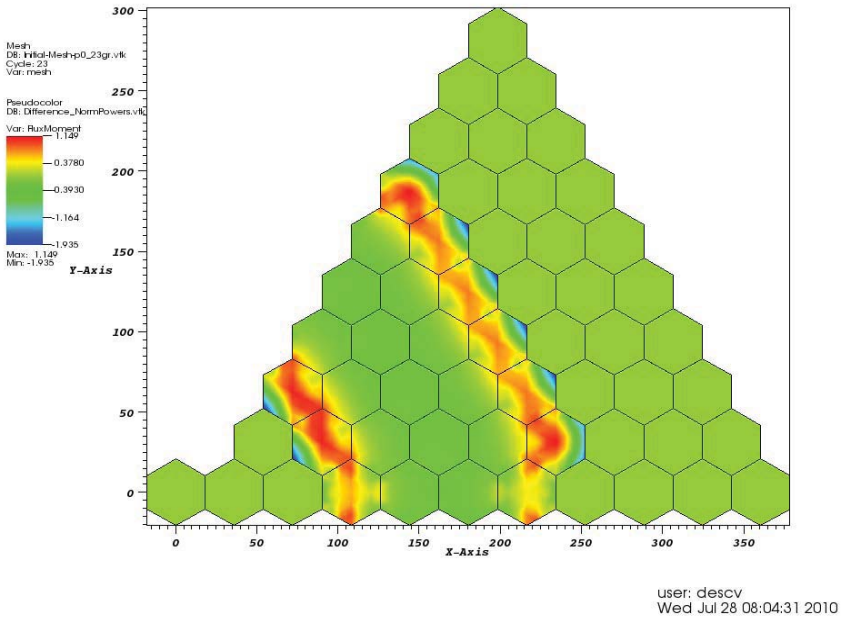

Figure A-21. Percent difference in power density between 23-group and 281-group INSTANT calculations, both using single block DRAGON lattice calculations.

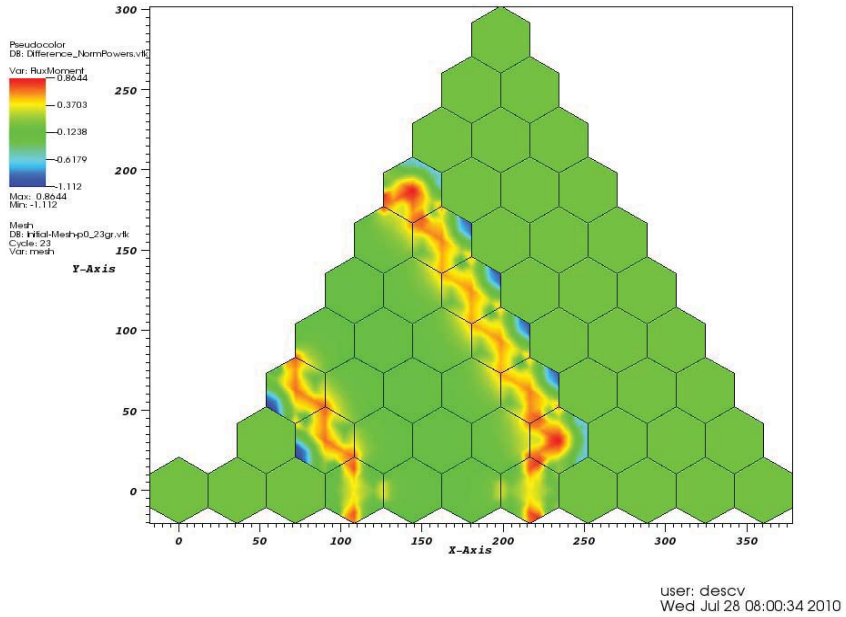

Figure A-22. Percent difference in power density between 26-group and 281-group INSTANT calculations, both using single block DRAGON lattice calculations.

Table A-5. Summary of maximum point differences between coarse group and 281-group INSTANT calculations, all using single-block DRAGON lattice calculations.

Number of Groups	Maximum Positive Difference (%)	Maximum Negative Difference (%)
26	0.8	-1.1
23	1.2	-1.9
12	2.2	-4.6
6	2.7	-6.6
4	12	-28

Table A-6 shows the eigenvalues calculated by INSTANT for each of the group structures used in this work, all with cross sections from single block DRAGON calculations. This shows that the global Eigenvalue parameter converges more quickly than the local power shape to the 281-group solution.

Table A-6. Eigenvalues calculated by INSTANT for each energy group structure using cross sections from single block lattice calculations.

Number of Groups	k_{eff}
281	1.27173
26	1.27193
23	1.27173
12	1.27162
6	1.26978
4	1.23550

A-2.6.4 DRAGON 1/12 Core Models

Lattice calculations were also performed using a 1/12 core model in DRAGON. A schematic of this domain is shown in Figure A-23. In this figure, the white hexagons represent solid graphite, the light gray cells represent homogenized coolant channels, and the dark gray cells represent homogenized fuel cells. The aim of performing the calculation on this domain was to capture the influence of the reflectors on the spectrum in the various fuel blocks (and thus the homogenized cross sections) in a single calculation before passing this information to the whole core calculation in INSTANT. Eight fuel blocks representing different types of fuel block locations in the core were then homogenized and used for the INSTANT calculations on the same core model. These are shown in Figure A-24 in red. Figure A-25 shows how these are mapped onto the 1/6 core model in DRAGON. As can be seen in these figures, the grouping was based on both the number of reflector blocks in contact with a fuel assembly, but the fuel block's distance from the reflector row if it is not in direct contact with any reflector blocks. As before, a reference calculation was performed without energy condensation, only this time the lattice calculation is performed on the 1/12 core domain.

The different energy condensations shown in Table A-4 were also tested using the 1/12 core DRAGON model. The six reflector rings were still modeled with the same cross sections coming from the simple cylindrical model of the core so that only the fuel parameters will be changed in INSTANT. Boundary conditions were set to void at the periphery in the DRAGON model. Convergence was achieved in approximately 150 minutes after 50 outer iterations.

Again, there is a problem with the boundaries of each block not matching the real geometry. In the same way as above, the boundary layer is modeled using an additional row of cells of graphite whose density has been adjusted to keep the average homogenized graphite density of a fuel block in the core. In addition, some of those cells are shared between two blocks, which prevent using the cells in the homogenization process when two adjacent blocks are considered. Therefore, some of the mixtures are prepared with boundary cells from a different location as the right one. It is believed that the most important parameter to be kept in this case is the average homogenized graphite density and that incorrect spectrum in a small fraction of the graphite cells should have a small effect overall.

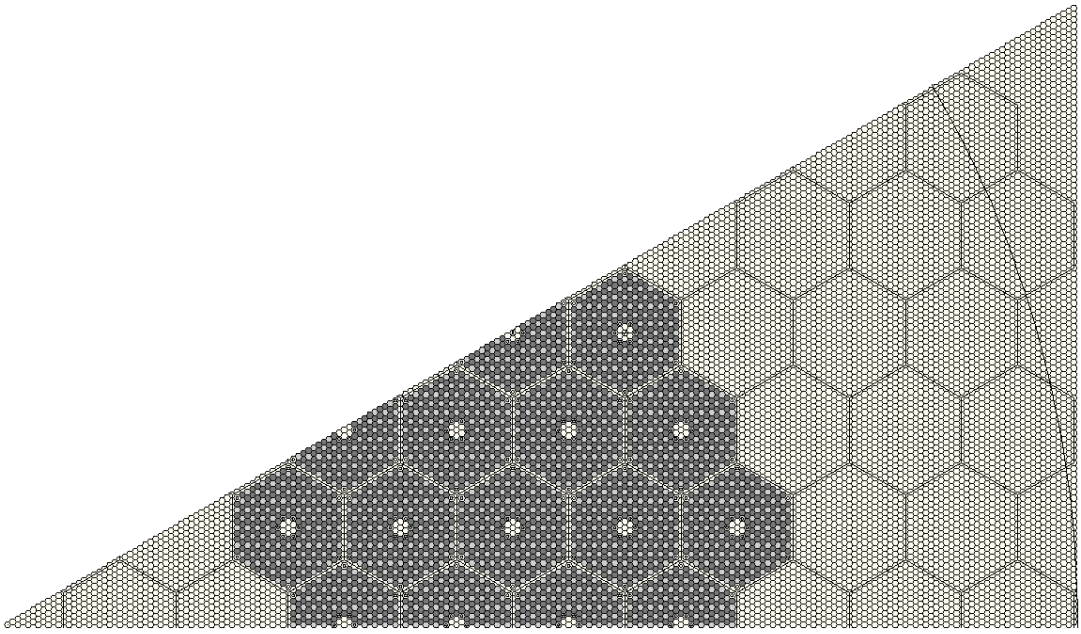

Figure A-23. Schematic of 1/12 core model in DRAGON with location of core barrel (not modeled) shown.

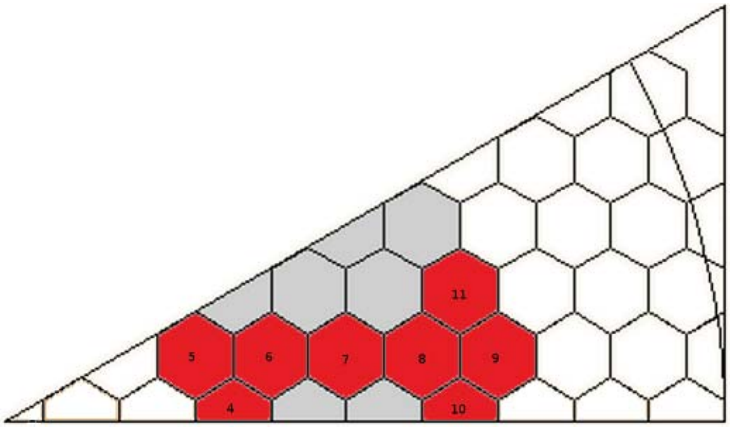

Figure A-24. Diagram showing eight blocks identified as belonging to a unique group based on their surroundings.

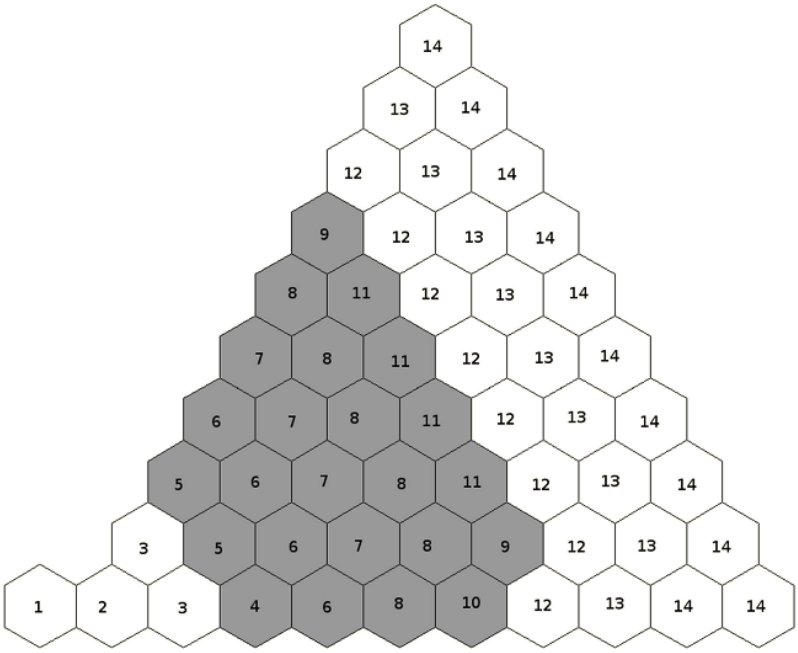

Figure A-25. Diagram showing grouping of unique cross section sets used in INSTANT.

A-2.6.5 Results from 1/12 Core DRAGON Calculations

Figure A-26 shows the percent difference between INSTANT results from a 1/12 core lattice calculation with energy condensation to four groups and the reference case with no condensation. From this, we see that again the discrepancies are near the interface between fuel and reflector. The magnitude of the peak differences is reduced from the single-block four-group case shown in Figure A-18. This is expected since we are calculating cross sections in various blocks based on a more accurate representation of the flux at the lattice level. From Figure A-26 to Figure A-30, the trend of decreasing error can be observed with increasing number of energy groups kept at the whole core level. For a given number of energy groups at the whole core level, the calculations which come from 1/12 core lattice calculation carry less error with respect to the uncondensed calculation than do those which come from the single block calculations.

Another difference in the 1/12 core calculations is that sharp discontinuities in power are observed at block boundaries. This is simply because unlike the single block calculations, which yielded only one set of cross sections to be used in all fuel blocks, the 1/12 core model allowed multiple cross section sets to be homogenized separately according to the schematic of Figure A-24. The discontinuities are simply the result of discontinuous fission cross sections at these boundaries. Table A-7 shows a summary of the peak differences between the different energy condensations and the reference solution. In the case where a 1/12 core calculation was performed and then cross sections homogenized and collapsed to 26 energy groups, the error was below 1%.

Table A-8 shows the eigenvalues calculated by INSTANT for each of the group structures used in this work, all using cross sections from 1/12 core DRAGON calculations. This shows that the global eigenvalue parameter converges more quickly than the local power shape to the 281-group solution. From the 12-group solution to the 281-group solution, the reactivity changes by less than 100 pcm between any two of the group structures.

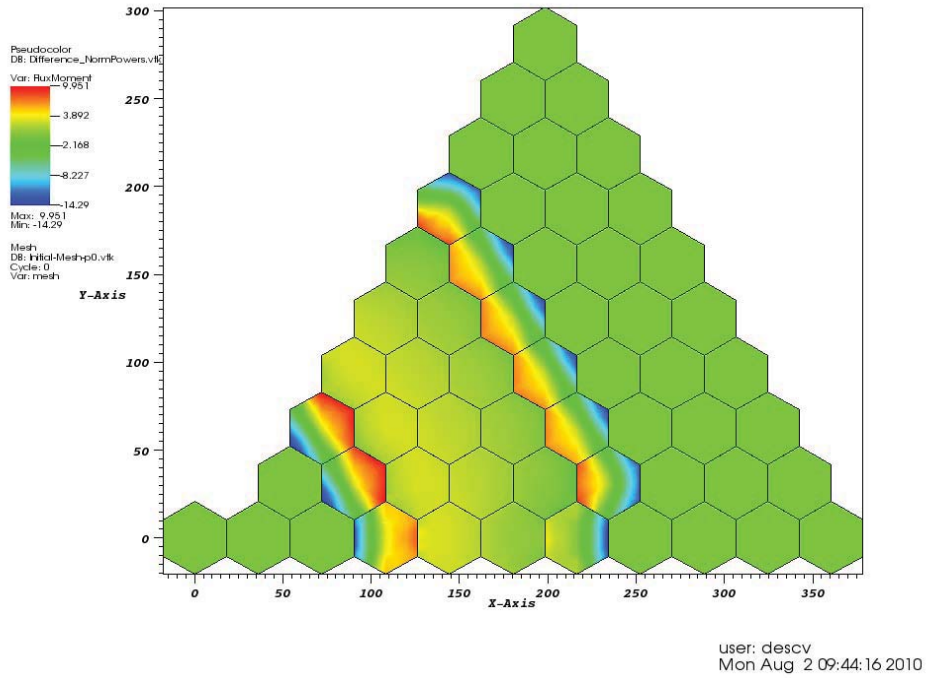

Figure A-26. Percent difference in power density between four-group and 281-group INSTANT calculations, both using 1/12 core DRAGON lattice calculations.

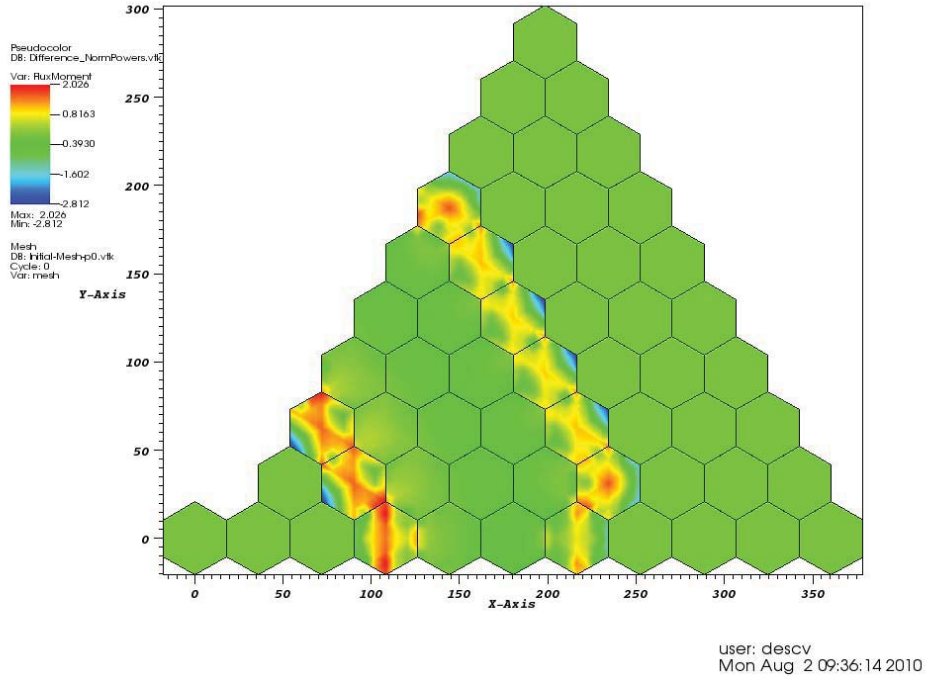

Figure A-27. Percent difference in power density between six-group and 281-group INSTANT calculations, both using 1/12 core DRAGON lattice calculations.

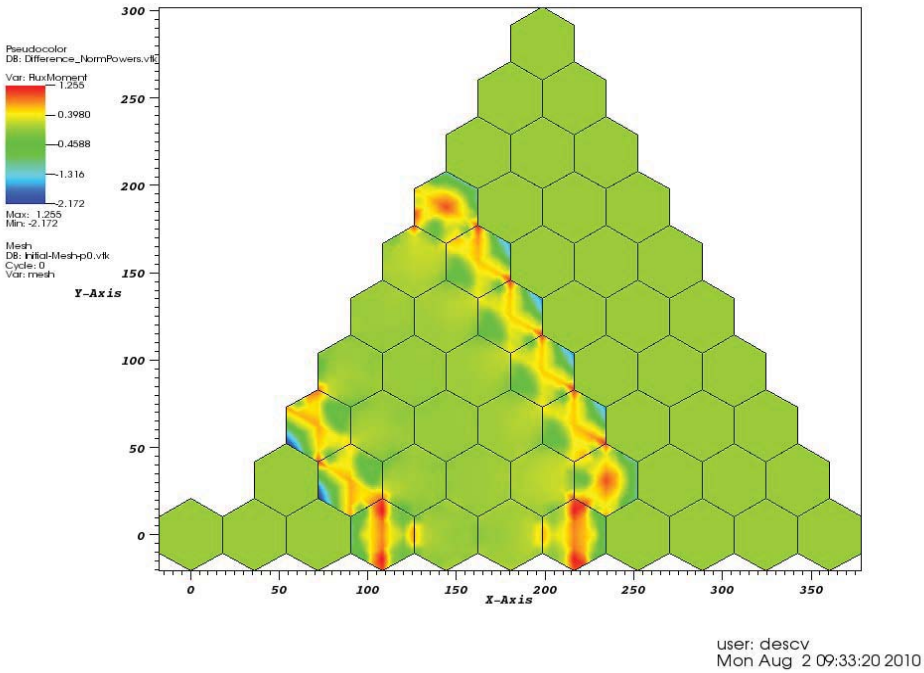

Figure A-28. Percent difference in power density between 12-group and 281-group INSTANT calculations, both using 1/12 core DRAGON lattice calculations.

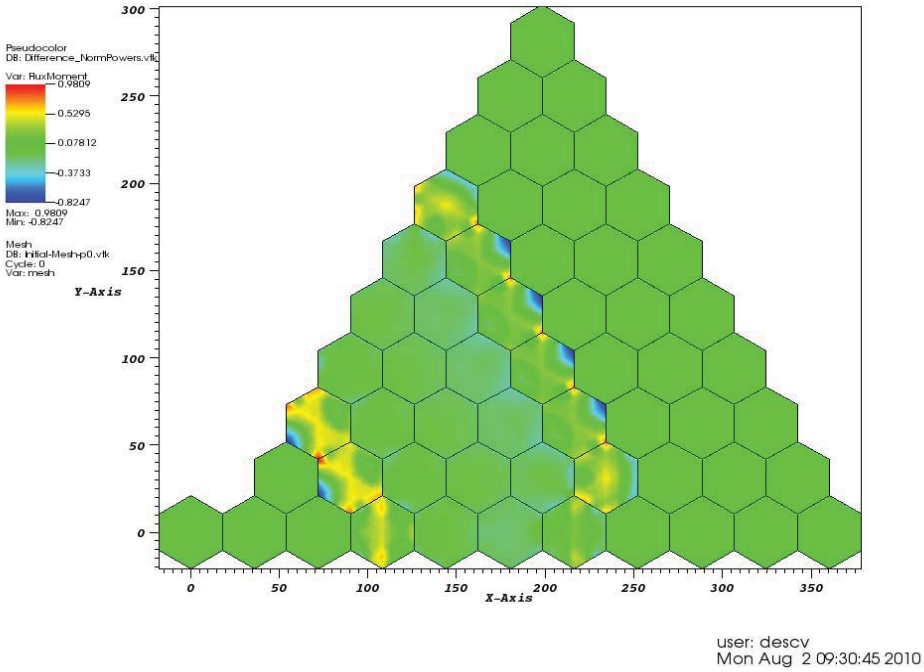

Figure A-29. Percent difference in power density between 23-group and 281-group INSTANT calculations, both using 1/12 core DRAGON lattice calculations.

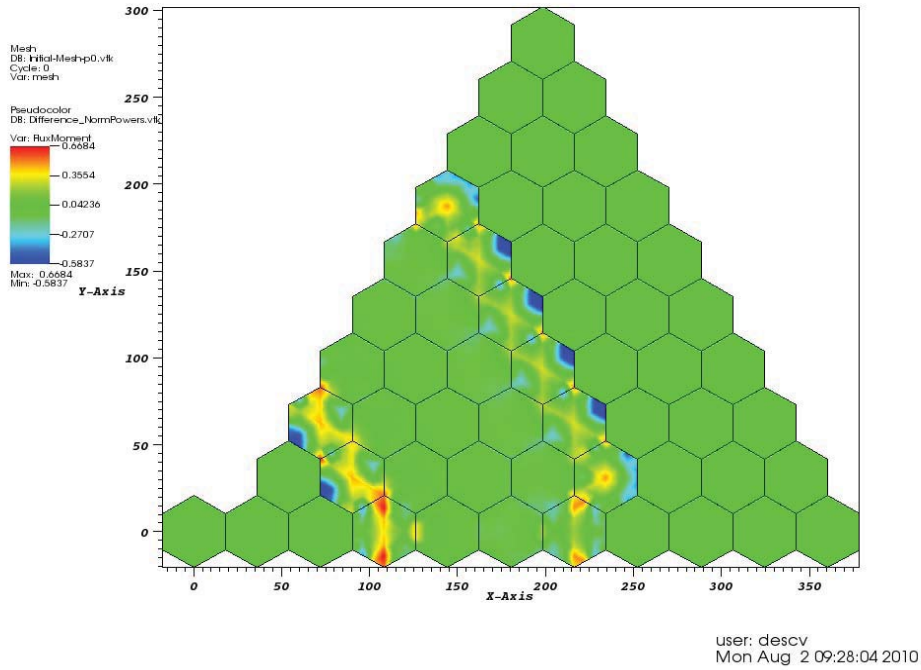

Figure A-30. Percent difference in power density between 26-group and 281-group INSTANT calculations, both using 1/12 core DRAGON lattice calculations.

Table A-7. Summary of maximum point differences in power density between coarse group and 281-group INSTANT calculations, all using 1/12 core DRAGON lattice calculations.

Number of Groups	Maximum Positive Difference (%)	Maximum Negative Difference (%)
26	0.67	-0.58
23	1.0	-0.82
12	1.3	2.2
6	2.0	2.8
4	10	14

Table A-8. Eigenvalues calculated by INSTANT for each energy group structure using cross sections from single block lattice calculations.

Number of Groups	k_{eff}
281	1.26457
26	1.26410
23	1.26491
12	1.26491
6	1.26280
4	1.23844

Between the two reference cases (single block and 1/12 core, both keeping all 281 groups at whole core level), up to 5% differences were observed in local power density, meaning that in the most rigorous single block case examined, the single block calculation still carries somewhat significant error. Figure A-32 shows the same data as in Figure A-31, only on a block averaged basis. This shows that by block, the power differences have maximum values of around 4%. Future calculations should examine the performance of supercells of various sizes at producing whole core solutions close to the reference calculations with 1/12 core lattice calculations.

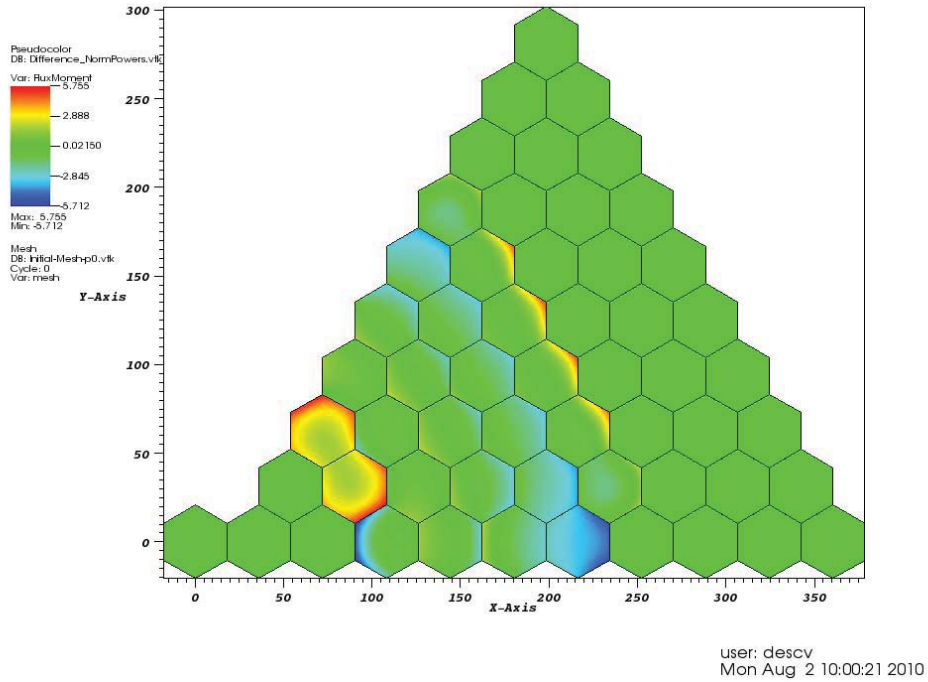

Figure A-31. Percent difference in power density between 281-group INSTANT calculations, one from single block and other from 1/12 core DRAGON calculations.

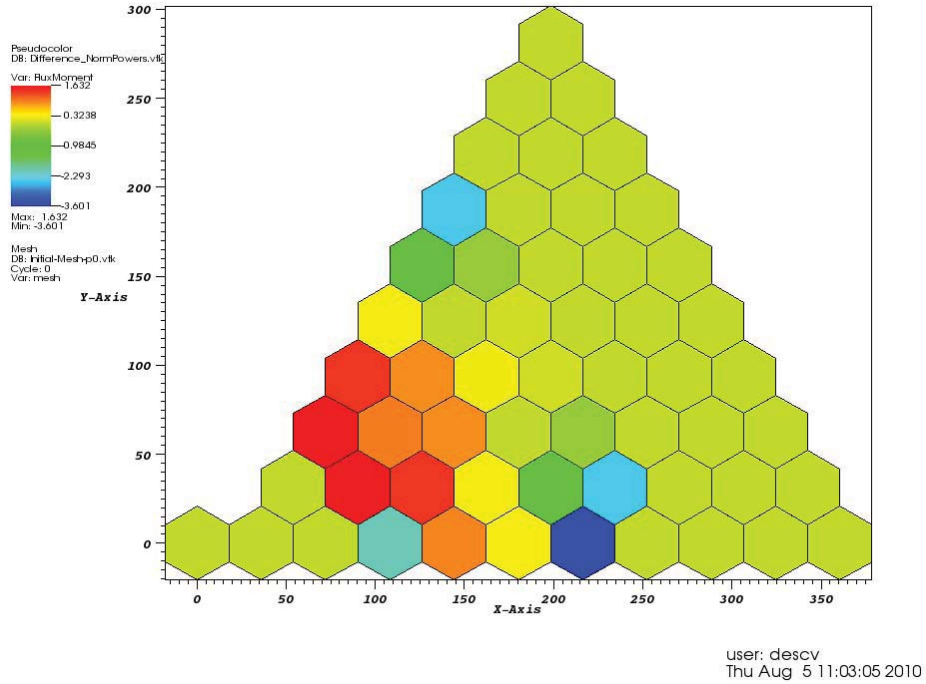

Figure A-32. Block average percent difference in power density between 281-group INSTANT calculations, one from single block and other from 1/12^{h} core DRAGON calculations.

A-2.7 Conclusions

In the preceding sections, several studies are described aimed at evaluating the effects of various lattice calculation assumptions on homogenized cross sections and to begin quantifying their effect on whole core solutions for DB-VHTR simulation. Spectra were examined directly and homogenized parameters were calculated as a function of domain size for supercell calculations. These results showed that traditional colorsets (domain sizes encompassing one half of each neighboring block) were not decoupled from their surroundings in this test case and thus would not produce a true estimate of the neutron spectrum. The much larger supercells performed much better than the colorsets, but were still not completely decoupled. In fact, in order to fully decouple the domain from its surroundings for the block of interest selected, one would have to extend the domain beyond the physical boundary of the outer reflector.

The homogenized thermal (<2 eV) cross sections, however, did stabilize much more quickly with increasing domain size. Furthermore, the supercell was able to predict power shape in the block of interest for this simple test case quite well, which means that it could play a role in a compact power reconstruction technique.

Because an imperfect estimate of neutron spectrum at the lattice level can be ameliorated by using more energy groups at the whole core level, it was of interest to examine and quantify the interplay between lattice calculation domain size and coarse energy group structure with respect to their influence on whole core results. It is intuitive that given a number of energy groups to be used at the whole core level, a large supercell will produce cross sections with better accuracy than a single block in infinite lattice or a traditional colorset. Furthermore, a 1/12 core lattice calculations should theoretically provide the most accurate cross sections of the three different schemes.

Both single block and 1/12 core DRAGON calculations were performed from which cross sections were taken for use in whole core calculations using INSTANT. For both the single block calculations and the 1/12 core calculations, a reference case was generated by omitting the energy condensation step. The results showed that, as expected, for a given energy condensation, the 1/12 core lattice calculation gave results closer to the reference case.

Between the two reference cases (single block and 1/12 core, both keeping all 281 groups at whole core level), up to 5% differences were observed locally, meaning that in the best case examined, the single block calculation still carries somewhat significant error. Future calculations should examine the performance of supercells of various sizes at producing whole core solutions close to the reference calculations with 1/12 core lattice calculations.

A-3. References

1. Y. Kim, F. Venneri, "Optimization of One-Pass Transuranic Deep Burn in Modular Helium Reactor," *Nuclear Science and Engineering*, 160, No. 1, p. 59, 2008.
2. G. Marleau, A. Hébert, R. Roy, *A User Guide for DRAGON Version 4*, IGE-294, École Polytechnique de Montréal, October, 2008.
3. A. Hébert, "A Collision Probability Analysis of the Double-Heterogeneity Problem," *Nuclear Science and Engineering*, 115, No. 2, p. 177, 1993.
4. N. Hfaiedh, A. Santamarina, "Detemination of the Optimized SHEM Mesh for Neutron Transport Calculations," *Proc. Mathematics and Computation, Supercomputing, Reactor Physics and Nuclear and Biological Applications*, Avignon, France, 12 Sept. – 15 Sept. 2005.
5. X-5 Monte Carlo Team, "MCNP – A General Monte Carlo N-Particle Transport Code," Version 5, LA-UR-03-1987, Los Alamos National Laboratory, 2003.
6. F. B. Brown, W.R. Martin, "Stochastic Geometry Capability in MCNP5 for the Analysis of Particle Fuel," *Annals of Nuclear Energy*, 31, Issue 17, p. 2039, November, 2004.
7. C. Rabiti, G. Palmiotti, Y. Wang, M. Assawaroongruengchot, H.S. Abdel-Khalik and W. C. Proctor, LDRD NE153 – "Development of Reactor Physics Sensitivity Analysis, Uncertainty Quantification, and Data Assimilation Capability at INL for Validation Methodology," Idaho National Laboratory Report INL/EXT-09-17391, March 2010.